TECHNISCHE UNIVERSITÄT MÜNCHEN
Institut für Nanoelektronik

Nanotransfer Printing and Kinetic Monte Carlo Simulations of Metal-Oxide-Structures

Benedikt Weiler

Vollständiger Abdruck der von der Fakutät für Elektrotechnik und Informationstechnik der Technischen Universität München zur Erlangung des akademischen Grades eines Doktors der Naturwissenschaften genehmigten Dissertation.

Vorsitzender: Prof. Dr. Thomas Hamacher
Prüfer der Dissertation: 1. Prof. Paolo Lugli, Ph.D.
2. Prof. Dr. Alexander Holleitner

Die Dissertation wurde am 23.11.2015 bei der Technischen Universität München eingereicht und durch die Fakultät Elektrotechnik und Informationstechnik am 10.10.2016 angenommen.

Zusammenfassung

Leitfähige Oxide, insbesondere Titandioxid, zeichnen sich durch ihre hohe Dielektrizitätskonstanten, per Dotierung veränderliche Leitfähigkeiten und relativ hohe Bandlücken aus. Dies verortet sie in einem Übergangsbereich zwischen Halbleiter und Isolator. An ihnen lassen sich fundamentale physikalische Effekte studieren, sie sind aber auch von hoher praktischer Relevanz für neuartige kapazitive oder auch photokatalytisch aktive Strukturen. Zentraler Gegenstand dieser Arbeit war daher die experimentelle Fabrikation von funktionalen Titanoxidstrukturen auf der Nanometerskala mittels einer Kombination von Nanotransfer Printing ('nTP') und der Plasmaoxidation von Titan sowie eine theoretische Untersuchung der elektrischen Eigenschaften derart wie auch anderweitig hergestellter Metall-Oxid-Strukturen mittels kinetischer Monte Carlo (kMC) Simulationen.
Die Herstellung einer dielektrischen Titanoxidschicht erfolgte erstmalig mittels eines adaptierten Plasmaveraschungsschritts im nTP-Verfahren. Dabei wurden Titanhaftschichten von 5 bis 10 nm Dicke, die inherenter Bestandteil des Transferprozesses sind, erfolgreich mit einem Sauerstoff-Plasma zu Titanoxid oxidiert. Nach weiterer Konfektionierung des nTP-Protokolls hinsichtlich Druck, Temperatur und Zeit konnten die nanostrukturierten Metall-Oxid-Schichten auf (hoch)dotiertes Silizium übertragen werden. Für die hypothetisch entstandenen MOS oder MS-Diodenkontakte ergab sich eine hohe Ausbeute $\sim 95\%$, bei hoher Integrationsdichte (> 4 Millionen Diodenstrukturen pro cm^2), einer minimalen lateralen Ausdehnung von weniger als 70 nm und ein guter Erhalt ihrer Morphologie. Eine Analyse der Strom-Spannungs-Charakteristik bestätigte die elektrische Funktionalität der Dioden. Ferner wurde die Enstehung einer dielektrischen Oxidschicht nachgewiesen. Auch das vertikale Dickenwachstum des Titanoxids wurde in Abhängigkeit von applizierten Plasmazeiten zwischen 30 s und 1200 s und Plasmaleistungen von 200 W und 600 W anhand der Transportcharakteristiken von MOS-Dioden in Kombination mit Referenzproben und einer Parameterisierung mit kMC-Simulationen quantifiziert. Dabei zeigten sich zumindest qualitativ einstellbare Oxiddicken zwischen 4 nm und 12 nm. Ferner ergab sich eine typische relative Dielektrizitätskonstante von etwa 13. Die Kombination von nTP und Plasmaoxidation von Ti erwies sich so als prinzipell zur Fabrikation von Metall-Oxid-Strukturen mit nm-dünnen Schichten auf Silizium-Substraten

geeignet.
Die elektrischen Eigenschaften von nm-dünnen Titandioxid-Schichten wurden mittels der kMC-Simulationen weiter untersucht mit einem Fokus auf deren Herstellung. Dazu wurden die wichtigsten elektronischen Transportprozesse in Titandioxid in einem 3D-Monte-Carlo-Simulationscode definiert und implementiert. Nach Sensitivitäts- und Konsistenztests des Transportmodells erfolgte eine umfassende Parameterisierung experimentell untersuchter MOS- und MOM-Strukturen. Durch die exakte Parameterisierung des Modells unter Einbezug experimenteller und theoretischer Studien zu Materialparametern von Titandioxid konnten mehrere experimentell gemessene jV-Charakteristiken (insgesamt 15 Proben, 6 aus externen Studien, 7 selbst hergestellte) mit dem Transportmodell reproduziert werden. Ausschlaggebend für die Simulationsergebnisse war dabei die Variation von Defektenergien und -positionen in Titandioxid und die Berücksichtigung des Fermi-Level-Pinnings an der Metall-Oxid-Grenzfläche. Aus den extrahierten Parameterisierungen der so gewonnenen "Fits" der jV-Profile konnten weitere Aussagen bzgl. Defektenergien und deren Kategorisierung in Abhängigkeit der technischen Prozessierung des Titandioxids abgeleitet werden. Besonders für Typ und energetische Lage der Defekte kamen je nach Verfahren entweder nur flachere Titan-Zwischengitteratome bei 0.2-0.4 eV oder tiefe Sauerstoff-Leerstellen bei 0.9-1.1 eV in Betracht. Dies ist wichtig für die Optimierung des Filmdepositionsverfahrens von Titandioxid im Anwendungsbezug, welches bei der Diskussion der Ergebnisse berücksichtigt werden musste.
Ergänzend wurde eine ähnliche kMC-Analyse an einer weiteren Al/AlO_x/Au-Struktur wiederholt. Für dieses MOM-Materialsystem wurden ebenfalls die Transportcharakteristiken von 2 experimentellen jV-Profilen 'gefittet' und Leckströme in Abhängigkeit der wichtigsten Materialparameter, Defektenergie, Defektdichte, Tunnelbarriere und Oxiddicke, für einen breiten Bereich von Einsatzspannungen analysiert. Es ergaben sich hier Defekte bei 2.6 eV unterhalb des Leitungsbandes. Dadurch wurde die Flexibilität des kMC-Modells anhand von Aluminiumoxid als weiteres, technisch relevantes Beispiel demonstriert und Implikationen für dessen anwendungsbezogene Optimierung abgeleitet.

Abstract

The focus of this work was the experimental fabrication of functional titanium oxide structures on the nm-scale fabricated by a combination of nanotransfer printing (nTP) and plasma oxidation of metallic Ti as well as the theoretical investigation of their electrical properties by kinetic Monte Carlo (kMC) simulations.
First, the fabrication of a dielectric layer of titanium oxide was accomplished within the nTP-process by confectioning this integrated step, usually used for surface activation of 5 to 10 nm-thin Ti adhesion layers, towards an oxidation of those metallic layers. The formed metal-oxide-layers were reliably transferred onto (highly-)doped Si substrates by optimizations of existing nTP protocols. Thus diodes (potentially MOS or MS ones) were produced at a high yield of $\sim 95\%$, high integration (> 4 million diode structures/cm^2) over macroscopic areas at good fidelity of their morphology and sub-70-nm features. The diodes were electrically functional and a comparison of the current-voltage-characteristics of nm-scale and μm-scale showed both MS and MOS-characteristics depending on the plasma treatment. The vertical growth of the titanium oxide tunneling dielectric was quantified in dependence of the applied plasma times between 30 s and 1200 s and powers of 200 W and 600 W assisted by e-beam-reference samples and a kMC-parametrization of the transport behaviour. Thus the oxide thickness was controlled qualitatively between 4 nm and 12 nm. For the layer a relative permittivity of 13 was determined. This supposes the applied combination of nTP and plasma oxidation as a highly-efficient method to fabricate metal-oxide-structures with nm-thin layers - in particular with respect to typical applications. Secondly, electronic properties of titanium dioxide nanostructures were implemented in and analyzed by a 3D-kMC-simulator with respect to electronic transport processes and fabrication methods. Supplementary sensitivity and consistency checks of the transport model for titanium dioxide were performed, followed by an extensive parameterization of MOS and MOM-structures. By accounting for the Fermi-level pinning at the metal-oxide-interface to parameterize the injection barrier, the simulations were driven to high accuracy. Defect energies, types and defect positions were of particular interest and examined into more detail by an extensive literature study on titanium dioxide. We found that for an acurate reproduction of measured jV-characteristics (15 samples were fitted in total, six taken from literature and seven own ones) also the specific

film-deposition method had to be respected to explain the outcomes of the simulations. Thus results on defect energies and their categorization in dependence of the fabrication method could be drawn from kMC-parametrizations of and fittings to jV-characteristics of differently processed samples. Most importantly, the defect energies in the band gap of titanium oxide were found to lie either in shallower levels at ∼0.2-0.4 eV, attributed to Ti interstitials, or deeper ones at ∼0.9-1.1 eV attributed to oxygen vacancies. This is of high significance for choosing a method of titanium oxide convenient with the specific application.
Next, the kMC-simulations were performed for an Al/AlO_x/Au-structure. For this further MOM-system the transport characteristics from two measurements were reproduced, too, and gate oxide leakage currents were analyzed by kMC in dependence of the most important material parameters, i.e. defect energy, defect density, tunneling barriers and oxide thickness for operating voltages up to 4.2 V. Here we found defects at 2.6 eV below conduction band minimum. The further example of AlO_x demonstrated the flexibility and validity of the kMC-model and implications for practical optimizations of AlO_x comprising structures were derived.

Contents

Chapter 1

Introduction

Historically, research and development on semiconductor materials was driven to a big part by device miniaturization, a main cost factor, governed by the well-known paradigma of semiconductor industry, Moore's law,[1] see Fig. 1.1a, which is about to reach its physical limits, especially in terms of SiO_2-based MOS-devices, see Fig. 1.1b.[2, 3] Today, however, low environmental-impact establishes as a further technological criterion for novel functional semiconductor materials next to cost-efficient fabrication and integration. Despite of all progress, rooms for improvement in modern material science and engineering remain large.

One of the most promising materials in this context is titanium dioxide, TiO_2. TiO_2 is low-toxic and environmentally friendly and has already been of great scientific interest for decades, because it combines the remarkable properties of a conductive metal oxide and of high-k dielectrics.[4, 5] Research on "titania", referring to the oxide minerals of Ti, has been accelerated also by their broad applications for electronic, photovoltaic or photocatalytic devices comprising metal-oxide-semiconductor (MOS) or metal-oxide-metal (MOM) junctions. The challenge of research on TiO_2 is twofold: On the one hand, new materials like TiO_2 are by far not as well understood theoretically as industrially as established ones, such as Si and its oxide SiO_2, and their electronic properties are still debated. On the other other hand processing technologies for it have to be controlled better to promote its theoretical understanding.

These aspects motivate the approach of the present work, outlined in the subsequent two sections. Firstly, from the experimental side, nanotransfer printing (nTP) technology, as a versatile enabling technique in semiconductor device fabrication, is employed in order to tailor the nTP protocol towards the efficient fabrication of MOM and MOS-junctions comprising such titanium oxide layers. Going from micro- to nanoscale functional electronic devices, such as MOS-diodes, were succesfully fabricated, characterized and analyzed. Secondly, coming from a theoretical perspective, kinetic Monte Carlo-simulations, a computational tool placed between ab initio calculations and macroscopic experimental observables, is employed in order to study the properties and electronic characteristics of TiO_2. By extensive parameterizations and improvements to a simulation code for high-k

dielectrics, developed during a work by G. Jegert, first published in [6], valid fits to jV-curves of experimental MOS and MOM structures were obtained and conclusions on important material parameters were drawn, also respecting fabrication techniques. The same kMC-model was also validated and used to parametrize aluminium oxide, AlO_x as a further gate dielectric of high technological relevance.

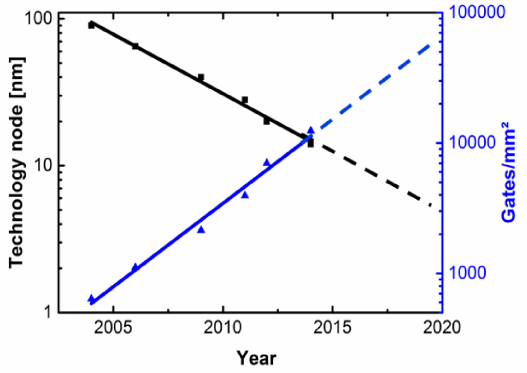

(a) *Miniaturization of devices: Structure size has kept on halving and number of gates doubling every two to three years in accordance with Moore's law from 1965.[1] Data after [7].*

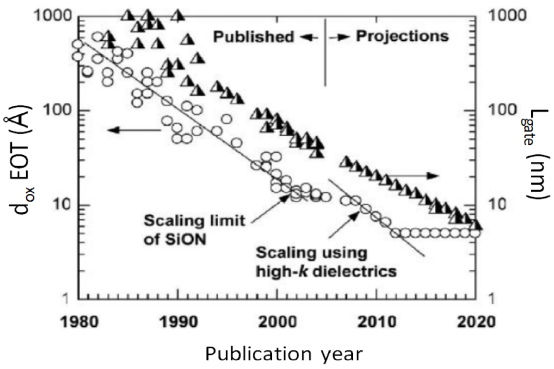

(b) *Minimizing characteristic structure sizes, i.e. effective oxide thickness (EOT) d_{ox} and gate length L_{gate}, of Si-CMOS logic transistors and potential of high-k dielectrics taken from Hiwai.[3]*

Nanotransfer-Printing of MOS-diodes comprising TiO_x

Regarding the first, experimental, part of this thesis, lithographic printing techniques were central. Those establish more and more not only for the efficient fabrication of fundamental, mostly electronically active, micro- and nanoscale structures but also entire devices. A highly compact overview on the huge variety of readily transfer-printed materials and structures contains: [8]

1) inorganic semiconductors, e.g. nanomembranes, nanowires or quantom dots,
2) metals, e.g. as flat or nanostructured thin films or nanoparticles, see below,
3) carbon, e.g. thin diamond films, carbon nanotubes and their broad applications,
4) organic materials, e.g. thin films, nanomembranes, self-assembled structures,
5) colloids, biological materials, e.g. thin films, nanomembranes, self-assembled structures.

A more extended summary of the possibilities and state-of-the-art of printing techniques will be provided in chapter 2.1. Due to the diverse fabrication possibilties, the focus will be strongly placed on the applications of the two most basic transfer methods actually used in this thesis, i.e. nTP and μCP, whereas nano imprint lithography (NIL), which was of minor importance here, is briefly reviewed only in section 3.3.
NTP combined with a plasma oxidation process was investigated to fabricate functional MOS-stacks comprising Au and p^+-Si as electrode materials of broad and common use and nm-thin TiO_x-films as a functional dielectric layer. This is motivated from the fabrication perspective. Former deposition techniques for TiO_2 include sol-gel-derivation[9], (plasma-enhanced) atomic layer deposition (PE-ALD)[10, 11, 12, 13], thermal oxidation[14], e-beam evaporation[15], metal-organic chemical vapor deposition (MOCVD)[16] and reactive magnetron sputtering[17]. But most of them are not or only hardly compatible with state-of-the-art nTP- or μCP-protocols for transfer of metals or transfer of metal oxides from Si or polymer stamps, because certain (noble) metals, as the prototypically catalytic active Au or Pt are not available, temperatures during deposition are too high, or the conditions of the techniques during the deposition of transfer materials on templates are inconvenient, especially for polymer stamps. The TiO_2-deposition by sol-gel-methods, MOCVD and ALD must be considered too dirty, making a malfunction of created MOS junctions very likely. Sputtering is generally too hot to preserve the structures on the stamps. This leaves behind basically two ways to form the desired nm-thin titanium oxide/metal-stacks: Firstly, there is direct e-beam or thermal deposition of TiO_2 from a precursor which was already investigated and applied for TiO_2 by many other groups before.[14, 15]. This physical vapor deposition (PVD) from a precursor, explained in section 3.1.1, was used only as a reference techniques in chapter 6.2. The second remaining approach is the plasma oxidation of an e-beam or thermally deposited nm-thin Ti adhesion layer which is by iteself integrated and approved in our nTP protocol, as also in the ones by others.[18] The second approach was in the focus here, since the oxide formation by a plasma application is still badly understood. Only the studies by Tinoco and Romero[19, 20] are some of the few on it. Additionally, it is supposed to be compatible with nTP making a controlled plasma oxidation step a technologically useful extension of the existing nTP protocol to fabricate MOM and MOS devices.
NTP is generally known to provide large area patterning at shorter process time and lower costs than other nanolithography techniques, such as e-beam lithography (EBL), for example. Since it is a young technology, the capabilities of nTP to maintain or even improve the electronic properties of transfer-printed structures have not yet been fully investigated. Aside from the start-of-the-art of structures and devices from nTP given in chapter 2.1, this is particularly true for nanostructures containing functionalized metallic oxides, such as titanium dioxide. Especially the integration of TiO_2 into MOS-diodes or photoactive MOS-structures by printing techniques has not been investigated in a systematic way, see also chapter 2.1.[8, 21] A titanium oxide from naturally oxidized Ti adhesion layer has already been assumed to be present in the first microscale-

Contact-Printing (μCP) studies.[18, 22] Although the potential benefits for the electrical functionality of devices is almost evident, if fabricated in a controlled manner, a systematic investigation of a controlled oxidation of the TiO_2-layers is still missing. Moreover, printed ordered structures comprising a functional TiO_x-layer used to be either not of nanoscale in contrast to this work, or, if they were nanoscale, they were no ordered structures, but Au islands of random size and location on TiO_2 surfaces, for example.[23, 24] So available works have not yet looked closer at the on-stamp-formation and direct printing of titanium oxide layers and must rather be considered complementary to the present work. Here the plasma-activation process of nTP is exploited to introduce a titanium oxide into the ordered nanostructures transfer-printed by nTP, finally trying to control the oxide thickness at the same time. This extends the work by Bareiss et al. that concentrated on nanorectennas comprising TiO_x for energy harvesting[21] which did not yet quantify the oxide formation in dependence of plasma parameters. Eventually, it is for certain that the plasma-grown-TiO_x-layer present due to the surface activation step of nTP is detrimental for all typical electronic applications: MOS-diodes, rectennas using TiO_x as tunneling dielectric as well as photocatalytic structures using anatase as photoactive material or amorphous titania as passivation or hole blocking layers for water splitting[25, 26, 27, 28], storage capacitors with TiO_2 as high-k dielectric or resistive switches, one of today's hot topics in electron device research.

Therefore, in the practical parts of this thesis, the nTP process was specifically confectioned and demonstrated for geometrically highly-ordered Au-TiO_x-Si (MOS) structures of sub-70-nm-size over large areas, see section 6.2.1. Remarkably, the morphology of the transfer-printed nanostructures resulting from the nTP process is comparable to conventional nano-scale lithography, as the transferred nanojunctions were completely intact at a high yield of over 95% and minimum lateral structure-sizes below 70 nm over extensive substrate areas, as characterized by SEM imaging in section 6.2.2. Next, an understanding of the formation and the dielectric properties of both plasma-grown and transfer-printed TiO_x films was considered detrimental for any of the potential applications of the titanium oxide. Therefore, most importantly, the plasma oxidation process of the Ti layer itself and the formation of the plasma-grown TiO_x intregrated into the nTP-protocol, was investigated systematically. The focus is placed here on the electronic quality and the characteristics of the oxide in terms of MOS-diodes, whereas the phase of these titanium layers is explicitly not studied (appropriate characterization methods, such as XPS, were either not available or not applicable). Hence, titania are also generally referred to as TiO_x instead of TiO_2 in this work, when talking about experimentally produced oxides of Ti. It is shown that after a temperature-enhanced-nTP process this TiO_x-layer is comprised between the Si substrate and the nanostructured Au-part of the transferred pillars.

Results on an electrical characterization performed by conductive Atomic Force Microscopy (c-AFM) measurements confectioned to electrical measurements on the nTP-structures are discussed in section 6.2.3 indicating the existence of nm-thin oxide tunneling barriers under appropriate plasma conditions. The j-V-characteristics of these

nTP-samples are compared to an ensemble of probe station j-V-measurements on μm-scale pads fabricated by the same protocol as used for the nTPs and similarities are discussed in section 6.2.4. The thickness of the oxide layers fabricated under varied electrical work (="time × power") applied by a radio-frequent microwave to the plasma are estimated by a comparison to optically defined pads comprising TiO_2 layers which were directly e-beam-deposited from a precursor and whose thickness could be measured by a Dektak-profilometer. On the basis of the approximate plasma-oxide thicknesses from this comparison and TiO_2 parameters from literature, kMC-fits to the measured j-V-curves were accomplished. These kMC-simulations, see section 6.2.5, provide the dominant conduction mechanisms through the oxide in the MOS-pillars and further material parameters, such as oxide thicknesses. Moreover, from these thicknesses derived by kMC the effect of the oxygen plasma on the oxide formation is quantified in section 6.2.6 in form of a coarse calibration of the oxide thickness in dependence of the RF-applied plasma work, i.e. plasma time × power. Finally, in section 6.2.7, transport processes are anaylzed and relative permittivities of the layer were determined by the means of kMC-derived oxide thicknesses and additional CV measurements resulting into a value of $\epsilon_r \approx 13$ in agreement with other studies on nm-thin titanium films.[15, 29] We conclude on our findings in section 6.2.8.

Device Characteristics and Material Parameters of TiO_2 and AlO_x from kMC

The second task besides the experimental one, was the simulation of MOS- and MOM-structures comprising the technologically prominent oxides TiO_2 and AlO_x, as a supplementary example, by kinetic Monte Carlo methods in order to extract parameters of these materials and compare them with ab initio as well as experimental values. Having approved the validity of the kMC-model by a parametrization, experimentally hardly examinable extreme cases of material parameter combinations were tested.
In the very first place, the different phases of TiO_2 are repeatedly discussed as promising candidates for high-k-dielectrics due to their dielectric constant of 90 ($\epsilon_{||}$) to 180 ($\epsilon_{\perp}$) for rutile [30, 31, 32, 33], 10-20 ($\epsilon_{||}$)[29] and 30-40 ($\epsilon_{\perp}$) for anatase[33, 34, 35, 36, 36, 37] and ∼80 for brookite [38]. Both in sections 2.2 and 6.3.1 an overview on experimentally and theoretically determined electronic properties and applications of TiO_2 is given. Except for a few studies that provide thorough analytical experiments on surfaces combined with DFT calculations [39, 40], most of the studies provided in sections 2.2 and 6.3.1 are either only application-oriented or fundamental ab initio calculations on ideal models of titania. But a reliable way to attribute experimental characteristics to certain types of defects, to distinct defects by their properties and link the type of defect to chemical processing has not been achieved, although it would be very practical and illustrative. KMC-simulations are a viable method in this context to expand the explanatory power of measurements and the relentless practical limitations of analytic calculations.[41, 42] Thus kMC has established as a further computational tool to bridge the gap between experiments and ab-initio calculations. By its definition it provides a modular way to implement a physical model of any rate-determined system, in particular transport pro-

cesses in semiconductor-structures. However, the particular assumptions applied in the physical models must be valid for the specific material and are in need for a very reliable parameterization with an exact and consistent choice of many input parameters, especially the trap levels.
Therefore, the simulation part of this thesis aims at gaining a better understanding of titanium dioxide as a conductive oxides, fabricated by typical methods, like MOCVD and ALD, but especially thermal and e-beam evaporation, with respect to their particular usage for MOS-device fabrication. To simulate charge transport of nm-thin dielectric TiO_2 films properly, kMC-simulations must take into account electrical properties and material parameters of TiO_2 induced by these fabrication methods, especially the defect levels which were a focus of our kMC-parametrization. Having understood and implemented the theoretical properties, the central goal of the simulations was to reproduce experimental j-V-characteristics ('fits') of real devices, both such ones from literature and own ones measured on the nTP-fabricated Au/Ti/TiO_x/p^+Si-junctions. As soon as the applicability of the kMC-model is validitated in terms of TiO_2 or also AlO_x, conclusions on the material properties, especially on defects, with regard to devices were drawn.
The kMC-scheme and appropriate charge transport rates were derived from first-principles already decades ago, as presented in chapters 4 and 5 and the major part of them was already implemented in a working kMC-simulator by G. Jegert.[43] Extensions and adaptions were necessary for the simulation work. The titanium-oxide-specific adaptions required new consistency tests of the model in terms of TiO_2 parameters, sensitivity analysis and preliminary model validations which are summarized always right after the introduction of the processes in the model chapter 5. Thus, finally, the principle applicability of the model for TiO_2 is concluded, supported by supplementary drift-diffusion-simulations, in section 5.5. Having accomplished this task, the fundaments for the actual kMC-study were laid satisfying the state-of-the-art of TiO_2-current simulations, as outlined in section 2.2.2.
Chapter 6.3 actually resembles the most central results of this thesis. It begins with an overview on the nature of the defect levels in titania and a theoretical evaluation of their effects in section 6.3.1, because these are essential for the electronic properties of the oxide and a correct parametrization of the simulations is a non-trivial part of the model. Defects are categorized by types and energies in TiO_2 found in recent literature, focusing on anatase, and their dependence on the chemical treatment of the sample is discussed. Up-to-date literature on the most important spectroscopic studies as well as ab initio (DFT) calculations on the type and energetic location of defects in TiO_2 is evaluated in section 6.3.1. From this information the material parameters can be varied more specifically to TiO_2, so that fits to actually measured MOS- and MOM-characteristics are found for differently fabricated samples in section 6.3.5. The determined parameter sets for the fits are also discussed in terms of their physical viability and correctness in section 6.3.5. Thus further conclusions on the nature of defects in TiO_2 are drawn from kMC.
These convincing results on TiO_x induced the idea to transfer the kMC-model to other

technologically relevant oxides, such as AlO_x, presented in section 6.4 starting with an introduction in 6.4.1. This oxide was produced by a plasma-oxidation process at our chair. It was simulated as a MOM-contact with an Al cathode and Au anode with the model being specified in section 6.4.2. Again fits to experimental jV-profiles of such MOM-structures were determined by a parametrization of AlO_x that is performed in section 6.4.3 like for TiO_2. By transferring the kMC-model to this further oxide material, its versatility is demonstrated. Corroborated by three materials in total, i.e. by ZrO_2 in the thesis of G. Jegert [43], as well as TiO_2 and AlO_x here, it is a viable assumption to expand the parameter space with this kMC-model further from the fits and use it to qualitatively predict the device behaviour of the AlO_x-comprising MOM-structures in terms of important material parameters, as done in section 6.4.4. The conclusions of these results are summarized in chapter 6.4.5. Finally, an outlook on future studies involving the plasma-assisted fabrication of ultrathin oxide films combined with nTP and further kMC-simulations of these nanostructures is provided in section 7.

Chapter 2

State-of-the-art

2.1 Functional metal structures fabricated by nTP

In nTP and μCP, two additive transfer techniques, one or more layers of transfer materials, the 'ink', is transferred onto a substrate directly from a mold which can be previously patterned on the nano- or microscale, respectively. As enlisted above many other materials apart from metals have already been combined with nTP technology.
In the first demonstrations of transfer printing by Loo and Rogers et al. [18, 22], still called μCP, as stamps were patterned on the microscale, an e-beam evaporated flat Au film was transferred directly from a prefabricated mold to a Si substrate assisted by a SAM. For example, 3-mercaptopropyltrimethoxysilane on PDMS stamps[44] or 1,8-octanedithiol functionalization of GaAs stamps[45] is possible. Many further demonstrations of nTP-transferred thin Au nanopatterns followed. [46, 47, 48, 49, 50] Both μCP and nTP as additive transfer printing techniques, but also NIL, the "side topic" here, are simple, well scalable and versatile, since they can be combined easily with various materials as well as chemicals or physical methods. Thus many further variations of these techniques exist, such as step and flash imprint lithography (SFIL), UV-NIL, RT-NIL, to name just a few which are extensively discussed in several review papers, such as the one by Rogers et al. [8] which we refer to for the given section.
Generally, most experiments tested different environmental conditions and preprocessing techniques, combined new different materials, or transfer-printed complex, integrated two- or three-dimensional hierarchical structures on micro- to nanoscale - all with respect to a functional electrical integration and reliable fabrication at high yield and high resolution. Thus nTP became an attractive technique for materials assembly and device fabrication.[21, 51, 52, 53, 54, 55, 56, 57]

Concerning resolution, positive structure sizes have been demonstrated that range from macroscopic, flat layers over several cm^2 [58] down to several tens of nm over large areas for transfer-printing, as outlined in this work. Even smaller, few tens nm-thin gaps ($\lesssim$ 50 nm), i.e. negative structures, were achieved, e.g. as insulating gaps between Au

electrodes by suspending layers touching the underlying substrate [59], and by NIL even only 20 nm wide gaps are possible [60].
The further overview here shall concentrate on the state-of-the-art of the additive transfer of thin, patterned metal films for electronic devices.
For the resolutions of transfers of metal nanopatterns from Si stamps by nTP the benchmark achieved in this work in terms of smallest lateral features is about 50 nm, while also 40 nm are possible at our chair.[61] Even smaller resolutions around 20 nm over large areas using polymer stamps were reported most recently by the leading groups in this field, as depicted in Fig. 2.1. [62]

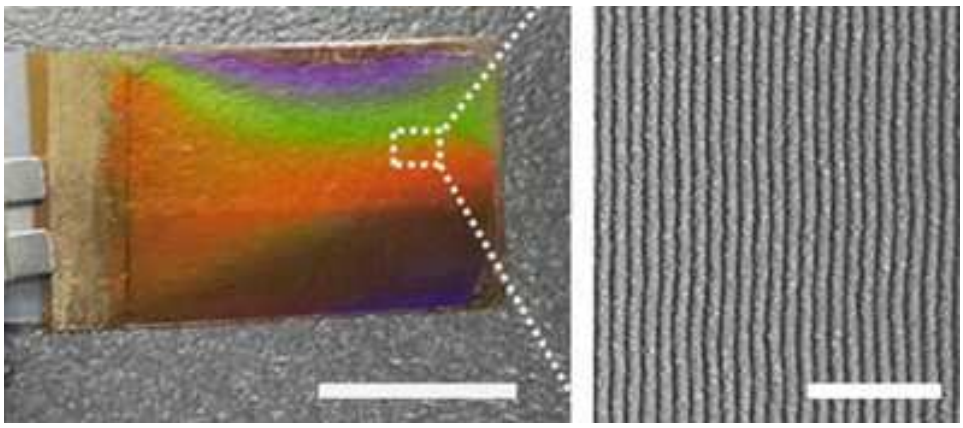

Figure 2.1: *State-of-the-art in nTP as reported by Jeong et al. in 2014: 20 nm-wide Au lines were transferred from polymer stamps on replica/PI-films, image taken from [62], scale bar not specified.*

Transfer yields of metal films, like Au, from Si stamps onto Si substrates are tremdendously improved by the deposition of Ti films on Au that turn into a native oxide and form Ti-O-Si bonds when transferred on Si or also SiO_2 [18, 63, 64, 65]* Removing water from the air, enhanced even more by heating, promotes this building of oxygen-bridges which improve the adherence of stamp and substrate surfaces.[66, 67] An advanced technique for this is laser-induced heating enabling "laser decal transfer" (LDT). [68, 69] This allowed recently for the 3D fabrication of layers of metallic bridges between printed silver paste contact electrodes. Having thicknesses below 10 μm such bridges morphologically beat wirebonding or other commonly used interconnect techniques.[69]
Complex, hierarchical 3D structures are generated by the sequential deposition of various material layers on the stamp followed by a single transfer step [49, 70] or optional, further transfer printing steps, repeated on the same spots of the sample. Different material- and structure-specific processing methods exist which are helpful to accomplish ordered multilayer structures, such as the usage of anti-adhesion-SAMs or cold welding to create contacts between two well-sticking gold regions.[53, 70, 71] From the device perspetive, entire MIM rectennas [72, 73] or diodes [56, 57], but also MIM capacitors [18] and nega-

*The same effect can be used for Al films forming Si-O-Al bonds, too.

tive index metamaterials [74] have been transferred this way. Its capability to structure non-planar, more complex substrate morphologies is one of the biggest advantages of nTP of metals compared to more established lithographic techniques.[49, 75, 76]
NTP protocols for metallic films were also adapted to lower-dimensional structures such as nanowires, nanorods and nanoparticles, as demonstrated for example for the additive transfers of superlattice nanowire patterns, SNAPs, from various metals like Au, Pt, Ti, Al, Ni or Cr.[77] To bring nanoparticles onto structured stamping templates, colloidal suspensions that predominantly fill recessed regions of stamps and resemble an ink of nanoparticles that can then be transferred.[78]
Besides Si stamps also GaAs and glass are etchable stamp materials of common use.[18, 22] The template fabrication for lower-dimensional structures is mostly performed via molecular beam epitaxial (MBE) multilayer growth of alternating GaAs and AlGaAs, subsequent selective etching of AlGaAs, e.g. by hydrofluoric acid (HF), producing positive GaAs ridges.[72, 77, 78, 79]
The major challenge with such hard, inorganic stamp materials compared to soft stamps, e.g. from PDMS or PFPE, is bringing them into conformal contact with the target substrate. Thus, polyurethane acrylate (PUA) polymers received attention as flexible backing layers [80, 81], e.g. to print Au on functionalized ITO or PET surfaces in the form of nanocones.[47, 82]
In terms of electronic properties of the transfer materials, the focus of this thesis, the quality of electrical contacts between transferred metal films and semiconductor substrates [22, 45, 83] or the thermal conductivity of such an interface are essential.[84] Transfer materials also behave differently in terms of their morphological and electrical properties before and after the transfer, e.g. Cu becomes more insulating after a transfer.[50] The reported electrical performance of Au contacts brought onto either 1,8-octanedithiol/GaAs or pure GaAs substrates, either by nTP or by direct evaporation, is also interesting, as comparable to the present work. The latter method (evaporation) turned out to be worse for a controlled large-scale fabrication of such electrical contacts, since always a number of shorts are created by direct Au-GaAs contacts dominating the current-voltage characteristics and covering the transport behaviour of the 1,8-octanedithiol-layer.[83] Transfer-printed contacts, however, preserved the electron-insulating behaviour of the octanedithiol-layer.The cited studies are of particular interest for the present thesis, because comparable behaviour of the transport characteristic of the Au/Ti/TiO_x stacks brought onto Si substrates by nTP are expected from stacks with a thicker TiO_x-film, reported to act as a hole blocking layer, in contrast to such ones that are supposed to have a negligible TiO_x layer in between, as presented in chapter 6.2.
In terms of the state-of-the art at our chair the functionality and reliability of our central nTP protocol was approved by the results reported in [54, 57, 59, 61, 72, 85]. These results were optimized for the used Au/Ti combinations. As remarked above, the next logical step for the extension of our transfer protocol using the noble metal Au and the transition metal Ti, especially with respect to potential devices, was the systematic in-

vestigation of the plasma-oxidation of the Ti adhesion layer in nanoscale MOS-junctions. Thus different TiO_x-comprising material stacks were to be transferred reliably and characterized electrically with a special respect to a potential application for electrochemical or memristors, as outlined in chapter 1. In terms of TiO_2 for energy harvesting of photovoltaic and photocatalytic devices, the transferred oxide must not only be easy but reliably producable preserving its specific electronic properties and low environmental impact.[86] Designing the electronic properties of titanium oxide towards such specific purposes is a complex task and vivid field of research of its own, as seen by the studies in [87, 88, 89, 90, 91, 92]. At the same time nTP is a viable large-scale manufacturing technique with high reliability and optimized throughput at minimized process cost. This makes it very attractive, especially for the approach undertaken in this work.

State-of-the-art of nTP aside from Metals: Inorganics and Organics

To provide an overview on the possibilities of nTP besides the processing of metals, also progress on further inorganic and organic materials, esp. semiconducting ones, shall be given briefly here. Just as for nTP of metals, the most intersting fields in terms of nTP here are electronics [93, 94, 95], photonics [96, 97] or sensors.[98, 99] Their processing and structuring for nTP is frequently combined with the other lithographic methods like EBL, NIL or AFM to name just a few.[100, 101] Thus thin film transistors[102, 103] or ultracompact Fano filters have been demonstrated, for example, using inorganic semiconductors in nTP.[104, 105] Inorganic semiconductos, e.g. CVD-grown, single-crystalline GaAs, GaN and InP, are also applicable as inks by the same principles as for Si.[103, 106, 107, 108, 109, 110, 111] Their main attractivity lies in direct band gaps, high electron mobilities, high saturated drift velocities and a wide window of temperatures for processing and operation.[110]
Many industrially-attractive semiconductor devices have been accomplished this way, such as transistors [112, 113], light emitting diodes (LED) [114], photodetectors [115] and solar cells [116]. A remarkable benefit of nTP in terms of the combination of inorganics with plastic electronics is that it allows to separate the mostly temperature-affected organic substrates from the high temperatures for the processing of inorganic semiconductors, e.g. during their growth or for establishing ohmic contacts, which happens readily on the template before a transfer-print.
From the structural perspective, nanowires and nanoribbons of GaAs and InP, for example, created by anisotropic chemical etching on the template were already transferred by nTP protocols similar to the ones for Si wafers[110, 111] As a further example, etching anisotropic undercuts into Si allowed also for the selective release of AlGaN/GaN or GaN/AlN sheets originally grown on <111> Si wafers.[108] Also sacrificial layers have been successfully introduced to enhance fabrication protocols.[116]
Besides transfer of metals and inorganic semiconductors, a very important variant of nTP is the transfer-printing of organic materials. It is interesting for large-area electronic devices based on low-cost plastic materials, such as OLED displays or patterning

of electrodes with organic materials, e.g. printing pentacene onto ITO,[117], PEDOT onto pentacene [118] or also PEDOT:PSS bilayers on Au [119] for OLEDs and photovoltaic devices. Transistors from pentacene on organic substrates were accomplished with channel lengths and mobilities comparable to the ones from high-resolution patterning methods.[113, 120] Moreover, functional multilayer thin film capacitors have been printed onto plastic substrates by nTP which can compete with traditional Si-based capacitor structures with gates defined via photolithography and lift-off.[102, 103] Further organic-based devices include optoelectronic components, like integrated photomasks or thermal actuators.[76] Also the seemingly simple printing of photoresist in a structured manner has been investigated, since controlling such an efficient printing process on the nanoscale brings about many new opportunities for structuring, scaling and integrating devices in all dimensions.[121]
To conclude this overview on the state-of-the-art on nTP, speaking for metal, organics and inorganics, apart from the focus of this work, simplification and easier-handling of process steps, easier handling of equipment and facilities, e.g. in terms of stamp fabrication, even larger patterning areas and higher throughput are the main challenges that have to be mastered for industial mass production by the nTP technology in the future.

2.2 Electronic properties and kMC-simulations of TiO_2-films

Furthermore, thin TiO_x-films are of a theoretical interest on their own. Hence, in the first place a short overview of the most significant scientific advances in the research on titania in general, but with a focus on anatase TiO_2, and its electronic and electrochemical applications shall be provided. Then special emphasis is put on previous works on the simulation of currents through such dielectric layers of functional metal oxides by kMC-methods similar to the one applied here.

2.2.1 Electronic properties and applications of TiO_2-films

Most prominently of all applications of TiO_2, nanocrystalline, mesoporous anatase TiO_2 forms the basis for dye sensitized solar cells (DSSCs) which have pushed experimental research on this crystaline phase to a high extent, starting with the works by Grätzel et al. [123, 124, 125, 126, 127, 128, 129], evolving to hybrid solar cells [130, 131, 132, 133, 134, 135] and finally to the currently increasing work on perovskite solar cells.[136, 137]
The principle of such a DSSC is shown Fig. 2.2a. This is a representative device making use of the special properties of conductive oxides, in this case typically fluoride-doped tin oxide (FTO), which is even a transparent conductive oxide (TCO), and TiO_2 as charge separation layer with a high surface-to-volume ratio which is additionally also itself photocatalytically active. The anode of a DSSC is covered with a mesoporous layer of anatase TiO_2 on which fluorescent dye molecules, for example Ruthenium, $Ru^{2+/3+}$, are attached. The spacings inside the mesoporous layer is filled with an electrolyte, e.g. I^-/I^{3-}. Impinging photons are absorbed by dye molecules and excite electrons. The

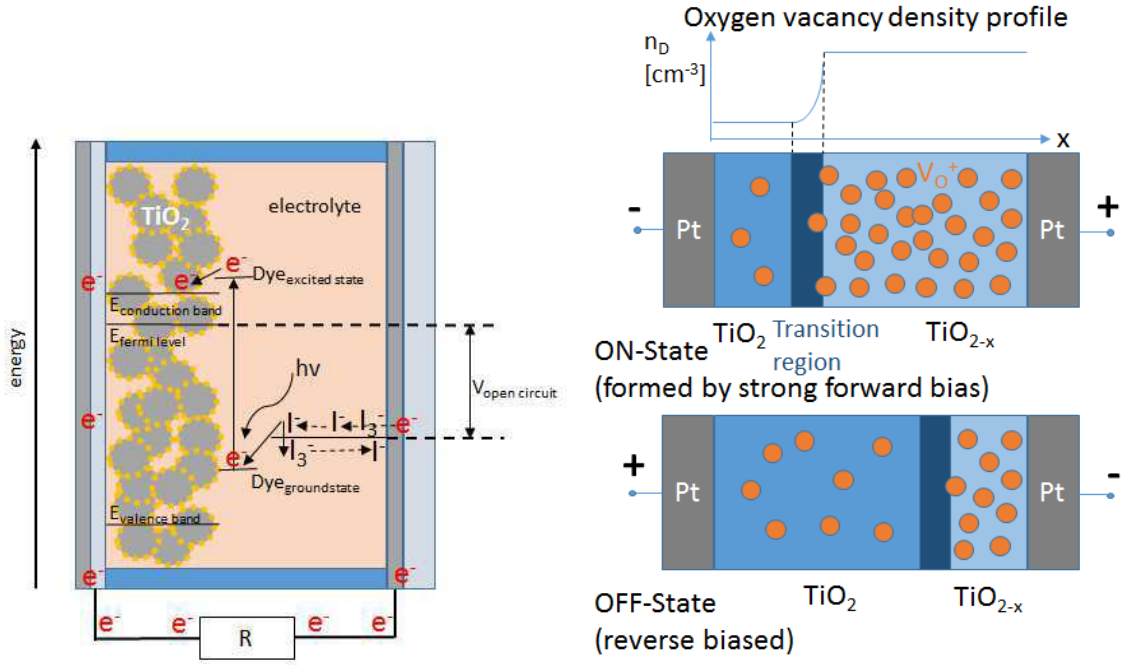

(a) *DSSC schematics with sketched band diagram of TiO_2, $Ru^{2+/3+}$-Dyes and I^-/I^{3-}-electrolyte. Dyes are excited by incident light and inject electrons into the TiO_2 charge separation layer transporting the e^- to the FTO electrode.*

(b) *Simplified switching principle in TiO_2-based memristors due to the formation of the filamentary regions with an excess of oxygen vacancies V_O^+ corresponding to the ON- or OFF-state, e.g. after [122]. Note that the filament could also stretch over the whole oxide region and that the proposed metallic layer of Ti_4O_7 at the anode is omitted for reasons of simplicity.*

Figure 2.2: *Two prominent exemplary devices using TiO_2-films: (a) Dye-sensitized solar cells (DSSCs) and (b) TiO_2 memristors.*

energy band structure of the materials favors the direct injection of the electrons into the conduction band of the adjacent TiO_2. Therein, they are transported to and finally injected into the FTO cathode. It has been shown that the performance determining steps are rather the transport processes inside the TiO_2 than the much faster dye excitation and injection rates at the interface. [131, 132, 138] The excitation and injetion rates from Dye molecules are chemically and physically a matter of their own and shall not be treated in this work, whereas the transport processes, especially the measurement and effects of electron trapping times, inside the TiO_2 have been the matter of many experimental studies and are still debated today.[131, 132, 138, 139]
The high electrochemical stability and photocatalytic activity of TiO_2 renders it also particularly useful for the photocatalytic reduction of CO_2[86, 91, 140, 141, 142, 143, 144] and for water splitting applications [92, 145, 146]. Therein it can act as a passivation layer protecting the underlying Si substrate against corrosion and allowing for charge

transport transport through it at the same time.[25, 26, 27, 28, 128]

Most of the experimental studies deal also with the rates associated with electron transport that are in turn influenced to a big part by the nature and energetic levels of defects in TiO_2. Thus, only recently, there has also been a big number of ab initio calculations dealing with the specific properties of defects in rutile and anatase which are mostly employed in DSSCs or photocatalysis, which will be detailed in section 6.3.1.
Furthermore, TiO_2 also promoted and got promoted by research on structurally similar perovskites, like $SrTiO_3$ or $BaTiO_3$, which have even higher k-values.[35, 147, 148, 149] Besides, rectifiers for energy harvesting[72], infrared detection[150] and field-emission cathodes[151] became the subject of studies, as well as new highlighted applications of titanium oxide, also of non-stoichiometric, amorphous TiO_x, such as the passivation layers for photocatalytic structures just mentioned. In terms of device miniaturization, the high dielectric constant of TiO_2 of 80 to 180 for the rutile and also even 40 for the anatase phase, as cited above, made it an attractive alternative to Si which suffers from leakage currents above $\sim 10^8 A/cm^2$ for thicknesses below 3 nm. So by anatase the effective oxide thickness (EOT), determining the capacitance of a floating gate device, would be the same already for a 30 nm thick TiO_2 oxide layer, while for rutile the oxide could be accordingly 60-120 nm thick. These activities also revived research on resistive switching behaviour in titanium oxide films after this effect had been known since the 1960s already with the work by F. Argall being one of the first works on it.[152] The filamentary switching mechanism, depicted in Fig. 2.2b, is the common explanation for the switching behaviour observed in memristors. Despite of heavy debates on it, there is agreement that it is the particular physical behaviour of its defects which makes TiO_2 a prototypical material for resistive switches.[153, 154, 155, 156]

For TiO_2, like for other memristor materials, the switching behaviour is supposed to be determined by the stoichiometric composition of the oxide layer which is strongly related to the defect density profile in the oxide slab. As depicted in Fig. 2.2b, switching occurs basically by the initial application of a sufficiently high positive or negative voltage ("electroforming"). A metallic filament of under-stoichimetric TiO_{2-x}, which is connected to a metallic region of Ti_4O_7 at the anode (not shown), is supposed to be formed causing a switch to the "ON-state" when stretching (almost) over the entire oxide. For an opposite voltage ramp the ON-state is present and allows for a higher current at lower voltages. Although the exact mechanism is not entirely clarified, there is common agreement that with increasing voltage the positively charged defects, probably oxygen vacancies, in the TiO_{2-x}-layer are decreased in density or deactivated, probably by migrating to the negative electrode, and the TiO_{2-x}-layer is spatially replaced by a less defective, more insulating, ideally stoichiometric TiO_2-region of several nm thickness for a sufficiently high reverse biases. This resembles the OFF-state. By a new positive voltage ramp, the defect density is increased again and the former under-stoichiometric, conductive, filamentary region of TiO_{2-x} is rebuilt. The conductivity of these nm-thin regions changes by orders or magnitude potentially due to the extreme change in the density of oxygen vacancies. We will analyse this effect by our model in section 6.3.5.

Evidently, in this picture the conducting or insulating properties of such oxide layers are determined by the nature and amount of defects inside. Although resistive switching effects have been known for long, actual memristor devices still have to prove their practical applicability before their potential for further device miniaturization can be exploited.[157, 158, 159, 160]
In total these research activitities demonstrate the broad scientific scope of TiO_x. Since nearly all of the aforementioned applications of TiO_x rely on or are at least strongly related to the physical and chemical nature and energetic position of defects in the band gap and their spatial distribution, the study of their properties has been a vivid field of research. For TiO_2, specifically, this stimulated a further heavy debate whether the defects in this oxide stem either from oxygen vacancies V_O or titanium interstitials Ti_{int} or both, and if they are rather shallow or deep. While more phenomenological models, like the multiple trapping model, cf. next section, assumed shallow traps to be decisive [161, 162, 163, 164, 165, 166], recent experiments confirmed that deep traps contribute notably to electronic transport through TiO_2 layers. This would be also in accordance with results on other transition metal oxides, like ZrO_2, Al_2O_3 or HfO_2, as well as DFT calculations. [38, 167, 168, 169, 170, 171, 172, 173, 174] The nature of defects in TiO_2 as derived from first-principles in a number DFT-calculations will be reviewed with respect to their relevance for the parametrization of the kMC-simulations in chapter 6.3.1.

2.2.2 Modelling currents through oxides by Monte-Carlo-methods

Former Monte-Carlo Studies with Emphasis on DSSCs

Orginally, the kinetic Monte Carlo method has been formulated by D. T. Gillespie in his seminal article in 1976.[41] It will be outlined in chapter 4. Subsequently, in 1993, H. Baessler successfully applied a similar ensemble Monte-Carlo approach to the charge transport in disordered organic systems using a Miller-Abrahams hopping model.[175] Transport properties in amorphous TiO_2, assumed as a disordered inorganic system, were tackled soon by similar Monte-Carlo methods. One of the first and most important works applying Monte-Carlo simulations for TiO_2 was the one by J. Nelson,[176] aiming at an explanation of electron lifetimes in TiO_2 as an electrode material for DSSCs. [131, 132, 138] Nelson modelled photocurrent transients and charge recombinations in nanocrystalline TiO_2 electrodes for DSSCs by a continuous-time random walk model of the transport, referred to as "multiple trapping model". In multiple trapping electrons are supposed to drift-diffuse stepwise in the CB until they encounter a trap on a discrete grid and get trapped for a certain period of time. This so-called waiting time in a trap was modelled via a density of band gap states, i.e. electron traps, that decays exponentially into the band gap of TiO_2 and the model could reproduce exponentially stretched photocurrent transients and charge recombination kinetics measured in experiments before.[176] Moreover, Nelson et al. used this multiple trapping model with deep, localized states and diffusion in the CB to simulate the bulk mobilities and conductivities of electrons and holes in TiO_2 as a continuous time random walk.[177] Later on she

included also competing Miller-Abrahams hopping rates for the long range transport of electrons between traps in dependence of electron density and varying random spatial trap distributions and exponential energetic ones which resembles essentially a simple version of a kinetic Monte Carlo model.[178] Watkins, Walker and Peter et al. developed this method further to electron trapping on a 3D network of spherical grains to resemble the morphology of mesoporous TiO_2 networks and study the mentioned quantities (mobilities, diffusion coefficients) characterizing the transient photoresponse and transport. Since the electron trapping times change, if they get closer to grain necks, and inter-grain transport has different injection rates, this kind of multiple trapping model corresponds to a two-timescale random-walk. It was also employed to reproduce the time varying photoresponse in DSSCs under the assumption of different trap concentrations and distributions. [163, 179, 180] Parallel to this and also more recently, J. Bisquert et al. performed several similar studies using multiple trapping to simulate surface photo voltage transients by "random walk numerical simulations", a simplified MC-method, for the charge transport through defects, distributed in an exponential DOS, in order to determine the characteristic activation energy, also called "transport level" in TiO_2.[181] His group also added porosity-dependent, i.e. position dependent, transport rates in networks of grains, electron-hole-recombination and Miller-Abrahams hopping rates, allowing for a direct trap-trap-transport in TiO_2, in order to simulate the chemical diffusion coefficient and determine once more the transport level of electrons at different carrier concentrations which strongly influences electron lifetimes in high-efficiency solar cells.[182, 183] Completing the state-of-the-art of Monte-Carlo models for TiO_2 given here, most recent random walk models by Bisquert included also Marcus injection rates from the dyes attached to the TiO_2 surface. Again they reproduced diffusion lengths and electron lifetimes in TiO_2 from the average distance travelled and the average survival time between recombination events.[184] The trap-mediated recombination was analyzed more profoundly by deriving impedance functions in DSSCs from their model, however, still using essentially hopping rates and an exponential energetic distribution of traps.[185]

To summarize, the cited MC-studies can explain already a number of transport characteristics of experimental importance, e.g. electron lifetimes, diffusion coefficients and complex impedances, by relatively simple models. Although the models have good explanatory power, they actually refer only to the photoresponse of TiO_2, i.e. first charge carriers must be excited by incident light to measure the simulated quantities. This simplifies the physical situation in DSSCs in a way that the number of involved processes is reduced to simplify and accelerate the MC-simulations, but it also cuts off big parts of the physical situation, such as injection into the anode and the physics inside the electrode or the possibility of phonon-assisted tunneling or PF emission from traps as well as the actual spatial or energetic location of traps in dependence of their chemical nature, to name just a few drawbacks. So there are no further studies known to the author at this point that would have modelled an electronically closed system and would have reproduced the electron transport in the form of experimentally measurable current

densities through TiO_2 from an electron injecting cathode to an opposed anode.

Recent kMC-simulations of Metal-Oxide-Structures

Metal-oxide-structures, some of which are considered as conductive oxides today, have been analyzed in terms of quantum mechanical expressions for the rates of transport processes inside such materials already from the 1950s onwards which is textbook knowledge today. [186, 187] This laid the mathematical fundaments and accelerated the development of further closed models for such materials, among which are drift-diffusion simulations or non-equlibrium-greens-function calculations.[†] But in particular these analytical models allowed also for more capacious kMC-models with much more processes included than in the ones used up to now for TiO_2. This is also one of the biggest strengths of the closed kMC-model presented in detail in chapter 5, originally implemented and employed in the thesis by G. Jegert to simulate leakage currents through $TiN/ZrO_2/TiN$.[6, 188, 189, 190] There are similar models by others, also for ZrO_2, as well as $SrTiO_3$ (STO) or $BaTiO_3$ (BTO), but in particular hafnium oxide, HfO_2, which have been considered more interesting than TiO_2 up to now as high-k dielectrics for DRAM storage capacitors and also resistive switching applications.[149, 168, 191] Not yet a MC-simulation, but a basic work in the fields of thin dielectrics was on "Leakage currents in high-permittivity thin films" of STO or BTO by Schroeder et al.[192] who compared electrode-injection-limited thermionic emission against bulk-limited PF and hopping mechanisms for electrons and stated that the latter ones explain the characteristics. Thus bulk-processes gained interest and Jegert et al. were one of the firsts to establish an acutal kMC-model in this field. At first, they demonstrated the principle functionality for leakage currents through ZrO_2 in [6], explaining it into more detail for $TiN/ZrO_2/TiN$ capacitors in [189] later on. Then they included surface roughness effects [188] and finally also the relaxation of defects in the oxide when occupied or not [190]. Bersuker et al. established a Monte-Carlo model for resistive switching in $TiN/HfO_2/TiN$ electrodes also including all trap related processes and modelling conductive filament formation. With this MC-model they were able to successfully reproduce measured currents through such resistive switching structures.[193] Later on, Larcher, Padovani and Vandelli also included a SiO_2 layer into stacks with HfO_2 as gate dielectric and studied the effects of trap-assisted-tunneling conduction processes. This allowed again for a reproduction of experimentally observed gate leakage currents from differently doped Si substrates through the oxide stacks using realistic material parameters.[168] Recently, Padovani et al. studied the effects of phonon-assisted trap-trap tunneling of electrons in hafnium oxides of different stoichiometry, i.e. HfO_x and HfO_2, where the leakage current through the former, sub-stoichiometric phase could be explained by a higher density of oxygen vacancy defects.[191] Popescu et al. analyzed leakage currents in STO capacitor structures using the TCAD framework.[149] This is no MC-method, but can account

[†]Such models shall be omitted at this reason for reasons of brevity, as they exceed the focus of this work.

for oxygen vacancies at least in the form of single traps, which was indispensable to explain leakage currents through this high-k dielectric. This has been shown before by Manger et al. for STO.[194] Schroeder et al. examined resistive switching mechanisms in dependence of material parameters of (unspecified) MOM structures with a focus on the influence of defect levels and densities at the electrode-oxide interfaces.[195] By these studies on leakage currents in high-k capacitors and the strongly related effects of charge transport in resistive switching layers, the necessity to include at least single, if not multiple defect processes into the simulations to get realistic results has been demonstrated. This can only be accomplished by an extensive kMC-model.
To summarize, the simulations on the technologically outstanding material TiO_2 performed until today e.g. by Nelson et al., Walker et al. or Bisquert et al. do not meet the state-of-the-art for the simulation of current densities, because the effects of multiple traps have to be included by an appropriate kMC-framework. This is done here, as has already been approved by other important dielectrics, such as ZrO_2 and HfO_2. AlO_x is one of the next important oxides besides TiO_2, ZrO_2 and HfO_2 and will be introduced and discussed shortly in chapter 6.4 in order to finally adapt the TiO_2-validated model also to this material and to show the flexibility of the presented kMC-algorithm.

Chapter 3

Experimental Methods

3.1 Fabrication Methods

3.1.1 Thermal and E-Beam Evaporation

The most important method to deposit the nm-thin films was thermal evaporation using resistance heating and e-beam evaporation. Both are physical vapor deposition (PVD) methods * and rely on - differently accomplished - heating processes where the material of choice is melted quickly so that it vaporizes inside an evacuated evaporation chamber. As depicted in both images in Fig. 3.1, the evaporated atoms then travel to the target sample where they are gradually deposited as a thin solid film. In this thesis only metals were evaporated, which are compatible with both thermal and e-beam deposition. †
Since thermal evaporation and e-beam evaporation are similar except for the heating process, both methods shall be explained jointly here. The principle of the resistance heating method is sketched in Fig. 3.1a, while e-beam evaporation is sketched in Fig. 3.1b. Substrates were usually fixed upside down on a special specimen holder using little needles, clamps or also scotch tape. In both cases, the specimen holder had to be located over the evaporation metal source. For the resistance heating method, Fig. 3.1a, the specimen holder was rotatable at different speeds allowing for isotropic, homogeneous growth of the films, while the source material was placed in a little tungsten boat. The boat is heated by a high current (∼160 A 300 A) driven through it until the metal vaporizes. For e-beam evaporation, Fig. 3.1b, accelerated electrons from an electron gun (a heated filament) are directed by beam-bending magnets onto a crucible containing the metallic source materials. These are heated by the hitting electrons (kinetic energy: 12 keV) and thus vaporized, too. Shadow masks were used to prevent sample areas from being deposited. If not stated otherwise, evaporations in this work were done at a constant metal deposition rate (between 0.5 $\AA/s$ to 10.0 $\AA/s$) measured in situ by oscillating

*Just as sputtering, pulsed laser depositon (PLD) or MBE.

†Also pentacene or silicon dioxide can be evaporated by PVD. For semiconductors, however, MOCVD, a chemical growth method, or MBE is necessary.

quartz crystals. Together with the shutter systems that block the way between source and substrate immediately, a control of the metal layer thickness in a range of around ±2 nm is possible. As soon as the desired thickness is reached, shutters are closed and the heating of the boat or crucible is stopped. Finally, samples are removed from the chamber.
For thermal evaporation a UNIVEX 350G High Vacuum Experimentation Systems from Leybold was available. After a vaccum pumping time of about 5 min pressures around 10^{-7} mbar to 10^{-6} mbar were reached inside the evaporation chamber. The direct environment outside of the evaporation chamber itself was continuously kept under Nitrogen atmosphere. The N_2-atmosphere avoids the degradation or oxidation of the samples by having less than one oxygen or water molecule per 10^6 gas molecules inside. For that purpose the chamber must be inside a glove box which allows for the handling of samples from the normal laboratory environment.
For e-beam evaporation a Leybold L 560 evaporator system was used. In this system the evaporation chamber itself was under a constant high vacuum $\sim 10^{-7}$ mbar to guarantee low contamination and a stable evaporation rate. [196] Therefore samples had to be introduced into the evaporation chamber via an air-lock, i.e. a pre-chamber that is flooded with air for introducing samples from outside and that is pumped down to $\sim 10^{-7}$ mbar, separately, before introducing samples into the evaporation chamber.
The e-beam evaporation process was mostly used for the metal deposition in this thesis, as far as not stated otherwise. It is advantageous that the electron beam only heats the source material and not the entire crucible in contrast to resistance heating. Thus the evaporated metal is less contaminated from the material of the crucible compared to the boat in resistance heating. Also multiple materials can be put into a magazine of crucibles in e-beam evaporation which can be evaporated without flooding the evaporation chamber in between. For both machines the high vacuum inside the evaporation chamber avoids the oxidation, deposition of impurities and degradation of the samples during evaporation and subsequent changes of the structural and electronic properties. This is important for less inert metals, like Ti or Al.

3.1.2 Atomic Layer Deposition

Atomic layer deposition (ALD) shall be briefly introduced at this point. Although it was not used directly in this work, samples grown by this method will be analyzed by kMC-methods in the results chapter, too. In contrast to the two previous PVD-methods, ALD is a chemical growth method. It relies on a self-limiting growth-mechanism to obtain monomolecular layers from the vapor phase. The process based on alternating chemical reactions on the surface of the target substrate offers good film homogeneity and conformal coating with exact control of the film thickness. In contrast to other vapor-phase-deposition techniques like PVD or molecular organic chemical vapor deposition (MOCVD), ALD is a cyclic process. In principle gas pulses of the educts are introduced into the reaction chamber, alternating with purging steps. First a pulse of educts is introduced (1), followed by a purging step and evacuation of the reaction chamber (2).

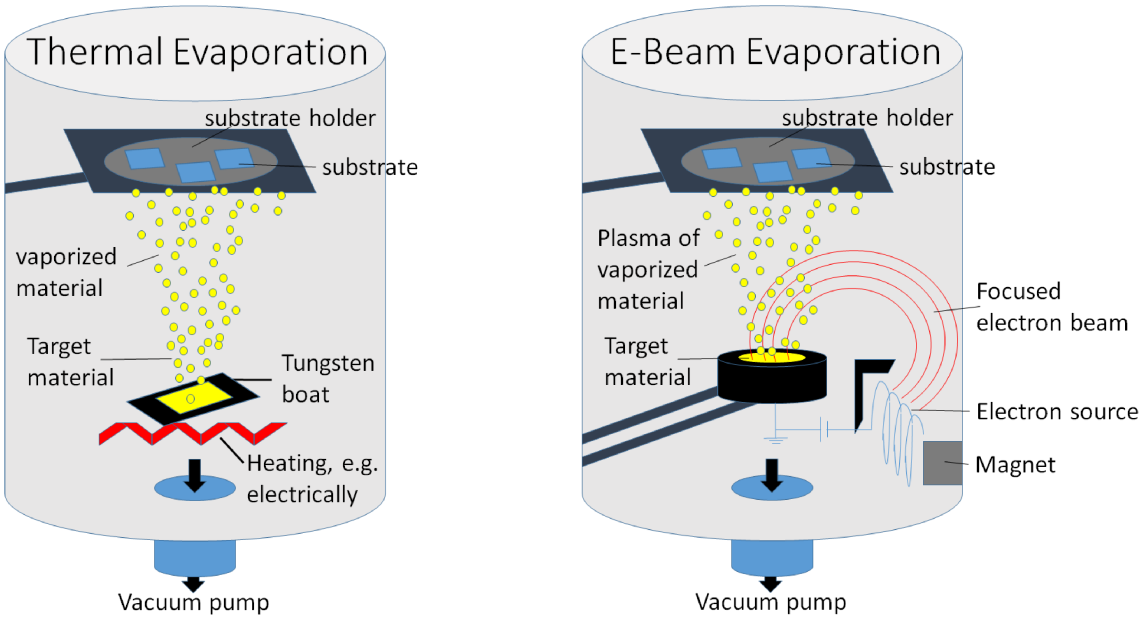

(a) *Principle of thermal evaporation.*

(b) *Principle of e-beam evaporation.*

Figure 3.1: *Physical vapor deposition (PVD) methods.*

Then the second pulse of educts is introduced (3), followed again by another purging step and evacuation of the reaction chamber (4). Every process step terminates the surface with a monolayer of the educts (or "precursors"). This cycle can be repeated until the desired films thickness is obtained.[197]

3.1.3 Plasma Ashing

Conventionally, a plasma asher is used to etch down organic materials on the surface of a sample, such as for dry ashing of photoresist or cleaning the surface from dust particles, without wet chemistry. For that purpose samples are placed on a petri dish and loaded into the reaction chamber. Then the reaction chamber is evacuated and either O_2 or Ar_2 gas molecules are introduced into the reaction chamber at a certain flow rate determining the partial pressure for the particular gas species, e.g. 10-50 mTorr. At a certain ignition voltage of the microwave radiation with a frequency of max. 2.6 GHz the gas molecules are ionized and create the plasma. The system used here was a barrel asher like the one sketched in Fig. 3.2.[198] In such a setup the etching takes place isotropically, i.e. homogeneous in vertical and lateral directions. The most important property of the plasma for nanotransfer processes is to activate the surface by forming hydrophilic hydroxyl-groups. This increases the hydrophilicity and thus the adhesion between the transfer metal and the substrate. On Ti surfaces evaporated on top of the stamp, a very intense oxygen plasma up to 600 W applied at a long etching time up to 1200 s, cf. section 6.2, is supposed to oxidize less inert metals like Ti thereby creating

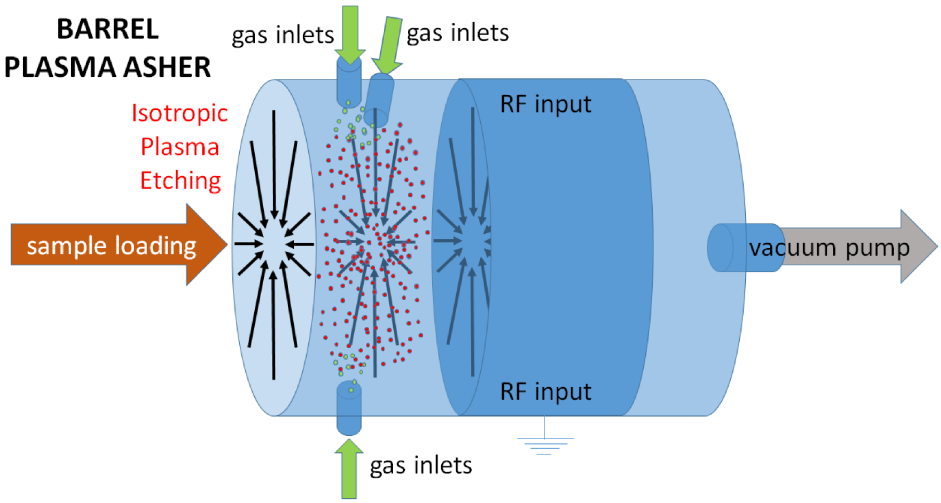

Figure 3.2: *Principle of isotropic plasma ashing in a barrel reactor, drawn after [198]. It has a loading for samples, a vacuum pump, several gas inlets for the oxygen and a larger contact to apply a high RF voltage inducing a microwave that ignates the plasma (red, oversized ions).*

the functional metal oxide TiO_x.[19, 20, 199] The process behind this oxide-growth is considered to be similar to the already approved growth of AlO_x and TiO_x layers by a RIE plasma, cf. section 3.1.4 and 6.4.4. The functionality of such an oxide can have welcome or undesired effects for the final application. Hence the growth process had to be quantified. This was a central research question here and will be discussed repeatedly in section 6.2.

3.1.4 Reactive-Ion Etching

Reactive-Ion-Etching (RIE) is in its working principle quite similar to plasma ashing and was also used here as a complementary technique to plasma ashing, primarily to etch down resist. In contrast to a plasma asher, however, a RIE setup includes magnetic coils that direct the charged ions in the reaction chamber perpendicular to the plane of the substrate. Thus the plasma etching process is anisotropic with the direction of preference along the symmetry axis of the magnetic coils. After the preparation steps and ignition of the plasma, just as for the plasma asher, the generated ions are accelerated perpendicular onto the substrate. The etching rate can be adjusted by an additional negative potential under the sample. Another main difference of a RIE system are the various process gases that can etch not only organics, but also oxides or semiconducting surfaces, e.g, to transfer a positive pattern defined by a resist or an oxide into the underlying substrate in optical lithography or NIL, cf. section 3.3. One major drawback using RIE-processses is that it can easily be contaminated by metals that were once etched from a surface of a sample and will be accelerated onto any newly introduced sample in all subsequent processes. In previous works it has already been shown that a reactive-ion-etching (RIE) plasma can form pure and compact insulator layers of 3.6 nm thin AlO_x on Al or a 2.0 nm

thin layer of TiO_x on Ti. Such oxides can serve as tunneling or gate dielectrics featuring unexpectedly good physical resistance and interesting electrical characteristics.[21, 56, 57, 72, 73]

3.2 Conventional Lithography

With the ongoing evolution of the lithographic technology, it is recommendable to define it more generally in the first place as a process that patterns certain areas on a target surface. Formerly just flat structures were produced, but today also 3D-lithography is available. Subsequently, optical and e-beam lithography shall be explained briefly as, the two conventional fabrication techniques of highest relevance for this thesis. The common element of them is that first a mediating material, like a polymer or metal on a substrate or a "stamp" must be patterned. Then chemical processing, (UV-)light and/or ion exposure is performed to transfer the desired pattern onto the substrate. Despite of the similarities and common items single steps are done in different physical, chemical or logical ways for the specific techniques.

3.2.1 Optical Lithography

In the first step of optical lithography, the fluid photoresist is spread through a syringe on the plane target substrate, which was usually pure crystalline Si. The substrate is rotated on a spin coater at a speed (usually $\sim$ 3000 rpm) and time (usually $\sim$ 30 s) that produce a thin film of a predetermined thickness (usually $\sim$ 200 nm). The thickness goes reciprocal with the product of speed and time. A SAM can be brought onto the substrate before coating it with the photoresist to make the latter adhere better to the substrate. Afterwards a baking step at about 100 °C to 110 °C is done to vaporize solvents and water in the resist and stabilize the photoresist. Then the substrate with the photoresist is put into a maskaligner and a mask is placed and aligned on top of the substrate. The mask has a negative of the pattern desired to transfer in the resist, if positive photoresist is used, or a positive pattern of it, if negative photoresist is used. After a subsequent UV-light-exposure of a positive resist the areas which are not covered by the patterned photomask, so exposed to the light, change their phase and can then be dissolved by a treatment with developer. This uncovers the negative pattern of the mask on the underlying substrate. For negative photoresist it works the other way round. Having transferred this pattern into the resist on the substrate, the pattern can be transferred pertinently into the substrate by etching it into the substrate, analogous to Fig. 3.4d, or by depositing metal (methods above) in the space between the metal. Finally, all the remaining photoresist on the substrate is removed by a wet chemical or dry plasma cleaning and the substrate is ready for further processing steps. These processing steps are part of the lift-off processes in section 3.3.

3.2.2 Electron Beam Lithography

Though still being considered a “next-generation-lithography”-technique, electron beam lithography (EBL) is already a standard technique in industry, e.g. to fabricate masks for optical and X-ray lithography. In so far it is related to conventional photolithography. However, it suffers from low throughput and high cost. Technically, the main difference is that in EBL the polymeric resist is directly exposed to a finely focused electron beam instead of UV-light through a mask as in photolithography. The process starts with coating the flat substrate with a resist. The desired pattern on the substrate is digitally designed before the process. The process steps themselves are defined at the control station of the EBL-machine and then the structures and features are written into the polymeric resist on the substrate directly by the focused electron beam. In contrast to photolithography there is no shadow mask needed, because only the digitally predefined areas are hit by the electron beam. The electron beam is focused by electromagnetic lenses allowing for high resolution of several nm a fundamental advantage over photolithography which is limited by the diffraction of light. Secondary electrons scattered in the resist and beam drift put restrictions on the resolution of EBL. [200] After e-beam-structuring the developed resist is dissolved, just as explained for photolithography beforehand, and the pattern is optionally, but usually transferred into the substrate via a combination of subsequent plasma etching and/or evaporation steps, analogous to the processes in Fig. 3.4.

3.3 Nanoimprint Lithography

In 1995 Chou presented for the first time a successful fabrication of gratings with 25 nm width and 100 nm depth in polymer using this novel approach.[201] With the resolution of photolithography being limited by the diffraction of light ($\lambda/2$-law) and EBL being simply to slow and too expensive, new techniques to obtain nanopatterned substrates gained increasing interest especially at the beginning of the past decade. Nanoimprint lithography (NIL) was introduced as such a manufacturing technology that could provide comparably high resolution as EBL while maintaining the high throughput and little costs of conventional photolithography. In the meantime, NIL turned out to be even applicable for roll-to-roll fabrication underlining the potential of this technology. Many variants of this principle have been developed, such as nanoindent lithography, dip-pen lithography (DPL), step and flash NIL (SFNIL), ultra-violett NIL (UVNIL), as well as thermal NIL, which shall be focused on in the following subsections, and most importantly for this thesis μCP and nTP, explained in section 3.4.[8, 79, 202] While the former two techniques form the structures during the process self-organized and do not require a custom template, which comes on the cost of control and structure definition, the latter five all rely on previously patterned stamps.
Generally, NIL-methods mostly focus on pattern replication by one or two imprint steps. More complex patterns can be obtained by prefabrication of confectioned templates using

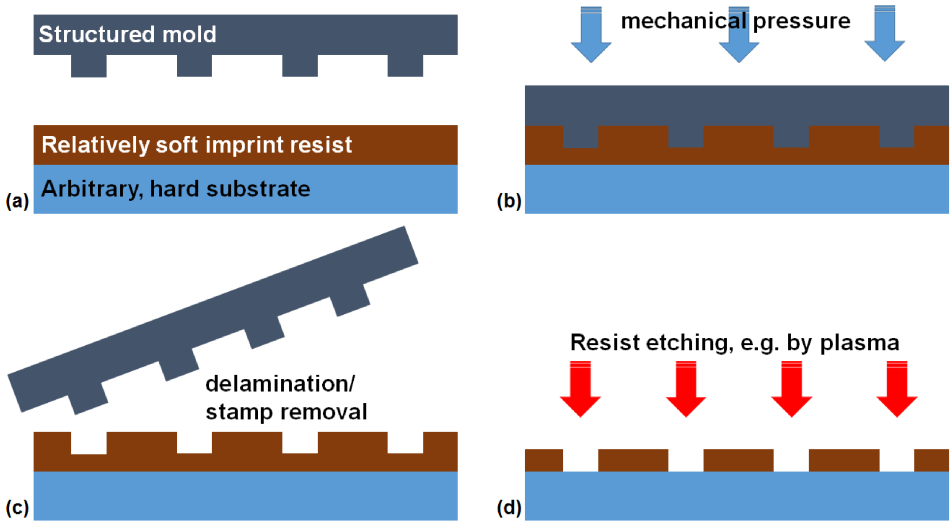

Figure 3.3: *Basic NIL process: (a) Master template defined by other lithographic techniques, normally EBL, is positioned above the substrate spin-coated with a resist. (b) Imprinting step under application of pressure p and temperature T. (c) Demolding of the stamp fom the substrate leaving behind a negative of the stamp structure in the resist. (d) Further (optional) etching steps, e.g. in a RIE, to transfer the negative structure into the substrate. Other options outlined in the text.*

other lithographic techniques, like EBL, or, alternatively sequential imprints with a single template are possible. However, for this purpose room-temperature (RT)NIL must be used, as many intermediate curing steps alter the results of previous process steps. Note that fabricating a custom template is one of the most expensive and time-consuming steps in conventional NIL. Therefore only multistep RTNIL with one simple template is used as established in a prior PhD thesis by S. Harrer at the institute.[79]

3.3.1 Basic Principles of Nanoimprint Lithography

The working principle of NIL, thermal NIL specifically, shall be briefly explained referring to the steps depicted in Fig. 3.3. Initially a template with a certain pattern is placed on a soft imprint resist, a polymer or a photoresist that has been spin-coated onto a substrate beforehand. Here usually 3000 rpm for 30 s were used resulting into a 200 nm thick layer of imprint resist mr8010. Then the resist is annealed at 100 °C for 5 min and cooled down for 5 min in our process. With the template on top of the baked resist-substrate-stack a mechanical force, i.e. pressure, is applied under variants of time, temperature and pressure. The imprint step here was usually done for 5 min at 30 bar pressure and heating up to 175 °C. The glass transition temperature of the polymers used in thermal NIL typically lie around 150 °C. After the thermal curing step (cool-down for 3-5 min)[‡] of the resist, with the pressure being still applied, it becomes

[‡]Alternatively, the curing process can be achieved by ultraviolet light when a UV-sensitive polymer is used, referring to UVNIL then.

rigid again and the stamp must be removed carefully, normally in vertical direction. The substrates were Si wafers, but any kind of metal or even a rigid polymer can be used. Then, the obtained negative pattern of the template printed into the resist is supposed to be transferred into the substrate. For that purpose the interlayer has to be etched down to the substrate by a chemical or physical process. This point, referring to Fig. 3.3c, is crucial for the further sample processing depending on the objective. To transfer the pattern into the Si substrate by etching steps, first the residual layer has to be etched down by an oxygen plasma O_2, as in Fig. 3.3d. However, this can be done already either by an unisotropic RIE-plasma, as depicted in Fig. 3.4a, preserving the lateral dimensions of structures, Fig. 3.4b, or by an isotropic barrel asher plasma, Fig. 3.4e, reducing the lateral dimensions, Fig. 3.4f. One could also continue from the situation in Fig. 3.4a with other etching processes to transfer more complex structures on the substrate, apply (electro-)chemical or physical deposition methods to functionalize the open spaces on the substrate with further materials, even do optical, electrical and measurements or simply stay with the result and do morphological characterizations depending on material combinations and the preferred result.
Referring to Fig. 3.4a, however, this direct etching process starts with vertical RIE etching by an anisotropic (directed) oxygen plasma to remove the residual layer of imprint resist at the bottom of this negative of the master structure in the imprint resist layer. Thereafter, the width of the positive polymer lines and trenches is supposed to have remained approximately as imprinted during vertical etching, Fig. 3.4b. The dimensions given in the image refer to typical ones as expected from the stamp used for most NIL experiments here (60 nm lines stamp with 240 nm spacings). Undercuts are improbable to be created making RIE etching less suitable for Lift-Offs in the first place. Subsequently, Fig. 3.4c, the trenches in the polymer are echted into the Si substrate with sulfurhexafluoride, SF_6, or tetrafluormethane, CF_4, gas in the RIE. This transfers the imprinted pattern directly into the substrate creating a negative of the lines on the master template. Finally, Fig. 3.4d, an oxygen plasma cleaning step is applied to remove the remaining imprint resist on the substrate. After this process, ideally, a negative of the structure on the master stamp is obtained made from the substrate material. Alternatively, there is the lift-off-process, skteched in Fig. 3.4e-h, which will be explained in the next section.

3.3.2 Calibration of the etching rates for NIL-Lift-Offs

The first possibility of a RIE-based NIL-process with a subsequent transfer of the pattern into the Si substrate as depicted in Fig. 3.4a-d was just explained and had been demonstrated for Si in principle by Harrer et al..[79] Referring to Fig. 3.4e-h, the Lift-Off-NIL-process, as focused on in the present work, starts with an isotropic plasma etching of the polymer down to the substrate in a barrel asher, Fig. 3.4e. The residual layer at the bottom is removed, polymer lines get narrowed while trenches grow due to isotropic etching, Fig. 3.4f. Thus undercuts are supposed to be created. Then, the subsequently evaporated Au-layer, Fig. 3.4g, is supposed to be not entirely connected at the bottom

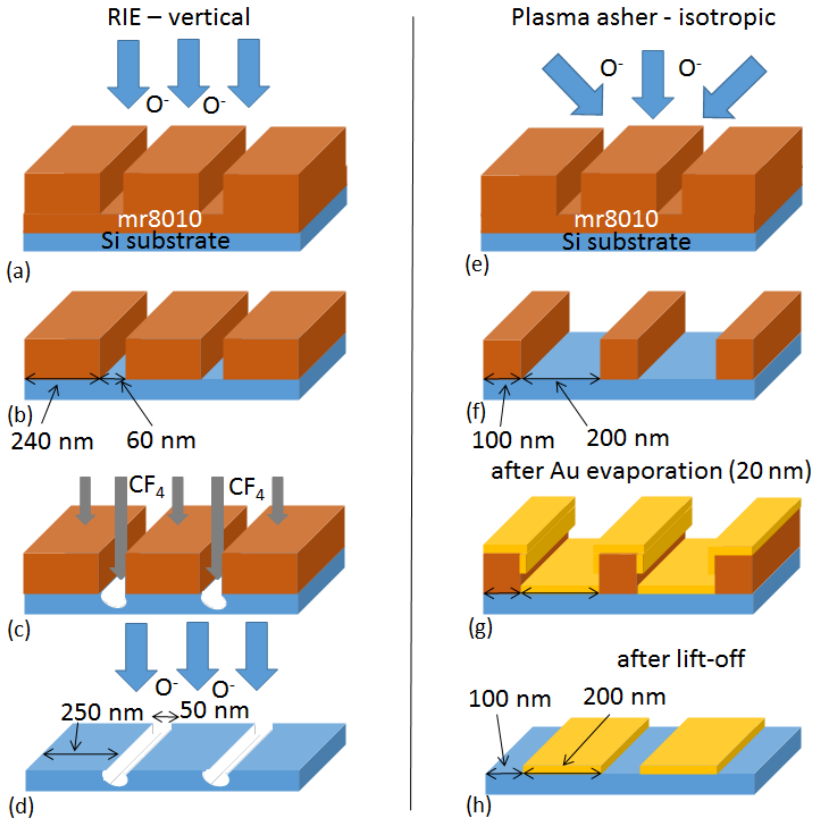

Figure 3.4: *(a) Direct etching process starting with vertical RIE etching process by an anisotropic oxygen plasma. (b) Width of the positive polymer lines and trenches remain approximately as imprinted. Given dimensions mirror the ones on the stamp (60 nm lines stamp with 240 nm spacings). (c) Etching the trenches into the Si substrate by CF_4 in the RIE. (d) Final oxygen plasma etching step. (e) Lift-Off-NIL-process starting with an isotropic plasma etching. (f) Polymer lines narrowed from isotropic etching. (g) Structure after Au-evaporation. (h) Lift-Off of the polymer by a final acid treatment leaving behind the gold.*

of the positive lines due to such undercuts from the precedent anisotropic etching step. Thus, the Lift-Off of the polymer by a final acid treatment could remove the polymer together with the Au layers evaporated on its top, Fig. 3.4h. Ideally, this leaves behind only the metal evaporated in the trenches and forms a negative of the original structure made from Au. As a part of the present work, accomplishing this lift-off process, was more attractive the former way above, because it is an outstanding enabling technique for further experimental investigations on photocatalytically active structures containing highly ordered Au metal structures. The work presented here is supposed to provide insights on possible solutions for accomplishing such lift-offs below ∼100 nm.

Calibration of the etching rates of the imprint resist

At first thermal NIL was performed starting as described above, i.e. using a p^+-Si substrate covered with ∼200 nm mr8010 resist by spin-coating it for 30 s at 3000 rpm. Then the imprint process was done, as depicted in Fig. 3.3a-d and explained above, with a lines stamp with 60 nm wide lines, with 240 nm distance in the Obducat 2.5 NIL-Imprinter. In theory, the sidewalls of imprinted structures should be straight. Then, if the evaporation is accomplished strictly perpendicular to the surface, the metals on the substrate at the bottom and on the polymer at the top should not be connected to each other. Hence, when removing the polymer, the metals on the substrate remain untouched there and the lift-off should be possible in theory. In practice, however, the lift-off process of a metal evaporated on the patterned and etched-down polymer on the substrate remains one of the most challenging tasks in nanoscale-patterning by NIL, because the walls of the imprinted trenches are not ideally straight, but slightly trapezoidal. This involves the problem of missing undercuts which was supposed to be solved by the isotropic plasma of the barrel asher instead of an anisotropic RIE-plasma, since the latter cannot create undercuts.
Therefore, the first crucial point was the accurate etching of the imprint polymer mr8010 in the barrel asher. For that purpose the etching rates of the barrel asher were calibrated on several reference samples, processed as given above, i.e. with 200 nm imprint polymer on top and imprinted with 60 nm wide lines at 240 nm distance and a height of 100 nm. The calibration of this etching process by the means of AFM measurements is depicted in Fig. 3.5 and described into more detail in the following referring to the image series and finally resulting into the trend lines for the resist height and trench width etching given in Fig. 3.5f. Fig. 3.5a shows the first AFM image with a lateral profile perpendicular to the lines after 0 s. The tip was not sharp enough to get to the bottom of the thin trenches at this point. Correspondingly the positive lines appear wider than 240 nm, the trenches thinner than 60 nm and the trenches are actually in fact deeper than the ∼85 nm seen in the profile. This was checked in another AFM setup with ultra-sharp tips with a carbon nanotube at the top, depicted in image Fig. 3.5e. Such tips can better intrude into the trenches showing the expected trench width of 60 nm in the resist and trenches with actually ∼95 nm depth, but they are limited by the length of the nanotubes of $\lesssim$100 nm, so they do also not reach the bottom of the trenches. At least they give a lower limit for the trench depth with ∼ 95 nm without etching here. This is less than one would expect due to the following argument: The polymer underneath the stamps is not completely compressed to the sides when imprinting or ”eliminated” by the intruding 100 nm high positive lines on the stamp. Quite the contrary, there is always a remaining layer of resist under the bottom of the trenches, called ”residual layer”, and most particularly “overspilling” polymer ("overthrows") extruding from the imprinted trenches at its edges. From experience, the overthrows are up to 20 nm high at maximum. Assuming an ideal imprint of the dedicatedly piranha-cleaned and new stamp with a full intrusion of its lines of 100 nm height into the polymer, the maximum height of the resist lines, i.e. depth of the trenches, is estimated as $h_{max} \lesssim 120$ nm

(100 nm imprint + 20 nm overthrow max.) resulting into a residual layer remaining at the bottom of ∼100 nm (200 nm original polymer minus 100 nm "full imprint"). The residual polymer has to be removed by a well-confectioned and calibrated oxygen plasma treatment. Thus even the ultra-sharp tip measuring a depth of 95 nm $\lesssim h_{max} \lesssim$ 120 nm did not reach the bottom of the trenches. Next, Fig. 3.5b shows the profile after 240 s plasma ashing. The trenches are wide enough so that the tip can get to the bottom and the actual depth could be determined as 110 nm. This depth corresponds almost to the just estimated $h_{max} \lesssim 120$ nm for the lines and is only some nm lower. Hence, it is reasonable to assume, that for this etching time the height or trench depth must have already been reduced slightly by the plasma. Thus also the residual layer at the bottom of the trenches of 100 nm must have already been etched down completely after 240 s. The lines, which are reduced starting from time 0 s - in contrast to trench depth which just started to cease - are already reduced to ∼170 nm and the trench width increased correspondingly to ∼130 nm. In Fig. 3.5c, after 420 s, the depth of the trenches is ∼55 nm, their width is ∼170 nm, while the positive lines are ∼130 nm wide. With the residual layer being removed, but the trenches still being relatively high, the AFM-images in Fig. 3.5b and 3.5c show typical dimensions of structures which were acceptable for further lift-off processing after the lateral etching processes. Fig. 3.5d shows the profile after 600 s. Here trenches are solely ∼5 nm deep, the width is ∼220 nm, while the remaining positive parts are narrowed down to ∼80 nm.
The results for the calibration of etching rates for the trench depth, i.e. line height, and line width of the polymer by these measured values are shown in Fig. 3.5f. We ended up with a rate of 0.29 nm/s at a power of 200 W for the reduction of the line height and 0.26 nm/s for the increase in the trench width, i.e. decrease in polymer line width. Thus after more than 600 s etching time the 200 nm polymer are quasi vanished. This has to be respected, as one is strongly limited for the maximally reducible height of protruding line in the polymer. As expected, the isotropic etching process of the plasma asher reduces not only the height, but also shrinks the imprint polymer laterally by 0.26 nm/s. Minding these isotropic etching rates in lateral direction besides the vertical ones of 0.29 nm/s, polymer lines vanish, if they are less than ∼130 nm wide at 0 s etching time and more than 100 nm residual layer have to be etched down. As deferred from the rates etching down ∼100-140 nm, corresponding to times of ∼360-500 s in the barrel asher for the given stamp, is a good compromise between sufficient removal of the residual layer and shrinking of positive structures. This calibration is necessary to adjust the etching times correctly for the actual lift-off process.

Preliminary Results of the Calibrated NIL-Lift-Off

For the actual lift-off, starting from a situation like in Fig. 3.5c the desired Au layer of circa 20 nm thickness was e-beam evaporated on the structured polymer lines on the sample. Then, the resolving of the remaining polymer under the evaporated Au layer was performed, which is also critical. This was done by a combination of a first cleaning step putting the sample into a beaker of acetone solvent placed in an ultrasonic bath

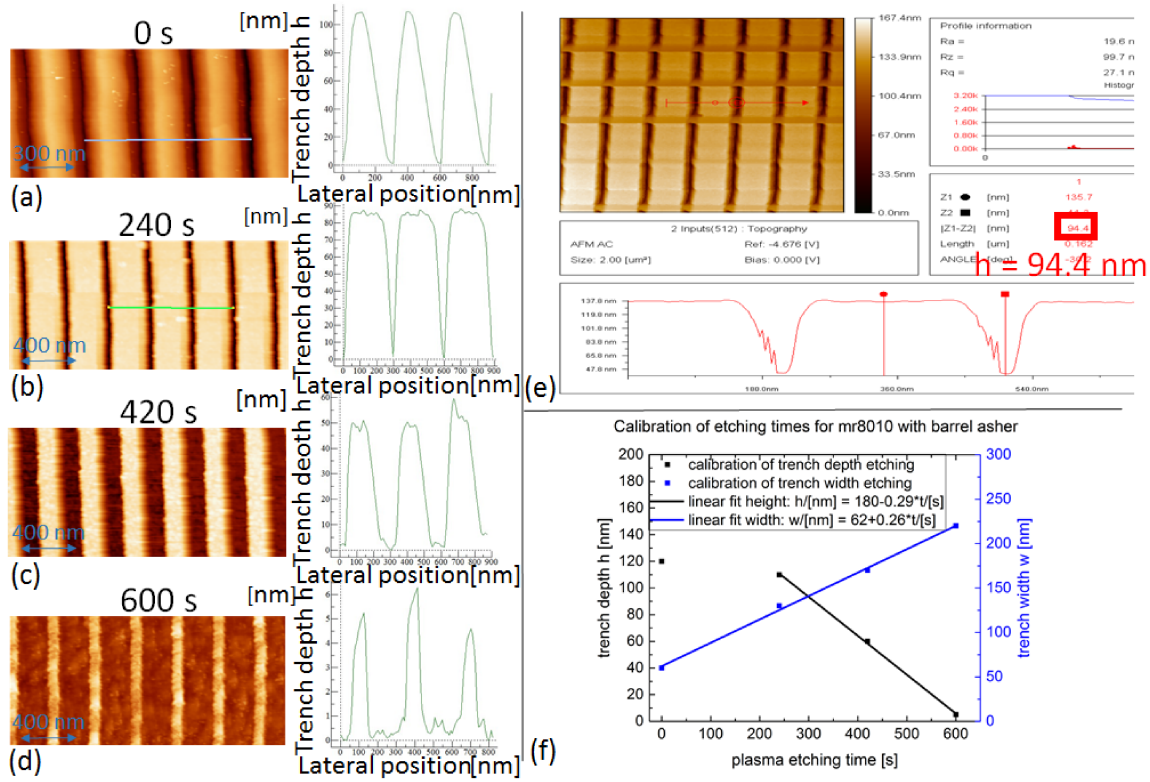

Figure 3.5: *Calibration of plasma asher etching rates for mr8010 imprint resist by imprint with a stamp with 60 nm wide lines and 240 nm trenches: (a) AFM image and profile of trench depth, i.e. line height h, of the sample after NIL-imprint, i.e. no etching. (b) AFM and profile after 240 s etching time. (c) Same after 420 s etching. (d) Same after 600 s etching. (e) Same situation as in (a), but measured with ultra-sharp tips intruding the trenches better, but not fully, as a depth of ∼94 nm is smaller than expected, see discussion in the text. (f) Final calibration of the etching times from the profiles for the lift-offs.*

at moderate power for about 15 min, followed by dips in perchloricacid and a finally dip into acetone again. Thus the Au layer was supposed to be lifted from the sample surface at the spots of positive polymer leaving behind the lines, as depicted in principle in Fig. 3.4h. An exemplary sample with ∼190 nm wide Au lines and ∼110 nm wide trenches obtained by ∼500 s plasma etching time stemming from this process has been characterized in the SEM, as shown Fig. 3.6. One can clearly see protruding lines on the sample which are also well-defined. The edges of the structures support the formation of Au lines, while the darker substrate background is supposed to be Si. However, up to the end of this work, it was not possible to clarify the actual composition of the surface of this sample. Nevertheless, the further optimization of the process should get higher priority than possible in the framework of this thesis.

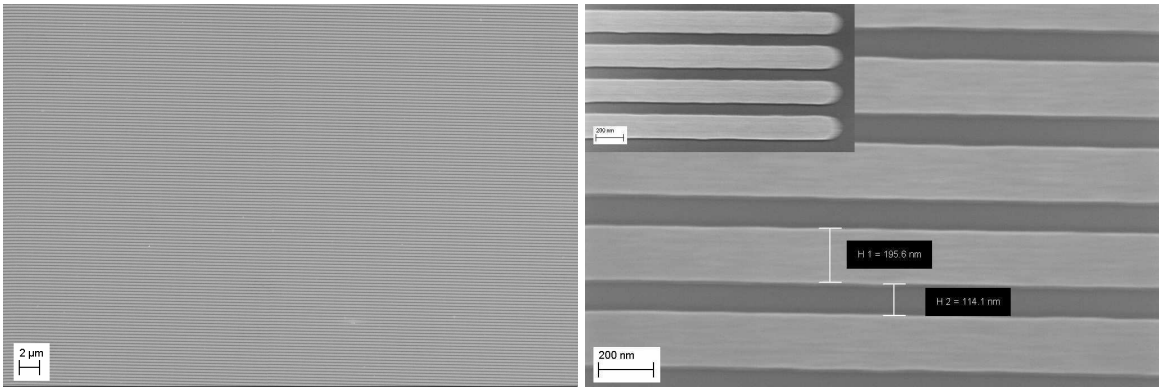

(a) *Large scale image of the sampl with ∼190 nm wide Au lines and ∼110 nm wide trenches.*

(b) *Highly magnified image of the same sample. In the inset the sample is tilted by 37.8 °.*

Figure 3.6: *SEM images of NIL-Lift-Off-sample with ∼190 nm wide Au lines and ∼110 nm wide trenches obtained by ∼ 500 s plasma etching time via a NIL from stamp with 60 nm wide lines and 240 nm wide trenches and subsequent Lift-Off, as described in the text. The imprinting polymer was mr8010. The inset of (b) shows an image of the edge of the fabricated Au lines tilted by 37.8 °. The good morphology with sharp edges indicates that the lift-off-process should have been successful.*

3.4 Nanotransfer Printing Technology

Besides the pre-processing techniques explained above nTP was most important fabrication technique of this work. Patterns on nTP-stamps have already been shrinked to minimum feature sizes in the range of EBL resolution. Though minimizing features was not the main goal of this work, lateral feature sizes down to 70 nm and horizontal ones of ∼3-5 nm could be achieved which is comparable to the state-of-the-art in terms of achievable morphologies, see section 2.1. Rather than morphological optimizations, a functionalization and optimization of the electronic properties of the fabricated structures was pursued. Therefore, having preprocessing techniques and nTP-fabrication well under control, the plasma oxidation process of the Ti interlayers was investigated into more detail in combination with nTP in section 6.2.

3.4.1 Working Principle of nTP

To begin with, the fundamental idea of nTP of ordered structures stems from its technological predecessor, metal contact printing lithography or also called micro contact printing (μCP) as developed by Loo et al. for ordered structures and reviewed broadly in terms of literature in section 2.1.[18] In both techniques one or more layers of transfer materials, the 'ink', e.g. metals, are transferred onto a substrate directly from a mold which can be previously patterned on the micro- or nanoscale, respectively.
The basic working principle of an additive transfer printing method like nTP can be condensed to the following three essential steps, as depicted in Fig. 3.7:

1. Covering the (nano-)structured stamp with the transfer material.

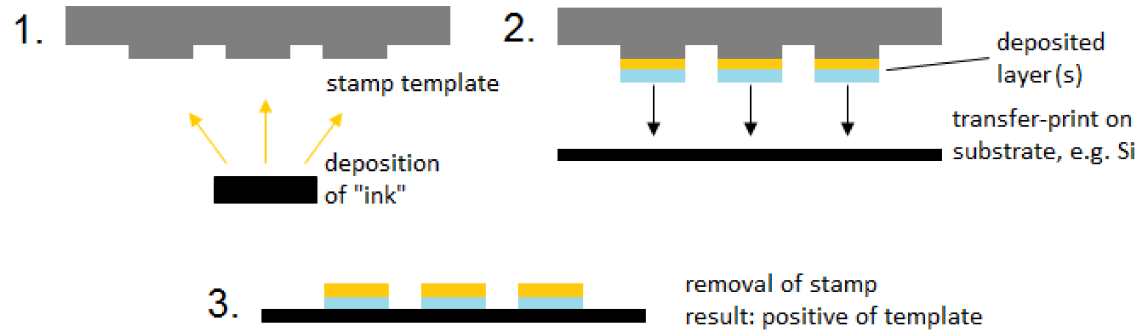

Figure 3.7: *Three most basic steps needed in nTP: 1. Deposition of the 'ink' on the stamp, 2. Transfer-Printing of the 'ink' from stamp to substrate, 3. Demolding of the stamp from the substrate leaving the structure behind.*

2. Transfer-printing: Establishing contact between stamp and substrate.

3. Removing the stamp from the substrate leaving behind a positive of the template.

Basically, this is a simple stamping procedure. The simplicity of the nTP process, however, allowed for an easy extension by further more complex, intermediate steps to eventually optimize the transfer results in terms of yield, reliability of the transfer process, fidelity of the features and especially sizes of the features which can be as small as several nm. Of course, this extends the process protocol and involves the following further steps comprising the complete state-of-the-art nTP process including most critical ones, which are number 2, 3, 4, 6 and 8, depicted in Fig. 3.8:
Pre-Processing:

1. Cleaning of chosen stamp and substrate

2. Application of a SAM either on the stamp serving as anti-sticking-layer or on the substrate serving as adhesion layer, Fig. 3.8a

3. Evaporation of the target metal-stack on the stamp, Fig. 3.8b, 3.8c

4. Activation of substrate and/or stamp in an O_2 plasma, Fig. 3.8d

Main nTP-Process:

5. Placement and alignment of substrate-stamp-stack in the Imprinter

6. Transfer-printing step consisting of, cf. Fig. 3.8e,
   a) Application of pressure $\sim$ 5 bar – 70 bar for $\sim$ 30 s – 120 s
   b) Application of temperature $\sim$100 °C – 200 °C for $\sim$ 1 min – 15 min

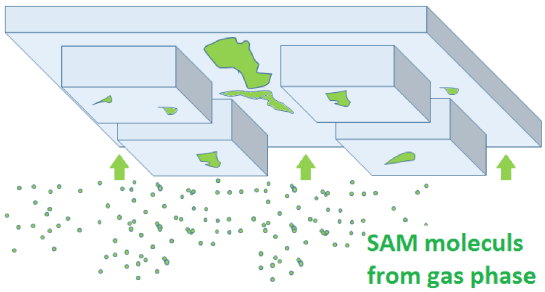

(a) *Application of self-assembled-monolayer (SAM) on previously cleaned stamp.*

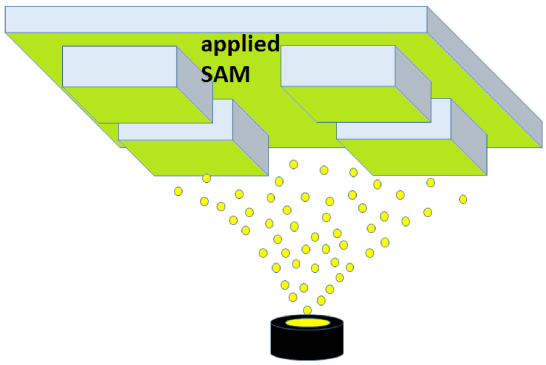

(b) *First evaporation of the Au layer (∼10-20 nm) by PVD-methods, section 3.1.1.*

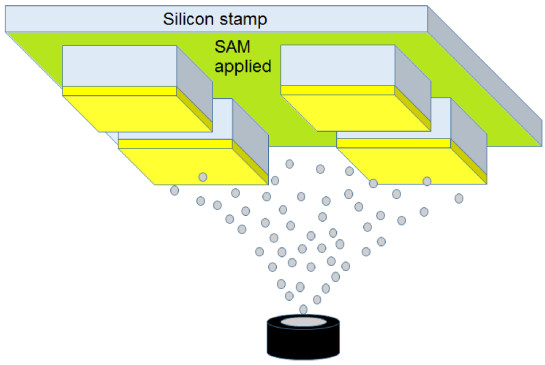

(c) *Second evaporation of the Ti layer (∼5-10 nm) by PVD-methods, section 3.1.1.*

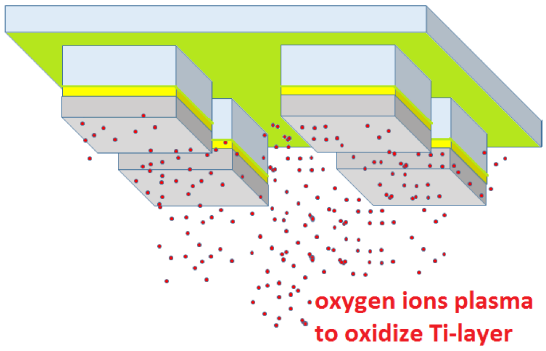

(d) *Activation of the Ti layer on top by microwave-ignated oxygen plasma forming OH-groups. The surface is supposed to be plasma-oxidized, see also results section 6.2.*

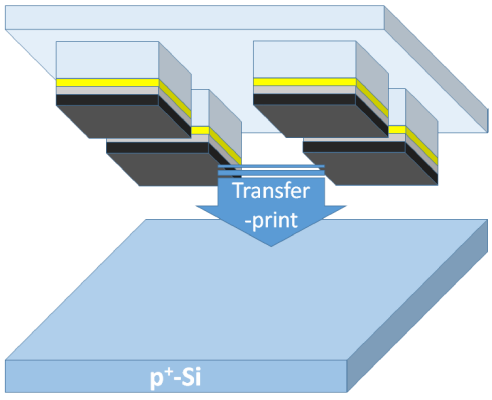

(e) *Transfer-Printing step, nTP or μCP according to pad sizes, pressures between 5 - 70 bar and temperatures of ∼100 °C – 200 °C are applied for times between several ∼1 min to 15 min. Adhesive forces of stack-to-substrate must be larger than to stamp.*

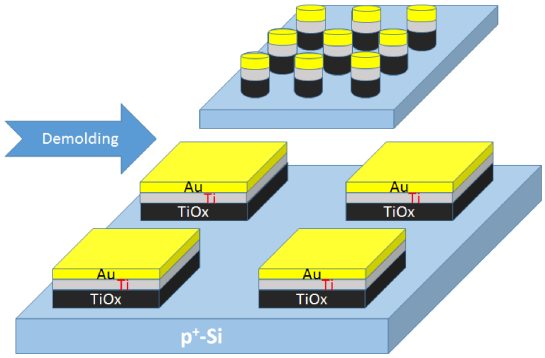

(f) *Vertical demolding of the stamp from the Si substrate with the transferred material stack (nano-pillars or micro-pads) remaining on top of Si. Demolding velocity $<$ 10 cm/s for optimal results.[8]*

Figure 3.8: *NTP protocol: (a) SAM application, (b) PVD evaporation of Au and (c) of Ti, (d) plasma-activation of the surface, (e) actual nTP-step and (f) demolding of the stamp.*

7. (Optional) Cooling of substrate-stamp-stack (time varies) for ∼30 s – 600 s

8. Removal of the stack and vertical demolding, Fig. 3.8f, at a certain velocity (<10 cm/s)[8]

Post-Processing:

9. Morphological analysis of the transfer results on the sample by SEM and AFM

10. Electrical characterization of samples by probe station or c-AFM

Though the complete, ideal process of this work consists only of standard, well-approved steps, the overall process must be performed quickly and sticking to the pre-defined protocol to obtain ideal results, because it is highly sensitive to experimental conditions, like temperature, pressure, sample exposure to contaminated or humid air or vacuum quality, to name just a few. Since already single dust particles can affect the whole transfer results very negatively, clean process conditions are most crucial for nTP. Hence actual transfer experiments were always performed under clean room conditions.

The NIL 2.5 Nanoimprinter (Obducat)

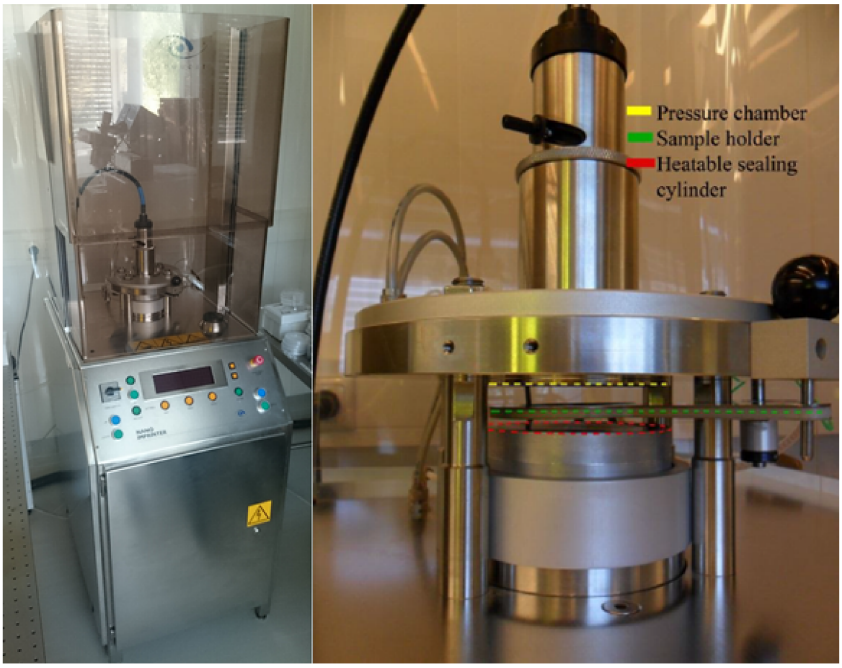

Figure 3.9: *The Obducat 2.5 NIL Nanoimprinter machine used for all transfer experiments (right) and a close-up (left)[203] of its sample holder, pressure chamber and sealing cylinder.*

For all transfer-printing experiments the NIL 2.5 Nanoimprinter from Obducat was used, described in the following.[204] Via a computer interface imprinting cycles can be controlled and data can be logged, saved and displayed graphically. As depicted in Fig. 3.9, the machine has a substrate holder for sample measuring up to 4" in diameter, e.g. wafers. Before any imprint this sample holder has to be cleaned, e.g. by pressurized air. For every imprint the subsrate and the stamp have to be placed on this holder, with the larger piece on the bottom in order to prevent a breaking of stamp or substrate. Then the stamp-substrate stack is covered with several (around 8) disc-shaped, common Al foils and the imprinting specifications are defined in the PC. The machine allows for a separate control of pressure, temperature and UV-light application for an individual time which are all monitored and regulated during the imprint. Note that for UV-assisted imprint transparent foils instead of Al ones have to be used, e.g. for UV-curing of polymer resist. Right before the imprint the sealing cylinder moves up and presses the sample holder with the foil-covered stamp-substrate-stack against the bottom of the pressure chamber. By filling this chamber with nitrogen during the imprint, a pneumatic pressure between 5 and 70 bar can be exerted constantly and homogeneously over the whole area of the Al foils compressing the stamp-substrate stack. If only mechanical pressure is applied, air in the space between foils and sample holder can already escape through a small vent in the sample holder. One can also evacuate this space by actively pumping air out through this vent. A temperature of up to 300 °C can be applied via a heating of the sealing cylinder which usually enhances the results of transfer prints.

3.4.2 Fabrication of Si-Stamps for nTP

A precondition of any transfer experiment is a suitable stamp. Throughout this work commercially available stamps were used, fabricated by IMS CHIPS, Stuttgart, Germany. The stamps consisted of flat Si wafers that were structured on the nm-scale with circular pillars in an e-beam lithography process followed by a dry RIE-etching process. The structured wafers are cut to the final stamp size of 1 cm x 1 cm. Before the transfer experiments, their quality and morphology was checked in the SEM, Figure 3.10. All the investigated pillars usually showed an equal height of 80 nm. The feature sizes on the different stamps comprised variously-sized pillars in accordance with specifications by the manufacturer. The active, i.e. structured area of the stamps ranged between 300 μm x 300 μm up to 5 mm x 5 mm. Stamps with larger, i.e. μm-scale, feature sizes were manufactured by structuring Si wafers with optical lithography, as described in section 3.2.1. This was actually done to accomplish the fabrication of transfer-printed μm-scale-MOS-structures. The results of these experiments are presented in section 6.1.2. For that purpose Si wafers were coated with positive photoresist and covered with a mask containing μm-scale squared pads in a maskaligner. After exposure to UV-light, the resist was dissolved by developer and the obtained negative resist pattern was transferred into the Si by a RIE-etching-step, resulting into a hard stamp consisting of Si structures with the predefined pattern, e.g. lines or pillars. To avoid the repetition of this process, such a hard Si template can optionally be copied into hybrid polymer stamps following

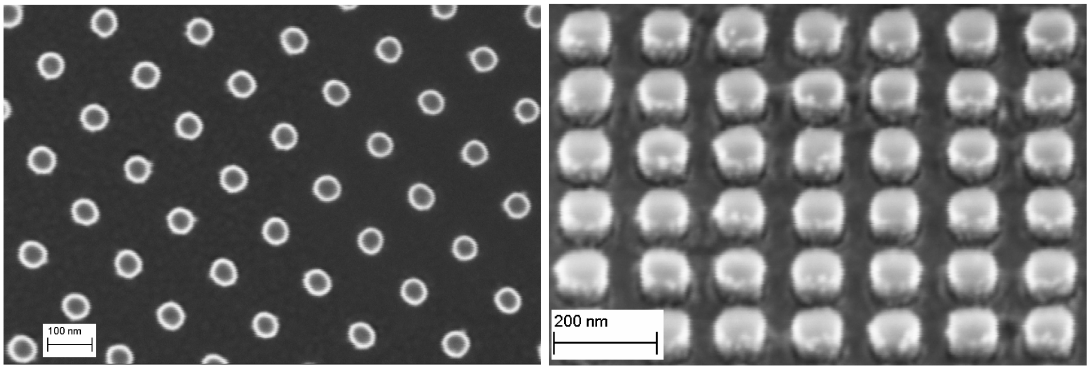

(a) *Pristine 50 nm x 100 nm pillars stamp.* **(b)** *Same stamp evaporated with Au/Ti.*

Figure 3.10: *SEM images of a 50 nm x 100 nm pillar stamp exemplary for the ones typically used in nTP experiments and provided in the list above.*

procedures reported in literature and improved at the Institute for Nanoelectronics.[61] The following types of structures were transferred:

1. Pillars:
   - **a)** 50 nm in diameter with a spacing of 100 nm between each pillar (referred to as "50 nm x 100 nm" in the following),
   - **b)** 75 nm x 75 nm
   - **c)** 100 nm x 75 nm
   - **d)** 100 nm x 100 nm
2. Lines:
   - **a)** 75 nm width, 50 nm spacing (referred to as "75 nm x 50 nm"),
   - **b)** 100 nm x 100 nm
   - **c)** 200 nm x 100 nm
   - **d)** 200 nm x 200 nm
   - **e)** 300 nm x 300 nm

3.4.3 Execution of the nTP-process

The actually applied nTP process, referring to Fig. 3.8 and its protocol in 3.4.1 in the following, starts with the previously described stamps from IMS CHIPS, which have to be cleaned at first, e.g. by a propanol/di-water rinsing or a thorough chemical "piranha clean" (a solution of sulfuric acid and hydrogen peroxide in a concentration of 4:1). The latter process, however, turned out to possibly contaminate the surface and was therefore

considered harmful for nTP and usually not applied anymore. The second important active step of nTP is the application of an anti-sticking layer on the stamps. For this procedure stamps were placed in a petri-dish and put into an exsiccator together with another petri-dish containing 3 drops of the organic SAM, perfluorooctyl-trichlorosilane (SIGMA-Aldrich). The exsiccator is evacuated at 15 l/min flow-rate for 1 min to $\sim$ 10 mbar thereby vaporizing the SAM material. After $\sim$15 min the stamps are covered with a hydrophobic monolayer of the SAM material that decreases the surface energy of the stamps. Finally, the layer on the stamps is hardened on a hotplate at 140 $°C$ for 30 min. Introducing a surface dipole, this monolayer increases the hydrophobicity of the surface and improves adhesion and delamination of the subsequently evaporated metal from the stamp onto the substrate during the transfer step.[73, 85] Third, the evaporation step of the nTP protocol is done as described in section 3.1.1. Generally, stacks consisted of a first layer of Au between 5 25 nm thick and a second 5 10 nm thin Ti layer. Since the thicknesses were significant processing variables, they are specified where relevant in chapters 6.2 and 6.1. For nTP material stacks were deposited on each stamp mostly by e-beam evaporation under a pressure of 10^{-7} mbar. Remarkably, the high vacuum in PVD ensured a high purity of the metal films. The Au as the later top electrode has low adhesion to the stamp for a better delamination during the transfer. The Ti layer promotes this good adhesion of the stack from the stamp onto the target surface.[72, 85] In the fourth step, the Ti on the very top of the stamp was activated by an oxygen-plasma treatment in a barrel asher. The plasma activation of the stamp is a crucial step in several nTP protocols for successful transfers. The O^- ions of the plasma, see Fig. 3.8d, break chemical bonds on the oxygen saturated surface thus producing reactive OH-groups on the stamp and on the substrate. During the later transfer, two OH-groups on the stamp and on the substrate are supposed to form a covalently binding O-bridge between the metal stack on the stamp and the substrate enhancing transfer. This is accompanied by H_2O-evolution which is supposed to be pumped away through the vessel thus promoting its formation in further O-bride-building reactions.[8, 18, 21, 22, 56, 57, 73, 205, 206] Here it was also employed with the intention to form an oxide in a controlled way, cf. section 1. The plasma time to form the titanium oxide was also varied and is of outmost importance for the electrical characteristics of the nTP-structures. A typical plasma ashing process was the application of a plasma of 200 W RF-power for 30 s at 30 mTorr O_2-partial pressure and 100 sccm flow rate.
The substrate material of choice was always (highly) p-doped Si. One of the main research questions was, if the Si substrate formed either an Au/Ti/Si-Schottky-diode or a Au/Ti/TiO_x/Si-MOS-diode via the transfer process. To remove the natural oxide layer, if desired, the Si wafers were dipped into HF before the transfer, if not stated otherwise. Alternatively, if stated, they were plasma-activated, too, to make the 1-1.5 nm thin natural SiO_2 surface layer more hydrophilic and enhance the transfer of the metal on the stamp to the substrate. As enlisted above, the "main nTP process" consisted usually of 5 steps in total. First (step 5 in the overall protocol) the prepared substrate and stamp are placed on the substrate holder of the pressure chamber of the NIL 2.5

Nanoimprinter (Obducat, Fig. 3.9), aligned on top of each other and covered with aluminum foils. Second, for the actual transfer (step 6a), first the pressure was raised to 30 bar and hold for about 1 min, while the temperature raised only slightly ∼35 °C. Thirdly, (step 6b) a temperature of 200 °C was set for about 400 s including a heating phase of ∼120 min, while the pressure was kept constant at 30 bar. This explicit heating step combined with the vacuum between the substrate holder and the covering foils which removes water molecules from the pressure chamber, is supposed to shift the chemical equilibrium of the H_2O evolving reaction towards H_2O evolution. Thereby it accelerates the surface reactions that form O-bridges during the transfer process. This improves the adhesion and thus the transfer of the metal to the substrate. Note that it is also always crucial to monitor and control temperature and pressure during the overall process, as these are the two most decisive process parameters for a successful transfer.[72, 73, 85] Fourth, (step 7) there is an optional cooling-down-step, or, alternatively, the still hot stamp-substrate-stack is removed from the Nanoimprinter at once. Finally, (step 8) the demolding of stamp and substrate is performed with or without the previous cool-down. Note that, due to the hydrophilicity of the two plasma-activated surfaces the stamp and the substrate usually stick together. Hence the stamp has to be separated vertically from the substrate by carefully moving the stamp and the substrate with respect to each other (Fig. 3.8f) at a delamniation speed of less than 10 cm/s maximum[8] for a proper demolding. After a correctly performed process the desired structures are transferred properly and available for further morphological (step 9) or electrical characterization (step 10) which is one major goal of this work. Morphological characterizations of the transfer results are shown for several test structures in section 6.1, while the main results of the SEM and c-AFM characterization are presented in section 6.2.
Because the temperature is raised during the transfer step this process is referred to as "temperature-enhanced" nTP. The increase in temperature during the process removes the H_2O evolving during the transfer step and this way supports the formation of O-bridges. The Ti adhesion layer is needed for the O-bridges to be formed. Cr is another common, more inert, but less efficient adhesion layer. The formation of an oxide due to the thin, functional Ti layer can be at the same time promoting or harmful for the mentioned applications. A Ti film thicker than ∼5 nm readily forms a closed film on the surface, see section 6.2. Thus an effect on electrical characteristics from this Ti adhesion layer, if kept thin enough, was not expected before this work. However, this central assumption turned out to be doubtful, because even few nm-thin Ti layers can be oxidized - in air already or in particular during the plasma activation process. Generated TiO_x-films with thicknesses of ∼3 nm[18] and ∼2.2 nm[21] have been reported. Generally, an evaporated Ti layer is supposed to form a TiO_x layer 2-3 times thicker than the initially evaporated Ti layer, as reported also by Tinoco et al.[19, 20, 20, 207]. Also for Al as top metal layer a ∼3.6 nm thick, compact dielectric layer of AlO_x created by a plasma-oxidation of 30 s has already been shown several times. [56, 57, 73, 205] The thorough experimental and computational investigation of the effects of different plasma treatments was a central task of this work. Results are found in section 6.2.

Secondly, the delamination promoting effect is not completely clarified, regarding the plasma-activation time and has just recently been reinvestigated for Au/Ti-transfers on Si.[61] Hence, it is desirable to understand if and to what extent such an oxygen plasma creates a thin dielectric film of TiO_x to judge the necessity and usefulness of the stamp-plasma-treatment in nTP. As presented in the results chapter 6.2 RF-powers were varied between 200 W and 600 W and times applied from 30 s up to 1200 s for Ti thicknesses of 5 nm and 10 nm to produce a measurement series and compare the influence of the plasma and the associated Ti thickness on the electrical characteristics of the transfer samples. The plasma-oxidation step on the e-beam-evaporated Ti layer could be performed also for polymer stamps, for details see chapter 6.2.

3.5 Characterization Methods

To quantify the effects of process variables on the samples and investigate the potential applications of nTP structures, basically four characterization methods, optical and electrical ones, were applied, which shall be explained in the following. These are optical microscopy, scanning electron microscopy, atomic force microscopy and the probe station.

3.5.1 Optical Microscopy

Optical microscopy is an ideal and mature tool for a quick and easy optical analysis of the surface of a sample and to check, if a transfer process was successful in principle. The available model was a Leica DM 2500 M. With magnifications of 5, 10, 20, 50 and 100 it was only useful on the microscale. Images could be recorded by a connected digital camera and saved on a PC. The light source was a 100 W Halogen (Hg/Xe). Although theoretically the optical diffraction limit of light, i.e. about 200 nm, should be the resolution limit, feature sizes smaller than ca. 2 μm are hardly visible corresponding to the maximum magnification of the microscope times the optical resolution of the human eye, i.e. 0.2' minimum.

3.5.2 Scanning Electron Microscopy

The most important characterization method for surface morphologies of the fabricated samples was scanning electron microscopy (SEM). It is a very practical imaging tool, widely used in science and industry. The model available at the Zentrum für Nanotechnologie und Nanomaterialien (ZNN) was a Zeiss NVision Dual Beam 40 with a Gemini column operating between 100 V and 30 kV, capable of resolutions of 1.1 nm at 20 kV and 2.5 nm at 1 kV. The NVision 40 includes a high resolution SEM function[§] The principle of a SEM is sketched in Fig. 3.11. It consists of an electron source at the top,

[§]It has also a high resolution FIB for precision milling and nanofabrication, yet the FIB function was not used here.

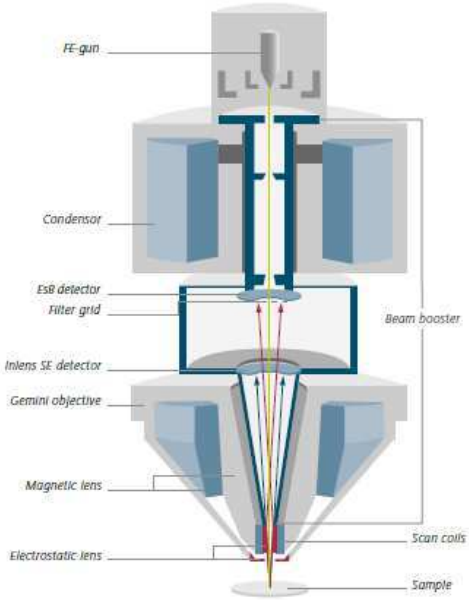

Figure 3.11: *Setup of the Gemini column of a ZeissNVision 40. Reprinted with permission from Carl Zeiss AG.[208] For details refer to the text.*

which is basically a tungsten filament emitting electrons by Schottky emission, and a vertical column, a "beam booster", along which the electrons are accelerated to energies between ∼0.2 keV and 40 keV. At lower energies the surface of the specimen is imaged, while at higher energies one can image deeper layers. In this work 15 keV was used as a moderate standard value. On its way down the column the electron beam is focused by a first electromagnetic condensor lens, passing a first objective aperture and is focused again by a second electromagnetic condensor lens onto the scanning plane. The scanning plane is defined by the scan coils which deflect the beam in the x-y-plane to direct it to a specific sample spot (or also "raster" it over an array of spots on the sample). A final electromagnetic objective lens focuses the electron beam onto the spot on the surface of a sample that is to be imaged. The spot size in the measurements was about 10 nm in diameter, while the interaction depth was about 1 μm.
Three special detectors measure the radiation and particles stemming from the interaction process between electron beam and sample: reflected high-energy electrons from elastic scattering (back scattered electrons), emitted secondary electrons from inelastic scattering and emitted X-rays. The detector signal from each detector pixel is amplified, digitally processed and displayed as differently bright spots on the image on a computer monitor. The sample chamber with the sample holder is evacuated to a pressure of $\sim 10^{-7}$ mbar. The magnification of a SEM can be varied between ∼10 up to 300.000, i.e. over about 4 orders of magnitude, and is defined by the specifications of the scanning coils. It has to be noted that insulating substrates are more difficult to image than conductive ones, because there is no ground potential for the electrons. Thus, the beam penetrates

into the sample and charges the surface. This surface charge deflects the reflected electrons in an uncontrolled way and reduces the resolution. A metallic, e.g. Au, covering layer of the sample is a work-around. Polymer samples can degrade, if the beam energy is too high. So in this case the energy must be reduced. In total, the SEM was the best tool available to determine the lateral extensions of sample features, whereas for measurements of vertical dimensions the AFM is the method of choice.

3.5.3 Atomic Force Microscopy

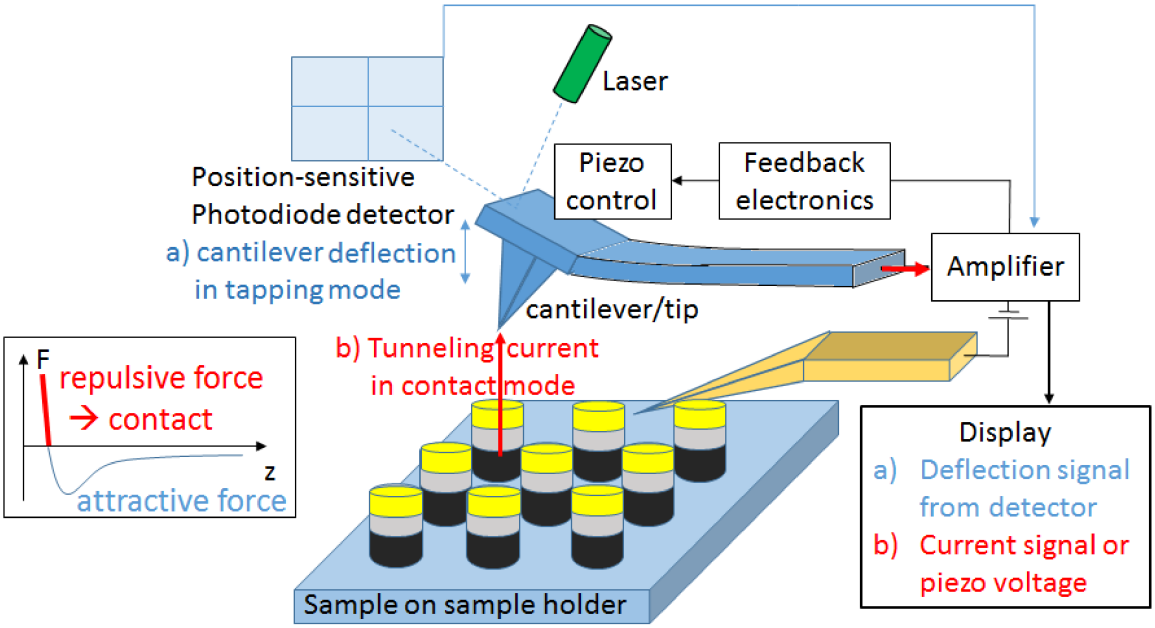

Figure 3.12: *Principle setup of an AFM with two imaging modes tapping mode (a) and contact mode (b) indicated, after [209, 210]. For details on the functionality refer to the text.*

An atomic force microscope (AFM) maps the atomic-scale topography of a surface by measuring repulsive electronic forces between surface and a probing tip moving over the surface. The probe is a sharp tip, typically made of Si and coated with special metallic layers, specified in the results 6.2.3 when used. In our cases the sizes of the actual tips were ~10 μm with 10-40 nm radius at the very end. The tip mounted in the measurement head influences the lateral resolution, which is rather low (~30 nm), and the vertical resolution which can be up to 0.1 nm. It is brought into very close contact to the surface (few nm) by a piezo-crystal that positions the tip vertically with high resolution. In atomic force microscopy, the force between atoms at the end of the tip and atoms in the specimen is measured. The presently used AFM was a MFP-3D atomic force microscopy setup from Asylum Research, California. A typical AFM setup like this is sketched in Fig. 3.12. It consists of the following components:[209, 210, 211]

1. a small spring-like cantilever that can oscillate, preferentially at its eigenfrequency,

2. a sharp tip that is fixed to the cantilever and mostly has a functional coating,
3. a laser that has to point onto the reflective coating at the back of the cantilever,
4. a photodiode detector for the reflected laser beam to detect the motion of the tip, connected to
5. an electronic feedback system to control the movement of the tip or the sample,
6. an xyz-drive controlled by piezo-crystals to move the tip or the sample,
7. the sample holder,
8. a display system that converts the measured data into an image plotted on the screen.

As sketched in Fig. 3.12 the cantilever is deflected by the interacting forces between tip and sample. In the used setup the degree of the cantilever deflection is detected optically by the correspondingly strong deflected laser beam focused on the back of the cantilever. The cantilever deflection is spatially stressed by a distantly placed detector system. The reflected laser beam hits the pixels of the multiply segmented photodiode detector. This signal is acquired, digitized and an image of the surface is reconstructed. The processed signal is also used to control the cantilever deflection via a feedback system and to re-adjust the movement of the tip (approach or withdrawal) by adjusting the voltage on the piezos of the xyz-drive according to the measurement mode. The setup is particularly sensitive to height variations of the tip, typically down to 0.1 nm. For tapping mode the oscillation amplitude is kept constant, while for contact mode the tip-sample-force is kept constant, see below.[210, 211] In the present setup the sample is mounted onto a platform controlled by the piezo actuator moving over the sample in the x, y and z directions underneath the tip. When the tip translates laterally relative to the sample surface, one measures the sample topography.
When approaching the tip towards the sample from a greater distance, first, there is no force due to Van-der-Waals-interaction s, i.e. dipole-dipole-interactions, between the two. At a certain distance z, the snap-in-point, the attractive part of the Van-der-Waals-forces becomes bigger than the repulsive part plus the repelling elastic constant, and the tip is adhered to the substrate. But when decreasing the tip-sample-distance z further, the repulsive interaction force increase - up to a user-defined point. At this point, the tip, though still adhering to the sample, will be rather repelled from it back to a greater distance when trying to get closer. Thus, tip and cantilever are established in equilibrium position and the interaction force is compensated to zero by the z-piezo. Forces measured by the z-piezo ranged from pN to nN. Scanning at a constant height might make the tip collide with the surface. Therefore, the feedback mechanism adjusts the tip-to-sample distance to maintain a constant force between the tip and the sample.[210, 211] Depending on the specific imaging purpose it can be operated with different tips and three separate operating modes, i.e. tapping mode, contact mode and non-contact mode. The former two will be explained in the next two sections.

Tapping Mode

Tapping mode is the standard measurement mode for stable, but gentle topological images and was used to characterize the transfer printing samples horizontally, especially to the check their quality. In this mode the cantilever is oscillated up and down at or near its resonance frequency with a relatively high amplitude between 20 and 200 nm (typically ∼100 nm) by the piezo mounted in the AFM tip holder.[209] The cantilever is positioned in a way that it just touches the surface for a very small fraction of its oscillation period. The signal responsible for the final image is the oscillation amplitude measured via the optical setup described above. The feedback control adjusts the height so that the cantilever oscillation amplitude is kept constant while scanning across the surface of the sample. This way, in tapping mode, the AFM measures the intermittent contacts of the tip with the surface in tapping mode. The main advantages of this imaging mode are a high lateral resolution (1 nm), stable imaging conditions, low lateral forces minimizing damages of the tip and surface compared to contact mode. The major drawbacks are low scan speed and relatively high normal forces.[209, 210]

Contact Mode

In contrast to standard AFM, in contact mode, as well as in c-AFM, a tip, with low spring-constant is in perpetual contact to the sample.[210] The cantilever deflection changes during low-speed scanning of the sample structure and this deflection is kept constant by a compensating piezo (voltage), adjusted for accordingly over a Z-feedback loop (feedback mode ON) in the head. The feedback circuit keeps the tip-pillar distance constant this way over the piezo actuator and the surface profile of the sample can be displayed either by the piezo voltage, giving a topological image of the sample, or the current flowing through the stack, which creates a “conductivity” map of the sample. This procedure is also referred to as “current mapping” or ‘’condutive AFM” (c-AFM) as carried out in section 6.2.3.[211, 212] This imaging mode with constant force and electrical feedback options switched on was also used for the conductive AFM characterizations to create conductivity maps of the nTP samples, which will be discussed in chapter 6.2.3 including typical contact mode images. Due to noise and drift of the signal, cantilevers with low spring constant are used to amplify the deflection signal. As described above, attractive forces can get that strong close to the surface, that the tip "snaps-in" to the surface. Contact mode AFM is done in the repulsive regime for distances below equilibrium with the tip being in firm contact with the solid surface. Advantages of the contact mode are high scan speed, the possibility of taking atomic resolution images and easier scanning of rough samples. But this comes at the cost of high shear and normal forces that make the tip prone to damaging softer samples.[209, 210]

3.5.4 Probe Station

Electrical characterizations (IV-curves, CV-sweeps) of transfer-printed samples with microscale pads were performed with a Keithley K2460a probe station setup connected to and controlled by a 4200-SCS parameter analyzer from Keithley. The 4200-SCS is a modular and fully integrated system that has nine measurement slots, e.g. for SMU or CV-modules.[213, 214] Relevant sample parameters that can be measured by such a setup, as depicted in Fig. 3.13a, are accumulation capacitance, breakdown voltage, flatband voltage, threshold voltage and oxide thickness, given the relative permittivity is known. Results of the characterization are given in section 6.2.7. The most important purpose of the setup were low-noise measurements of IV-characteristics following standard procedures. Particularly for the transfer printed samples, a special, most sensitive measurement technique had to be applied, as depicted for the probe station schematics in in Fig. 3.13b: The tip of the tungsten probe needles were dipped into indium gallium (InGa), a liquid metal, forming a drop of about $\sim 100\ \mu m$ diameter at the tip. When placed above a contact pad, e.g. of a transfer-printing sample, this liquid drop flows down onto the pad thus establishing a good electrical contact at the same time avoiding a direct physical contact of the sharp tip to the metallic pad. Hence the risk of pushing through the nm-thin metal and oxide layers of the investigated MOS- and MOM-transfer-printing samples was avoided. This allowed for a very soft contacting of the sensitive, nm-thin metal layers, such as the ones typically present on top of transfer-printed samples whose fabrication and characterization is the focus of section 6.2.

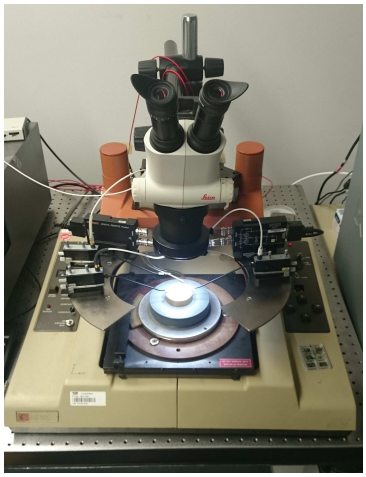

(a) *Image of the Keithley K2460a probe station setup.*

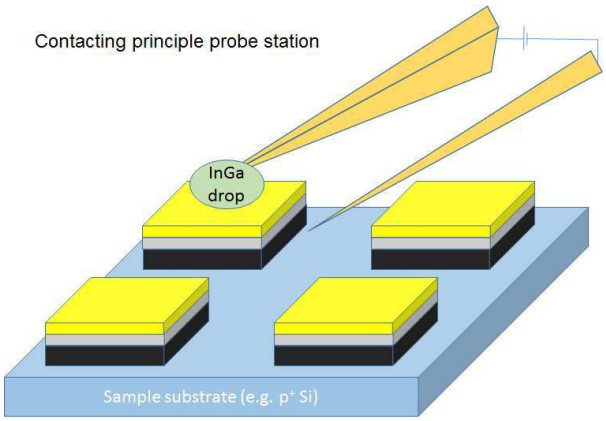

(b) *Top contacting principle of the fabricated nm-thin films by a tungsten needle with a fluid InGa drop at the tip.*

Figure 3.13: *Probe station measurement setup and contacting principle.*

Chapter 4

Kinetic Monte Carlo

'Monte Carlo' (MC) methods were developed as a mathematical tool to tackle complex physical or chemical systems undergoing many possible processes, i.e. "state transistions" or "reactions". The variable entities of such systems are on spatio-temporal scales between classical continuum equations and molecular dynamics, see Fig. 4.1 reproduced after Kratzer[215], and are usually described by a vector of state variables $\mathbf{S}$. The evolution of the system in configuration space is mostly described either by a nonlinear system of ordinary differential equations or stochastic differential equations. MC-methods are applied for a wide range of physical problems from the decay of nuclei, over transport of particles, e.g. electrons in semiconductors, to semiconductor device modelling and material growth processes which involve such fundamental mathematical problems like stochastic integro-differential equations or the inversion of big matrices.
Usually these problems are simply too complex to be solved analytically. Referring to Fig. 4.1, Monte Carlo simulation can at least take on input from solutions of underlying physical problems solvable by DFT or MD methods, as done earlier, for example in [216]. MC methods exploit (quasi-)random numbers to produce approximate solutions for physical problems. Thus they are not "exact" but rather "statistically rigorous", i.e. the solution is exact within a certain error range and a certain probability. Random numbers themselves are widely known for their usefulness in numerics, e.g. to numerically evaluate integrals by a stochastical procedure, also in a high-dimensional space, which is a MC method by definition. Therein the result of the intregral is replaced by a sum over the value of the integrand function at discrete, randomly chosen support points. One can also find more challenging examples, like the standard textbook one of the well-known Metropolis algorithm to simulate the final configuration of a polymer chain starting from an initial configuration.[217, 218] This problem, however, is still static and not dynamic, i.e. there is no time-evolution of the system included in the algorithm. The probability of the system configuration to undergo a macroscopic transition in ($\mathbf{x}$,t)-configuration space, meaning microscopically the movements of the N molecules of the polymer chain from certain positions described by the 3N-vector $\mathbf{x_i}$ at a certain simulation time t_i to the next $\mathbf{x_j}$ at the next simulation time t_j, is not linked to the real time needed for this

transition. So from the available information on the "artificial" time steps $t_j - t_i$ in this algorithm one cannot make a statement on the real time to reach a certain state.

In 1976 a stochastical algorithm for simulating the real time evolution of the chemical reactions in a homogeneous mixture of molecules was developed by Gillespie, named "kinetic Monte Carlo" (kMC) algorithm later on.[41] Analytically, this problem would require the solution of a set of coupled nonlinear integro-differential equations, a fundamental problem of stochastical analysis. A stochastic formulation of it can allow for a numerical solution whose computation is normally elaborate. But not so for the stochastic formulation of the time evolution of such systems derived by Gillespie. He considered the chain of single reactions (or more "general transitions between states") of the system as a chain of Markov processes and went from a concept of "reaction probabilities" to "reaction rates", which allowed for an efficient numerical computation of an approximate solution for the temporal evolution of the system using random numbers.[41] The sophisticated kMC-procedure could quite quickly be transferred to electron dynamics in semiconductor devices by follow-up researchers and still served as the very basis of the kMC simulations in this thesis.[42, 219]

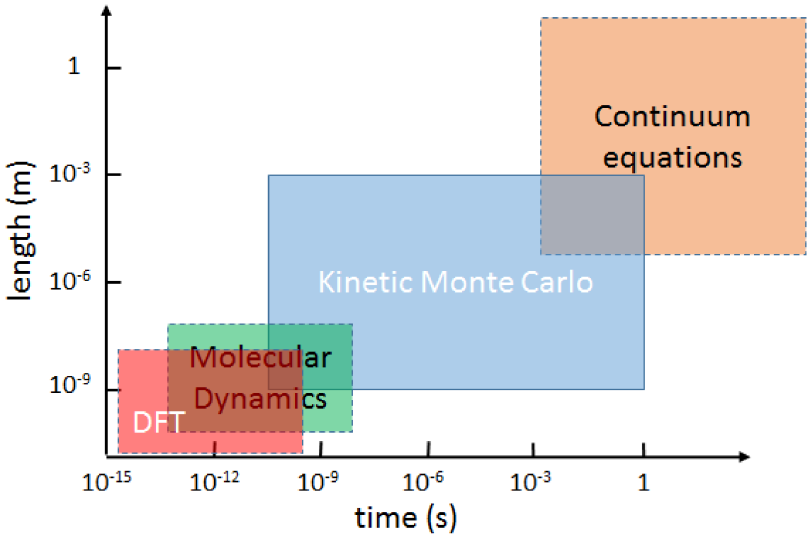

Figure 4.1: *Scales of common calculation methods compared to the kMC-method used here. While DFT and MD refer to shorter, also electronic, time and length scales, kMC covers broad scales located between the latter two methods and the classical continuum. The possibility to feed kMC with results of DFT or MD computations makes kMC even more attractive as versatile and valuable simulation tool and was also exploited in this work. It can be employed for reaction times between 10^{-10} s and 1 s. MD itself can also make use of DFT results or classical forces, which increases time and length scales it can handle. Image reproduced after P. Kratzer.[215]*

4.1 Introduction into the kMC-framework

For the derivation of the stochastic framework of kMC, the microscopic transitions of a state of the system to another must fulfill the conditions of a Markov process in the first place. The Markov property states that the transition from a present state $\mathbf{x_i}$ at time t_i to the next one $\mathbf{x_{i+1}}$ at time t_{i+1} is independent of all precedent states and transitions leading to that present state except the very last one.[220] Thus also the present state has been reached from a previous state $\mathbf{x_{i-1}}$ at time t_{i-1} with the conditional probability $p_{1|1}(\mathbf{x_i}, t_i \mid \mathbf{x_{i-1}}, t_{i-1})$ only depending on the initial and the final state. As a consequence, that can be shown via the Chapman-Kolmogorov equation for conditional probabilities of Markov processes, the total probability density to arrive at any state $\mathbf{x_i}$ at t_i can be expressed based on the initial state $\mathbf{x_0}$ at t_0. As derived in textbooks, in the limit of inifinitely small time intervals between two transitions (and under the assumptions that the Markov process becomes stationary) the so-called master equation holds, which describes the the temporal change of the occupation of discrete states:[220, 221]

$$\frac{dP_i(t)}{dt} = -\sum_{j \neq i} R_{ij} P_i(t) + \sum_{j \neq i} R_{ji} P_j(t) \tag{4.1}$$

where $P_i(t)$ is the probability to find the system at time t_i in state $\mathbf{x_i}$ and R_{ij} and R_{ji} are the transition rates, viewed as probabilities per unit time, to undergo the next transition from state i to state j and from state j to state i, respectively.
By its derivation the master equation governs the time evolution of any stochastic system constituted of Markov processes. This means the function $P_i(t)$ that satisfies the master equation measures exactly the probability to find such a system at time t_i in state $\mathbf{x_i}$, but it needs all transition rates R_{ij}.[41] Despite of the strong mathematical assumptions behind its derivation, practically, the master equation is even rarer solvable analytically than the mathematically equivalent deterministic formulation as a set of coupled differential equations for the reaction rates. Even more, a Monte Carlo algorithm which is able to construct such a probability density function that satisfies Eq. (4.1) offers the great benefit to study the interplay of a large number of possible transitions in configuration space, independent of their physical nature. The kMC-algorithm itself is essentially equivalent to the master equation, although it does not use the equation explicitly. Beneficially, it is that flexible that the multitude of possible atomic processes, e.g. many different transport processes and corresponding rates in the material, can be modularily coded in a simulation program to study the macroscopic outcome, e.g. the current, in a more reliable and simpler way than with former rate equations methods. But there is always a price to pay: It can still be a time-consuming algorithm, especially due to the computation of the rates. This can only be improved by using background knowledge on the physical system under investigation. Once the clear and unamendable kMC-framework is set up, it is the fundamental task of the researcher, to work out, define and insert additional information on individual physical processes into the simulation,

e.g. on energy levels or reaction rates obtained by first-principle calculations of the system, like in this thesis. The computation speed only becomes acceptable, if one clearly defines and reduces the quantities in the system that shall be computed, e.g. computing in the first place just the most probable value of the observable of interest instead of a whole probability distribution, or excluding certain processes which might be physically possible, but are virtually insignificant for the study. This is particularly true for certain electron transport, generation and recombination processes in TiO_2 which will be discussed in section 5.5.

4.2 The kMC-scheme

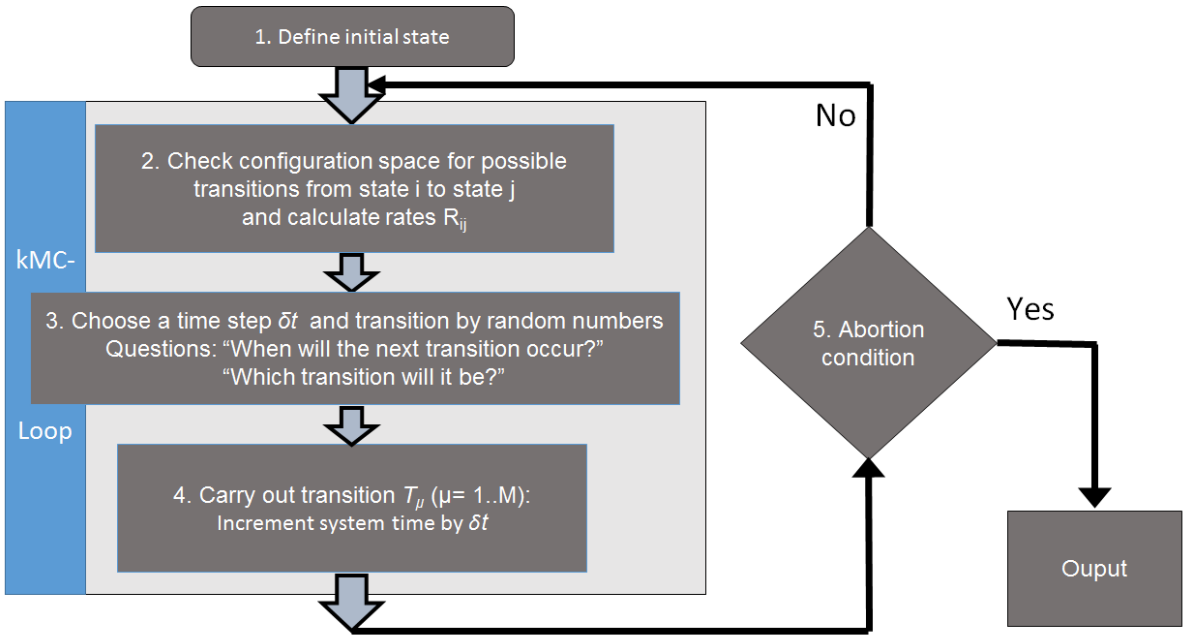

Figure 4.2: *General flow chart scheme of the kMC-algorithm - single steps detailed in the boxes. Depiction after Jegert.[43]*

Coming to the core of kMC, firstly, the fundamental principle of any standard kMC-algorithm is depicted in the flow chart in Fig. 4.2.

1. It starts by the definition of an initial macroscopic state i, usually via initializing a parameter set.

2. From this state i the algorithm has to check the configuration space of the system for all possible transitions from state i to any other state j, and to identify them and to calculate the corresponding rates R_{ij} according to the implemented physical model.

3. Then a transition from i to j combined with the related transition time δt has to be chosen. For this purpose the fundamental question "When to execute which transition?" is answered. This is done, for example, by the stochastic selection scheme by Gillespie, see 4.3.

4. The transition from state i to state j is undergone and the system time is incremented by δt, manifesting the end of one so-called "kMC-step".

5. Finally an abortion condition has to be checked which defines, if a further kMC-step shall be executed or not.

In the latter case the algorithm terminates with the final state j, while in the former the algorithm restarts at step (2) closing the kMC loop, as indicated in Fig. 4.2. Then the new initial state i must be redefined as the final state j and the list of possible transitions must be updated, since a new state is reached.
As a final remark, despite of its minor position in the scheme, the abortion condition can have important implications on the actual outcome of the simulations, e.g. up to which precision physical quantities of the dominated processes in the simulation shall be calculated. This determines how precise the analysis of the physical results can be performed after the simulation has finished.
By this scheme one can see that in order to move the system dynamically correctly forward in time the (two) central question(s) to be answered are:

- "When will the next transition occur?"
- "What kind of transition will it be?"

The answers can only be given in a probabilistic sense which is done by the Gillespie algorithm.[41]

Short analogy between numerical integration by random numbers and kMC

An analogy between the simpler numerical MC-integration by random numbers and the stochastical framwork for the more complex systems in kMC can be drawn. In short one can say that under the central limit theorem of statistics, the average of an ensemble of joint probability density functions of Markov chains of reaction processes, which are numerically approximated in kMC, converges towards the actual joint probability density function, just as the sum of the support points converges, in the statistical sense, towards the value of the integral. The error decreases proportional to the inverse square root of the number of evaluated support points, i.e. computed Markov chains. From this simplified picture one can better understand the fundamental philosophy behind kMC. It randomly draws support points, i.e. system states in time, and evaluates reaction rates in a way defined by the stochastical kMC-scheme, so that in the limit of "many" repititions of the algorithm one retrieves an approximation of the actual joint probability density function in equilibrium - or at least the maximum probability value - of the

specific observable. This can be also the current density through a slab of matter as in our case. If one knows the statistically correct way of how to construct the Markov chain and add specific support points in the configuration space, i.e. "when" to evaluate "what" intermediate rate, the repeated computation of such Markov chains and averaging over the computed ensemble, approximates - in a statistical sense - the solution of the master equation.

4.3 The Gillespie algorithm

Now, the kMC-algorithm, as introduced by Gillespie in 1976, shall be explained into more detail by the specific system of interest, i.e. the transport of an ensemble of electrons through a material slab of volume V.[41] The Gillespie algorithm generates statistically correct trajectories of such an ensemble according to the stochastic rate equations by answering the two basic questions posed above. At the beginning the system is in a macroscopic state, i.e. the volume V contains a composition of n_i electrons in states x_i, $i = 1, ..., N$, (usually all electrons are viewed as identical, so N is usually 1 in the simulations later on) and those states can undergo transitions through a set of M electron transport channels T_μ ($\mu = 1, ..., M$). Then M constants R_μ can be asserted to the transitions that depend on the physical properties of the electrons in the specific states as well as the environmental variables, such as temperature, pressure, geometrical dimensions of the system, and so on, by:

$$\begin{aligned} R_\mu dt = &\text{ the average probability that any electron state } x_i \\ &\text{will be occupied or emptied via the transport channel } T_\mu \\ &\text{within the next infinitesimal time interval dt.} \end{aligned} \tag{4.2}$$

This assumption manifests the fundamental hypothesis of the stochastic formulation of chemical kinetics, as described in Gillespie's paper from 1976.[41]
In this definition the term "average" means, that summing up the $R_\mu dt$ over all distinct transport μ yields the toal probability that a transition via aby T_μ will happen at all in the volume V within the interval $(t, t + dt)$. The time step dt has to be inifinitesimal, i.e. that small that no other transition can occur within this time step.
The definition on its own has not yet any relation to the dynamics of the specific system, as it does not answer the question, when to execute the transition. So in order to simulate the dynamical behaviour, this hypothesis has to be properly related to the temporal propagation of the system. For that purpose a so-called "reaction probability density function" $P(\tau, \mu)$ has to be defined via[41]

$$\begin{aligned} P(\tau, \mu)d\tau = &\text{ probability at a time t that} \\ &\text{in the differential time interval } (t + \tau, t + \tau + d\tau) \\ &\text{a reaction will happen and it is of type } T_\mu. \end{aligned} \tag{4.3}$$

Apparently the two variables τ and μ describe time and reaction type. In order to derive an analytical expression for $P(\tau, \mu)$, first numerical values for these two variables must be assigned by the algorithm according to the hypothesis in Eq. (4.2).
In contrast to Gillespie's original paper, we just have to deal with the simplest case of just one possible combination of reactants, i.e. an electron in a singly occupied state can just traverse into an unoccupied state or vice versa. Thus the mutiplicity of each transport channel is 1 and $R_\mu$dt directly becomes the average probability to first order that the particular channel T_μ will be taken by an electron in the volume V within the next infinitesimal time interval dt.
Then the reaction probability density function becomes the product of the probability $P_0(\tau)$ at time t that no reaction occurs within $(t, t+\tau)$ multiplied by the probability to first order in $d\tau$ that within the next inifinitesimally small time interval $(t+\tau, t+\tau+d\tau)$ a transition T_μ takes place:[41, 43]

$$P(\tau, \mu)d\tau = P_0(\tau)R_\mu d\tau \tag{4.4}$$

To calculate $P_0(\tau)$ the interval from the present time t up to the time τ $(t, t+\tau)$ is divided into K subintervals of equal length $\epsilon = \tau/K$. Then the probability that none of the transitions $T_1, ..., T_M$ will occur in the first subinterval $(t, t+\epsilon)$ is

$$\prod_{\mu=1}^{M}[1 - R_\mu\epsilon + o(\epsilon)] \approx 1 - \sum_{\mu=1}^{M} R_\mu\epsilon \tag{4.5}$$

The expression for no transition to occur remains the same for all of the subsequent intervals $(t+\epsilon, t+2\epsilon)$, $(t+2\epsilon, t+3\epsilon)$, ..., and probabilities for each of single intervals are independent of each other. Thus the total probability $P_0(\tau)$ is (in first order of ϵ)

$$P_0(\tau) = \left[1 - \sum_{\mu=1}^{M} R_\mu\epsilon\right]^K = \left[1 - \sum_{\mu=1}^{M} R_\mu\tau/K\right]^K \tag{4.6}$$

One can easily see that in the limit of large K, i.e. infinitely small subintervals ϵ, this equation takes on an exponential form

$$P_0(\tau) = \lim_{K\to\infty}\left[1 - \frac{\sum_{\mu=1}^{M} R_\mu\tau}{K}\right]^K = \exp\left[-(\sum_{\mu=1}^{M} R_\mu)\tau\right] = \exp[-R\tau] \tag{4.7}$$

with $R \equiv \sum_{\mu=1}^{M} R_\mu$ being the cumulative transition rate. This corresponds to an exponential decay of the present state at time t through all possible transition channels T_μ. By inserting Eq. (4.7) into (4.4) ones gets the exact reaction probability density function:

$$P(\tau, \mu) = \begin{cases} R_\mu \exp[-R\tau], & \text{if } \tau \in [0, \infty), 1 \le \mu \le M \\ 0, & \text{otherwise} \end{cases} \tag{4.8}$$

It is also a straightforward task to show that this reaction probability density function is properly normalized to 1 over the whole definition set of τ. Eq. (4.8) is a rigorous mathematical consequence of the fundamental hypothesis above. It depends on all transition constants and on all available types of reacting electrons.
Making use of this reaction probability density the complete algorithm reads as follows:

1. Initialize time $t = 0$; define initial distribution of charge carrier positions and energies
2. Identify all possible transitions T_μ from the present state i into all possible states j of the system; calculate the transition rates R_μ for all electrons from present state i into all possible states j of the system; calculate the cumulative transition rate R.
3. Find a tupel (τ, μ) according to the joint probability density function $P(\tau, \mu)$ by an appropriate MC-method.
4. Increment time $t = t + \tau$; modify the set of electrons i according to the performed transition T_μ and define the new state j as initial state i.
5. Check finishing condition, e.g. if $0 < t < t_{stop}$ then go to step 2, otherwise terminate.

Choice of time step τ and transition T_μ by direct MC-sampling

For the choice of the tupel (τ, μ) according to the joint probability density function $P(\tau, \mu)$ a suitable Monte Carlo technique based on random numbers has to be employed. This can be the direct "inversion" method, found in standard textbooks, the "first-reaction", implemented and described e.g. in [161, 162, 179, 180, 181, 182, 183] or the "importance sampling" method. The former one shall be described here. First $P(\tau, \mu)$ has to be written as the product of $P_1(\tau)$ - with $P_1(\tau)d\tau$ being the probability for a transition to happen within the next time interval $[t+\tau, t+\tau+d\tau]$ - and of $P_2(\mu|\tau)$, the probability that this next transition will be of type T_μ given it happens at time $t + \tau$:

$$P(\tau, \mu) = P_1(\tau)P_2(\mu|\tau) \tag{4.9}$$

The calculation of $P_1(\tau)$ follows from the addition theorem of probabilities by summing up the probabilities over all transition possibilities μ:

$$P_1(\tau) = \sum_{\mu=1}^{M} P(\tau, \mu) = R \cdot e^{-R\tau} \tag{4.10}$$

Then the second probability has the form:

$$P_2(\mu|\tau) = \frac{P(\tau, \mu)}{P_1(\tau)} = \frac{R_\tau \cdot e^{-R\tau}}{R \cdot e^{-R\tau}} = \frac{R_\tau}{R} \tag{4.11}$$

Any tupel (τ, μ) distributed according to both Eq. (4.10) and (4.11) will also be distributed according to $P(\mu, \tau)$. Hence two MC steps are performed - not necessarily in the following order:[43, 189]

- A random time step τ obeying the continuous PDF $P_1(\tau)$ is chosen from a uniformly distributed random number r_1 by the well-known inversion method. In brief, after the generation of an uniformly distributed random number $r_1 \in [0, 1]$, τ has to be obtained via the formula:

$$\tau = -\frac{ln(r_1)}{R} \tag{4.12}$$

- The transition μ obeying the PDF $P_2(\mu|\tau)$ is chosen from a second uniformly distributed random number r_2 according to the inversion method for discrete variables by the formula:

$$\frac{\sum_{\mu'=1}^{\mu-1} R_{\mu'}}{R} = \sum_{\mu'=1}^{\mu-1} w_{\mu'} < r_2 \leq \sum_{\mu'=1}^{\mu} w_{\mu'} = \frac{\sum_{\mu'=1}^{\mu} R_{\mu'}}{R} \tag{4.13}$$

In the latter equation w_μ denote transition probabilities defined as the transition rate R_μ normalized by the cumulative transition rate R. Note that, since the two random variables are related to each other via the total transition rate R occuring in both MC selection conditions, their choice can be done without either of the two needed for the choice of the other. Then the tupel (τ, μ) will always obey the reaction-PDF $P(\tau, \mu)$ from Eq. (4.9). Eventually, the extensions to the simple kMC-algorithm from Fig. 4.2 outlined in this section can be completely summarized in Fig. 4.3. This flow chart, reproduced and extended after [43] virtually represents the structure of the implemented code. The essential physics of the system are reflected by the transition rates R_μ whose calculation will be detailed in the next chapter.

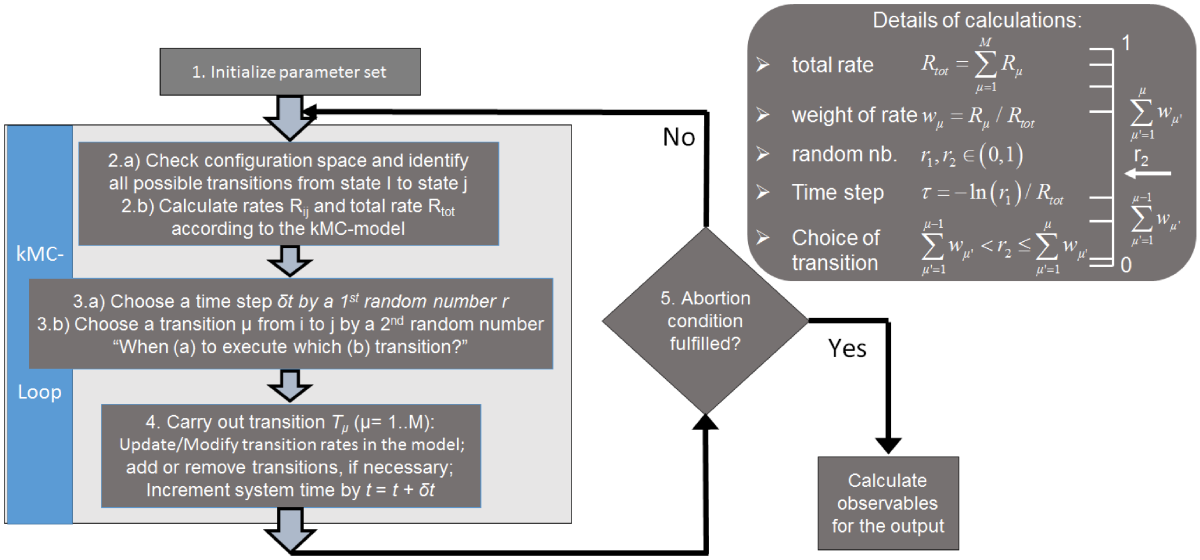

Figure 4.3: *Complete scheme of the extended kMC-algorithm after Gillespie - single steps are detailed in the boxes and the text. Depiction after Jegert.[43] The upper right box summarizes the most important equations and principles for the calculations, as detailed in the text. Note that the computationally most intense step is usually step 2.a and 2.b.*

Chapter 5

Kinetic Monte-Carlo Model of Conductive Oxides

In order to model the experimentally fabricated and characterized MOS- and MOM-contacts the focus of the subsequent work was the adaption, implementation and validation of the model for the current density through the oxide materials TiO_2 and AlO_x with the goal to reproduce the jV-characteristics of those samples accurately. The simulation of the current density consists of five, partly correlated, charge carrier transport process channels resembling the "transition channels" from chapter 4.3. These are explicitly: Schottky Emission (SE), Direct Tunneling (DT), Fowler-Nordheim-Tunneling (FN), the so-called "intrinsic", i.e. non-trap-related processes subsumed by an adapted version of the Tsu-Esaki-Formula, presented in section 5.1, as well as trap-related processes Poole-Frenkel-Emission (PF) and Trap-Assisted-Tunneling (TAT). These five processes compete and are selected statistically in each step of the kMC-simulation according to the Gillespie algorithm presented in the precedent section 4.3. One of the great benefits of the kMC-algorithm as derived beforehand is that even a complex system with arbitrarily many simultaneously present, invidual transport channels can be itemized into the implementation of acurate rate equations for each single transport channel, while the construction of the algorithm itself takes care of the statistically appropriate choice of a transport process within each simulation step.

However, if this is done without physical reasoning, this can lead to an overwhelming number of computationally intense equations to be solved in each simulation step which can cost lots of computation time and makes it difficult for the user to handle and adjust the simulation properly. Though we only concentrated on electron transport processes, because hole current was always neglected due to a large VB offset in the materials of interest, the included processes turned out to span up a wide parameter space. This is seen by a list of the relevant parameters of the model which are:

- the band gap E_g,

- the optical dielectric constant ϵ_{opt} and the static dielectric constant ϵ,
- the effective electron masses in cathode or anode m^*_{ca} and m^*_{an},
- the effective electron mass in the oxide m^*_{ox},
- the thickness of the oxide d (or d_{ox}),
- the trap energy in the oxide E_D
- the density of traps or defects in the oxide n_D and finally
- the conduction band offset(s) (CBO) between electron-injecting cathode and oxide layer $\phi_{B,ca} \equiv E_{B,ca} \equiv \phi_{B,l} \equiv E_{B,l}$ as well as oxide layer and anode $\phi_{B,an} \equiv E_{B,an} \equiv \phi_{B,r} \equiv E_{B,r}$.

Since essential parts of the kMC-model for MOM-contacts were already set up in the PhD thesis by G. Jegert in 2011 [43] in a very extensive and general way which included all theoretically known formulae for the rates of all processes important here, mostly the accurate parameterization of the simulations and certain necessary corrections of the model were studied in the framework of this thesis. Therefore more rational arguments for the specific, precise choice of the broad parameter space and justifications, how to simplify the problem, will be discussed in combination with actual results of the performed kMC-simulations in chapter 6. Due to the given reasons the corrected and adapted charge transport model shall be presented at this point, exclusively. Despite of unavoidably repeating parts and formulae that exist in common literature, the description is kept as concise as possible, but extensions are emphasized, when necessary. This applies especially for the adaption of the model to MOS-contacts using TiO_2 as dielectric, e.g. by supplementary DD-simulations or the MIGS-model in chapters 5.5 and 6.3.4, respectively. Moreover, due to the extensions and corrections renewed sensitivity analysis and consistency checks were necessary, following right after the introduction of the corresponding formulae for the transport processes in the model. A proper documentation of the sensitivity to the most important input parameters of a process is highly useful in order to forecast the outcomes of the model and predict the behavior of the material system without performing costly simulations.
Based on the energetic situation and transport processes for electrons, as summarized in Fig. 5.1 and 5.2, the model will be described in the subsequent sections. All parameters essential for the model are already defined in Fig. 5.1. The mechanisms of the important, initial process of charge injection, as described in chapter 5.2 is emphasized. Also the actually present band bending, especially for the MOS-structures, is sketched and the linear approximation for it is shown in accordance to the results of DD-simulations to be found in 5.5. The CB and Fermi-level is supposed to drop linearly over the oxide (thickness d), but for a Si contact the applied voltage can partly drop in the semiconductor, see 5.5. The offsets to the electrodes $\Delta\phi \equiv E_B$ determine the band energy according the Mott-Schottky-rule or the metal-induced-gap states-(MIGS)-model , cf.

section 6.3.3. Referring to an idealized and slightly simplified situation, justified by Fig. 5.1, Fig. 5.2 summarizes already all the basic transport processes implemented in the kMC-model across a MOS-junction according the specific rate equations, as introduced in the next section. Different colors indicate different formulae for the rates: SE, DT, FN (red, according to the Tsu-Esaki-formula), PF (violett) and TAT (green, elastic or inelastic under phonon absorption/emission with energy $\hbar\omega$) with Miller-Abrahams hopping (MA) or multiple-phonon-trap-assisted-tunneling (MPTAT) as intermediate processes in the oxide. PF and TAT need precedent electron injection events (also green) into traps (orange, trap density n_D, trap position x_D, trap energy E_D) to occur. The extraction is assumed to be performed into the CB of the anode (metal or Si). The DOS(E_e), reflected by $m^*_{ca/an}$ and Fermi-function $f(E)$ determines the number of available states.
The depicted physical situations and processes are the basis for the model in the next chapter and also of the simulation results presented in chapter 6.

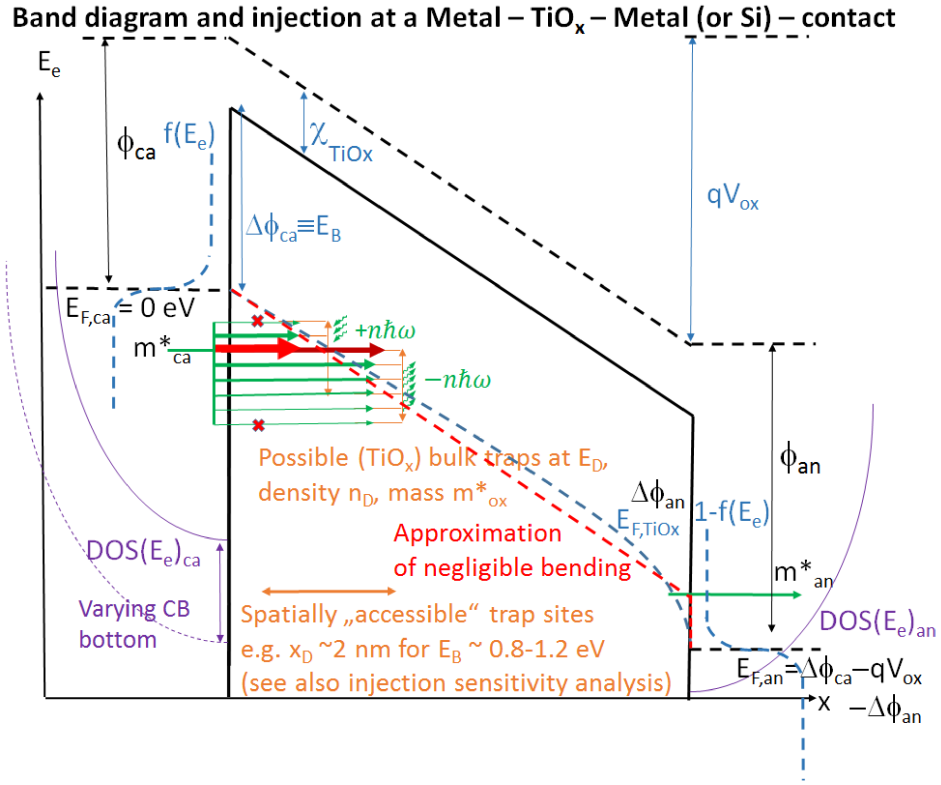

Figure 5.1: *Band diagram of a MOM or MOS-structure with of an arbitrary first metal then TiO_x and a second metal or p^+-Si.*

5.1 Direct Tunneling

To begin with, direct Tunneling (DT) in its general sense refers to coherent tunneling of electron wave packets through an energy barrier. This barrier is constituted by the energy

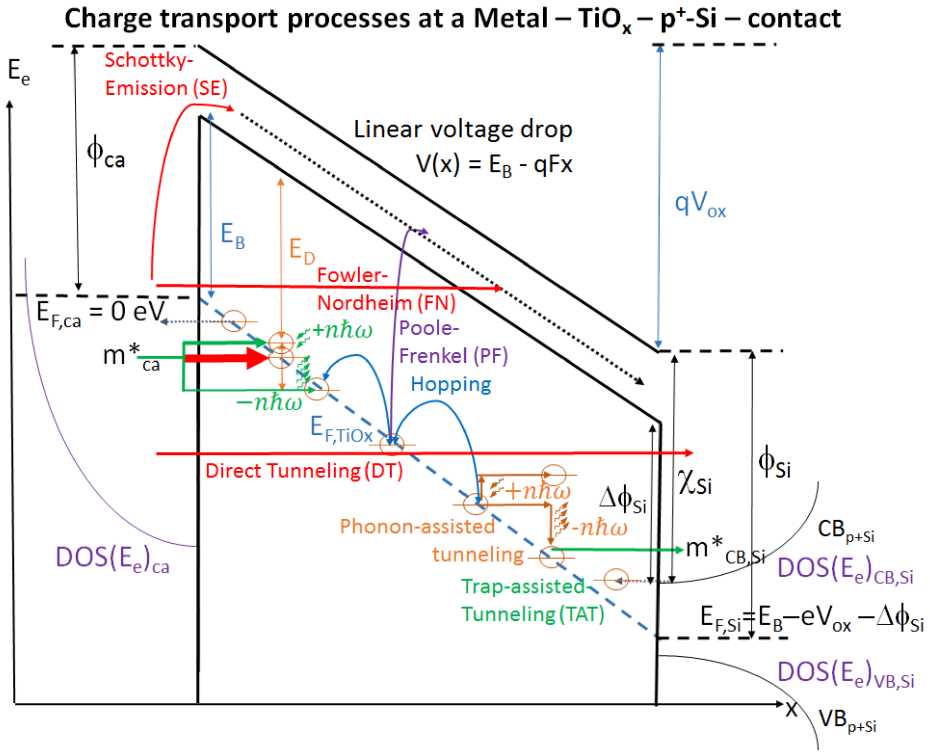

Figure 5.2: *Summary of all basic transport processes implemented in the kMC-model according the specific rate equations: SE, DT, FN (red, according to Tsu-Esaki), PF (violett) and TAT (green, elastic or inelastic under phonon absorption/emission with energy $\hbar\omega$) with Miller-Abrahams hopping (MA) or multiple-phonon-trap-assisted-tunneling (MPTAT) as intermediate processes in the oxide.*

gap of the oxide. For most conductive oxides this gap is quite large. Most important values here are 8.9 eV for SiO_2, 6.5 eV for Al_2O_3 and 3.2 eV for TiO_2. Furthermore, we make the assumption that the momentum parallel to the interface $\mathbf{k}_{||}$ is conserved and that the oxide is homogeneous. The situation including all relevant physical quantities is defined in Fig. 5.1 and 5.2. First of all, the conduction band offset(s) (CBOs) to the left and to the right of the oxide constitute the height of the potential wall and the thickness of the oxide constitutes the width of the barrier which the charge carrier has to tunnel through. Second, the externally applied field dropping over the oxide originates from the applied voltage between the two contacts. The validity of this assumption will be further studied by drift-diffusion-simulations in 5.5. Third, the electrons in the contacts obey fermi-dirac (FD) statistics. This is valid for the investigated material systems because thermionic emission over the barrier is usually neglectable and the charge carrier distributions in the contacts are in equlibrium. Fourth, zero energy is the Fermi-level throughout the material structure. It is determined by the Fermi-level in the metal cathode, i.e. the left electrode for a MOM-contact, while for a MOS-contact the only metal contact is the reference point corresponding to the Mott-Schottky-approximation. Finally, the energy dispersion in the contacts is parabolic and charge carriers of kinetic

energy in x-direction E_x have a certain momentum $\mathbf{k}_\perp$, corresponding to a velocity $\mathbf{v}_\perp$ with which they impinge onto the barrier.
Using these assumptions the derivation of the Tsu-Esaki formula can be done. This shall not be done completely, as it is can be found in textbooks.[187] The approximative formulae are also quite straightforward to derive and are regularly found in literature on tunneling models for MOM-contacts.[189] Thus, own approximations for the Tsu-Esaki formula were derived independently by the author and tested against the analytic formula from literature showing that results are nearly the same. The analytical Tsu-Esaki-formula could also be derived independently and even slightly extended by an additional exponent, as given in the following. To cut its derivation short, we want to pick it up at the point of the current densities from the cathode to the anode and vice versa. These current densities (differential in k-space) obey the equations

$$dj_{ca} = -\frac{e\hbar}{4\pi^3 m^*_{ca}} T(k_{x,ca}) f_{ca}(\mathbf{k_{ca}}) k_{x,ca} dk_{x,ca} d\mathbf{k_{y,z,ca}} \tag{5.1}$$

$$dj_{an} = -\frac{e\hbar}{4\pi^3 m^*_{an}} T(k_{x,an}) f_{an}(\mathbf{k_{an}}) k_{x,an} dk_{x,an} d\mathbf{k_{y,z,an}} \tag{5.2}$$

At this point the modification was done: The author introduced an effective electron mass in the cathode m_{ca} which is generally different to the effective electron mass in the anode m_{an}. This modification should allow to simulate asymmetric conctacts more accurately. Next the following terms are replaced: $k_{x,l} dk_{x,l} = m^*_{ca} dE_x/\hbar^2$ $k_{x,r} dk_{x,r} = m^*_{an} dE_x/\hbar^2$ and $d\mathbf{k_{y,z,l}} = d\mathbf{k_{y,z,r}} = dk'k'd\phi$. With the latter replacements one can split up the integration of the differential current densities over the whole momentum space into one integration over dE_x and one cylindrical integral over the space of k-vectors parallel to the interface yielding[187]

$$j_{ca} = \frac{e}{4\pi^3} \int_0^\infty dE_x \int_0^\infty dk'k' \int_0^{2\pi} d\phi T(E_x) f_{ca}(E_x) \tag{5.3}$$

$$j_{an} = \frac{e}{4\pi^3} \int_0^\infty dE_x \int_0^\infty dk'k' \int_0^{2\pi} d\phi T(E_x) f_{an}(E_x) \tag{5.4}$$

Replacing $k'dk'$ once again by $m^*_{ca} dE'/\hbar^2$ and $m^*_{an} dE'/\hbar^2$, respectively, and integrating over all possible energies, i.e. from zero to infinity and calculating the difference $j_{ca} - j_{an}$ one obtains

$$\begin{aligned} j_{DT} = \frac{e}{4\pi^3\hbar^3} \int_0^\infty dE_x T(E_x) \int_0^\infty dE' \left[m^*_{ca} f_{ca}(E_x) - m^*_{an} f_{an}(E_x) \right] = \\ \frac{e}{4\pi^3\hbar^3} \int_0^\infty dE_x T(E_x) \frac{m^*_{ca}}{m^*_{an}} \ln \left[\frac{1 + \exp\left(\frac{E_{f,ca} - E_x}{k_B T}\right)}{1 + \exp\left(\frac{E_{f,ca} - eV_{ox} - E_x}{k_B T}\right)} \right] \end{aligned} \tag{5.5}$$

where e is the electric charge, T the temperature, V_{ox} the voltage drop over the oxide*, m_{ca} and m_{an} are the effective electron masses in the cathode and the anode respectively, $E_{f,ca}$ is the Fermi-level in the cathode and E_x the kinetic energy of an electron in x-direction. For two metallic contacts with effective mass 1 there is no difference to the original formula, while for a semiconductor, like Si with $m_e^* = 0.32m_0$, the DT current is corrected by the corresponding factor m_{ca}^*/m_{an}^*. The temperature T was fixed at 298 K and the electric fields were higher than 0.17 MV/cm in all simulations, so thermionic emission supposed to be improbable and one expects to see usually only DT and FN, though three of the five processes, i.e. SE, DT and FN, are computed by this Tsu-Esaki-Formula corrected for asymmetric electrode contacts with different effective masses. The effective mass reflects also the band structure and determines the electron mobility in the electrode materials. The charge carrier statistics is included in the argument of the logarithmic term. The most decisive part of the model is the transmission coefficient $T(E_x)$ which will be treated in detail in the next section.
Fig. 5.3 shall summarize all possible situations for DT in dependence of applied voltage for an exemplary, ideal Al-TiO_x-Au MOM-contact. In this situation the energy barrier is rectangular or at least trapezoidal for 0 V bias, depending on the specific band structure inside the oxide, with the CBO as the height and d_{ox} as the thickness† Starting from 0 V at first, DT current densities from cathode to anode and back (almost) cancel each other. Then, secondly, with increasing voltages tunneling of electrons from occupied states in the cathode to unoccupied states in the anode increases, while the reverse process being suppressed. Thirdly, the reverse part is suppressed completely, while the way to the anode is enhanced even more with the tunneling process changing systematically from DT, i.e. a trapezoidal barrier (darker green) to FN tunneling, i.e. a triangular barrier (lighter green). Theoretically this starts for an oxide voltage of $V_{ox} > \Delta\phi_{B,an}/e$, although in the systems investigated here, it usually it only gets large enough to simulate or measure it for voltages above 1 V or 2 V in the sytems investigated here, when the triangular barrier gets sufficiently thin due to the voltage, as sketched in the fourth image of Fig. 5.3.

5.1.1 Analytical Version of the Transmission Coefficient

By definition the transmission coefficient is the ratio of transmitted intensity of a quantum mechanical wave packet to its total intensity impinging on a piece of matter. In quantum mechanics intensity is directly proportional to the square of the wave function. Thus, assuming a series of infinitesimally thin, piecewise constant rectangular energy barriers, $T(E)$ in its most general form, i.e. for arbitrarily shaped tunneling energy barriers and arbitrary energy dispersion relations, can be derived quantum mechanically by

*Ideally identical with the voltage at the anode for accumulation conditions in the MOS-contacts, but had to be recalibrated for Si in certain cases depending on the energetic conditions at the contacts.

†Refer to the section 5.5 on drift-diffusion simulations for a more detailed discussion on a potential band bending inside the oxide.

the transfer-matrix method[222]

$$T(E) = \frac{\exp(-2\int_{x_0}^{x_1} dx k'(E_x, x))}{1 + \frac{1}{4}\exp(-2\int_{x_0}^{x_1} dx k'(E_x, x))} \approx \exp\left[-2\int_{x_0}^{x_1} dx k'(E_x, x)\right] \tag{5.6}$$

with the last approximative sign resembling the Wentzel-Kramer-Brillouin (WKB) approximation, which simplifies the calculation and even allows for an analytical solution in certain cases.[186, 187] Therein, $k'(E_x, x) = \sqrt{\frac{2m^*_{ox}}{\hbar^2}(V(x) - E_x)} = \sqrt{\frac{2m^*_{ox}}{\hbar^2}V(x) - k(E_x)}$ is the complex wave vector of the electron wave propagating with energy E_x in x-direction between two classical turning points x_0 and x_1 subjected to the electrostatic potential $V(x)$. $k(E_x)$ is the x-component of the momentum vector (perpendicular to the barrier) of a free electron of energy E_x and mass m^*_{ox}. The energy dispersion relation is determined essentially by the band structure of the specific material and describes how the wave vector depends on the energy of a particle wave packet with the effective mass as a proportionality factor. So fundamental electronic and specific material properties are wrapped into this formula. Since the relation of these quantities enters the transmission coefficient exponentially, the current density resulting from the simulations depends considerably on the energy dispersion relation. Hence, accurate and valid assumptions on it are mandatory. Up to our knowledge, basically three different models for the energy dispersion relation are available in literature and were implemented in the kMC-code:
Firstly, there is the common parabolic effective mass approximation: Starting from

$$k_{pb}(E(x)) = \sqrt{\frac{2m^*_{ox}(V(x) - E_x)}{\hbar^2}} \tag{5.7}$$

and assuming a linear potential drop $V(x) = -eV_{ox}/d \cdot x$ one can analytically derive the exponent in the transmission coefficient by this relation:

$$\begin{aligned} -2\int_{x_0}^{x_1} dx k_{pb}(E_x, x) = &-\frac{4}{3}\sqrt{\frac{2m^*_{ox}d}{\hbar^2 eV_{ox}}}\times \\ &\left[(\phi_B - e\frac{V_{ox}}{d}x_1 - E_x)^{3/2} - (\phi_B - e\frac{V_{ox}}{d}x_0 - E_x)^{3/2}\right] \end{aligned} \tag{5.8}$$

The further two models for the dispersion relation, the Franz single-mass model[223] and the Franz 2-mass model[224], with their analytical evaluation for the transmission coefficient as done by Weinberg et al.[225] are found in the appendix, as they were only of academical interest in this thesis.
The parabolic dispersion is the simplest form of the energy dispersion. It comes from an approximatly constant curvature, resembling the effective electron mass, of the parabolic energy bands at the conduction band minimum in k-space which has already been approved in numerous experiments starting with the one by Dresselhaus [226]. Since one major goal of the renewed and adapted kMC-model was to speed up the cumbersome calculations of the former numerical computation of $T(E)$, we focused on the dispersion

relations that allowed also for a full analytical evaluation of the transmission coefficient and about a 10 to 20 times faster computation. Therefore, if not stated otherwise, the parabolic effective mass approximation (EMA) was used. The common analytical version using EMA seemed to be an appropriate approximation avoiding unuseful and unneccessary complexity of the model, since the other two Franz-type dispersion models only introduce a correction on the order of $\sim \frac{3}{10} \times \frac{\phi_B}{E_B} \approx \frac{1}{10} = 10\%$ and test simulations showed that differences between the presented dispersion relations were not considerably big. Since other mass models than the parabolic EMA one would have needed a numerical computation of the transmission coefficient, the parabolic one turned out to be the best compromise between computational speed and accuracy.

5.1.2 Effective Reduction of the Barrier Height by Image Potentials

In the ideal situation of a MOM contact, depicted in Fig. 5.2 or 5.3, the energy barrier for the electrons is rectangular or at least trapezoidal for 0 V bias, depending on the specific band structure inside the oxide, with the CBO resembling the height [‡] and the thickness of the oxide resembling the width of barrier. Obviously, the application of a positive voltage to the right contact introduces an electric field F tilting the electron potential down by $-eFd$ on the right and making the left contact the cathode and the right one the anode. Additionally, the cathode emits electrons inducing a positive image charge in the metallic electrode. This positive charge implies an attractive image potential that partly screens the repulsive potential of the negatively charged cathode. The closer the emitted electron is to the cathode, the stronger is the screening, while if the electron is further away from the electrode it decreases quickly with 1/r. This effectively reduces the energy barrier which exhibits a maximum at a certain distance from the cathode. So one can straightforwardly model the additional image potential as Coulombic force of the image charge and the total potential reads as:

$$V(x) = E_B - eFx - \frac{e^2}{16\pi\epsilon_0\epsilon_{opt}x} \tag{5.9}$$

By differentiating this expression for x and determining position and value of the maximum one obtains $x_m = \sqrt{\frac{e}{16\pi\epsilon_0\epsilon_{opt}F}}$ and $V_m(x) = E_B - \sqrt{\frac{e^3F}{4\pi\epsilon_0\epsilon_{opt}}}$, i.e. the effective barrier reduction.
Eq. (5.9) has to be inserted into Eq. (5.6) to calculate the transmission coefficient including the image potential. Although there are some cases where a closed analytical form exist,[225, 227] in general this has to be done numerically which is possible in the model, but slows down the simulations. Accordingly, there are also essentially two qualitative arguments against doing so:

[‡]Refer to the section on drift-diffusion simulations, section 5.5, for a more detailed discussion on a potential band bending inside the oxide and to the parameterization section 6.3.3 for a more details on the issues concerning the CBO, esp. in terms of the MIGS-model.

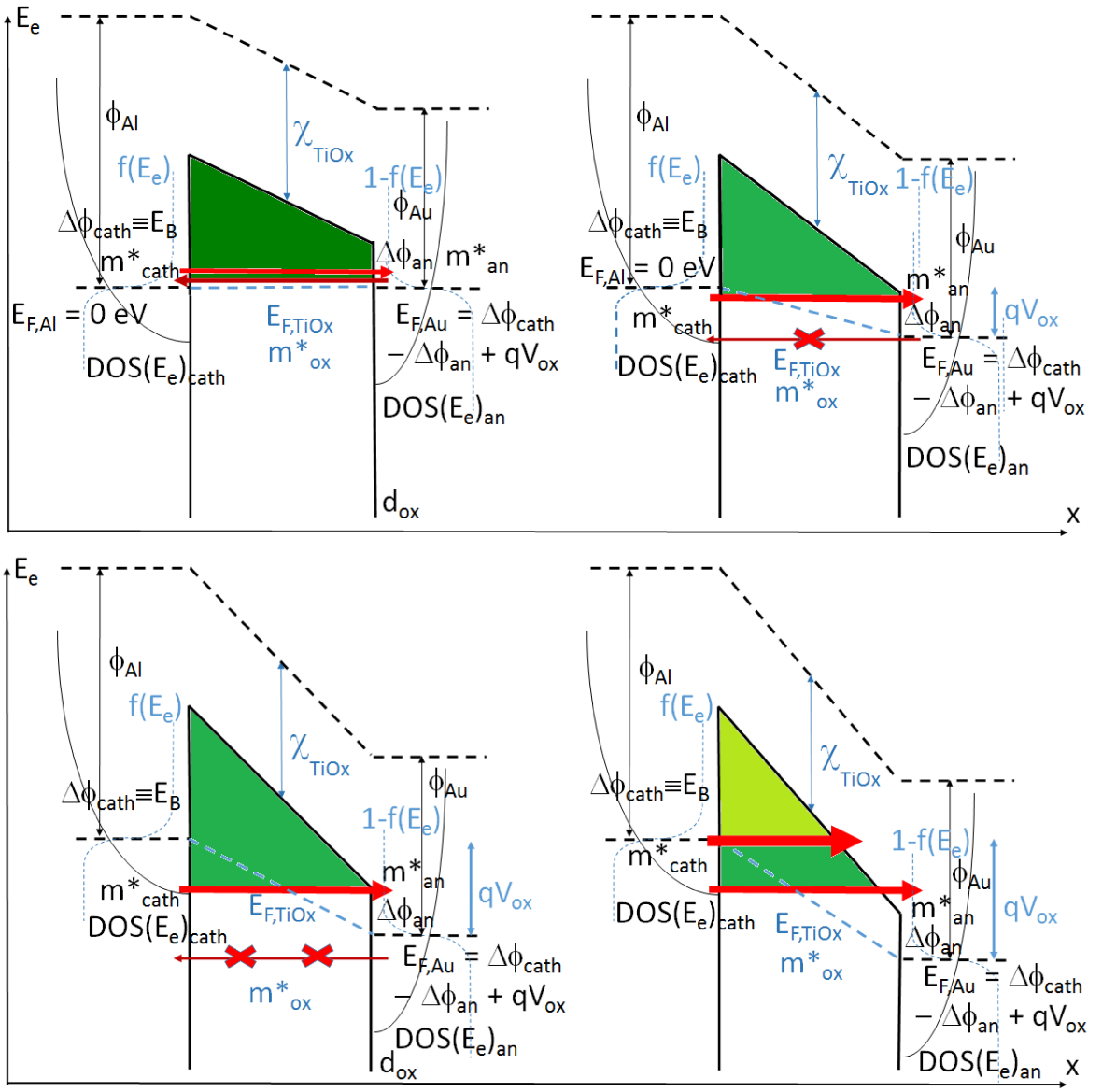

Figure 5.3: *Summary of all possible situations for DT of electrons in dependence of applied voltage for an exemplary Al-TiO_x-Au MOM-contact. From 0 V with no or almost canceling electron currents, to higher voltages with a trapezoidal barrier (DT), becoming a triangular one causing FN to start for higher voltages, which is finally more pronounced for higher biases.*

Firstly, including the image potential prevents the analytical evaluation of the transmission coefficient, while the accuracy is qualitatively improved. As given in Fig. 5.4a, simulations with and without the image potential term showed that it systematically reduces the barrier by a value between 0.1 eV (for lower voltages, i.e. SE-regime) and 0.2 eV (for higher voltages, i.e. FN regime) for a typical TiO_2 parameterization, cf. also

section 5.1.3. Hence, it is much faster and simpler to find a fit by a broad parameterization, as performed in chapter 6, to neglect the image potential at first. The systematic underestimation, approximately varying linearly between 0.1 eV and 0.2 eV with fields F in the range of 0 MV/cm to 5 MV/cm ($d = 10$ nm in Fig. 5.4a) has to be added afterwards to CBO values entered as parameters in the simulations. An even simpler, but not much less accurate correction of the extracted barrier is adding a constant mean value 0.15 ± 0.05 eV on the barrier extracted from simulations without the image potential and accepting the result with this accuracy of ± 0.05 eV or trying again to find a fit for such a higher barrier with the image terms respected.
Secondly, it has been discussed by Weinberg[228], Hartstein[227] and later on Herrmann and Schenk[229, 230], essentially stating that the image potential does not primarily affect the barrier height as long as the tunneling energy itself is small enough compared to the barrier height. According to them, to obtain the quantum mechanically correct image potental induced by an electron emitted into the dielectric, one must not assume the presence of the 'full' electron wave packet in the dielectric, as it would be the case in the classical particle picture. Much more one has to account only for that part of the electron wave function which is transmitted into the barrier, because only this part induces a positive image charge in the electrode. Thus the image potential term in equation (5.9) actually has to be multiplied by the transmission coefficient itself, to obtain the correct potential. Eventually, this makes the calculation of the transmission coefficient (5.6) a transcendent equation, which is (i) not analytically solvable in a closed form, (ii) also numerically laborous to solve and (iii) only provides notable changes to the barrier height E_B, if E_B is sufficiently small compared to k_BT or vice versa. Only then the thermally provided kinetic energy excitates electrons above or close to the conduction band edge of the oxide, so that $T(E)$ approaches 1. Then thermal emission, i.e. SE, over the barrier or the tunneling of electrons becomes that probable that the image term in (5.9) should be taken into account. In total this means effectively that apart from a relatively narrow intermediate range of elecron energies of $\sim 8k_BT \approx 0.2$ eV below the CB of the oxide, the image term is not relevant. Hence, it will reduce E_B by a fairly constant value between 0.1 eV and 0.2 eV - dependent on the other material parameters - which can be added up afterwards. This argument supports the fitting strategy given in the previous paragraph.

Finally, the implications of the just mentioned qualitative arguments are supported by Fig. 5.4a showing the exemplary, comparative simulation of the direct tunneling current through a materal system with a realistic parameter set applicable for TiO_2, as found in chapter 6. The results of the simulations of the model with the classical transmission coefficient computed numerically with a spatial resolution of $d/20$ with the image potential included and the other version of the model with transmission coefficient computed analytically without the image potential are brought to an agreement simply by increasing the CBO, i.e. E_B, going from "image" to "no image" by 0.1 eV for low voltages $\lesssim 1$ V and up to 0.2 eV for high voltages $\gtrsim 3$ V with a linear increase in between, while all other parameters remain identical. The exact value depends on the complete parameter set.

Thus curves with image potential are steeperthan the ones without the images terms in Fig. 5.4a and fit them best for E_B being ∼0.1 to 0.2 eV higher. One can clearly see that this approves the mentioned systematic but constant shift of the barrier height originating from switching the image potential on or off in the model.

5.1.3 Sensitivity Analysis

At this point the sensitivity of the DT model, with Eq. (5.5) containing SE, DT and FN, shall be analyzed into more detail to justify its validity for the parameter ranges of interest in our investigation. First of all, SE is basically thermionic emission over the potential barrier between the electrode (normally the cathode) and the oxide. This process dominates for high temperatures ($k_BT \quad E_B$) and low electric fields. This situation was mostly irrelevant in the simulations performed in this thesis as T was always 298 K, so $k_BT \sim 25$ meV, while $E_B \geq 0.2$ eV holds always, meaning that the occupation probability due to FD-statistics was already $< 10^{-4}$ in all cases. SE can be described by phenomenological equation,[186, 231]

$$j_{SE} = \frac{e m^*_{ca} k_B^2 T^2}{2\pi^2 \hbar^3} \exp\left[-\frac{1}{k_B T}\left(E_B - \sqrt{\frac{e^3 F}{4\pi\epsilon_0 \epsilon_{opt}}}\right)\right] \tag{5.10}$$

the so-called Richardson-Dushman equation. DT, however is relevant for lower temperatures and moderate fields which applies to most situations here. The term "moderate fields" is defined by the composition of $E_{B,r}$ and $F \times d_{ox}$ or the oxide voltage drop V_{ox}, as illustrated in Fig. 5.3, which must correspond to a trapezoidal barrier and a high CBO, i.e. $qFd = qV_{ox} < E_{B,r}$ and $E_{B,l} \gg kT$. As soon as fields are too "high", i.e. for $qFd = qV_{ox} > E_{B,r}$, the barrier becomes triangular and one speaks of the FN regime. To illustrate these arguments in Fig. 5.5 the approximate Richardson-Dushman equation for SE, pure FN according to[186, 231]

$$j_{FN} = \frac{e^3 F^2}{8\pi\hbar E_B} \exp\left[-\frac{4\sqrt{2m^*_{ox} E_B^3}}{3\hbar e F}\right] \tag{5.11}$$

and the implemented equation (5.5) are plotted for barriers between 0.6 eV and 1.4 eV, the relevant range for the kMC-parametrizations in chapters 6.2.5, 6.3 and 6.4. In general, one can see that SE is dominant at (very) low fields in all plots, while FN approximates the Tsu-Esaki formula extremely well for high fields. Mostly the simulations exhibit DT or FN, since voltages V_{ox} were larger than 0.1 V but smaller than 5 V, oxide thicknesses larger than 3 nm minimum, but smaller than 60 nm maximum. This means fields are moderate to high in the range of 0.17 MV/cm minimum and 17 MV/cm maximum. The CBO, however, was always at least 20 times larger than k_BT, making SE mostly much less probable than DT/FN or trap-related processes. Only fields below 1 MV/cm mark an arguable, but rare intermediate range. Hence, for most barrier values in Fig. 5.4b, SE is about to contribute to the current only at lowest voltages, followed by a transition

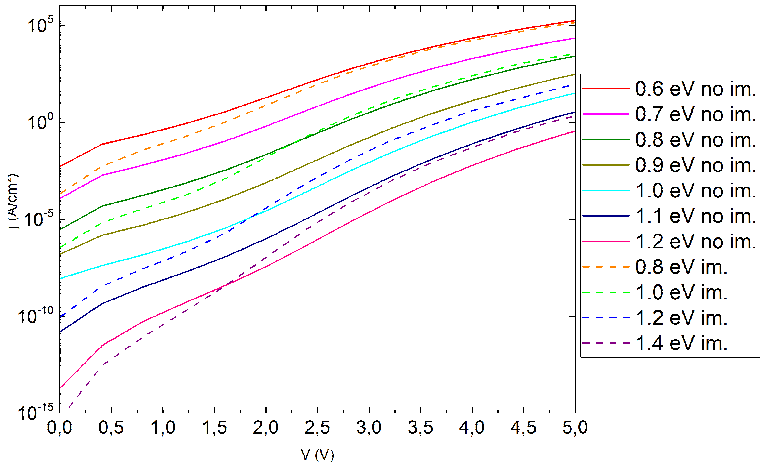

(a) *Numerical solutions of the Tsu-Esaki-formula as implemented in the kMC-model for barriers of 0.6 eV to 1.2 eV at 0.1 eV steps (without image potential, full lines) and 0.6 eV to 1.4 eV at 0.2 eV steps (with image potential), color code in the legend.*

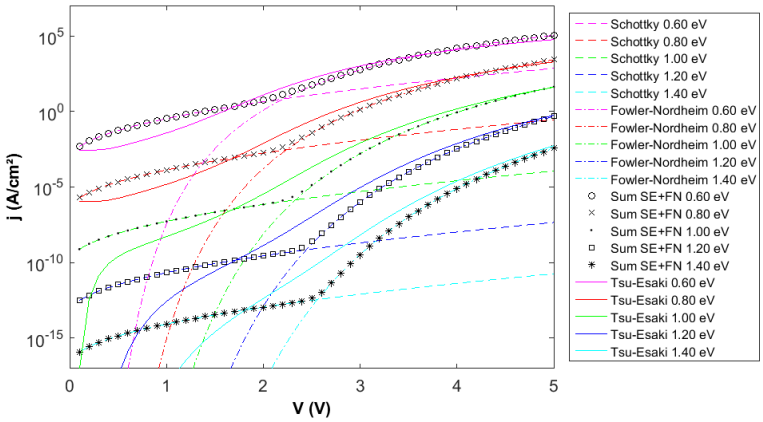

(b) *SE, FN and analytical Tsu-Esaki by a numerical script for barriers of 0.6 eV-1.4 eV, 0.2 eV steps (no image), color code in the legend. For low voltages SE current densities are higher than analytical Tsu-Esaki due to the image term. The difference increases for higher barriers. Current density profile from Tsu-Esaki is approximated well by FN for high voltages, i.e. high electric fields, for all barriers.*

Figure 5.4: *Sensitivity analysis of the direct "inter-electrode" transport processes. Parameters are set to* d *=10 nm,* $m^*_{ox} = 1.0m_0$ *and* $\epsilon_{opt} = 6.0$ *in both graphs and* E_B *is varied from 0.6 eV to 1.4 eV in 0.1 or 0.2 eV steps. (a) Numerical solutions of the implemented kMC-model without image potential terms (0.1 eV steps) lowering the barrier (full lines, 0.1 eV steps) and with them (dashed lines, 0.2 eV steps). (b) Corresponding result reproduced using the analytical Tsu-Esaki version for DT/FN (full lines) with the energy integral being evaluated numerically by a script, i.e. no image terms included. SE and DT/FN are plotted by the approximative formulas in equation* (5.10) *(dashed lines) and* (5.11) *(dashed dotted lines) and their sum (black symboles). For a detailed discussion see text.*

region where both approximative branches, SE and DT/FN, contribute. Note that as seen by the derivation of equation (5.5), SE and DT/FN rely on the same fundamental physical processes and are no different mechanisms. [43]
The plot in Fig. 5.4b confirms that SE and FN approximations and the analytically derived equation (5.5) (the integral was evaluated by a MATLAB script instead of the kMC-code) behave as expected. Additionally, the agreement of the independently implemented profiles is a confirmation that the formulas were implemented correctly. Note, that the SE current densities are slightly higher than the ones from the general Tsu-Esaki equation for lower barriers and become increasingly lower than Tsu-Esaki for higher barriers. This is because higher barriers reduce the "weighting" by the fermi-function too much compared to the stricter analytical treatment in formula (5.5), while the contribution of charger carriers thermally excited over lower barriers is comparably overstated by Richardson-Dushman, as it overstates the barrier reduction. Next, for all depicted barrier heights, the Tsu-Esaki formula is approximated extremely well by FN-equation of tunneling which increasingly surpasses the SE branch after a certain transition voltage. For high electric fields the FN-equation is, firstly, a very accurate approximation for the current densities and, secondly, its characteristic jV-profile is rather easy to tell from other transport mechanisms by an analytical plotting, as used for the discussion in chapter 6.2.7.

In Fig. 5.5a the current densities from SE, FN and Tsu-Esaki are shown in dependence of the thickness. The thickness values are set to 3 nm, as a lower limit, 5 nm, 10 nm, 15 nm and 20 nm, referring to the usual range for oxide thicknesses investigated by kMC later on. One can note that for thinner layers (3 nm and 5 nm) the FN branch resembles the result from Tsu-Esaki already for voltages below 1 V and the currents increase strongly with the voltage due to corresponding to high fields. For thicker layers, the fields are lower at a certain voltage, thus the Tsu-Esaki formula is better resembled by the SE branches, though the agreement between the two formulas is never perfect due to the reasons given in the previous paragraph. Thus the main message is that SE is expected to be less relevant for oxide thicknesses below ∼10 nm in terms for barrier heights $E_B \sim 1.0$eV. Those are of importance for the kMC-simulations of TiO_2 and for AlO_x they are even higher with $E_B \sim 3.0$eV. Therefore we recommend to rely on the more accurate analytical Tsu-Esaki model, which is also implemented and used in all follow-up simulations. This holds in particular for thin samples, because FN surpasses SE already for low voltages. For thicker oxides, the deviation between SE and Tsu-Esaki is present over a larger voltage range. Despite of slight deviations also for the FN branch at the largest depicted voltages of the thicker samples, the transition of the current from the "SE"-like to the "FN"-like regimes is clearly visible in the Tsu-Esaki tunneling model for all voltages. For thicker oxides, one can distinguish between the two by the flatter profile of the Tsu-Esaki formula at low voltages, which is SE. The way steeper positive slope at higher voltages indicates FN, in particular for thinner samples. The quantitative change of the current for a varying thickness depends on the voltage range and the specific oxide

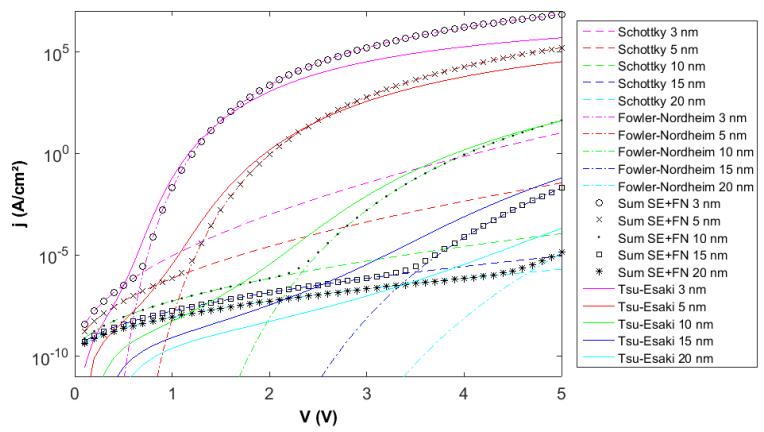

(a) *SE, FN and modified Tsu-Esaki for oxide thickness d set to 3 nm, 5 nm, 10 nm, 15 nm and 20 nm, color code in the legend. Most importantly, SE is fairly irrelevant for $d \lesssim 10$ nm at $E_B \sim 1.0$ eV and $m^*_{ox} \sim 1.0\, m_0$, as surpassed by the FN branch for low voltages. So FN approximates Tsu-Esaki well and image potentials are less relevant for smaller thicknesses.*

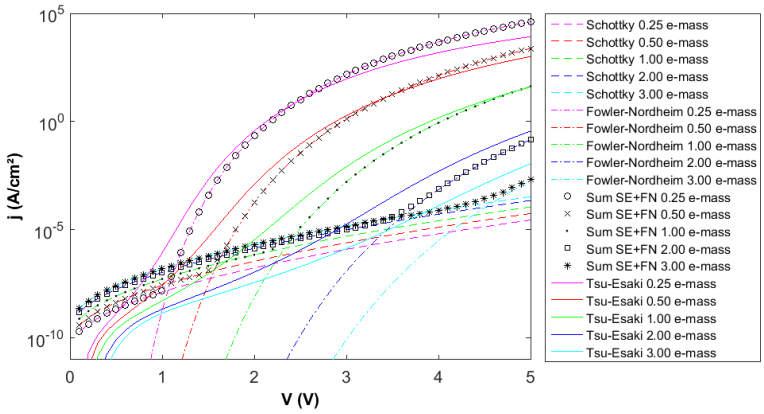

(b) *SE, FN and modified Tsu-Esaki for effective tunneling masses set to 0.25, 0.5, 1.0, 2.0 and 3.0 m_0, color code in the legend. Similar qualitative observations as for d. SE is less relevant for lower m^*_{ox} and DT/FN is more probable, so m^*_{ox} is a sensitive model parameter.*

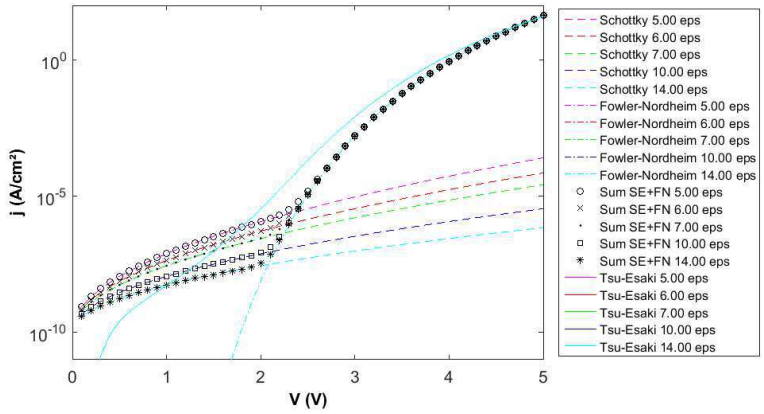

(c) *SE, FN and modified Tsu-Esaki for an optical dielectric constant set to 5.0, 6.0, 7.0, 10.0 and 14.0, color code in the legend. Note that only in the SE regime a change is present, as ϵ_{opt} enters only the image term in SE. The other two formulas are quite insensitive to it, making ϵ_{opt} less critical.*

Figure 5.5: *Sensitivity analysis of SE (dashed lines), DT/FN (dashed dotted lines), their sum (black symboles) and the partly numerically evaluated Tsu-Esaki formula without image potential terms (full lines). The parameters are $E_B = 1.0$ eV, d =10 nm and $m^*_{ox} = 1.0\ m_0$ in all images, except for the one parameter varied: (a) oxide thickness d set to 3 nm, 5 nm, 10 nm, 15 nm and 20 nm, (b) effective tunneling masses set to 0.25, 0.5, 1.0, 2.0 and 3.0 m_0, (c) optical dielectric constant set to 5.0, 6.0, 7.0, 10.0 and 14.0. For a detailed discussion see text.*

thickness. Keeping $E_B \sim 1.0$ eV and $\epsilon_{opt} = 6.0$ the current at $V = 2.0$ V (FN-regime for 3 nm, 5 nm and 10 nm) is about 1 order of magnitude less per additional nm in oxide thickess. At $V = 5.0$ V (FN-regime for 3 nm, 5 nm, 10 nm, 15 nm and 20 nm) the current density is only about 0.5 orders of magnitude lower per nm. For a double as high barrier about twice as many orders of magnitude per nm can be expected.
Third, the parameter variation of the tunneling effective mass in Fig. 5.5b implies the same qualitative observations as just given in terms of the thickness comparing the agreement of the SE and FN approximations with Tsu-Esaki and their prevailance in terms of voltages. Most interestingly, an increase in effective mass increases SE only linearly as expected from Eq. (5.10), whereas in the higher voltage regime the FN branch and the corresponding profile from Tsu-Esaki is decreased reliably by $\sim 1-2$ orders of magnitude per 0.5 m_0 increase in effective mass for the given thickness of 10 nm and a barrier of 1.0 eV, again depending also on the voltage range. Taking into account the effective mass is usually determined about 5-10 times worse on the scale of electron masses than the parameter E_B is determined on the eV-scale or the thickness d on the nm-scale, this makes the tunneling effective mass a sensitive input parameter of the model, meaning that it must be (and was) varied in range of about $\pm 2m_0$ for all kMC-parametrizations. However, for masses lower than 0.25 m_0 the current densities resulting from the model appear unrealistically high compared to the common ones maximally measured in experiments. Yet for the materials of interest here tunneling masses used to be at least 0.5 m_0.
Finally, also the variation with the optical dielectric constant was analyzed. However, as seen in Fig. 5.5c it affects the current density only in the SE regime which was mostly not in the focus in the subsequent simulations, as discussed. If SE was relevant due to high temperatures, low fields and comparably low barriers, a variation of ϵ_{opt} should be taken into account, since with a twice as high ϵ_{opt} the current density j is decreased by a factor of about 1/10 to 1/3 around 1 V, and by a factor of about 1/120 to 1/80 around 4 V. The other two models must stay unaffected by this parameter, because ϵ_{opt} enters the equations for FN or Tsu-Esaki tunnneling only in terms of a barrier reduction by image potentials which was neglected here. As ϵ_{opt} can also be well determined experimentally, it is a less sensitive input parameter and was mostly kept rather constant in the parameterizations.
The given considerations and sensitivies of the model on the most decisive input parameters in terms of direct tunneling processes, E_B, d and m^*, are of high importance to find fits quicker when parametrizing new materials by kMC, i.e. TiO_2 and AlO_x.

5.2 Injection and Extraction between Electrodes and Defects

Defects are one of the central issues of this kMC-study. In the simulations they come into play as traps which can be filled with electrons stemming from the electrodes. Initially, the traps can be occupied or unoccupied depending on the nature of the particular modelled defects in the oxide layer. Due to arguments presented in chapter 6 it is assumed

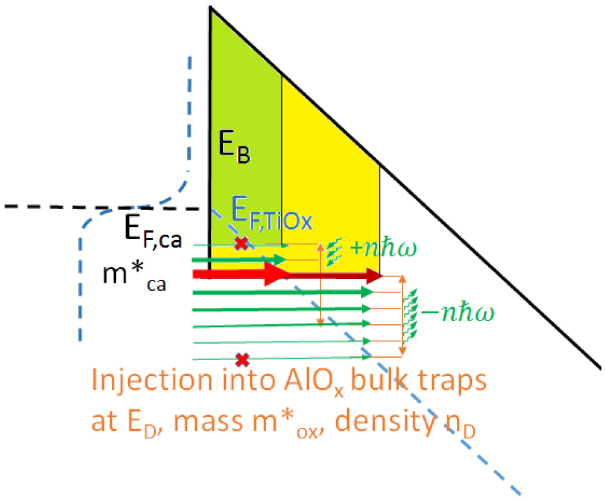

Figure 5.6: *Electron injection from the cathode: Elastic (red arrows) or inelastic injection (green arrows) under phonon absorption/emission (little green arrows, energy $\hbar\omega$) into traps in the oxide with parameters E_D, m^*_{ox}. At a given fixed energy of the injected electron E_e there is a trade-off between smaller trapezoidal barriers (light green compared to yellow) and lower probability for the number of participating phonons for trap states that are closer, but higher in energy and need phonon absorption to be reached, see sensitivity analysis in the text. Extraction into the cathode works equivalently, but reverted.*

that they are initially empty and positively charged throughout this study, if not stated otherwise. The mechanism to fill the traps is illustrated in Fig. 5.1 and the close-up in Fig. 5.6 depicting the situation at the contact between the cathode and the oxide into more detail. The situation for the extraction at the counter-electrode, the anode, is analogue. Both types of processes shall be discussed in parallel here, as the processes are just complementary and hence equations are nearly identical with only minor adjustments. One notes at once by Fig. 5.6 that the processes of injection or extraction are complex with an interplay of a multitude of material parameters influencing the final rate for either process, i.e. its probability per unit time. From the cathode an electron in the CB can be injected into an unoccupied defect in the band gap of the oxide, while electrons in defects can be extracted into the CB of the anode. Of course, the opposite path is possible, too, and implemented in the model, but much less probable due to the unfavourable energetics of this transition. Firstly, one has to distinguish between elastic and inelastic injection or extraction. The former, elastic case, means the tunneling of electrons of a certain energy in the CB of the electrode into a defect level in the oxide that has a comparable - or ideally identical - energy without assisting phonons. So to speak the energies of the electron in the electrode and the defect levels must be more or less in "resonance" for this process to happen, which is a mechanism of outmost importance for TAT transport in conductive oxides and hence will be analysed into more detail below. The latter case, the inelastic injection or extraction also relies on the ”resonance” between the electron energy in the electrode and defect levels, but this resonance can be accomplished by an assisting emission or absorption of phonons.

5.2.1 Elastic Injection and Extraction Rates

First the elastic injection shall be discussed. Essentially three different versions of tunneling transition rates or tunneling ”probabilities” that described this situation circulate

in today's literature. There are the ones by [§]:

- C. Henry and D. Lang: Nonradiative capture and recombination by multiphonon emission; interaction probabilities are expressed in terms of cross sections instead of rates, so they were not useful for the kMC-model.[233]
- B. K. Ridley: Multiphonon capture are in semiconductors; derivation in terms of rates, similar to the model by D. Pons and S. Makram-Ebeid[234], so a useful form for injection and extraction at electrodes and also applicable for trap-trap-tunneling processes; hence it was used for all phonon-assisted rates.[235]
- I. Lundstroem: most compact model for the elastic tunneling rates into and out of traps in insulators; also easiest to adapt to model injection from/into a Si contact instead of a metal.[236, 237]

In fact these three models are the only useful closed analytical descriptions of the injection from or extraction into a solid, crystalline material, i.e. a material with sufficiently dense electronic states forming a band structure (occupied according to FD statistics) into any other free electronic state. In particular the differences between the three analytical models by Henry, Ridley or Lundstroem are more formal, and the fundamental principles for their derivation are almost the same. In the following we want to provide the results of the derivation by Lundstroem:[236] First Bardeen's method[238] is applied to calculate the transition matrix element by the scalar product of the initial electron wave function in the metal with the energy projection operator H_E and the final wave function of the trapped electron. Using the transfer matrix element (which will be replaced via the WKB approximation of the transmission coefficient T(E)) and the electron density of states in the electrode the transition probability is then obtained by Fermi's golden rule: $p = \frac{2\pi}{\hbar}|T_{ED}|^2 \left(\frac{dN_E}{dE}\right)_{E=E_x}$. At the end of Lundstroem's derivation the transition probability per unit time for a single electron is given as an inverse time constant times the transmission coefficient:[236]

$$P = \frac{m_E^*}{m_{ox}^*}^{5/2} \left(\frac{8E_{x,kin}^{3/2}}{3\hbar\sqrt{E_D}}\right) T(E_x) \tag{5.12}$$

with index $E \in \{ca, an\}$ and $E_{x,kin}$ the kinetic energy of the electron impinging the barrier. All other parameters have been declared previously. Multiplied by the fermi-function $f(E_x)$, i.e. the probability that an electron is found at the specific energy E_x in the electrode, one obtains the transition rates from the electrode into the defect at E_D:

$$R_{ED} = \frac{m_E^*}{m_{ox}^*}^{5/2} \left(\frac{8E_{x,kin}^{3/2}}{3\hbar\sqrt{E_D}}\right) f(E_x)T(E_x) \tag{5.13}$$

[§]There are further injection models reported in literature which are essentially the model by Weinberg and Hartstein[227, 228] and by Herrmann, Schenk and Heiser[229, 230]. The ones by S. Fleischer and Cheng, by Entner and Selberherr[232] or by Schroeder et al.[192] are covered by the former two.

If Eq. (5.12) is multiplied by $1 - f(E_x)$, i.e. the probability that an electronic state in the electrode is empty, one obtains the extraction rate from the defect to the electrode:

$$R_{DE} = \frac{m_E^*}{m_{ox}^*}^{5/2} \left(\frac{8E_{x,kin}^{3/2}}{3\hbar\sqrt{E_D}} \right) (1 - f(E_x))T(E_x) \tag{5.14}$$

The model by Lundstroem and Svenson is kept that general that it is valid for both metallic and semiconducting electrodes,[236, 237] in particular, if combined with the assumptions on the electron states in strong inversion or accumulation layers in Si, like in the model by Z. Weinberg.[228] Its advantage is the modularity containing the Fermi-dirac-statistic as a separate factor, valid for both metal and semiconductor contacts, if one assumes the metallic bulk behavior also for the semiconductors. This is valid for a Si under accumulation conditions, in particular, if the Si is degenerately doped, as for all experiments done within this work. So the model in its current form is applicable for both types of materials.
Compared to former models, the parameters in Eq. (5.13) and (5.14) have to be adjusted to the specific materials. In particular, the energy of the electrons perpendicular to the barrier E_x needed a more exact treatment. Since both metals and semiconductor contacts should be modelled, it is not the same for all material combinations and not even the same for all situations within one material system. The kinetic energy of the electrons directly at the conduction band minimum (CBM) is zero for both metals and semiconductors. These electrons do not have sufficient energy to impinge the barrier perpendicular to the electrode-oxide interface. Hence, higher energetic states in k-space have to be populated. In metals this is naturally the case, since the Fermi-level lies far above the CBM, usually $E_F - E_C$ is at least ∼5.0 eV as for Au or Ti, ∼6.0 eV as for Pt or even ∼12.0 eV as for Al. However, also for metals, the energy $E_F - E_C$ cannot be the kinetic energy of the nearly-free electrons at the Fermi-level. It is rather a certain fraction of it. Since the electrons are thermally excited, charge carriers in the energy states at E_F will have a kinetic energy in the order of magnitude of k_BT to impinge and tunnel the barrier. It can be shown[43] that in metals this kinetic energy is on average ∼200 meV at RT which was used as a fixed value for E_x in the simulations.
In semiconductor electrodes, however, the situation is a bit different: Since also states at the CBM do not have an occupation probability of one, the approximation to use the Fermi-energy for the kinetic energy of the electrons E_x in free free electron approximation is justified. A formula valid for non-degenerate and degenerate semiconductors is:[186]

$$E_F - E_C = k_BT \left[\ln n/N_C + 2^{-3/2} \cdot (n/N_C) \right] \tag{5.15}$$

with n being the (approximate) density of conduction electrons in the semiconductor substrate, E_C the CBM in Si and N_C the effective electron density in the CB of Si. Usually highly-doped p-type Si substrates in strong accumulation were simulated to

reproduce the experiments. Then the kinetic energy takes on a value of ∼100-300 meV, too, for an effective mass in the Si electrode of $m_e^* \approx 0.3m_0$ ($N_C \approx 10^{22} cm^{-3}$) and an electron density of $5 \times 10^{19} cm^{-3}$ at the inverted interface, which was used as fixed value for E_x, while the CBM was adjusted according to the material as discussed above.

5.2.2 Resonant Injection of Electrons

During this thesis the elastic injection turned out to be the most decisive process for trap-associated transport through the oxide in the kMC-model. Elastic injection rates are generally larger than the inelastic ones, as given in Jegert's thesis, p. 49,[43], so they are more relevant for kMC. Therefore a sensitivity analysis taking a closer look at the parameterization of rates R_{ED} is of high importance and shall be given in this paragraph. Firstly, the injection rates according to Eq. (5.13) are plotted in Fig. 5.7 using the analytical version of $T(E)$ in Eq. (5.8). The plots in Fig. 5.7 are not kMC-simulated-raw-data but supplementary numerical plots of the formula in Eq. (5.13), parametrized and analyzed in terms of three important parameters, i.e. voltages of (a) 1.0 V, (b) 2.0 V, (c) 3.0 V, (d) 4.0 V, each for traps with a distance to the electron injecting cathode of 1 nm (magenta), 2 nm (blue), 3 nm (green), 4 nm (red), 5 nm (cyan) and trap energies varied continuously between 0.05 eV and 2.0 eV below CBM in the oxide. This covers the typical parameter space for TiO_x also used in the kMC-simulations later on. The barrier is set to a constant, typical value of $E_B = 1.5$ eV, the oxide thickness is $d = 10$ nm and temperature is $T = 300$ K (room temperature). Thus the elastic injection rates could be parametrized and tested in terms of the varied parameters. When discussing the results the term "resonance energy" is useful which shall be defined here as the energy at which the injection rate takes on its maximum in terms of a varying defect energy E_D for a fixed barrier E_B, voltage V and defect position x_D.
In Fig. 5.7 one can see essentially four qualitative effects, also indicated in the caption of the subfigures:

(1) The resonance energy (position of the maximum rate in E_D) obeys $E_D = E_B - e\frac{V}{d}x_D$. So for "resonance" E_D has to agree with E_B reduced by the specific combination of voltage and defect position, as the latter two parameters shift the particular defect down in energy by $e\frac{V}{d}x_D$.

(2) Accordingly the resonance energy shifts to smaller defect energies E_D for increasing voltage V and fixed E_B and x_D. This is seen best when comparing just one color in the four figures of Fig. 5.7. The shift in the resonance energy varies with the voltage V directly proportional to x_D, i.e. it varies stronger for defects which are more distant from the cathode than for closer ones.

(3) The maximum value of the injection rates increases stronger with increasing voltage for larger x_D, i.e. for defects which are more distant to the cathode than for closer

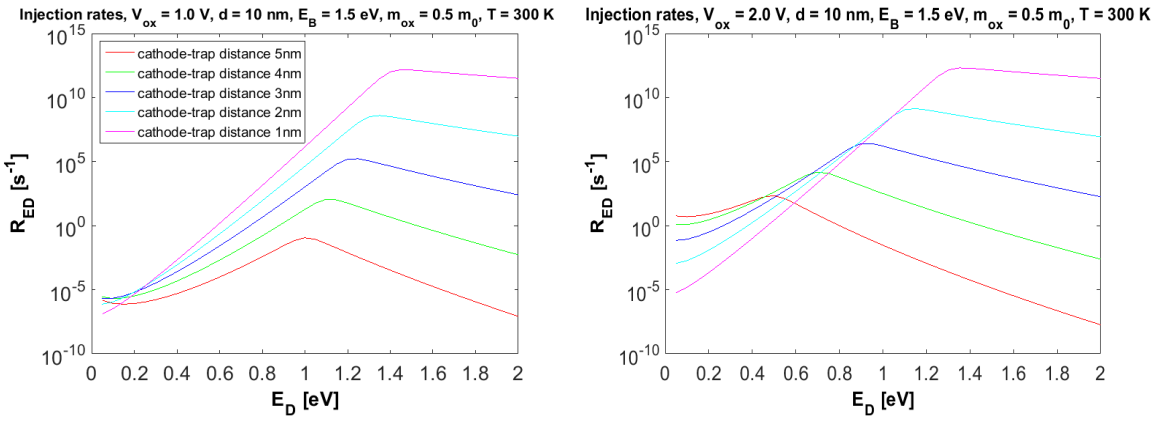

(a) *Injection rates R_{ED} for $V_{ox} = 1.0$ V: For shallow traps, $E_D \lesssim 0.5$ eV , traps located at all given distances compete and can contribute to the transport, while for traps deeper than $E_D \approx 1.0$ eV only those closest (1 nm or 2 nm) to the cathode are dominant.*

(b) *R_{ED} for $V_{ox} = 2.0$ V: Traps can be less shallow than in (a), 0.2 eV$\lesssim E_D \lesssim 0.8$ eV, to have all of them potentially contributing to the transport. For this voltage deeper traps, $E_D \gtrsim 1.0$ eV, dominate, especially if closer to the cathode than ~ 3 nm.*

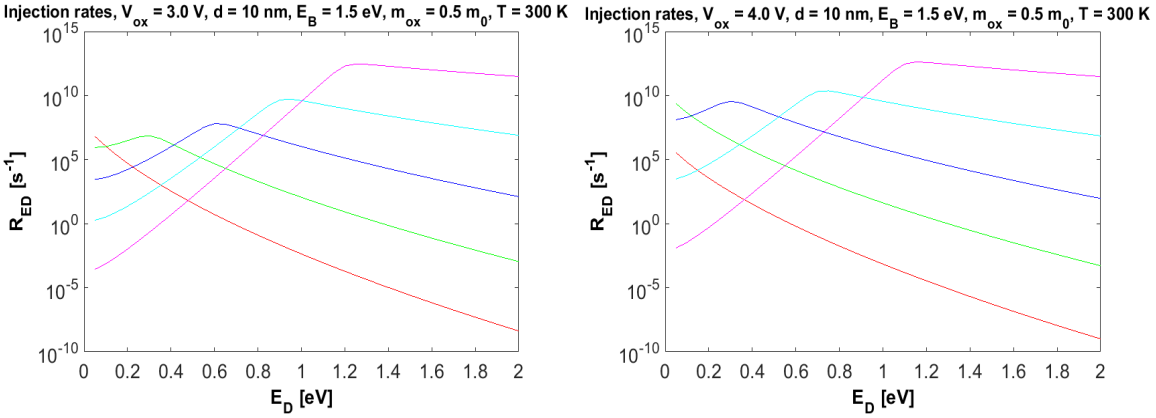

(c) *R_{ED} for $V_{ox} = 3.0$ V: For the shallow traps, $E_D \lesssim 0.5$ eV, rather the more distant "bulk defects" $x_D \gtrsim 3$ nm, are relevant, while for 0.5 eV$\lesssim E_D \lesssim 1.0$ eV, only the mid-distant ones, e.g. 3 nm from the cathode, compete. The latter can still contribute a bit for deeper traps, yet the 2 nm and 1 nm dominate already at this voltage.*

(d) *R_{ED} for $V_{ox} = 4.0$ V: Still for larger E_D the trap must be closer to the cathode to be relevant. This decrease of the dominant trap locations x_D is linear in E_D. For $E_D = 0.05$ eV the 4-nm-traps, $E_D = 0.3$ eV the 3-nm-distant traps, around $E_D = 0.7$ eV the 2-nm-traps and around $E_D = 1.1$ eV the 1-nm-distant traps are dominant.*

Figure 5.7: *Sensitivity analysis of the elastic injection rates R_{ED} for electrons from the cathode with three parameters varied: voltages of (a) 1.0 V, (b) 2.0 V, (c) 3.0 V, (d) 4.0 V, traps distance to the cathode of 1 nm (magenta), 2 nm (blue), 3 nm (green), 4 nm (red), 5 nm (cyan) and trap energies E_D from 0.05 eV to 2.0 eV below CBM in the oxide. The barrier is set to a constant, typical value of 1.5 eV, oxide thickness $d = 10$ nm and $T = 300$ K (RT). Further details see text.*

ones, but in absolute terms for more distant defects it remains smaller than the maximum rates of closer defects for all voltages.

(4) The increase of the rates (in general) when increasing E_D (going from shallower to deeper defects) from below resonance energy, is stronger than the decrease with increasing E_D above the maximum at the resonance energy. This effect is more pronounced the closer the defects are to the cathode (smaller x_D).

Observations (1) and (2) essentially express the relation between E_D, E_B, V and x_D manifesting "resonance" in the more phenomenological equation $E_D = E_B - e\frac{V}{d}x_D$. Despite of its simplicity this relation is a basic argument for the discussions in sections 6.3.5 and 6.4.4. As described exemplarily in the captions of Fig. 5.7a to 5.7d, a stronger shift with the voltage is visible for further distant defects, e.g. with maximum positions at 1.3 eV, 1.1 eV, 0.9 eV and 0.7 eV, i.e. 0.2 eV shift in energy per volt, for defects at 2 nm from cathode, while for defects 4 nm the values are 1.1 eV, 0.7 eV, 0.3 eV (fourth one not applicable anymore), i.e. 0.4 eV shift in energy per volt.
The qualitative reason for observation (3) is that the tunneling barrier is reduced more in absolute terms with increasing voltages, if the defect is more distant to the cathode. So the maximum injection rate increases stronger with voltage for more distant defects. For very close defects (1 nm, 2 nm) the barrier is already that thin that $T(E) \approx 1$ and not the limiting factor in Eq. (5.13).
As a consequence, for higher voltages new injection channels are primarily opened via further distant defects due to an increasing tunneling probability into these traps. However, it is still an interplay of all parameters, so the traps must not be too distant and the resonance conditions from observation (1) and (2) in terms of E_D, E_B, V and x_D must be fulfilled, too. Combined with observation (4) the result of this consequence of (3) is, that "medium-distant" defects (e.g. at 3 nm for d=10 nm) of an energy $E_D \lesssim E_B$ become relevant for low voltages, take on their increasingly higher maximum rates quickly for increasing voltages (observation (3)) and will still stay relevant for further increasing voltages (observation (4)). However, for sufficiently high voltages the defects close to the cathode still dominate. To give a numerical example, in Fig. 5.7d at $V = 4.0$ V defects at 3 nm and 2 nm with $E_D = 1.0$ eV, for instance, are already "off-resonant", while defects at 1 nm are about to take on their maximum value for a further increase in E_D. Thus the slowly decreasing cyan (2 nm) curve intersects the strongly increasing magenta (1 nm) curve for $E_D = 1.0$ eV, so the rates, i.e. kMC-contributions, are the same for these two different defect positions. But also the blue (3 nm) curve is "only" about 3 orders of magnitude lower than the other two for $E_D = 1.0$ eV, which could make such defects also still relevant in kMC-simulations (or experiments) with traps at $E_D = 1.0$ eV.
To quantify this obervation more, for small voltages ($V \lesssim 1$ V) and shallow-to-deep defects, i.e. 0.5 eV$\lesssim E_D \sim E_B \lesssim 1.2$ eV, the relevant range of this work, defects must be either close to the cathode, $x_D \lesssim 2$ nm, i.e "interface defects". If they are more distant defects ($x_D \gtrsim 2$ nm, i.e. "bulk defects"), they must be shallow enough ($E_D \lesssim 0.5$ eV

in the example), to contribute to transport, because only then the rates are comparable and compete in kMC-simulations. This changes going to medium voltages (∼2.0-3.0 V) referring to the relevant band of defect energies, 0.5 eV$\lesssim E_D \sim E_B \lesssim$ 1.2 eV, as in this energy range the rates for the mid-distant defects ($x_D \sim 3$ nm) take on their maximum values. These are at least competitive to the rates of defects close to the interface, $x_D \lesssim 2$ nm, which are relevant at all voltages. For the same defect energies and voltage range (∼2.0-3.0 V) bulk defects with $x_D \gtrsim 4$ nm are "off". Only for more shallow energies, i.e. $E_D \lesssim 0.6$ eV, they are competitive to closer defects at these voltages. But for $V \gtrsim 4.0$ V, they are irrelevant, even if they are most shallow in energy. However, the rates of interface-close defects, $x_D \lesssim 2$ nm, will dominate for medium (∼2.0-3.0 V) up to high voltages ($V \gtrsim 4.0$ V), especially for 0.5 eV$\lesssim E_D \sim E_B \lesssim$ 1.2 eV but also deeper defects. To put this into a nutshell, the defects closer than 2-3 nm at the electrode, i.e. "interface defects", are supposed to dominate injection into deep defects in TiO_2. If additionally trap-trap-transport-rates are on average faster than injection, such interface defects will resemble the bottleneck for the overall TAT transport.
Apart from that, observation (4) further implicates that once a defect at E_D has surpassed the resonance with E_B (e.g. 1.0 eV as "zero-volt-resonance-energy") due to increasing voltage V, its contribution to transport (in terms of injection rates) decreases less than its contribution increased before resonance. For defects close to the cathode (e.g. 1 nm, 2 nm also 3 nm) the rates remain fairly constant or at least that high for increasing V that these defects will still contribute to injection. This implies that for deeper defect energies and low voltages generally less defects (only those with $x_D \lesssim 2$ nm) are relevant for injection, while with increasing voltage there are more and more defects with an energy deeper than "resonance" which can contribute more to transport, even if slightly further distant, i.e. $x_D \lesssim 3$ nm. Thus, at a fixed voltage defects that lie at a certain energy E_D deeper than the maximum (for a specific, fixed voltage and position) are, relatively seen, more favored for injection than the ones which lie slightly higher. However, if a voltage sweep starting at zero volts is done, as often performed in devices and always done in simulations or characterizations, the deeper defects are "off-resonant" already for zero volts and become slowly less important for higher bias, while the more shallow defects can still be brought into resonance for increasing voltage and become quickly more important for higher voltages.
Together with (3) (and keeping the resonance arguments (1) and (2) in mind), observation (4) has important implications for devices, because then, during an extensive voltage sweep in a device, the shallower defects more distant in the bulk, will have contributed the most to charge injection "in total" during the sweeps and will be even more decisive for electron injection at high voltages. Hence, one would expect that deeper defects, even if located at the interace, are less harmful than shallow bulk defects when devices are desired that show a fairly constant or low overall electron injection (in terms of its consequences for electron transport and current through the oxide) during such broad voltage sweeps. If additionally deep defects can be avoided close ($x_D \lesssim 2$ nm) to the cathode interface, in particular, then injection and associated transport can be avoided

over the whole voltage range, keeping electron currents through such dielectic layers low or at least not increasing too much over the whole voltage range. This is important when thinking e.g. of leakage in memory devices or any other where the TAT or PF branch, though not completely avoidable, should at least be kept constantly flat and the current should be kept lower than a certain threshold. On the other hand shallower defects in the bulk are more 'useful' when much injection into traps and thus TAT and PF is desired, especially from a certain voltage onwards, as there will be a faster and more pronounced increase in injection for increasing voltage, especially into increasingly more defects farer away from the cathode, and in total more charge will flow through the device than for the same parameter configuration having only deep defects.
Thus, if producible, oxides with little deep interface traps and many shallow bulk defects would be useful to optimize the transport properties in photovoltaic, photocatalytic or also resistive switching devices. The arguments presented here will be discussed again in section 6.3 and 6.4.
To put it into a nutshell once more, for shallow defects the further distant defects can be relevant for all realistically applied voltages, while the closer defects are only relevant at low voltages and lose importance for higher voltages. The situation is the other way round for deeper defects. Medium distant defects ($\sim$ 3 nm in the plotted example) are always relevant for injection for (more or less) all voltages and also for all defect energies. From this statement it is straightforward to draw conclusions which kind of defects to "produce" or "avoid" in experimental or theoretical structures using conductive oxides, if certain properties of a device are desired.
A final conclusion can be formulated in terms of kMC: If the same statements are valid also for the extraction rates, than injection into interface-close traps followed by PF-emission will be the most relevant transport process for lower to medium voltages and shallow-medium defect energies, manifesting "PF" emission. This holds in particular, if the overall device thickness is high and thus multiple-step-processes are the less probable alternative competing to the two-step process PF. On the other hand injection into interface or medium-distant defects followed by tunneling processes and final extraction from medium-distant defects into the anode, manifesting "TAT" processes, will be dominant for higher voltages, especially if the traps are deeper in energy ($E_D \gtrsim 0.5$eV) and relatively thin dielectric layers.

5.2.3 Potential at Positively Charged Defects in the Oxide

Due to the importance of the examined injection arguments' it is recommendable to visualize and check, if the information that is processed during each kMC-simulation describes the related physical situation accurately. To demonstrate this the energetic or potential landscape inside the oxide, directly computed by the means of the implemented kMC-code can be extracted from simulations. At the beginning of each simulation, as well as, during the run of a simulation, defects are positively charged. This creates a

Coulombic potential that has to be added to the linear potential drop and is accounted for in the numerical computation of the transmission coefficient. Note that normally the analytical version was used, but the numerical computation is pointed out specifically, if it was necessary. The results of this computation are plotted in Fig. 5.8. The simulation box for the oxide was 10 nm x 10 nm x 10 nm in total. This box is discretized and the Coulombic potential is computed and added on the linear voltage drop between the two electrodes on every grid point. The three axis are the real space inside the simulation box, the fourth axis measures the (positive) value of the Coulombic potential below the CBM of the oxide. The z-component of all defects in the figure is fixed to 5.0 nm, while the x and y location was randomized. There are two defects visible which are placed at z = 5 nm (fixed input), while one was randomly placed at x = 5.9 nm, y = 2.0 nm, whereas the other has the coordinates x = 5.0 nm, y = 7.0 nm. For reasons of a better visibility of the Coulombic potential caused by the defects, the x-direction is depicted as slices with 0.1 nm distance. The computed potential landscape agrees with realistic expectations on the potential landscape caused by a linear drop plus Coulombic charges at positive defects. This demonstrates the correct computation. Furthermore, it shows that over a distance of less than 1 nm the Coulombic contribution to the potential is negligible. Since the defect densities in all simulations were chosen smaller than $n_D \lesssim 0.05nm^{-3} = 5 \times 10^{19}cm^{-3}$ the average distance was always at least $n_D^{-1/3} \approx 2.7nm$. Therefore the influence of the Coulombic potential of a defect is supposed to be irrelevant over the major part of the tunneling distance between two defects or into the cathode. This simplification is a natural part of the hopping model which we used mostly, see section 5.3.1.

5.2.4 Inlastic Injection and Extraction Rates

The inelastic injection and extraction of electrons from the electrode into defects and vice versa must be assisted by the emission or absorption of phonons, as depicted in Fig. 5.6. The implemented model was firstly derived by Kiveris et al.[239], improved by Dalidchik et al.[240], who introduced the WKB transmission coefficient into it, and was finalized by Herrmann et al.[229]. Herrmann described the capture and emission of free electron states and localized electron states, i.e. electron traps, via multi-phonon-assisted tunneling with Schockley-Read-Hall lifetimes.
Most remarkably, the model was also derived for tunneling from band tail states in semiconductor electrodes, so it is applicable to the MOS-systems investigated here, like elastic rates in section 5.2.1. The traps are still distributed randomly in the oxide with a density n_D with monoenergetic trap levels at a sharply defined energy E_D, while the according fraction of the oxide band gap above E_D constitutes the tunneling barrier, cf. Fig. 5.1. The phonons in the oxide with an energy $\hbar\omega$ couple to these traps proportional to the coupling constant S, the Huang-Rhys factor, which describes the phonon-electron-coupling strength.[168, 229]
Coupling of an electron to multiple-phonons of different energies is excluded in the model, so we refer to single-mode approximation. The possibility of phonon-coupling spans

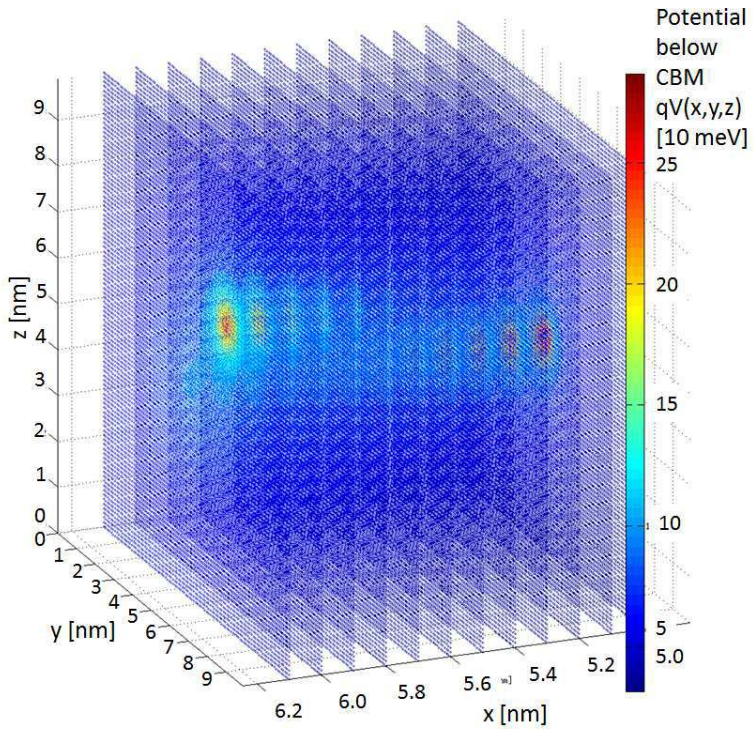

Figure 5.8: *Coulomb potential landscape from the simulations as computed by and extracted from actual kMC-simulations. The three axis are real space inside the simulation box, the fourth axis measures the (positive) value of the Coulombic potential below the CBM of the oxide. There are two defects visible which are fixed at z = 5 nm, while the x and y location was random. For reasons of a better visibility of the Coulomb potential caused by the defects, the x-direction is depicted as slices with 0.1 nm distance. The image confirms the realistic expectations on the Coulomb potential.*

up a range of virtual states located energetically above (phonon emission) and below (phonon absorption) the trap level into which the electron can be injected, so that it can subsequently "thermalize" into the actual trap level. Same is true for the extraction from a defect where the virtual states are located - the other way round - above the trap level for emission and below the trap level for phonon absorption. In the end the defect appears to be thermally broadenend. Note also that for the kMC-simulation not the total rate, equivalent to a current, is needed but the rate for an individual charge carrier (electron) that occurs during the simulation and tunnels at the specific energy E_D. In the model the rates for this tunneling process correspond to characteristic times to tunnel between electrode and defect or vice versa:[43, 229]

$$R_{ED}^{MP} = \frac{1}{\tau_{ED}^{MP}} = \int_{-\infty}^{\infty} N_E(E) f(E) T_{ED}(E, x_D) c_{ED}(E, x_D) dE \tag{5.16}$$

$$R_{DE}^{MP} = \frac{1}{\tau_{DE}^{MP}} = \int_{-\infty}^{\infty} N_E(E) [1 - f(E)] T_{DE}(E, x_D) c_{DE}(E, x_D) dE \tag{5.17}$$

$N_E(E)$ is the DOS of the free electron gas (parabolic bands) in the electrodes

$$N_E(E) = \frac{1}{2\pi^2} \left(\frac{2m_E^*}{\hbar^2} \right)^{3/2} \sqrt{E - E_C} \cdot \Theta(E - E_C) \tag{5.18}$$

which can be easily adjusted for metallic as well as semiconductor contacts in strong inversion or accumulation by adjusting the CBM, E_C, properly, as said in the previous section. Note, that by the choice of the electron DOS hole trapping from the electrodes and emission into them is neglected. $T_{ED}(E,x) = T_{DE}(E,x) \equiv T(E,x)$ are the transmission coefficients for an electron of energy E to tunnel between the electrode and the trap at position x_D, m_E^* is the effective electron mass in the electrode, so either cathode or anode, and Θ is the step function. Most essentially, the elastic version of the tunneling rates are convoluted with the capture and emission rates for phonon absorption or emission calculated from

$$c_{ED}(E,x) = c_0 \sum_{m=-\infty, m\neq 0}^{\infty} L_m(z)\delta(E - E_m(x_D)) \begin{cases} \exp\left(-\frac{E_x(x_D)-E}{k_B T}\right), & \text{if } E_x(x_D) - E > 0 \\ 1, & \text{otherwise} \end{cases} \tag{5.19}$$

$$c_{DE}(E,x_D) = c_0 \sum_{m=-\infty, m\neq 0}^{\infty} L_m(z)\delta(E - E_m(x_D)) \begin{cases} \exp\left(-\frac{E-E_x(x_D)}{k_B T}\right), & \text{if } E - E_{x_D}(x) > 0 \\ 1, & \text{otherwise} \end{cases} \tag{5.20}$$

The capture and emission rates for phonons describe "the price the system has to pay" for the excitation (emission) or absorption of m phonons, $m = 0, ..., \infty$ and their coupling to the electron reflected by the multiphonon transition probability $L_m(z)$.[168, 229] Assuming typical phonon energies of 40 meV.¶[241] The participation of more than 5 phonons reduces the rates by a factor of 10^{-4}, meaning that such processes are already improbable. Hence, no more than 10 phonons were allowed for absorption or emission in the simulations, i.e. virtually the upper limit of the sum in Eq. (5.19) and Eq. (5.20) was $m = 10$. The single-mode approximation is modelled by the δ-function in Eq. (5.19) and Eq. (5.20) permitting only energies $E_m = E \pm m\hbar\omega$ to appear after evaluation of the integral in Eq. (5.16) and Eq. (5.17). The prefactor c_0 is calculated under the approximation of a 3D delta-like potential of the traps[229]

$$c_0 = \frac{(4\pi)^2 r_D^3}{\hbar E_g}(\hbar E_0)^3 \tag{5.21}$$

Due to the approximations it contains the localization radius of the trap located at E_D below CBM and the so-called electro-optical energy in the oxide

$$\hbar E_0 = \left(\frac{e^2\hbar^2 F^2}{2m_{ox}}\right)^{1/3} \tag{5.22}$$

¶Debye temperature $T_D \approx 500K$, thus $\hbar\omega_D = k_B T_D \approx 0.04$ eV.

To complete all entities of the model only the multiphonon transition probability $L_m(z)$ is missing:

$$L_m(z) = \left(\frac{1+f_{BE}}{f_{BE}}\right)^{p/2} \exp\{-S(2f_{BE}+1)\} I_m(z) \tag{5.23}$$

It contains the Huang-Rhys factor S, the modified Bessel functions $I_m(z)$ of order m, the argument $z = 2S\sqrt{f_{BE}(1+f_{BE})}$ and f_{BE}, the Bose-Einstein distribution giving the phonon occupation number,

$$f_{BE} = \frac{1}{\exp\frac{\hbar\omega}{kT} - 1} \tag{5.24}$$

Inserting equations (5.19) and (5.20) delivers the rates as derived by Herrmann[229] and firstly used in the thesis by G. Jegert[43]

$$\begin{aligned} R_{ED}^{MP} = c_0 \sum_{m<0}^{-\infty} N_E(E_m) f(E_m) T_{ED}(E_m, x) L_m(z) \exp\left(\frac{m\hbar\omega}{k_B T}\right) \\ + \sum_{m>0}^{\infty} N_E(E_m) f(E_m) T_{ED}(E_m, x) L_m(z) \end{aligned} \tag{5.25}$$

$$\begin{aligned} R_{DE}^{MP} = c_0 \sum_{m<0}^{-\infty} N_E(E_m)(1 - f(E_m)) T_{DE}(E_m, x) L_m(z) \\ + \sum_{m>0}^{\infty} N_E(E_m)(1 - f(E_m)) T_{DE}(E_m, x) L_m(z) \exp\left(-\frac{m\hbar\omega}{k_B T}\right) \end{aligned} \tag{5.26}$$

Except for the phonon-specific ones, all of the parameters in the presented rates had already been defined in previous chapters. Only the Huang-Rhys-factor S, the phonon number m and the phonon energies $\hbar\omega$ are essentially new, with the latter two being experimentally determinable. The Huang-Rhys-factor, the coupling strength, entering $L_m(z)$ can numerically outweigh the exponentially decreasing probability for higher phonon numbers. Since it reflects the maximum number of phonons involved in the transition processes, it is commonly misused as a fitting parameter, although only values around 1 (maximum 10) can be considered realistic.[235]
The effects of varying S and $\hbar\omega$ on the inelastic injection rates into defects had already been done in the thesis by G. Jegert, p. 49,[43] and shall only be referenced here for reasons of brevity. He analyzed the inelastic injection rates into a defect at $x_D = 2$nm with $E_D = 1.0$ eV and $E_B = 1.0$ eV in dependence of phonon number, phonon energy and Huang-Rhys-factor S, in particular. Temperature $T = 298$ K, and electric field

$F = 1$ MV/cm (and/or 5 MV/cm) are about the same here. So the values presented there can be referred to as similar parameter configurations as in this work. Further parameters like the band gap of TiO_2, i.e. $E_g = 3.2$, or the oxide mass $m^*_{ox} \approx 1.0 - 5.0 m_0$ deviate from his ones only linearly and also enter these rates only linearly. Hence they won't change the orders of magnitude for the rates reported in [43]. Thus three important points can be found from his sensitivity analysis: First, the Huang-Rhys factor reflects, as implemented, a direct measure for the maximum number of phonons involved in inelastic processes, as rates start dropping exponentially for phonon numbers above this value. Second, the rates go down exponentially with increasing energy difference ΔE between initial and target state, for which the involved phonons have to come up. Third, the rates increase just linearly with a higher phonon energy for a certain, fixed ΔE and S. So if a state is exponentially shifted to "off-resonance" by increasing ΔE, the involvement of phonons of an accordingly (unphysically) higher energy or number is improbable, as it can account for it only linearly. Thus S is rather the parameter to increase the average energy of all phonons involved, i.e. $S \cdot \hbar\omega$, to ΔE. So the model is heavily influenced by this parameter, which is on the other hand theoretically well-determined. Therefore, it is not supposed to be varied for fitting or adjusting the rates without physical reason.
Due to this it is recommendable, to choose and fix a phonon energy on the range of 40 meV ($\hat{=} k_B\Theta_D$,Debye temperature) and keep the Huang Rhys factor around 1 (maximum 5), as done for TiO_2.[235] Then a maximum number of $m \lesssim 10$ phonons (fixed value in all simulations) will be observed, which amounts to a maximum energy difference of $\Delta E = 0.4$ eV to be absorbed or emitted via phonons. Note, that such a value is already quite large in terms of "off-resonance" and implies rates, which are reduced that much, that the corresponding inelastic injection processes can realistically considered to be irrelevant compared to elastic injection. So phonon-associated effects of higher order are very unlikely to affect the accuracy of our results and the extensive discussion of the elastic injection rates in section 5.2.2 is considered even more important, because numerically elastic injection appears way more probable.

5.3 Trap-Trap-Transitions in conductive oxides: Hopping vs. Tunneling

5.3.1 Hopping Conduction

Most articles in literature agree that deep defects in TiO_2, TiO_x and AlO_x are localized states, cf. sections 6.3.1 and 6.4.3, and that transport occurs via small polarons then. Accordingly, the trap-trap-transport should be properly described by the well-known Miller-Abrahams-hopping rates used in the kMC-model, as also orginally developed to

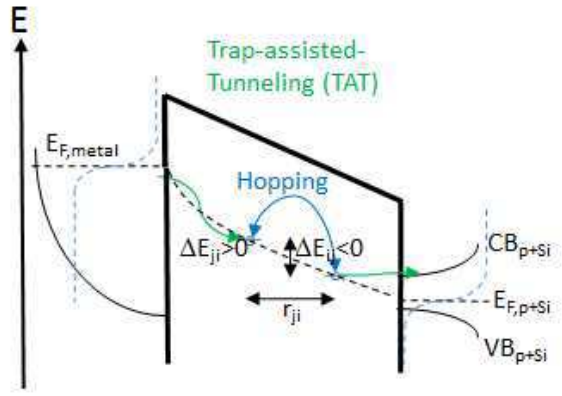

Figure 5.9: *Close-up on hopping between two traps in the oxide. For this process, modelled via the Miller-Abrahams-rates, localized defect states have to be assumed. Hopping upward in energy by ΔE is exponentially discriminated. For most of the results on conductive oxides this was the model of choice, see below.*

describe such impurity conduction in semiconductors:[242]

$$R_{ij} = \nu \exp \frac{-2r_{ij}}{r_D} \cdot \begin{cases} \exp -\frac{\Delta E}{k_B T}, & \text{if } \Delta E > 0 \\ 1, & \text{otherwise} \end{cases} \tag{5.27}$$

where ν is a typical phonon frequency 10^{13} Hz, $\Delta E = E_j - E_i$ the energy difference between initial and final state, r_{ij} the trap-trap-distance and r_D the localization radius, given as $r_D = \frac{\hbar}{\sqrt{2m^*_{ox}E_D}}$. Since the localization radius is defined by the wave function of the localized defect states, for an exact description of the specific defect an analytical form for the wave function, e.g. of oxygen vacancies in TiO_2 would be needed. [‖] Thus we stick to the simpler reasonable approximation for it which is an exponentially decaying wave function $\Psi = \sqrt{\frac{r_D}{2\pi}}\frac{1}{r}\exp(-r/r_D)$ leading to the given trap radius r_D which gets smaller with increasing defect depth E_D. The high attractivity of the Millar-Abrahams-formula is its simplicity and versatility. The particle transfer in a big variety of different physical systems, ranging from the Ising-lattices in magnetism to organic semiconductors, has already been accurately modelled by this simple "hopping" process backed up by the derivation by A. Miller and E. Abrahams in [242]. It was also very useful for the material systems of interest here, as it handles likewise elastic processes ($\Delta E = 0$) and inelastic ones.

5.3.2 Elastic and Inelastic Trap-Trap-Tunnneling - The Ridley Rates

Essentially two alternative long-range tunneling models exist for the phonon-assisted elastic and inelastic tunnling, as depicted more closely in Fig. 5.10, as presented also in the PhD thesis by G. Jegert.[43] On the one hand there is the tunneling model, assuming that the electrons in the initial trap at $\mathbf{r_i}$ tunnel into virtual states around the trap level at $\mathbf{r_j}$ and then thermalize via phonons, i.e. relax energetically, to the trap level E_j.

[‖] Defect wave functions can usually just be approximated by supoerpositions of basis set functions in first-principle methods.

This simple picture is described by the formula similar to equation (5.27), but using the transmission coefficient instead of the exponential factor in equation (5.27):

$$R_{ij} = \nu \cdot T_{ij} \cdot \begin{cases} \exp -\frac{\Delta E}{k_B T}, & \text{if } \Delta E > 0 \\ 1, & \text{otherwise} \end{cases} \tag{5.28}$$

This model appears intuitive, but more phenomenological, since a concise physical derivation from first principles is not known. On the other hand there is the formally well-supported model by Ridley.[235] Its derivation is quite similar to the one presented for the inelastic electrode-trap injection/extraction rates already presented in section 5.2.4, is already summarized in [43] and shall be omitted here. In brief, assuming δ-functions for the defect-DOS, an occupation probability of 1 or 0, if a trap is empty or occupied, as well as absorption and emission rates introduced analogous to Eq. (5.16) and (5.17), the resulting Ridley-rates for defect-defect-tunneling are:

$$R_{ij} = T_{ij}(E_i, r_{ij}) c_{ij}(E_i, E_j) \tag{5.29}$$

where Ridley quantum-mechanically derived the expressions for c_{ij} for tunneling assisted by absorption of m phonons

$$c_{ij}^{abs} = R_0 f_{BE}^m \exp(-2 f_{BE} S) \tag{5.30}$$

as well as for tunneling assisted by emission of m phonons

$$c_{ij}^{em} = R_0 (f_{BE} + 1)^m \exp(-2 f_{BE} S) \tag{5.31}$$

where the prefactor R_0 is

$$R_0 = \frac{\pi}{\hbar^2 \omega} \frac{S^{p-1} e^{-S}}{(p-1)!} \left[0.26 |V|^2 + 0.18 \frac{|V\Delta|^2}{S} (p-1) \right] \tag{5.32}$$

One notes that the Huang-Rhys-factor S, already introduced in section 5.2.4 as a measure of the strength of the electron-phonon-coupling, and the number of emitted or absorbed (excited) phonons m are central for the order of magnitude of this prefactor. The matrix elements were introduced here defined by the equations

1. $|V|^2 = \sum_{\mathbf{q}} |V_{\mathbf{q}}|^2 \quad$ with $\quad V_{\mathbf{q}} = < \Psi_j | U_{\mathbf{q}} | \Psi_i >$
2. $|V\Delta|^2 = |\sum_{\mathbf{q}} V_{\mathbf{q}} \Delta_{\mathbf{q}}|^2 \quad$ with $\quad \Delta_{\mathbf{q}} = < \Psi_j | U_{\mathbf{q}} | \Psi_j > - < \Psi_i | U_{\mathbf{q}} | \Psi_i >$
3. $V_{\mathbf{q}} = < \Psi_j | U_{\mathbf{q}} | \Psi_i >$

4. $\Delta_{\mathbf{q}} =< \Psi_j|U_{\mathbf{q}}|\Psi_j > - < \Psi_i|U_{\mathbf{q}}|\Psi_i >$

which explicitly show the dependence of the final rates on the electron-phonon-coupling potential $U_{\mathbf{q}}$ for the phonon wave vector $\mathbf{q}$ which was assumed to be an optical deformation potential $U_{\mathbf{q}} = U_D \cdot \exp(i\mathbf{q} \cdot \mathbf{r})$, Furthermore it shows the dependence on the wave functons Ψ_i and Ψ_j of the initial and final defects, which are, however, not known analytically and can only be approximated. According to the discussion above those wave functions were modelled by a step-wise constant function

$$\Psi = \begin{cases} \left[\frac{4\pi}{3} r_D^3\right]^{-1/2} & \text{if } -\frac{R}{2} < x, y, z < \frac{R}{2} \\ 0, & \text{otherwise} \end{cases} \tag{5.33}$$

with $R = (4\pi/3 \cdot r_D)^{1/3}$, which had to be evaluated numerically in the simulations. Since it is mostly argued that electron states are localized, the hopping model is favorable to investigate deep traps in conductive oxides. Therefore generally the hopping model was employed to produce the results reported in chapter 6, while the latter two models for the defect-defect-transitions were only tested against the hopping model, if necessary.
But G. Jegert already analyzed and compared in his thesis the difference between the phenomenological "coherent tunneling"-model in Eq. (5.28) and the more complex, but more profound Ridley-model. [43] Most interestingly, he found that for parameters similar to the ones used here, such as no more than 10 phonons of 40 meV energy allowed, $S = 1$, $T = 298$ K, $r_{ij} = 2$ nm, and defect energies of 0.5 eV and 1.5 eV, it is only for the deepest defects and, even then only for fields higher than ~ 3.0 MV/cm, that one obtains a considerable difference in the tunneling rates for the two models. Additionally, all tunnelling rates for the parameter sets were decreased with increasing external fields, because the defects are less and less resonant and tunneling becomes less probable. This decrease was more pronounced for the Ridley-model. Finally, one has to note that all rates are smaller than $10^7 s^{-1}$, even for defects at 0.5 eV. This is an important reference number for the qualitative argumentation of the applicability of the model in section 5.5. To conclude, though physically less profound, the "coherent tunneling" model is a good and fast approximation to compare the results of the tunneling models (Ridley or coherent tunneling), whose scaling is dominated by T_{ij}, to the ones of the hopping model. Hopping is favored here and once fits to actual experimental curves are obtained, one can use the "coherent-tunneling" model at first to test the validity of the former or the latter model.

5.4 Poole-Frenkel Emission

Aside from the electrode-electrode transitions and purely defect related transport beginning with a direct injection and final extraction there is a third category of mechanisms which is of outmost importance for the kMC-model: The Poole-Frenkel effect. It is based on field-emission of electrons from trap levels and depends on both the applied field and

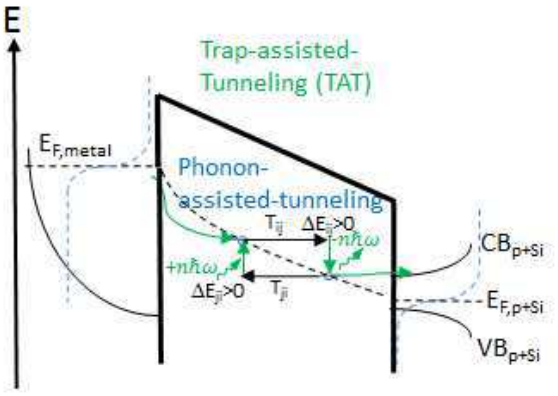

Figure 5.10: *Close-up on multiple-phonon-assisited tunneling between two traps in the oxide. Defect energies are in most situations shifted by an energy ΔE, as depicted here, and this difference is accounted for by the emission or absorption of an appropriate number of phonons to create a situation as under resonant tunneling.*

the defect-depth. Its simplest form was published in 1938 by Y. Frenkel and describes 1D-emission rates as, $R_{PF} = \nu \cdot \exp\left[-\frac{1}{k_B T}\left(E_D - \sqrt{\frac{e^3 F}{\pi\epsilon_0 \epsilon opt}}\right)\right]$ with ν being the typical lattice vibration energy assumed to be 10^{13} Hz. It explains an increasing conductivity for increasing external fields in electrical insulators due to an increased density of free charge carriers in the CB of the insulator. For the physical mechanism one assumes charge carriers to be initially trapped in a neutral, localized state, i.e. neutral defects, in the band gap at an energy E_D below CBM. Since the measured conductivity enhacements are too strong to stem from purely thermal excitation of the charge carriers, further terms had to be introduced into the potential which are responsible for an enhanced emission by a lower barrier for the electrons to leave the trap in an increasing applied electric field. Besides the crystal potential $V_C(x) = V_0$, modelled as a constant, and the negative linear potential drop due to the electric field $V_F(x) = -eFx$, a Coloumbic potential is introduced accounting for the attraction between the negatively charged electron at position x which is about to leave the initially neutral defect at the position x_D and the positively ionized defect according to

$$V_D(x) = -\frac{e^2}{4\pi\epsilon_0\epsilon_{opt}|x - x_D|} \tag{5.34}$$

The superposition of the three contributions gives the overall potential

$$V(x) = V_C(x) + V_F(x) + V_D(x) = V_0 - eFx - \frac{e^2}{4\pi\epsilon_0\epsilon_{opt}|x - x_D|} \tag{5.35}$$

which indicates already that, due to the combination of the electric field and the Coloumb attraction, the potential must show a local maximum for $x > x_D$ which resembles a smaller barrier for the electron emission compared to the model of a δ-like potential-well of depth E_D in the vicinity of the defect. It is a straightforward task to find the position of the maximum $x_m = x_D + \sqrt{e/(4\pi\epsilon_0\epsilon_{opt}F)}$ and the value of the potential there,

$V(x_m) = V_0 - eFx_D - \sqrt{\frac{e^3F}{\pi\epsilon_0\epsilon_{opt}}}$. This leads to an effective barrier height reduction of $\Delta E_{PF} = V(x_D) + E_D - V(x_m) = \sqrt{\frac{e^3F}{\pi\epsilon_0\epsilon_{opt}}}$ which justifies the additional term in the phenomenological 1-D model already.
Note that the barrier reduction due to the image charge for the thermionic emission over the energetic barrier between cathode and oxide amounted to exactly half of this value. The most accurate version for PF-emission as implemented in the code is given by the 3D-version of the model,as derived by Hartke in 1968[243],

$$R_{PF} = \nu \cdot \exp\left(-\frac{E_D}{k_BT}\right)\left\{\left(\frac{k_BT}{\beta\sqrt{F}}\right)^2\left[1+\left(\frac{\beta\sqrt{F}}{k_BT}-1\right)\exp\left(\frac{\beta\sqrt{F}}{k_BT}\right)\right]+\frac{1}{2}\right\} \quad (5.36)$$

where ν is the typical phonon interaction frequency (set to a standard value of 10^{13} Hz), $\beta = \sqrt{\frac{e^3}{\pi\epsilon_0\epsilon_{opt}}}$, with ϵ_{opt} being the optical dielectric constant (reference value: ∼5.8 [30, 244] and$F = V_{ox}/d$ is the electric field, i.e. oxide voltage drop V_{ox} over oxide thickness d.

It is important to note that in the model, an electron that has once left a trap by PF-emission into the CB is considered to be transported to the anode quasi-instantly and is not considered to be retrapped, as CB-processes are known to happen much faster, cf. also 5.5. It is straightforward to see by Eq. (5.36) that the rate decreases by about 1-2 orders of magnitude for every 0.1 eV increase in E_D. This makes the model very sensitive to the location of traps in the band gap: Shallow traps tend to dominate the current transports in insulators, while deep traps become neglectable, quickly, if located too deeply in the gap. This property will be employed frequently for the discussions in chapter 6. The formula is also sensitive to changes in the dielectric constant, but much less compared to the defect values. Moreover ϵ_{opt} is also well documented especially for TiO_2 as oxide material and could be fixed in most of the simulations.

5.5 Applicability of the Model to TiO_2 supported by Drift-Diffusion Simulations

Supplementary DD-simulations were performed in order to show the applicability of the model from the previous section to the new material TiO_2. Details on the working principle of TiberCAD can be found in references [245, 246] and the underlying, determining Poisson and drift-diffusion equations, to be solved simultaneously in the simulations, are provided in the appendix. At this point the simulations were just applied in a straightforward way as derived from existing exemplary configurations in the tutorial. Thus only the device geometry and material parameters had to be defined according to the information on material parameters of TiO_2 that was already reviewed from literature and used

for the kMC-simulations. First, the 2D-geometry of a typical trapezoidal Metal/TiO_2 nanopillar of 25 nm height with a 5 nm oxide layer on p^+-Si, as also produced experimentally by nTP with Au or Ti as metal, has been modelled. Then TiberCAD generated a 2D-finite-difference grid meshing the structure, as depicted in Fig. 5.11. Having defined all material parameters, see below, the current over the MOS-structure as well as the band diagrams were simulated in dependence of the gate voltage at the metal top contact which was sweeped from -2 V to 2 V. Typical band diagrams for an applied gate voltage of V=-2 V, V=-1.27 V, V=-0.55 V corresponding to accumulation conditions as simulated with TiberCAD are given in Fig. 5.12.
All material parameters of Si and TiO_2 were defined according to common literature values in accordance to the ones used in the kMC-simulations in chapter 6. However, in particular, the CBOs at the Metal/TiO_2 and TiO_2/p^+-Si-contact (doping density 10^{18} cm^{-3}) had to be calculated manually and defined strictly according to the MIGS-model, cf. section 6.3.4, in order to account for the typically present Fermi-level pinning at the interface, because this was not included in TiberCAD itself. For this purpose two kinds of metal contacts of experimental relevance were modelled: A higher work function metal, like Au or Pt, with $\phi_{Pt} = 5.3$ eV, and a lower work function metal, like Ti or Al with $\phi_{Ti} \approx \phi_{Al} = 4.3$ eV. Furthermore a pinning factor of TiO_2 of $S = 0.3$ and charge neutrality levels of $E_{CNL,TiO2} = 0.6$ eV or $E_{CNL,TiO2} = 1.0$ eV and $E_{CNL,Si} = 0.8$ eV were assumed. One has to note that the CNL values for TiO_2 found in literature are a bit spread. Both 0.6 eV[247] and 1.0 eV[244, 248] have been reported, but the latter one more often. Therefore, we report the results with the latter CNL 1.0 eV for both higher work function, see Fig. 5.12c, and lower work function metals, see Fig. 5.12b, and with the former CNL 0.6 eV only for the lower work function of Ti, see Fig. 5.12a. Although, band-related parameters can also be seen in the resulting band diagrams, the corresponding tables of input parameters that are consistent with the MIGS-model as well as exemplary parameter files can be found in the appendix. The images in Fig. 5.12 show in the first place that there is a band bending and associated part of the total gate voltage that drops in the Si substrate itself. Thus the oxide voltage drop has to be calibrated correctly in dependence of the gate voltage applied over the whole structure. The insets of the images show the equations of the fittings curves determined from six corresponding pairs of (V_{gate},V_{ox}) for each of the three simulated energetic situations. This allows for a recalibration of the voltage drop over the oxide, which is the actual input parameter for the kMC-simulations, in dependence of the gate voltage, which is usally reported in experiments. To obtain accurate and physically valid fits to samples with an essentially comparably doped p^+-Si and comparably thick TiO_2-contact ($d_{ox} \sim$ 5 nm) this re-calibration is necessary. Having valid equations corresponding to realistic material combinations at hand, its usage is emphasized where necessary for the fits presented in the results chapter 6 at the specific point.
Most remarkably, however, the DD-simulations of our material structures of interest for kMC confirmed that the band bending in the conductive oxide TiO_2 is negligible. The band diagrams in Fig. 5.12 show negligible band bending inside TiO_2 itself, as it is only

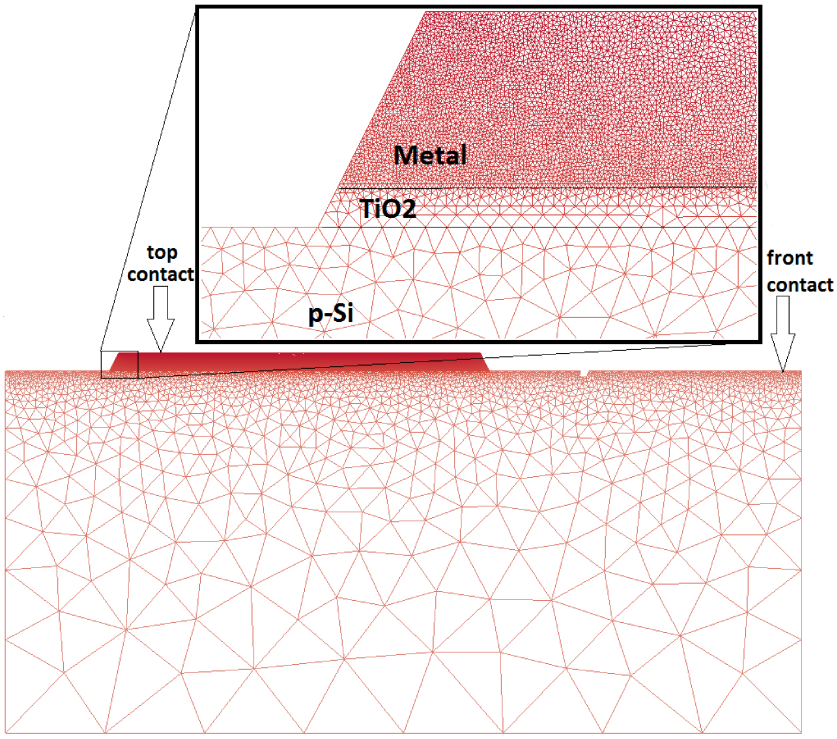

Figure 5.11: *Image of the finite-difference grid to mesh the structure resembling a 2D-trapezoidal Au/TiO_2 nanopillar of 25 nm height with a 5 nm oxide layer on p^+-Si.*

present at the very interface to the semiconductor Si. This means that even if thermally emitted electrons from the electrode ("SE") are included, the drift-diffusion terms as in Eq. (5.37) do not predict a noteable band bending. This justifies the approximation in the kMC-model, depicted already in the initial Fig. 5.1. So the material properties of the Ti/TiO_2/p^+-Si, Au/TiO_2/p^+-Si or also Pt/TiO_2/p^+-Si junctions allow for kMC-simulations without respecting the band bending in TiO_2, i.e. assuming a linear drop of the CB and hence also of the barrier. Therefore, the Poisson-equation does not have to be solved in every simulation step, which has been done and simplified and accelerated the simulations.
Moreover, these results can also be qualitatively understood by the rational argument, that conduction band processes as well as retrapping, leading to multiple phonon-assisted ionization processes, as discussed in [249], occur on much shorter time-scales than the processes down in the band gap, such as trap-trap-tunneling and -hopping, PF-emission or injection/extraction from and into traps. To justify this, first, we refer to the flux conservation equation

$$\frac{\partial n_{CB}}{\partial t} = G(x) - R_n(n_C) - \frac{\partial J_n}{\partial x} - \frac{\partial n_L}{\partial t} \tag{5.37}$$

describing the temporal change of the density of free electrons in the CB, n_{CB}, in dependence of the position x due to the four processes: generation at a rate G(x), recombination in to the VB at a rate $R_n(n_C)$, i.e. depending on the number of electrons in the CB n_{CB}, the change of the flux of electrons J_n in space, plus the (negative) rate

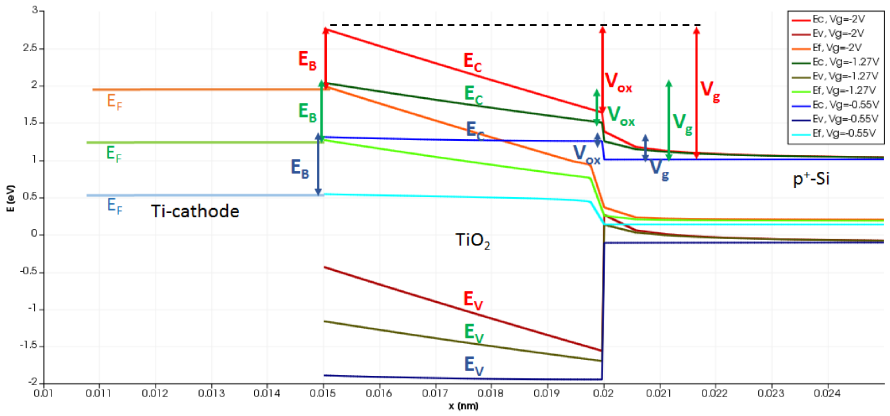

(a) *DD-Calibration of the oxide voltage drop V_{ox} in dependence of the gate voltage V_G for lower work function metals (Ti/Al) with $E_{CNL} = 0.6$eV.*

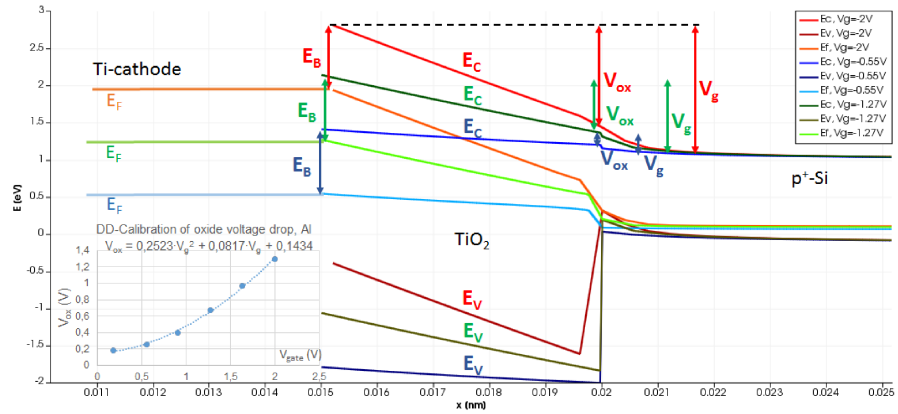

(b) *DD-Calibration of the oxide voltage drop V_{ox} in dependence of the gate voltage V_G for lower work function metals (Ti/Al) with $E_{CNL} = 1.0$ eV.*

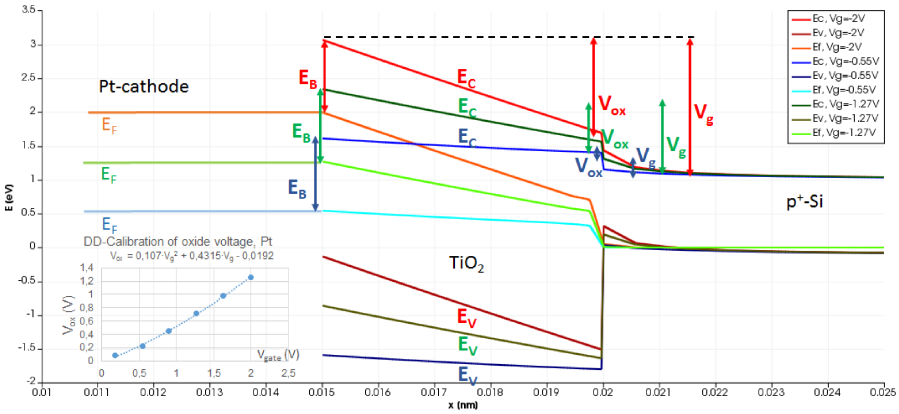

(c) *DD-Calibration of the oxide voltage drop V_{ox} in dependence of the gate voltage V_G for higher work function metals (Pt/Au) with $E_{CNL} = 1.0$ eV.*

Figure 5.12: *Results of DD-simulations with TiberCAD with the structure from Fig. 5.11. (a)-(c) Typical band diagrams for an applied gate voltage of V=-2 V, V=-1.27 V, V=-0.55 V (accumulation), calculated by the simulations having band offsets according to the MIGS-model, cf. section 6.3.4 with pinning factor S=0.3, $\phi_{Pt} = 5.3$ eV, $\phi_{Ti} \approx \phi_{Al} = 4.3$ eV, $E_{CNL,TiO2} = 1.0$ eV, $E_{CNL,Si} = 0.8$ eV. For a detailed discussion see text.*

$\frac{\partial n_L}{\partial t}$ of electrons (per volume) that get trapped in localized states in the band gap.[185] This includes all processes that could potentially influence the band bending. If they had to be respected due to the specific magnitudes of the rates in the material of interest, i.e. here TiO_2, the validity and applicability of our kMC-model would be affected. Subsequently, we justify by a realistic parameter estimate that this is not the case for TiO_2 and that the CB-related processes in Eq. (5.37) can be reasonably neglected in our kMC-simulations - in accordance with the DD-simulations above.
To begin with the estimate, for a typical ∼10 nm TiO_2 slab, as assumed in most examples for the rates above, the transit time through TiO_2 is considered to be ∼0.1 ps, while trapping (or "recombination") needs at least tens of ps[250] to several ns,[131, 132, 139] even μs are reported.[133] The fastest potentially competing processes in the band gap are PF-emission from shallow traps, which influences the $\frac{\partial n_L}{\partial t}$-term in Eq. (5.37), and injection from the cathode into shallow traps. To be associated with a maximum rate of $10^{12}s^{-1}$ for injection and also $\sim 10^{12}s^{-1}$ for PF traps must be placed below 0.5 eV and fields must be extremely high, i.e. as of ∼4 MV/cm. Even then, the corresponding times of these most extreme examples of the parameter sets and processes in our kMC-simulations are still on the upper edge of the times needed for an electron in the CB to transit through a typical ∼10 nm TiO_2 slab. Therefore, re-trapping or recombination to the VB of electrons is also less probable to occur than the successful transition of the electron through the slab in the CB, as just indicated. Electron-hole recombination or generation over the band gap is also negligible without incident light. Thus all recombination or generation terms in Eq. (5.37) are negligible for TiO_2 in our kMC-simulation.** Hence, it is a reasonable assumption in our kMC-simulator that electrons once excited into the CB either by SE (even slower than PF) or by PF will simply drift-diffuse through the CB of the TiO_2 slab to the anode without any disturbations by trap-related processes in the band gap. With electron movements in the CB being much faster, they are irrelevant on the simulated kMC-time-scales and its additional computation according to drift-diffusion-equations would affect the band bending only negligibly, but cost lots of computation time. Furthermore, the previous DD-simulations using TiberCAD, which omits exactly the trap-related processes in the band gap, approved that in this situation even drift-diffusion with CBOs, as used for our kMC-studies, alters the linear drop only in a negligibly thin region close to the anode. Of course, this holds only if the gate voltage is recalibrated to the oxide voltage because of the band bending in Si as outlined before.
As a final issue, the model also neglects hole tunneling transport between the electrodes. This can be also justified by the generally high valence band offsets of TiO_2 of at least 1.6 eV in the most conservative estimate on p^+-Si as well as the few hole-transporting traps known to be present in TiO_2. This was also approved by supplementary kMC-simulations modelling the energetic situation for holes, where no or no realistic currents were visible. Hence they are also not presented for reasons of brevity.

**An analogous argumentation for AlO_x is possible due to even deeper traps and higher CBOs there, but this shall be omitted for reasons of brevity.

In total we conclude from these rational, numerical arguments on the magnitudes of the rates and terms in Eq. (5.37) backed-up by the DD-simulations above that (i) accounting for the band bending due the electron transport in the CB or retrapping would not alter the results compared to the (much more efficient) kMC-model without it, (ii) TiO_2 is a prototypically well-suitable material for the presented kMC-model and can be properly simulated with it and (iii) only electron transport over or through the barrier or via trap-tunneling is relevant here.

Chapter 6

Results of nTP-experiments and kMC-simulations

Having understood the working principle of nTP and related processes as well as the kMC-algorithm and the model, various nTP-fabrication processes could be performed and with the kMC-tool being set up correctly, the actual kMC-simulations were done in order to analyse fabricated MOS and MOM structures making use of titanium oxide. This way the potential for improvement of both the nTP-fabrication and the kMC-model could be shown. The focus of our investigation are nanometer-thin TiO_2-layers both experimentally based on the methods presented in chapter 3 and theoretically by the simulator outlined in chapters 4 and 5. For reasons of comparisons and due to their experimental importance for new devices also experimentally studied nm-thin AlO_x layers were simulated. So, basically four tasks were performed which will be shortly introduced in the specific section. The remainder of this chapter is organized as follows:

1. First, two experimental series are shown and briefly discussed, i.e. results of stamp recycling in section 6.1.1 and reliable transfer of different pillars and lines morphologies in section 6.1.2. These experiments demonstrate the potential of the nTP protocol, detailed in section 3.4.3, in terms of process advancements and morphological capabilities to a bigger extent and prepare the basis for the more specific next point.

2. The fabrication of nm-sized MS and MOS-structures consisting of Au/Ti/(TiO_x)-stacks transferred on Si by nTP and μCP and the investigation of their morphological and electrical characteristics supported by kMC-simulations of TiO_x is performed. This was to demonstrate the reliable nTP-fabrication of actual electronically functioning devices and the applicability of the kMC-model at hand for produced MS or MOS-contacts.

3. The simulation of fits to jV-characteristics of anatase TiO_2-samples which was one of the core and most elaborate tasks of this work. Intentionally, samples from

literature were chosen being fabricated by different physical and chemical methods. Here the emphasis was put on deriving statements on the nature of the dominant defects in anatase from the trap-assisted processes in the kMC-model in dependence of the chemical and physical treatments of the specific sample. This is motivated by the on-going heavy debate in literature on the defects in TiO_2 and the capability of our kMC-trap model to study them microscopically. Finally, implications on electronic processes and recommendations on the fabrication technique with respect to electronic and catalytic applications are derived from the kMC-results. This core task had to be performed most accurately and required an individually adapted, thorough parameterization of the model - in particular with respect to defect levels in TiO_2, which precedes the presentation of the results.

4. The last result was the adaption of the parameterization, similar as for number 3, to the simulation of AlO_x, which is an important oxide material, studied more frequently in experiments. Starting with a short introduction into its applications, also here an accurate review on possible defect levels and a parameterization as for TiO_2 is provided. Validating the kMC-model once more by proper fits to experimentally measured jV-curves, the multiple parameter space could be studied by the kMC-simulations and implications for electronic properties of such AlO_x layers under certain conditions are derived. This might serve as a reference for future experimental investigation on this oxide.

6.1 Preparatory nTP-experiments

In the framework of this thesis preparatory nTP-experiments were necessary to improve the handling of the process. First experiments presents here dealt with overcoming issues regarding stamp cleaning and recycling, while the second transfer experiments prove the functionality of the nTP-concept in terms of different structures and confirm the reliability and fidelity of the transfer results.

6.1.1 Recycling of nTP-stamps by Cleaning in Acidic Solutions

Because the production of nano-patterned silicon master stamps is time- and cost-intensive and one single stamp can only be used for one transfer print and is wasted afterwards, possibilties were considered to solve this problem. A first option is to make replicas of the stamps made from another material, e.g. hPDMS or hybrid polymer, which needs a careful control and understanding of the prodution process. A second, directer option is to develop an appropriate chemical and/or physical cleaning for the stamps, referring to "stamp recycling". This was the topic of the Bachelor's thesis by Robert Morasch, conducted as a part of this work. The quality of the developed cleaning processes were monitored mainly by SEM imaging of the samples.
Different acidic solutions were tested to etch off the initially evaporated Au and Ti remaining on the stamp after the transfer. Being known to etch off Au (but also the Si

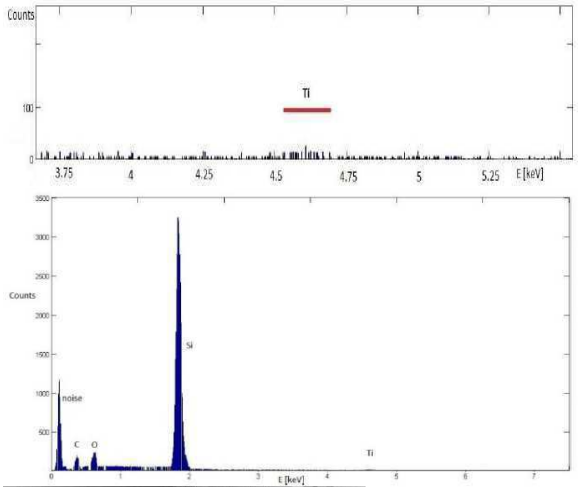

(a) *EDX spectroscopy on used Si stamp after aqua regia cleaning. No Au peaks, but Si and Ti peaks are observed. The energy region of the latter ones are magnified in the inset showing that there is still Ti on the stamp. Its amount is small but non-negligible because it is agglomerated on the surface of the stamp.*

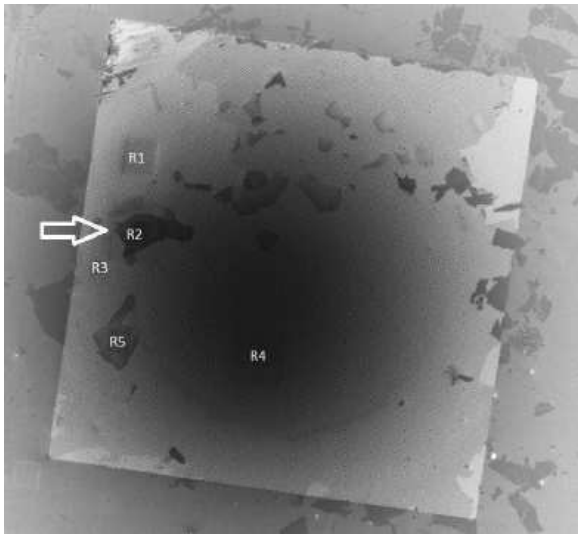

(b) *SEM image of the used stamp characterized by EDX under (a). One can see the strong contaminations still present after aqua regia cleaning alone. The spots marked by white letters were characterized and the one depicted in (a) is indicated by the white arrow.*

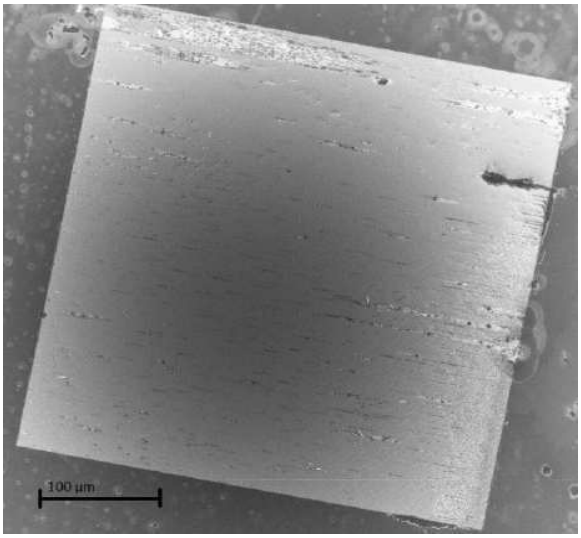

(c) *A typical stamp contaminated by metals and organic substances right after the transfer, before cleaning.*

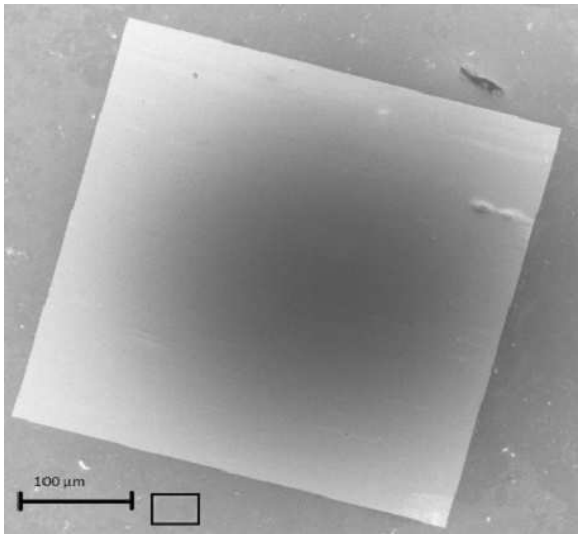

(d) *The same stamp as in (c) after treating it 5 s with HF, 2 x 5 min with aqua regia in an ultrasonic bath and with HF for 5 s again. Nearly all Au and Ti could be removed.*

Figure 6.1: *Summary of the results on the stamp cleaning processes in acid solutions.[203]*

substrate) efficiently, aqua regia was tested amongst others. Finally, a solution of hy-

drofluoric acid and aqua regia turned out to clean the stamps most properly. A brief summary of the results before and after the optimal treatment is shown in Fig. 6.1.
Firstly, the most important findings were energy diffraction x-ray spectroscopy (EDX) measurements, such as in Fig. 6.1a. In EDX the intensity of secondary roentgen quants is measured over energy. The peaks correspond to the characteristic Bremsstrahlung of certain elements, thus indicating the composition of chemical species on the sample surface. The measurements were performed on "used" (post-transfer) stamps that were already cleaned only by a first aqua regia treatment, such as the one shown in Fig. 6.1b. In the complete spectrum, depicted in Fig. 6.1a, there are no peaks for Au, expected at 9.7 keV. But as seen in the magnified region between 3.5 keV and 5.6 keV energy in Fig. 6.1a manifested by the peak at 4.5 keV to 4.6 keV, there are also still non-negligible traces of Ti present which could not be removed by aqua regia only. Hence the remaining impurities on the surface had to be attributed to Ti and a method was developed to etch not only Au, but also specifically Ti, while not degrading the Si stamp. This could be achieved successfully by essentially using also hydro fluoric (HF) acid but keeping etching times very short not to attack the Si. Therefore, the Ti-etch rate of the solution was determined to be 14.6 nm/s. A welcome coincidence was the low amount of Ti on the stamp, usually only about 5 nm to 10 nm. Hence etching times of 3 s or less were sufficient to remove the remaining Ti while not having attacked the Si structures yet. Results before and after such a treatment can be found in Fig. 6.1c and 6.1d. It shows that after the transfer the stamp is actually wasted without any treatment. After the combined AR-HF treatment the stamp was almost completely cleaned and the fidelity of the structures seemed to have suffered only at certain spots. This could stem from the mechanical stress applied in the transfer process which is hardly avoidable to a certain extent. Though further optimization of this process are desired, this is already an interesting result showing the potential of this recycling process and suggesting to investigate it into further detail e.g. by varying the application of the ultrasonic bath in terms of power and time. Especially damages to the small surfaces of pillars by the HF cleaning are more severe than for extended lines, while a even shorter dip into HF is sufficient to remove the Ti. But etching times are still to be improved. In any case stamps must be cleaned directly after the transfer to minimize other contaminations and must be characterized directly after such cleaning steps.

6.1.2 Structures Fabricated by Si-Stamps

By the optimized nTP process outlined in detail in section 3.4.3 various nanostructures were produced. Selected, exemplary results of these nTP tests are depicted in Fig. 6.2. These results demonstrate the vast versatility and broad applicability of the nTP approach. The transferred feature sizes range from 50 nm to 100 nm for pillars and from 50 nm to 300 nm for lines according to the stamps enlisted in 3.4.2.
Although the shown hard-to-hard transfer printing technique was only used for stamps structured with nm-pillars or lines with Au/Ti/TiO_x stacks on top, transferred onto Si or Si/SiO_2, it is supposed to be applicable to various other kinds of stamp structures

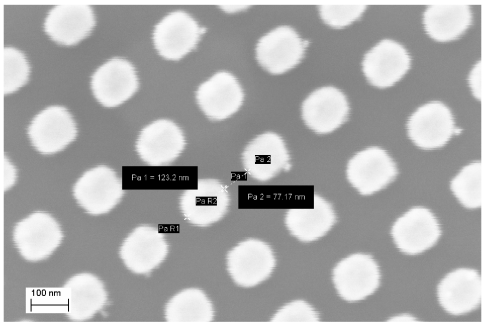

(a) *100 nm x 75 nm pillars-transfer at maximum magnification.*

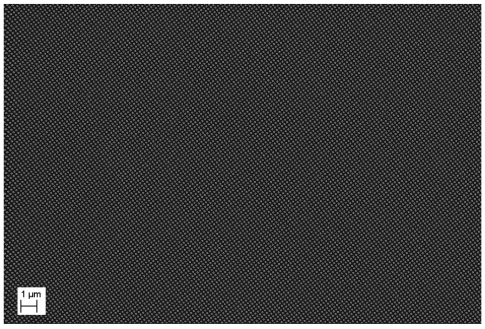

(b) *100 nm x 75 nm pillars-transfer on large scale (3860 x magnification).*

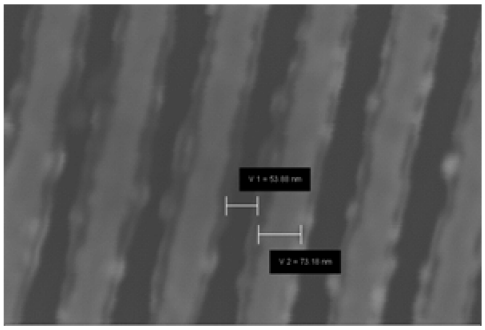

(c) *75 nm x 50 nm lines-transfer maximum magnification.*

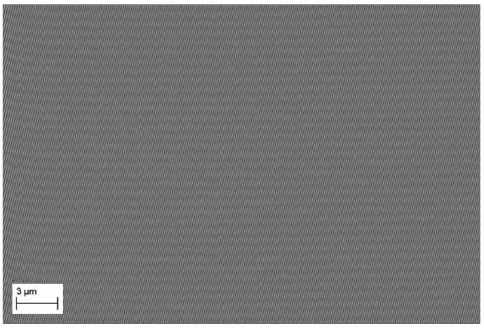

(d) *75 nm x 50 nm lines-transfer over ∼27 µm x 33µm (3370x magnification).*

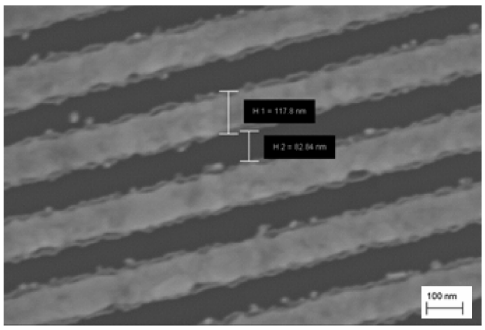

(e) *100 nm x 100 nm lines-transfer maximum magnification.*

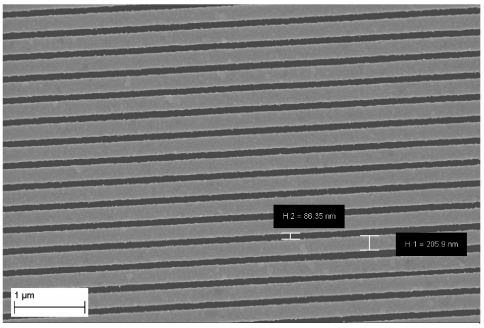

(f) *200 nm x 100 nm lines-transfer maximum magnification.*

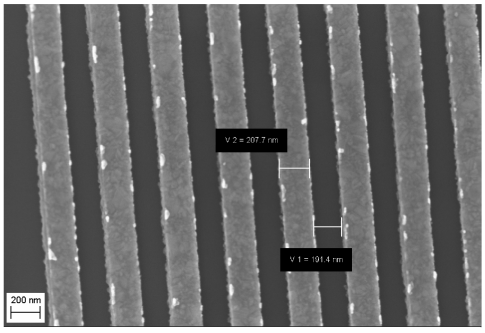

(g) *200 nm x 200 nm lines-transfer maximum magnification.*

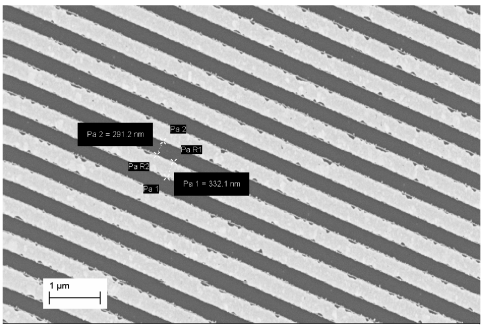

(h) *300 nm x 300 nm lines-transfer maximum magnification.*

Figure 6.2: *Exemplary SEM images of nTP-samples, remarkable quality for all structures.*

or evaporated metal stacks and has been demonstrated already e.g. for Au/Al/AlO_x, AuPd or Au/Cr.[85] This shows that the nTP approach is not only versatile in terms of possible morphologies but also material systems to be transferred. Besides it is very fast and cost-efficient, it does not need any organic adhesion promoters or flexible buffer layers. Also chemical post-processing is not necessary. One major drawback is the non-reusability of the elaborately produced master template. Being able to preserve them was the subtask to be tackled by a proper cleaning process of the stamps, as explained in section 6.1.1. Further results and investigations of the morphological and electrical properties of the structures resulting from the described nTP process with the goal to optimize it in terms of device applications is presented in section 6.2.

6.2 nTP and μCP-structures with Plasma-Grown TiO_x-layers

Functional metallic oxides, especially the prototypical titanium oxides, turned out to be very compatible with the nTP-process, as they naturally occur e.g. via the oxidation of Ti adhesion layers. Nevertheless, the capabilities of nTP to maintain or even improve the electronic properties of printed structures comprising TiO_x-layers have rarely been studied yet, in particular not with respect to the aforementioned applications of TiO_2 detailed in the introduction, section 1, and the state-of-the-arts chapter on it, section 2.2.1. With respect to nTP, in particular, former characterizations of transfer-printed MS or MOS-structures were both not specifc to nm-thin oxide formation and mostly fabricated by microscale-Contact-Printing (μCP) [18, 22]. So in contrast to the transfer-printed, ordered nanopillars studied here, today's literature refers rather to non-nanoscale or only unstructured material systems, such as Au nanoislands on TiO_2 surfaces.[23, 24] In the subsequent parts, highly-ordered, sub-70nm-junctions of Au/Ti on p^+Si, comprising potentially a TiO_x-layer and thus resembling MOS-diodes, were efficiently and reliably fabricated by nano-transfer-printing (nTP) over large areas and their functionality was investigated with respect to their application as MOS-devices. Firstly, we used a temperature-enhanced nTP process and integrated the plasma-oxidation of a nm-thin titanium film being e-beam evaporated directly on the stamp before the printing step without affecting the p^+-Si substrate. Secondly, morphological investigations (SEM) of the nanostructures confirm the reliable transfer of Au/Ti/(TiO_x)-pillars of 50 nm, 75 nm and 100 nm size of superior quality on p^+-Si by our transfer protocol. Thirdly, the fabricated nano devices are also characterized electrically by c-AFM. Fourth, the results are compared to probe station measurements on identically processed, i.e. transfer-printed, μm-MOS-structures including a systematic investigation of the oxide formation. The jV-characteristics of such MS or MOS-junctions demonstrate the electrical functionality as plasma-grown tunneling oxides and the effectivity of the transfer-printing process for their large-scale fabrication. Next, our findings are supported by fits to the jV-curves of the plasma-grown titanium oxide by kinetic Monte Carlo (kMC) simulations. These fits allowed to determine dominant conduction mechanisms and other material parameters of the oxides and, in particular, a calibration of the thickness in dependence of applied

plasma time and power. Finally, also a relative dielectric permittivity of 13 was found for such plasma-grown TiO_x-layers, which agrees with the one of TiO_2.

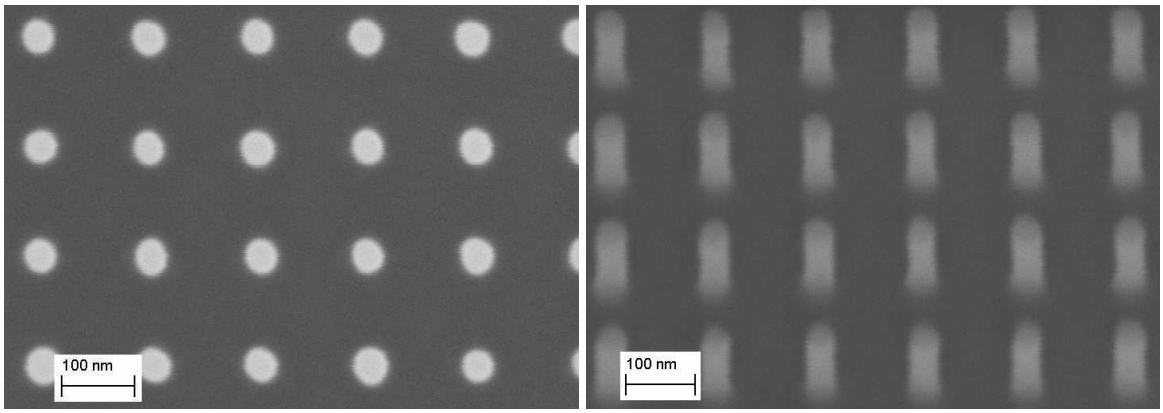

(a) *Top view of the 50 x 100 Si stamp.*

(b) *Tilted view of the 50 x 100 Si stamp, tilting angle 40°.*

Figure 6.3: *SEM image of the 50 nm x 100 nm Si stamp used in the nTP process previous to the transfer.*

6.2.1 nTP - Fabrication of μm-Pads and nm-Pillars

The MS and MOS-junctions investigated in this section were all fabricated in principle by the nTP-protocol described already in section 3.4 after [21, 56, 57, 73, 85, 205] The basic fabrication steps of the nTP-process are depicted in Fig. 3.8. Compared to formerly reported nTP-protocols, the steps in Fig. 3.8c-3.8f had to be slightly adapted to the transfer of Au/Ti/TiO_x-stacks. The applied nTP-process started with a silicon stamp produced by IMS CHIPS, Stuttgart, Germany. The surface of the stamp was structured with nm-scale pillars by an e-beam lithography process and a subsequent dry etching process, and cut into 1 cm x 1 cm pieces with an active area of about 300 μm x 300 μm. Two scanning electron microscopy (SEM) images of stamp (3) are given in Fig. 6.3, once from the top, Fig. 6.3a, and a tilted one, Fig. 6.3b, to check their quality previous to the transfer. The images confirmed the manufacturer's specifications of the pillars which were 80 nm vertical height, 50 nm diameter with a spacing of 100 nm between each pillar. Three Si-stamps with nm-sized structures were used for the transfer experiments:

(1) pillars with 100 nm diameter and 100 nm spacing ("100 nm x 100 nm" - stamps)

(2) pillars with 75 nm diameter and 75 nm spacing ("75 nm x 75 nm" - stamps)

(3) pillars with 50 nm diameter and 100 nm spacing ("50 nm x 100 nm" - stamps)

The transfer experiments, summarized in Fig. 3.8, were done under clean room conditions. The stamps were first covered by an alkylsilane self-assembled-monolayer (SAM),

as explained in [56, 57, 205]. Material stacks consisted of a first layer of 15-20 nm Au and, secondly, a 5 nm thin Ti layer, so ∼20-25 nm in total, that were deposited on each of the stamps by e-beam evaporation (in a Leybold L 560 evaporator system) under a pressure of 10^{-7} mbar.[57] Then the second metal layer of Ti on top of the stamps was supposed to be plasma-oxidized by an oxygen-plasma treatment in a barrel asher. The plasma time to form the titanium oxide was set to 120 s at 200 W power and 30 mTorr O-partial pressure for the nm-scale samples. Also μm-samples were produced, for which the plasma work was varied as outlined in the next paragraph. Note that the plasma activation of the stamp is a necessary step in several nTP protocols.[18, 21, 22, 54, 56, 57, 73, 85, 205] * Subsequent to the delamination-promoting SAM-step and plasma-step, the nTP-step was performed in a NIL 2.5 Nanoimprinter (Obducat) by a (5-step-)transfer-protocol. First, as step 1, the evaporated stamps were placed on previously cleaned and plasma-activated p^+-Si substrate (resistivity: <0.01 Ωcm, doping: $\sim 10^{18}$cm^{-3}) resembling a substrate-stamp-stack as depicted in Fig. 3.8e. Deviating slightly from previous transfer protocols [21, 56, 85] in step 2 only the pressure is raised pneumatically from p = 5 bar to p = 30 bar at once, while the temperature was kept at room temperature, for a total time of t = 60 s. In Step 3 the stamp-substrate stack is heated up to a temperature T = 200 C at constant imprint pressure of p = 30 bar for a time t = 170 s and the temperature is hold constant then for t = 220 s, still at the same constant pressure. Then, in step 4, the pressure was removed immediately. Finally, with no cooling-down-phase, in step 5 the stack was taken out of the imprinter and the stamp was carefully and vertically demolded from the substrate. Thereby optimal results for nTP pillar structures were achieved as analyzed in section 6.2.2. Due to the separate, central heating step, the applied nTP protocol is referred to as temperature-enhanced nTP.[56, 85]
Two additional sets, "A" and "B", of microscale MOS-junctions were fabricated by nearly the same nTP protocol in order to compare them to the nanoscale samples, to investigate effects of the plasma-oxidation step into more detail and prove the electrical applicability and functionality of the printed structures over larger scales. The protocol basically differed in the stamp production where first a silicon master stamp with 200 μm x 200 μm squares on top was produced by standard photolithography and then polymer replicas of this stamp were made from UV-curable OrmoStamp resin. The full fabrication process of exactly these polymer stamps as well as the reliability and fidelity of the transfer results is reported by Nagel et al. [61]. Structures transferred from such polymer stamps have the same quality as those from corresponding silicon stamps. The μm-stamps were evaporated with 15 nm Au and 5 nm Ti on top (sets "A"), as well as with 10 nm Au and 10 nm Ti on top (sets "B") as depicted in Fig. 3.8b and 3.8c. Then the O_2-plasma was applied directly to the material stack on the stamp, like for the nm-stamps as depicted in Fig. 3.8d, yet using seven different plasma works for each of the two sets, as

*Originally, an oxygen plasma-treatment with 30 s time was introduced into the nTP process to break up hydroxyl groups that terminate the surface of the Ti adhesion layer on the stamp by O- ions. However, e.g. for Ti oxide thicknesses of ∼3 nm[18] and ∼2.2 nm[21] have been reported. Also for Al as top metal layer a ∼3.6 nm thick, compact dielectric layer of AlO_x created by a plasma-oxidation of 30 s has already been shown several times.[73, 205, 251]

given in Table 6.1. Performing transfer-prints onto identical p^+Si substrates as for the nm-samples before (resistivity: <0.01 Ωcm, doping: $\sim 10^{18}cm^{-3}$), these two stamp sets (5 nm Ti, set "A", or 10 nm Ti, set "B") with seven plasma times resulted into the 14 samples, A1-A7 and B1-B7, with Au/Ti/TiO_x/p^+Si junctions, yet with μm-dimensions like on the master stamp, i.e. 200 μm x 200 μm pads. Finally, note that even on the polymer stamps with the μm-structures it was possible to perform long plasma-oxidation processes of the evaporated Ti of up to 20 min (1200s) plasma time at 600 W power without degrading the polymer stamps or the results of the transfers.

Sample Name	Evap. Ti [nm]	Plasma power[W]	Plasma time [s]	$p(O_2)$ [mbar]
A1	5	200	30	30
A2	5	200	120	30
A3	5	200	1200	30
A4	5	600	30	30
A5	5	600	120	30
A6	5	600	600	30
A7	5	600	1200	30
B1	10	200	30	30
B2	10	200	120	30
B3	10	200	1200	30
B4	10	600	30	30
B5	10	600	120	30
B6	10	600	600	30
B7	10	600	1200	30

Table 6.1: *Compilation of fabricated μm-pad samples.*

6.2.2 Topological Characterizations of the nTP-structures by SEM

First, scanning electron microscopy (SEM) images of the total nTP area were taken with a Zeiss NVision40. The yield is defined as the entire area of transferred pillars (defined by structured area minus defective area) divided by the structured area on the stamp. The defective area is determined by the sum of the black squares which mark defective spots. The resulting images (Fig. 6.4) show yields above 95 % of the metal nanopillar transfer for all three stamp geometries. Such results can be achieved in about 80 % of the cases by the previously described fabrication process.[54, 61, 72] Explicitly, Fig. 6.4a and 6.4b show the result of Au/Ti/(TiO_x) pillars transferred by nTP on the p^+-Si substrate from a 100 nm x 100 nm stamp, Fig. 6.4c and 6.4d show results from a 75 nm x 75 nm stamp and Fig. 6.4e and 6.4f show results from a 50 nm x 100 nm stamp. Obviously, the structures were transferred successfully over the entire structured stamp area of 300 μm x 300 μm, see Fig. 6.4a, 6.4c and 6.4e providing a slightly morphed, but also disc-shaped

transferprint of the nanopillars from the master template. Fig. 6.4b, 6.4d and 6.4f are images over high scales at which the transferred structures from the three stamps can still be recognized. They demonstrate the extremely high regularity and similarity of all pillars and only minimal defective spots. Comparing, for example, SEM images of the stamp with 50 nm diameter and 100 nm spacing (Fig. 6.3) with the corresponding ones of the transferred pillars (Fig. 6.4e, 6.4f), in particular at maximum magnification (inset of Fig. 6.4f), we find only a morphological enlargement of the diameter accompanied by a reduction of the spacing. This observation is attributed to a conic growth of the deposited metal layers during the evaporation on the stamps. For each newly deposited metal layer the metal atoms also attach at the edge of a single pillar's top plateau, thereby increasing its diameter in all lateral directions. The ratio of the average growth in the lateral directions in relation to the vertical growth must be at least ∼1:2, but cannot be more than 1:1. This is in agreement with the measured thickness of the evaporated metal stacks of 25 ± 2 nm in our processes which would hypothetically result into a lateral increase of 12.5 nm to 25 nm. The diameters and spacings of the transferred pillars were determined to be 69 ± 5 nm at a distance of 81 ± 5 nm , 91 ± 5 nm at a distance of 68 ± 5 nm and 112 ± 5 nm at a distance of 89 ± 5 nm, corresponding to a lateral growth of the pillars by ∼19 nm, ∼16 nm and ∼12 nm for the 50 nm x 100 nm, 75 nm x 75 nm and 100 nm x 100 nm samples (see insets of Fig. 6.4b, 6.4d and 6.4f), which is in good agreement with the estimate from our simple, invoked growth picture. The height was also checked by complementary AFM images that confirmed these values. The insets of Fig. 6.4b, 6.4d and 6.4f taken at maximum magnification show that the shape of the transferred nanopillars is almost identical to the ones on the stamp, except for some irregularities at the edges that could also be caused by noise in the SEM setup and slightly irregular growth. Note that these deviations are negligible compared to the difference from the enlargement of the diameter of the pillars and the accompanied reduction of the spacing discussed above. In conclusion, these transfer experiments demonstrate that nanostructures down to 50 nm (giving sub-70-nm-structures) can be transfer-printed reliably from the stamps by nTP. Relative structural enlargements of about 12 %, 25 % and 32 % (100 nm, 75 nm and 50 nm diameter) were found in the lateral directions. Apparently, these values depend on the geometry of the structure. No considerable deteriorations from nTP could be found. Both the quality of single structures as well as the regularity of the overall nanostructured array, being free of shear, did not suffer considerably during the nanotransfer and defective areas were rare which results into a high total yield. Phenomenologically, such improved and reliable nano transfers have already been explained by the plasma treatment and the temperature-enhancement, as done in reference [72]. Our more detailed morphological investigation performed here is a further indicator for the negligible impacts of the temperature-enhanced nTP process on the quality of the nm-structures and hence a precondition for their further integration and usage in electronic devices.

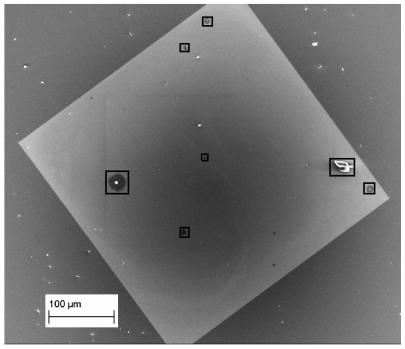

(a) *Morphology of 100 nm x 100 nm nTP-pillars, transfer yield ca. 98%.*

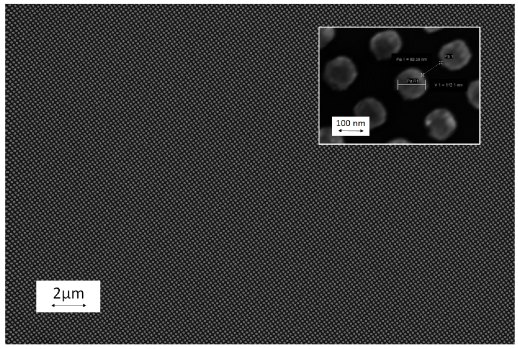

(b) *Zoomed in image of 100 x 100 pillars confirming good quality. The inset shows a lateral growth of* $\sim 12\pm5$*nm.*

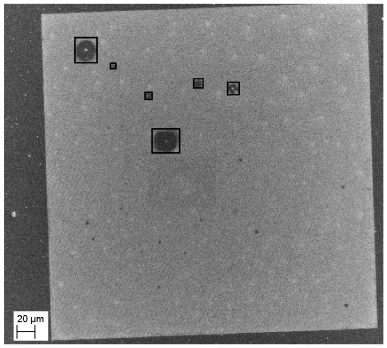

(c) *Morphology of 75 nm x 75 nm nTP-pillars, wide scale, transfer yield ca. 97%.*

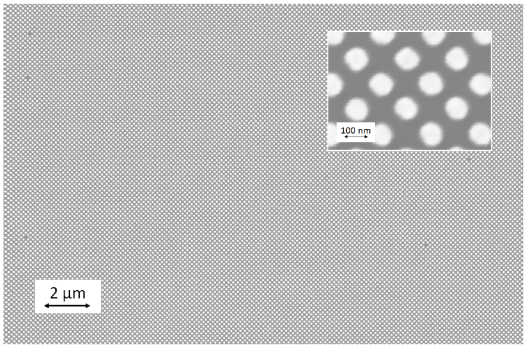

(d) *Zoomed in image of 75 x 75 pillars confirming good quality. The inset shows a lateral growth of* $\sim 16\pm5$*nm.*

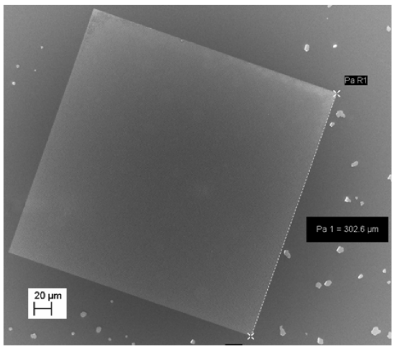

(e) *Morphology of 50 nm x 100 nm nTP-pillars, wide scale, transfer yield almost 100%.*

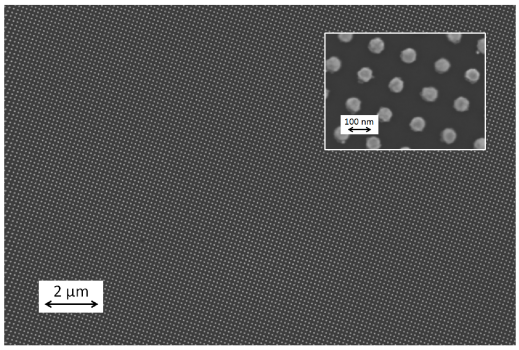

(f) *Zoomed in image of 50 x 100 pillars confirming good quality. The inset shows a lateral growth of* $\sim 19\pm5$*nm.*

Figure 6.4: *SEM images of nTP-samples with the nm-size Au-on-top-pads for the electrical investigation of the TiO_x formation via plasma oxidation. Images (a),(c),(e) show the morphology of the nTP-transfer results over the whole scale of the structured area on the stamps and demonstrate the transfer yields of over 95% from structured area with only very few defects. As approved by images (b),(d),(f) for all structure sizes a remarkable quality over maximum areas could be achieved, from the biggest pillars of just 100 nm (a) down to the minimum diameter of 50 nm (e).The insets of (b),(d),(f) show the maximum magnifications possible with the SEM setup confirming the good quality once more with almost no deteriation of the structures as defined on the corresponding stamps. Blurring at the edges of the pillars is attributed to noise in the setup.*

6.2.3 c-AFM-Characterizations of nTP-Au/Ti/(TiO_x)/Si-pillars

Current Mapping by c-AFM of Au/Ti/(TiO_x)/Si-pillars

The c-AFM characterizations were performed with a conductive MFP-3D atomic force microscopy setup (Asylum Research, California) operated in contact mode with constant force (and electrical feedback) options switched on. This procedure is also referred to as "conductivity mapping" or “current mapping” [252], cf. section 3.5.3. During a low-speed scanning a current is driven through the Au/Ti/(TiO_x)-Si-top contacted structure and fed into the readout electronics. As sketched in the equivalent circuit given in Fig. 3.12, the top of the Si substrate is contacted by an Au-coated contact needle clamped tightly onto the sample to push through the natural SiO_2 layer and establish a Schottky contact as counter-electrode. This is, however, no current limiting contact, since the trapezoidal Schottky-tunneling barrier here should be very thin, if detectable at all. The counter-electrode was grounded and connected to the cantilever holder in the measurement head. A very short tip-sample distance (few $\AA$) resulting from a perpetual tip-pillar-contact allows for tunneling currents that close the current loop, as shown in Fig. 3.12. C-AFM measurements were performed with two kind of tips, mounted into the cantilever holder: Either a Pt/Ir (3/17) coated n^+-Si tip (PPP-EFM-10 from NANOSENSORS, resistivity 0.01-0.02 Ωcm, tip radius $\sim$30 nm, force constant 0.5 9.5 N/m) or a diamond coated p^+-Si tip (DCP 11 from NT-MDT, 5×10^{20}cm^{-3} Boron doping, tip height 10-15 μm, tip radius 35 nm, force constant 2.5-10.0 N/m) were used. The specific tip in perpetual contact with the Au-layer on a pillar manifests the repulsive regime of the tip-pillar-interaction force (see inset of Fig. 3.12). The set-point voltage was 1.5 V, the tip driving frequency was 154.2 Hz, the deflection was $\sim 20 - 30$ [a.u.], scanning speed 0.5 Hz and the imaging area was set to a value of $\sim$5 μm x 5μm. Both with the diamond coated p^+-Si tip (Fig. 6.5a) and with the Pt/Ti coated n^+-Si tip (Fig. 6.5d) we were able to create conductivity profiles of typical sample regions by the current through the Au/Ti/(TiO_x)/p^+Si-contact. By the diamond coated p^+-Si tip (DCP 11 from NT-MDT) also height profiles measured by the piezo-voltage corresponding to the cantilever deflection and shown in Fig. 6.5b and tapping mode images depicted in Fig. 6.5c were taken to cross-check the topological results from the actual c-AFM images.
Comparing the images in Fig. 6.5a-6.5d one can defer the following statements:

(i) Diamond coated p^+-Si tips provided a more homogeneous conductivity image with better contrast, higher resolution and higher currents for the pillars compared to such ones obtained by the Pt/Ti-coated n^+-Si tips, see Fig. 6.5a and 6.5d. For the latter the contrast of conductive pillars in front of the background of less-conductive spacings and defects is worse. Some less conductive pillars are hardly visible while better conductive pillars are overpronounced due to a high current flow. This implies a bad contact of this kind of Pt/Ir coated-tips to the Au top of the stacks. Hence the diamond coated p^+-Si tips are recommended for the specific Au/Ti/(TiO_x)/p^+Si-contacts investigated here. We attribute this to the matching doping of both the p^+-Si tip and p^+-Si substrate to ensure a low contact

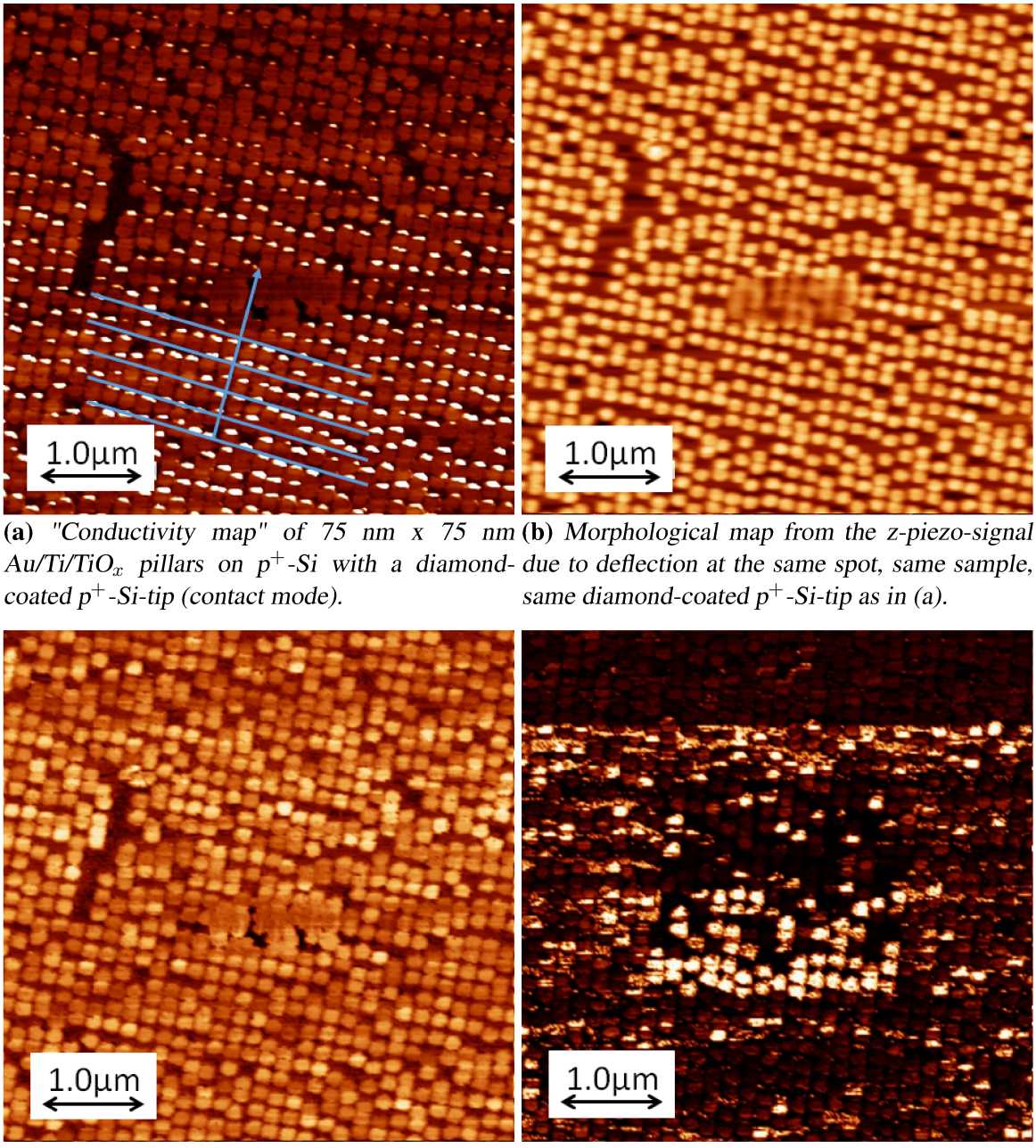

(a) *"Conductivity map" of 75 nm x 75 nm Au/Ti/TiO_x pillars on p^+-Si with a diamond-coated p^+-Si-tip (contact mode).*

(b) *Morphological map from the z-piezo-signal due to deflection at the same spot, same sample, same diamond-coated p^+-Si-tip as in (a).*

(c) *Tapping mode image from cantilever deflection at the same spot, same sample, same diamond-coated p^+-Si-tip as in (a) and (b).*

(d) *"Conductivity map" of 75 nm x 75 nm Au/Ti/TiO_x pillars on p^+-Si taken with a Pt/Ir-coated n^+ Si-tip, contact mode, different spot.*

Figure 6.5: *(a) "Conductivity mapping" by c-AFM of Au/Ti/TiO_x junctions (75 nm x 75 nm pillars) in contact mode with a diamond coated Si-tip taken by current measurements. For a further discussion see text and Fig. 6.6. (b) Deflection measurements of Au/Ti/TiO_x junctions in contact mode taken with the same tip by the z-piezo-voltage signal. (c) Tapping mode images taken with the same tip as in (a) and (b) for reasons of comparison. (d) "Conductivity mapping" like in (a) but with a Pt/Ir coated n^+ Si-tip at a different sample spot, worse contrast with this tip, cf. text.*

resistivity and an ideal contact, as well as to the force constant of ∼5-20 N/m for the diamond-coated tips, which provides the best combination of low force constants needed for contact-mode-AFM[209] with a higher mechanical strength and robustness of diamond compared to the Pt/Ti-n^+-Si-tips.

(ii) The electrical functionality of the transferred diodes, potentially MS or MOS ones, in "current mode" on the extended surface can be demonstrated on large-scale by c-AFM. By defective sites and the spacings between pillars one can see that only the pillars are electrically conductive. Currents are higher at the edges (bright spots within a pillar) and for parallel rows of pillars (marked blue). Thus 3D-current maps are useful for micro- and nano-scale characterizations of such nTP-structures. As one would expect, in contrast to the conductive pillars, the sites without pillars resembling a direct tip-substrate contact turned out to be less conductive. Moreover, the high similarity of the tapping mode images measured from the cantilever deflection in Fig. 6.5c as compared to the other three contact mode images proves the correctness of the morphology from c-AFM characterizations and confirms the reliability of these measurements.

(iii) Some pillars conduct more current than others in the images. Indicated by the blue lines in Fig. 6.5a, or even better visible by the 3D-current image Fig. 6.6a, one can see a systematic decrease of the current densities in one certain direction, perpendicular to rows of pillars which show a similar conductivity, i.e. current density. As the current decreases continuously from row to row, the decrease is most likely not simply random, but systematic. It could be attributed to nm-scale changes in the oxide thickness over μm-scale areas on the surface.

(iv) The current density through single nanopillars fluctuates also from one single pillar to the next, as in the 3D-current-map 6.6a. These fluctuations could be attributed to the number and positions of defects in an oxide layer under single pillars which fluctuates statistically from one pillar to the next.

(v) The current at the edges of the transferred pillars is remarkably larger (by a factor of ∼10). This indicates a better contact at the edge of a pillar. One explanation would be that during the pressure-assisted transfer of the pillars, higher mechanical pressure is applied at the edges, hence the underlying oxide is quenched stronger at the edges than at the center of a pillar. This results into a thinner barrier or possibly even a cracking of the oxide accompanied by better conducting regions under the edges of a pillar. This observation emphasizes the need for further characterizations of the quality of nTP-samples and specifically the TiO_x before using the structures for devices.

The assumption made in (iii) can be tested and supported by kMC-simulations modelling such a system. The employed kMC-model and its parametrization for TiO_x is explained in chapter 5 and also in [189]. Note that the presumable reason for the pillar-to-pillar

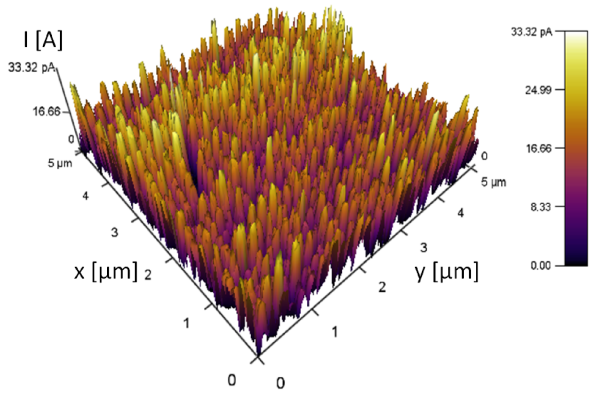

(a) *3D depiction of the c-AFM current through the 75 nm-pillars from Fig. 6.5a at 1.5 V set point voltage measured in contact mode. One can see an inhomogeneous distribution of the currents with a systematic continuous decrease of it. For details see text.*

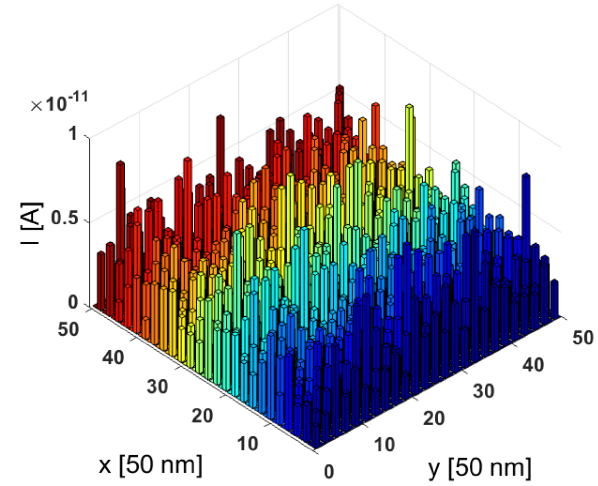

(b) *kMC-simulation of Au/Ti/TiO_x/Si pillars (size 50 nm x 50 nm) with a random defect distribution in a homogeneously-5 nm-thin TiO_x layer.*

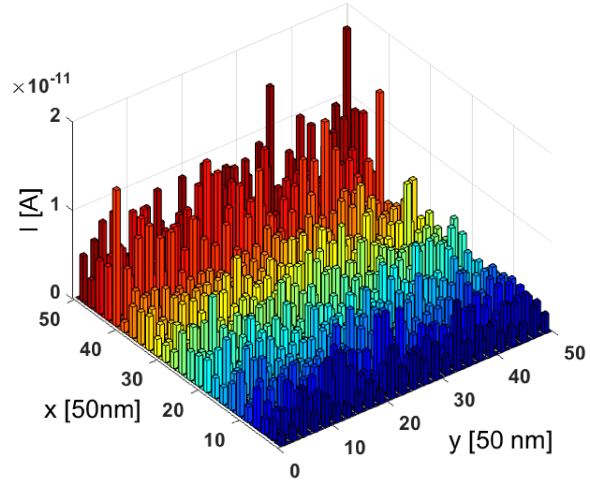

(c) *kMC-simulation with same model parameters as in (b) except for the five (red) rows of 25 pillars in the back of the image having a 4 nm thin TiO_x layer defined in the simulation.*

Figure 6.6: *(a) 3D-c-AFM current images measured for 75 nm-pillars. One can see an inhomogeneous distribution of the currents with a systemetatic, continuous decrease going perpendicular to the parallel rows of pillars with a higher current in the back of the image to regions of pillars conducting less current. As described in the text this observation is assumed to stem from an inhomogeneously distributed oxide thicknesses. (b) 3D-depiction of current images simulated by kMC for slightly smaller, 50 nm-pillars using a the same set point voltage as in the measurements of 1.5 V and (c) kMC-simulation of the same system with same parameters except for the 5 rows of pillars in the back of the 3D-image where a step from a 5-nm to a 4-nm-thin TiO_x oxide layer was introduced.*

fluctuations in the current, as presented in (iv), cannot be tested without knowing the exact spatial defect distribution below the certain pillars. This spatial distribution is impossible to determine by common experimental methods. Without such methods, results of kMC-simulations with a certain defect distribution would be always ambiguous and could never prove that the defects are indeed responsible for the current. Concerning the hypothesis from observation (iii) the situation is different: The simulations of such fluctuations in the oxide thickness is exactly what the kMC-tool is designed for. Hence, the system was parameterized by fixing all values to typical parameters of TiO_x and after further fine-tuning the average current through a pillar was about ∼10 pA for the experimental set point voltage of 1.5 V. This was the case for the parameter set (see section 6.2.5 or chapter 5 for an explanation of the variables): $d = 5$ nm , $\phi_{B,l} = 0.7$ eV, $n_D = 5 \times 10^{18}\text{cm}^{-3}$, $E_D = 0.5$ eV, $m^*_{ox} = 5$ m_0, $\epsilon_{opt,TiO_x} = 5.8$, $\phi_{B,r} = 0.4$ eV, $E_g = 3.2$ eV. Note that the defect energy E_D was set to the lowest value found in literature for oxygen defects in TiO_2,[171] so the maximum possible contribution from defect-related transport channels to the total current is expected. Thus the image depicted in Fig. 6.6b was obtained showing the simulated current through 25 x 25 Au/Ti/TiO_x pillars of 50 nm width and with 50 nm pitch having a constant oxide thickness of 5 nm underneath. To check, if the current fluctuations could be caused by a varying oxide thickness, estimated to change not by more than ±2 nm, the thickness was varied from 3 nm to 7 nm in 0.5 nm steps for the 5 rows in the back of Fig. 6.6c each consisting of 25 pillars, while the thickness for the other 20 rows in the front was kept at 5 nm as before. Comparing the plots of the two simulated situations in Fig. 6.6b and 6.6c, the increase in current by a factor of about 2 from the thicker to the thinner oxide region is well comparable to the corresponding regions in the experimentally measured image 6.6a. So, for the simulations in Fig. 6.6b and 6.6c, going from an oxide thickness of 5 nm to 4 nm, but only for those 5 rows with 25 pillars in the back of the 3D image, the current increase from the experimental measurements are adequately reproduced. The good agreement and easy-remodelling of such a non-trivial experimental situation demonstrates the capabilities of our kMC-simulation-tool and indicates that the oxide thickness is indeed responsible for the inhomogeneous current distribution with the systematic continuous decrease of the current perpendicular to certain parallel rows of pillars as in Fig. 6.5a. With all other system parameters kept constant, these kMC-results strongly indicate the validity of the assumption that the current fluctuations are caused by a fluctuating oxide thickness under the pillars. The next question to answer would be the origin of these thickness fluctuations which could originate from inhomogeneous variations in the oxide-creating plasma density during the plasma oxidation process of the sample in the barrel asher. In summary the c-AFM images confirm the reliability and quality of the sub-70-nm-nTP process, as the shape of the pillars in the current map agrees with the shape of the pillars on the stamp. Moreover, by such large-scale c-AFM-current maps the electrical functionality of the nanopillars for further electrical characterizations can be proven, in particular with respect to devices. Thus, c-AFM current mapping is supposed to be useful for rather uncomplicated, microscale electrical quality-control. Finally, they could

successfully be simulated by the kMC-model, which indicates the validity of the model and the ideal quality of the junctions.

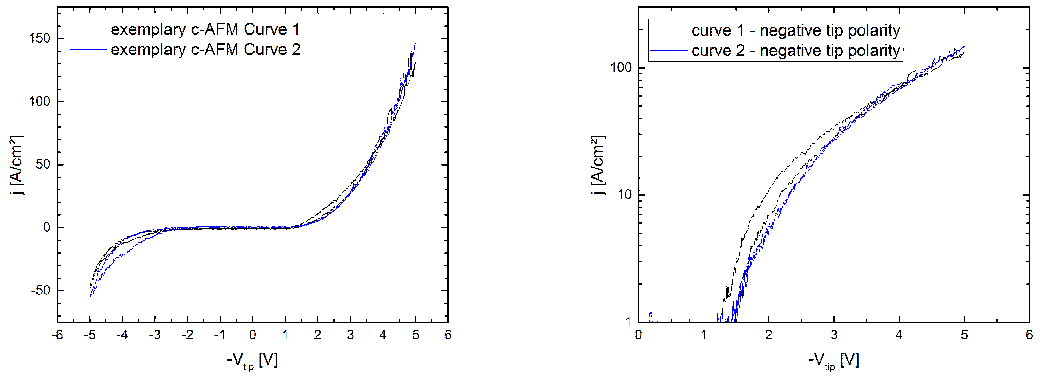

(a) *Two exemplary j-V-characteristics on linear scale for positive and negative bias applied at the tip. Note* $V = -V_{tip}$.

(b) *Positive branches of the j-V-curves from (a) on log-scale. Negative bias at tip,* $V_{tip} < 0$, *i.e. accumulation in* p^+*-Si.*

Figure 6.7: *Typical j-V-characteristics on linear (a) and log-scale (b) of 100 nm x 100 nm-sized Au-Ti-*TiO_x*-pillars transfer-printed on* p^+*-Si comprising a circa 5 nm thin plasma-grown* TiO_x *layer.*

jV-Characterizations by c-AFM of Au/Ti/(TiO_x)/Si-pillars

In a next step, single Au/Ti/(TiO_x)-pillars on the Si substrate were contacted directly by the diamond-coated p^+−Si-tips, an electrical bias between -5 V and +5 V was applied through a cyclic, triangle wave pattern and IV-characteristics were measured. For this sweeping range no dielectric breakdown was expected. Two typical jV-curves are shown in Fig. 6.7. They are corrected for an externally set current offset of ∼12.5 nA around zero bias and normalized to the typical pillar area (of $\sim 90^2/4\pi nm^2 = 6.4 \times 10^{-11} cm^{-2}$). In particular, we report a current sensitivity of less than ∼100 pA, compared to a theoretical value of 12.5 pA as reported by the manufacturer. This is more than acceptable considering the small pad size of <100 nm x 100 nm which emphasizes the occurrence of statistical fluctuations on the nanoscale, as the number of defects below one pad can range between ∼100-300 for a trap density of $10^{12} - 10^{13}$ cm^{-2}. Thus they influence transport heavily. The current range lies between ∼0.1 nA up to over 100 nA which is comparable to currents reported by c-AFM measurements on titania in literature[23, 24, 57, 209, 252, 253]. Particularly for resistive switches with TiO_x layers usually currents around ∼1000-10000 nA are reported for the ON state in c-AFM-measurements with (similar) tips of comparable size. [34] † The plotted, noteably

†Currents reported in other studies are much larger than the ones here mostly due to different contact pads with at least a factor of 100-10000 larger size.[254, 255, 256]

asymmetric jV-curves of the Au/Ti/(TiO_x) nanopillars on p^+-Si have the shape of MS-diodes or MOS ones, but just with a very thin tunneling dielectric and low CBO enabling direct tunneling of electrons. Thus we report the rectifying behaviour of our nanopillars with a rectifying ratio of about 5:1 (positive bias:negative bias). The barrier height extracted from the curves amounts to 0.75 eV, in agreement with typical literature values for comparable contacts.[14, 15, 257, 258] For reasons of comparison the positive polarity of the two curves is replotted again between 0 V and 5 V on log-scale showing resemblance to identical contacts using e-beam-evaporated and thermally annealed Ti, yet of larger thickness.[15] This electrical characterization indicates that the nTP-process formed Schottky-contacts on the p^+-Si-substrate consisting of Au/Ti pillars with an almost negligibly thin TiO_x-layer and a lateral diameter of ∼75-90 nm.

6.2.4 jV-Characterizations of μm-Pads with Plasma-Grown TiO_x

The 14 samples A1-A7 and B1-B7 fabricated as described in section 6.2.1 and summarized in Tab. 6.1, were electrically characterized in a low-noise Keithley K2460a probe station setup allowing for the simultaneous measurement of current and voltage characteristics following standard procedures. We used a liquid, metallic drop of InGa eutectic at the top contacting needle to ensure a soft contact to the thin Au layer which could have been destroyed easily otherwise. All represantive jV-curves in Fig. 6.8 are statistical averages of at least 15 to 23 curves. This allowed for the calculation of standard deviations of $< j >$ given as statistical log-scale errors in the plots in Fig. 6.8. They were all measured independently for negative bias at top contact, i.e. accumulation in the p^+-Si, on 200 μm x 200 μm-sized Au/Ti/TiO_x-pillars transferred on p^+-Si with nm-thin TiO_x-layers grown from 5 nm Ti (set "A") or 10 nm Ti (set "B") evaporated on the stamps and treated by different oxygen plasma strengths as given in Tab. 6.1
The thickness of the comprised, plasma-grown nm-thin TiO_x-layer is supposed to vary with the electrical work applied to the plasma. To quantify the thickness crudely, the current densities through samples of set A and B were compared to 200 μm x 200 μm-sized Au/Ti/TiO_x-pads on identical Si substrates defined by optical lithography with 3 nm, 7 nm and 10 nm thin TiO_x-layers which were e-beam evaporated directly from a precursor by a process like the one reported in [15]. The thickness of the e-beam-evaporated TiO_x-layer of such MOS-junctions could be controlled at a precision of ±2 nm by both the deposition rates in the evaporator and profilometer-measurements. ‡ Thus comparing these three curves ('3 nm' = 'empty squares', '7 nm = empty circles', '10 nm = empty diamonds') to the ones of the plasma-grown MOS-samples in Fig. 6.8 allows to estimate the oxide thickness of the latter sample roughly, giving an estimate of 3 nm $\lesssim d_{ox} \lesssim$ 20 nm for all plasma-grown samples, except for the 200 W, 30 s, 5 nm Ti sam-

‡For that purpose on flat Si-wafers only the TiO_x-layers, but no Au, was evaporated and the pads were also defined by optical lithography, as for the parallelly processed actual e-beam-samples with Au on top. The profilometer measurements were performed in a Bruker Dektak-XT Stylus Surface Profiling System scanning with a tip across the edge of a mere TiO_x pad. After levelling-out thus oxide thicknesses were determined as 3 ± 2 nm , $7nm \pm 2$ nm, $10nm \pm 2$ nm.

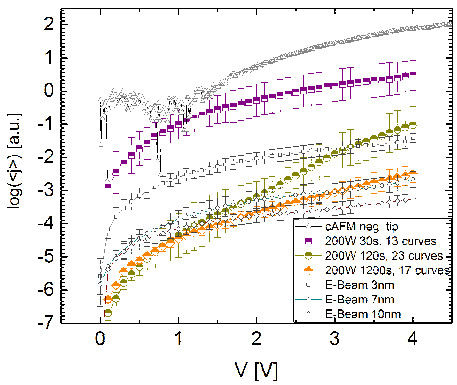

(a) *j-V-characteristics samples A1-A3 ('5 nm Ti=half-filled symbols', 200 W power) plus one cAFM (75 x 75 pillars, 5 nm Ti, plasma 200 W, e-beam-references, see legend. 120 s) plus 3 e-beam-references, see legend.*

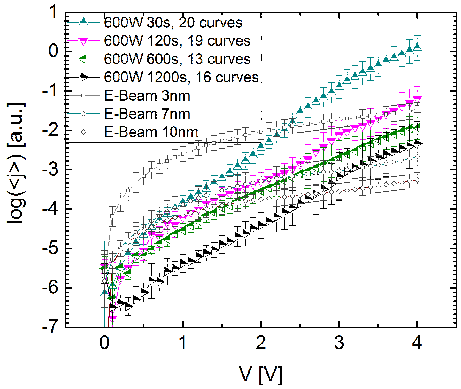

(b) *j-V-characteristics of samples A4-A7 ('5 nm Ti = half - filled symbols', 600 W power) plus 3 cAFM (75 x 75 pillars, 5 nm Ti, plasma 200 W, e-beam-references, see legend.*

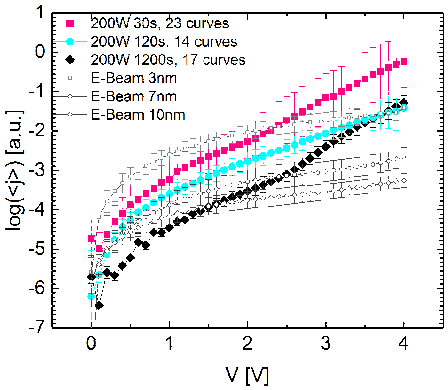

(c) *j-V-characteristics of samples B1-B3 ('10 nm Ti = full symbols', 200 W power) plus 3 e-beam-references, see legend.*

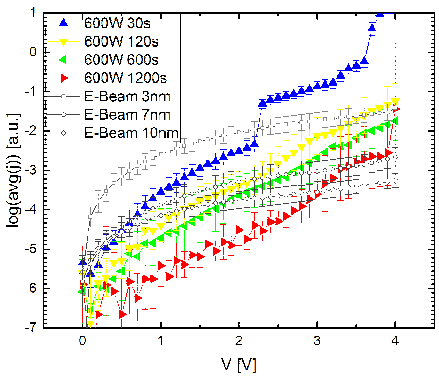

(d) *j-V-characteristics of samples B4-B7 ('10 nm Ti = full symbols', 600 W power) plus 3 e-beam-references, see legend.*

Figure 6.8: *μm-scale characterizations: Each curve is a statistical average of 15 to 23 j-V-curves on 200μm x 200μm-sized Au/Ti/TiO_x/p^+-Si junctions, plasma-treatments as given in Tab. 6.1, to study the relation between current densities, oxide thicknesses and plasma work. Plots of $< j >$ on log-scale with statistical errors. Negative bias at the top contact, i.e. accumulation in p^+-Si. j-V-curves of optically defined e-beam-Au/Ti/TiO_x-pads with oxide thicknesses of 3 nm (empty squares), 7 nm (empty circles), 10 nm (empty diamonds), measured by a Dektak-profilometer, given for comparison. Essentially, the insulating TiO_x increases by a stronger plasma. Further discussions in the text.*

ple, i.e. the violett curve in Fig. 6.8a, which conducts higher current densities than the 3-nm-thin e-beam reference oxides. The microscale MOS-junctions with 5 nm Ti evaporated and a lighter plasma treatment of 200 W power, 30 mTorr O_2 partial-pressure and

30 s oxidation time (violett squares), depicted in Fig. 6.8a, ought to be compared to the c-AFM curves measured on the 75 nm x 75 nm nTP-pillars (grey diamonds), as given in section 6.2.3. The characteristics of the nano- and microscale MOS-contacts agree well. They are produced by the same transfer-printing protocol, under same evaporation conditions and similar plasma-oxidation processes. Just the pad areas deviate by more than 3 orders of magnitude. This finding, which could be seen on any functioning pad and repeated by further identical transfer-prints, validates the electrical characteristics of the nanoscale diodes and proves the good scalability and reliability of the process ranging from more than 100-μm down to $\sim$100-nm pad sizes. Moreover this good agreement as well as supporting previous results of functioning devices from nTP[21, 72, 205, 251] propose that the electrical properties of Au/Ti/(TiO_x)/Si-contacts produced by nTP can be tested and characterized in an efficient manner regarding time and equipment by probe station measurements on the microscale instead of more elaborate nanoscale c-AFM-measurements. Deviating from the single 200 W, 30 s, 5 nm Ti curve A1 and the c-AFM curves in Fig. 6.8a, the average jV-characteristics obtained for all other samples in Fig. 6.8b, 6.8c and 6.8d are evidently lower. One observes - also within the uncertainties indicated by the error bars - a clear trend of decreasing current densities with increasing electrical work applied to the plasma via the radiofrequent microwave of the barrel asher. This indicates already the formation of an oxide and supports the intuitive idea that a stronger plasma treatment in terms of power, increases the insulating properties of the dielectric which are known to be essentially determined by its thickness, the tunneling barriers and defects. While defects in the oxide were not controllable by our process and are addressed briefly by kMC-simulations in section 6.2.5, we cannot comment further on this matter. However, the very similar current densities for most of the samples, except A1, as discussed below, indicate that their barrier heights are at least comparable, not to say almost identical which will be confirmed by kMC-simulations, too. Thus, the increasing oxide thickness is supposed to be responsible for the decreasing current densities with stronger plasma.
Next, comparing two specific curves with identical plasma times, e.g. A5 and B5, i.e. 600 W, 120 s plasma, for 5 nm and 10 nm thickness, no considerable difference in the magnitudes of the current densities is seen. Only the samples from set A, 5 nm, exhibited more stable currents than set B, 10 nm, e.g. with less fluctuations, as e.g. A7 (black right triangles) in Fig. 6.8b is smoother than B7 (red right triangles) in Fig. 6.8d. Set A also showed higher stability to dielectric breakdown, as e.g. A4 (dark cyan up triangles) in Fig. 6.8b did not break down in contrast to B4 (blue up triangles) in Fig. 6.8d which broke in all measurements on this sample. Since the magnitudes are always at least comparable for both 5 nm and 10 nm Ti evaporated on the stamps we assume to get closed Ti films on the stamps in both cases, which are both not completely oxidized. Otherwise the current densities should stop to decrease further for one of the plasma works applied here and for stronger ones, and at first for the 5 nm Ti, because it would need less work to be oxidized than samples with 10 nm Ti. This is not the case. Hence we suppose that both are gradually oxidized into an amorphous TiO_x and grow from building in oxygen

atoms, ideally by a factor of 3, i.e. 2 additional oxygen atoms per Ti atom, if TiO_2 was formed. In literature growth factors of about 2 are reported for Ti films annealed to TiO_2 [259], but an oxide thickness of up to 15 nm is possible in theory. It is reasonable to assume that the oxide thickness remained below this value, as seen from comparing the magnitudes of the lowest current densities through the plasma-grown samples to the ones of the 10 nm thick e-beam reference sample which are maximally a factor of 10 to 100 lower between 1 V and 3 V. Referring to the kMC-simulations with TiO_2-like parameters in Fig. 5.5a, section 5.1.3, confirmed by the accurate kMC-fits in the next section 6.2.5, the plasma-grown oxide of samples A7 and B7 having the strongest treatment, 1200s at 600 W, the thickness is estimated to be maximum 5 nm more than the 10 nm e-beam references nearby. From this comparison, we suppose A7 and B7 have a TiO_x-layer of about 13±2 nm thickness, i.e. ∼15 nm maximum.
Comparing the characteristics for different plasma times for either of the two thicknesses on its own, i.e. either 5 nm in Fig. 6.8a and 6.8b or 10 nm in Fig. 6.8c and 6.8d, one notes that a longer oxygen plasma reduces the current density by up to four to five oders of magnitude maximum for the 5 nm samples and by up to three orders of magnitude for the 10 nm samples for the whole voltage range (up to a potential dielectric break down, e.g. for sample B1). This indicates the gradual formation of the oxide, since, firstly, its thickness must show a dependence on the plasma treatment as visible in the images, and, secondly, it must show a breakdown behaviour, as seen for sample B1.
In particular the current density decreases the most with additional plasma work when coming from the weakest treatments, especially for 5 nm, Fig. 6.8a, with 200 W, 30 s plasma, i.e. A1, to 200 W, 120 s plasma, i.e. A2. This trend continues in a slowed down way going to higher plasma treatments at 600 W in Fig. 6.8b. Therefore the largest structural changes of this TiO_x are supposed to take place at the beginning of the plasma treatment. But also for B1 (magenta squares) to B2 (cyan circles) in Fig. 6.8c the decrease is evident. The current densities decrease even more with plasma time for a stronger plasma, as seen for B4 (blue up triangles) to B5 (yellow down triangles) in Fig. 6.8d, i.e. from 30 s to 120 s at 600 W, and from B6 (green left triangles) to B7 (red right triangles) in Fig. 6.8d, i.e. from 600 s to 1200 s at 600 W.
Thus, from the present discussion, samples A2-A7 and B1-B7 are readily considered to resemble MOS- and not MS-contacts, in opposite to sample A1. By the kMC-analysis in section 6.2.5 and a supplementary plotting analysis in section 6.2.7 the existence of the TiO_x layer will be scrutinized further and even quantified. .

6.2.5 kMC-Simulated jV-Characteristics of Au/Ti/TiO_x/p^+-Si-Junctions

Since a systematic quantification of the oxide thickness in dependence of the plasma work has not been done yet, it was investigated by the means of kMC-simulations, as explained in chapter 5, and a supplementary analysis plotting the jV-data in different ways in section 6.2.7. The kMC-model for this purpose was set up and discussed extensively in chapter 5. The kMC-framework after Gillespie [41] calculates and choses

sample	d (from Fit) [nm]	$\phi_{B,l}$ [eV]	n_D [cm^{-3}]	E_D [eV]	m^*_{ox} [m_0]	ϵ_{opt,TiO_x}	$\phi_{B,r}$ [eV]	E_g [eV]
B1	4.0	0.85	5.0×10^{18}	1.0	3.0	5.8	0.40	3.2
B2	4.5	0.85	5.0×10^{18}	1.0	3.0	5.8	0.40	3.2
B3	5.0	0.85	5.0×10^{18}	1.0	3.0	5.8	0.40	3.2
B4	6.6	0.85	5.0×10^{18}	1.0	3.0	5.8	0.40	3.2
B5	7.0	0.85	5.0×10^{18}	1.0	3.0	5.8	0.40	3.2
B6	8.0	0.85	5.0×10^{18}	1.0	3.0	5.8	0.40	3.2
B7	12	0.85	5.0×10^{18}	1.0	3.0	5.8	0.40	3.2

Table 6.2: *Overview on fixed or varied parameter values of the kMC-model for the 6 fitted curves of the 5 samples.*

transport processes thousands of times statistically and evaluates them to calculate the current density in the end using the following essential parameters: barrier to the cathode $\phi_{B,l}$, barrier to the anode $\phi_{B,r}$, trap energy E_D, trap density n_D, effective electron mass in the oxide m^*_{ox}, optical permittivity ϵ_{opt}, band gap E_g and, in particular, thickness d_{ox} of the oxide. By this compact model we could accomplish fits to all of the curves measured on the seven samples from set B, shown in Fig. 6.9 split up into Fig. 6.9a for samples with 200 W and Fig. 6.9b for the ones with 600 W plasma power. The fits agree well with the jV-curves up to a voltage of ~ 3 V which marks the transition to effects related to dielectric breakdown or a dynamically pronounced contribution of defect sites to transport which is not included in the kMC-model. Most remarkably, however, nearly all sensitive model parameters could be kept constant for all differently treated samples, i.e. the effective electron mass in the oxide $m^*_{ox} = 3\ m_0$, the injection barrier from the negatively biased Au/Ti cathode to TiO_x is $\phi_{B,l} = 0.85$ eV, the defect energy is $E_D \gtrsim 1.0$ eV at a typical defect density $n_D = 5\times10^{18}\text{cm}^{-3}$ for TiO_x.[248] This approves the high physical similarity of the plasma-TiO_x samples from series B that deviate from each other only by the oxide thickness d_{ox} in terms of kMC and it confirms the expectation that the plasma oxidizes the Ti surface uniformly. The deviation in the barrier height for sample B1 is low and could be attributed to a deviating interface quality with more defects. This is known to pin the Fermi-level lower in the bandgap for a Ti/TiO_x-contact. The chosen material parameters to model TiO_x by kMC-simulations as summarized in Tab. 6.2 are also in good agreement with theoretical and experimental material parameters found in literature. The bandgap $E_g = 3.2$ eV and the optical dielectric constant $\epsilon_{opt,TiO_x} = 5.8$ are very well determined.[248]. In most experimental or theoretical studies the defect density n_D is usually cited between $1\times10^{18} - 1\times10^{20}\text{cm}^{-3}$ and the defect energy E_D is either given rather shallow at 0.4-0.6 eV, attibruted to Ti interstitials, or deeper around 0.7-0.9 eV or also around 1.0-1.2 eV, with both latter energy ranges being commonly attributed to oxygen vacancies. Hence, we assume oxygen vacancies to be present in this plasma-TiO_x layer. Note, however, that E_D is highly

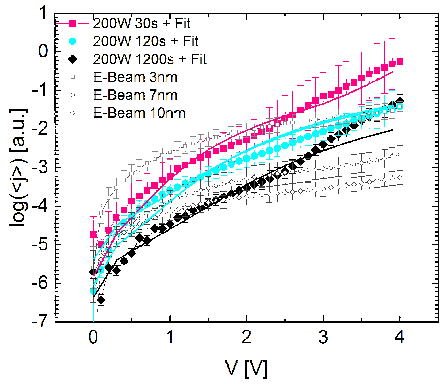

(a) *Fits to 200 W samples (thick lines) from set B up to 3V, as defined in the legend and text.*

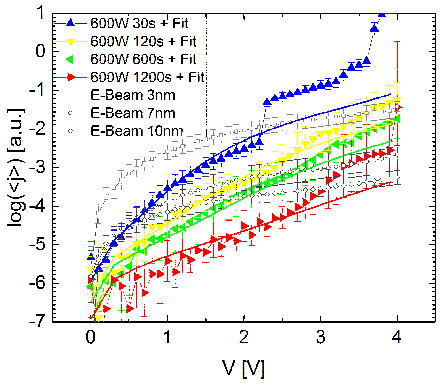

(b) *Fits to 600 W samples (thick lines) from set B up to 4V, as defined in the legend and text.*

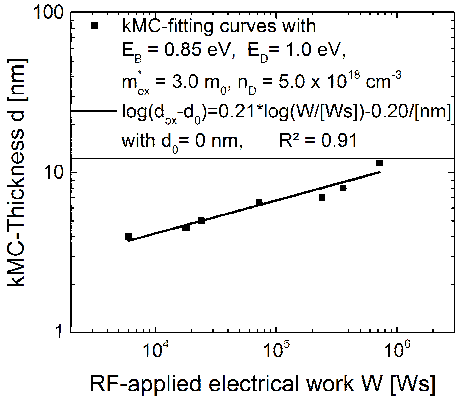

(c) *Calibration of the TiO_x-layer thickness d_{ox} in dependence of the plasma work (time × power) by kMC-fits.*

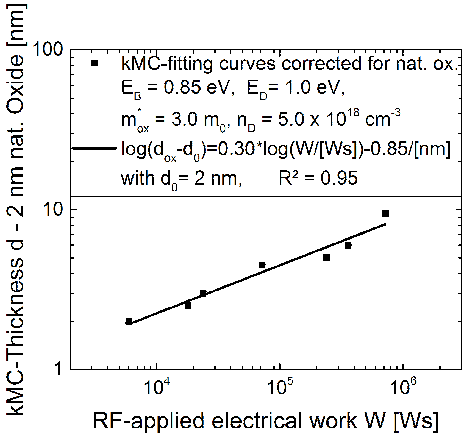

(d) *Calibration of the TiO_x-layer thickness d_{ox} in dependence of the plasma work by kMC-fits corrected for 2 nm natural oxide.*

Figure 6.9: *kMC-Fits to measured, averaged jV-curves from Fig. 6.8a and 6.8b with the kMC-parameterization given in Tab. 6.2. (a) Fits to 200 W samples from set B up to 3V, as defined in the legend and text. (b) Fits to 600 W samples from set B up to 3 or even 4V possible, as defined in the legend and text. (c) Calibration of the oxide thickness d_{ox} in dependence of the plasma work, i.e. time × power, for plasma-grown, nm-thin TiO_x-layers from the 7 kMC-fitted j-V-measurements on 200μm x 200μm-sized Au-Ti-TiO_x-pillars transfer-printed on p^+-Si. Linar fit on log-log-scale with Deal-Grove-model. (d) Same calibration of the TiO_x-layer thickness including a correction for 2 nm due to a natural oxide.*

dependent on the defect type and crystalline phase of TiO_2 or the method applied in a specific study. [88, 89, 91, 260, 261, 262] A detailed discussion of this is out of focus of this part, but a thorough kMC-study on defects in TiO_2 by our group is submitted elsewhere. The cathode-oxide barrier heights $\phi_{B,l}$ of 0.85 eV is in good agreement with

the ones expected from the MIGS-model[248] assuming the electron affinity, charge neutrality level and pinning factor of TiO_x, if one takes the literature values of $\chi_{TiO_2} = 3.9$ eV, $E_{CNL,TiOx} = 1.0$ eV and $S = 0.3$, respectively, and the work function of Ti to be $\phi_{Ti} = 4.3$ eV.[38, 248]
The biggest advantage of our statistical kMC-model, originally developed for high-k dielectrics,[189], is that we can analyze and determine the dominant current transport channels. Though not depicted for reasons of brevity and avoiding an overload of the figures, for all samples in this study TAT was explicitly irrelevant up to an applied voltage of 3 V. This was confirmed via kMC-simulations with parameter variations that would have favored TAT. However, such simulations showing considerable TAT-profiles are not able to reproduce the measured jV-profiles. Only the step-up in slope or the breakdown of some dielectric samples at voltages above 3.5 V can potentially be attributed to defects and TAT. For the given, best fitting parameters, however, the TAT branch as well as PF-emission is considerably lower than DT or FN-tunneling up to voltages of 3 V. The defect energy had to be chosen at 1.0 eV or deeper to get these inappropriate TAT and PF contributions fairly suppressed in the simulations and obtain an approprate fit the experimental curves. Thus the given simulated current densities over voltage in the curves in Fig. 6.9a and 6.9b are attributed to tunneling processes, mostly FN-like, and we propose that these are dominant in the measurements on the transfer-printed and plasma-oxidized TiO_x samples. Comparing the results from our kMC-analysis to others, e.g. one of the few studies on plasma-grown TiO_2 by Tinoco et al., a standard data analysis of differently plotted j-V-curves supposed that PF conduction is the dominant transport mechanism in plasma-oxidized TiO_2 layers.[20] However, their oxide layers were sputtered which is known to produce way more defects than e-beam evaporation.[248] So this does not contradict our result that defects are less important or even negligible for transport in these samples.

6.2.6 kMC-Calibration of Plasma-Grown TiO_x-Thickness

Finally, we are able to quantify the oxide growth roughly and calibrate the obtained oxide thickness of the sample set B (10 nm Ti) in dependence of the electrical work W applied to the plasma. Taking the thicknesses given in Tab. 6.2 and plotting them on log-log-scale over the electrical work W, i.e. time × power, RF-applied to the plasma in Fig. 6.9c, a linear trend is visible making the plasma work an appropriate variable to explain the oxide thickness. By applying a regression with a power-law to the data points, a trend line (linear on log-log-scale) is found providing the fitting values of the Deal-Grove-model for the oxide thickness d_{ox} in dependence of W, as done similarly before by Tinoco et al., yet in dependence of the plasma time only and not $W = P \cdot t$ in [19, 20, 199], using the law

$$d_{ox}(W) = A \times W^B + d_0 \tag{6.1}$$

Even for $d_0 = 0$ nm , that is under the assumption that there is no oxide present before the application of the plasma and the whole oxide is formed by plasma-oxidation, the R^2 value of this fit is 0.91, with parameters $A = -0.20$, $B = 0.21$. This means that the electrical work W applied to the plasma as RF-microwaves (units Ws), is able to explain 91 % of the proposed thickness variation. This is more than acceptable considering the non-trivial physical system to be explained by this very compact growth model. The trend can be explained even better in the model, if one assumes a thermally grown titanium oxide layer of $d_0 \approx 2$ nm already before the plasma treatment. By substracting this correction from the kMC-fitting-thicknesses, the fitting parameters change to $A = -0.85$ and $B = 0.3$, while R^2 increases by 0.04 to 0.95. So from this fit 95 % of the grown oxide thickness can be attributed to the independent variable W, electrical work applied to the plasma, thus increasing the explanatory power of this variable.

6.2.7 Analysis of jV- and CV-Profiles of the MOS-Structures

As described in a very accurate way with respect to titanium dioxide layers in a work by Mikhelashvili et al.[15], measured jV-profiles can be analyzed quite straight-forwardly for different charge transport mechanisms by plotting them renormalized according to the phenomenological equations for the corresponding charge transport processes. Although CV-measurements are most recommendable to analyze dielectrics, as they can provide way more information on oxide parameters, such as interface trap charges, dielectric permittivity, threshold voltage or flatband voltage, they are also more complex and difficult to accomplish and interpret correctly. Therefore, before doing the CV-measurements, the subsequently provided variations of the 'jV'-plots are a quick and useful complementary method to derive statements on transport processes through the contacts at the respective bias. In particular, they can validate the existence of an oxide already distinguishing electrical transport processes. Also the validity of the kMC-results in terms of dominant transport processes can be checked. Results of this plotting-procedure, e.g. given in [15], applied to the jV-profiles of the transfer-printing samples from section 6.2.4 are given in Fig. 6.10 and Fig. 6.11.
We start with comparing sample A1 to the nTP-samples characterized by c-AFM in Fig. 6.10a-d. For both samples, the oxide is considered to be negligibly thin, i.e. maximum 1-2 nm, if present at all. This is concluded by the Schottky behaviour, which is linear in a j-$V^{1/2}$-plot, between 0 V and ∼1.8 V in Fig. 6.11a, followed by a linear ohmic, i.e. bulk-limited, behaviour between 2 V and 3 V, seen in Fig. 6.10a, even clearer visible in the zoomed in image, Fig. 6.10b. Most remarkably, both sample A1 in Fig. 6.10c and the 75 nm x 75 nm nTP-pillar sample characterized by c-AFM in Fig. 6.10d exhibit clear space-charge-limited-current (SCLC) characteristics with a linear dependency of j on V^2 above 3.5 V for A1 and above the voltage V_{noise} where the current exceeds the noise level for the nTP-sample. The ohmic behaviour, but especially the SCLC-profile, are usually visible at Metal-Semiconductor-contacts. Thus, one can clearly defer that these junctions resemble Metal-Semiconductor-contacts, probably of Ti-p^+-Si. Additionally, the ohmic or SCLC-like characteristics were not visible for any of the other, stronger treatments,

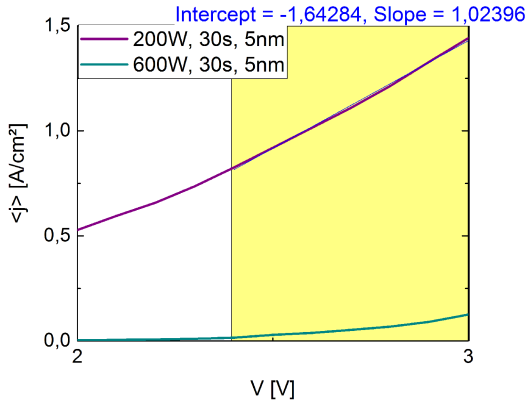

(a) *Linear-Plot: j over V for sample A1 and A4.*

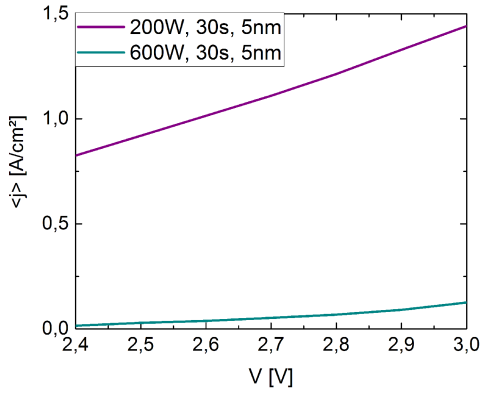

(b) *Linear-Plot: j over V for zoomed in voltage range, sample A1 and A4.*

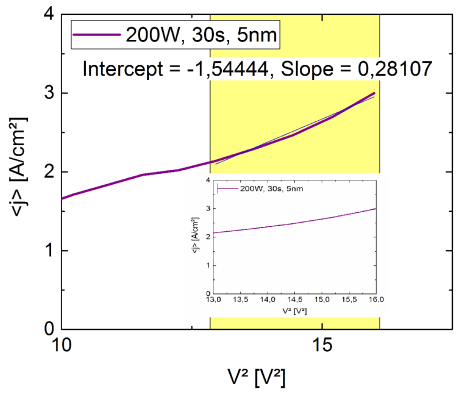

(c) *SCLC-Plot: j over V^2 for sample A1.*

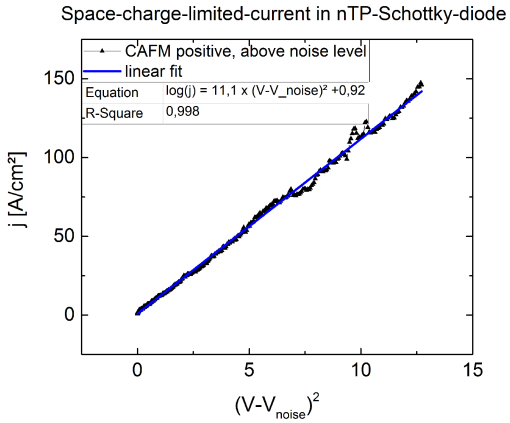

(d) *SCLC-Plot: j-V^2 for 75 nm x 75 nm pillars.*

Figure 6.10: *Analysis of oxide parameters by different types of plots of measured j-V-profiles. Depicted are 200 W for 30 s plasma and 5 nm Ti transfer-printed Au/Ti/TiO_x/p^+-Si samples plus the 600 W, 30 s, 5 nm Ti sample for the ohmic plot in (a). Only A1 exhibts linear regions. (b) Zoom into voltage range between 2.4 V and 3.0 V, only 200 W curve is linear, 600 W curve is not. (c) j-V^2-plot for sample A1, linear range indicating a SCLC-current, as evident also in the inset. (d) Similar j-V^2-plot for the characteristics of the jV-profiles measured by cAFM above noise level.*

i.e. A2-A7 and B1-B7, demonstrated exemplarily by sample A4 in Fig. 6.10a which is not at all linear but increases by about 3 orders of magnitude in this voltage range.

Coming to the 600 W series with 5 nm Ti evaporated on the stamp, samples A4-A7 are analyzed in Fig. 6.11 and also the only systematically deviating $< j >$-V-curve of sample A1, i.e. 200 W, 30 s, 5 nm Ti, is analyzed further. In the Schottky-Plot, i.e. j over $\sqrt{V}$ of samples A4-A7 in Fig. 6.11a one can see first a linear region between 0 $V^{1/2}$ and 0.3 $V^{1/2}$as well as a second one between 0.5 $V^{1/2}$ and 1.3 $V^{1/2}$. This means, as one

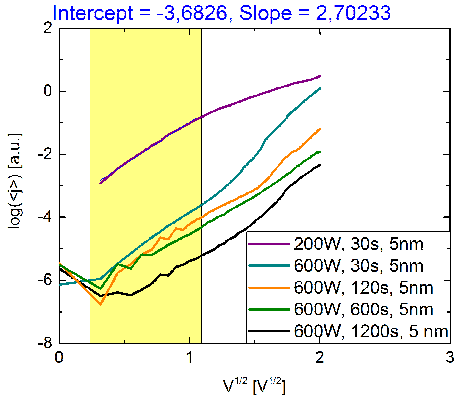

(a) *Schotty-Direct-Tunnelling-Plot:* j/V *over* $\sqrt{V}$ *for samples A1 and A4-A7.*

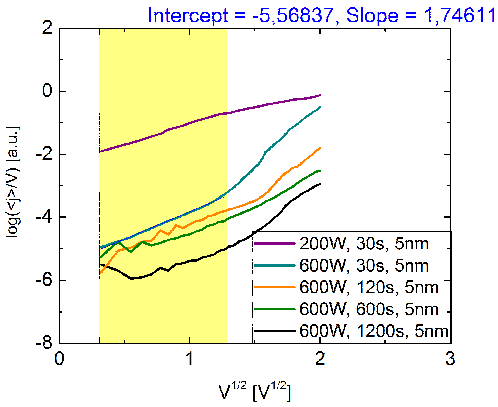

(b) *Poole-Frenkel-Plot:* j *over* $\sqrt{V}$ *for samples A1 and A4-A7.*

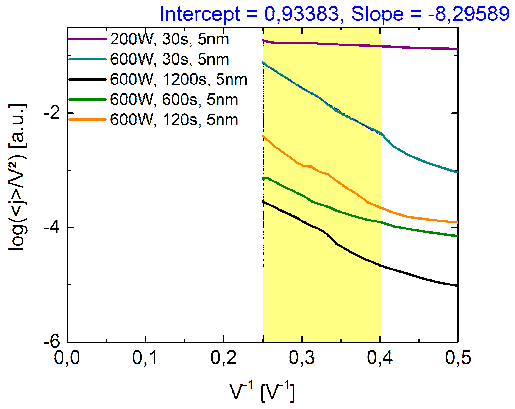

(c) *Fowler-Nordheim-Plot:* j/V *plotted over* $1/V$ *for samples A1 and A4-A7.*

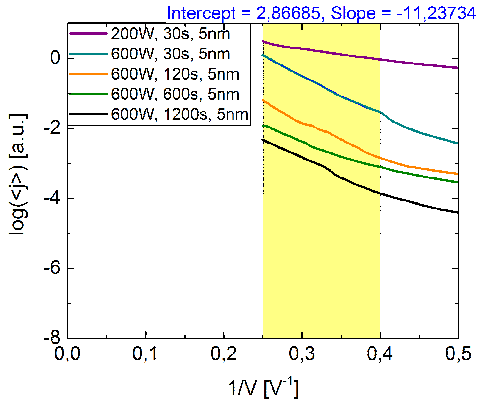

(d) *Trap-assisted-tunneling-Plot:* j/V^2 *plotted over* $1/V$ *for samples A1 and A4-A7.*

Figure 6.11: *Analysis of oxide parameters by different types of plots of measured j-V-profiles. Depicted are five different transfer-printed Au/Ti/TiO_x/p^+ - samples with 600 W power for times 30 s, 120 s, 600 s and 1200 s and 5 nm Ti evaporated, as well as 200 W for 30 s plasma and 5 nm Ti.*

can tell from the phenomenological equations, that for the first linear region Schottky emission and for the second linear region DT must be dominant. The argument that the first linear region resembles SE is supported by the observation that all 600 W samples had a similar intercept around -6.1 corresponding to a similar Schottky barrier around 0.55 eV as calculated from the phenomenological formula. This is quantitatively at least in the range of what is expected for these samples, qualitatively it makes sense that the barriers are similar for identical treatments, Moreover, theoretical, cf. MIGS-model, section 6.3.4, and values determined by kMC-simulations, which gave 0.85 eV for the barrier, see 6.2.5, are at least comparable. For the 200 W, 30s sample A1, however, the intercept is -3.6 and the Schottky barrier is 0.48 eV. In the PF-plot in Fig. 6.11b the

trend cannot be considered linear for all 5 nm samples. Hence, in agreement with the results of the kMC-simulations that resulted into DT to be dominant and not PF in this voltage range between 0.5 $V^{1/2}$ and 1.3 $V^{1/2}$, even for low trap levels and high densities, this range is attributed to a SE/DT conduction mechanism for both the samples A4-A7 and A1. Then the j/V over V^{-1}-plots and j/V^2 over V^{-1}-plots in Fig. 6.11c and 6.11d, respectively, have linear regions for higher voltages than 2.2 V for all the samples A2-A7 and B2-B7, whereas samples A1, and B1 with 600 W, 30 s, 10 nm Ti have no linear profile in this plot and repeatedly showed break down here, cf. Fig. 6.8d. This jV-behaviour of A4-A7 requires an oxide. Furthermore, by the slopes in the linear region of the "FN-plot", i.e. j/V plotted over $1/V$ in Fig. 6.11c, one can derive the barrier height using Eq. (5.11). We do this exemplarily for the 600 W, 30 s, 5 nm sample A4 again. Its slope had a value of 8.3 here, which corresponds to a barrier height of around 0.97 eV. This is calculated using the kMC-parameter for the effective mass $m^*_{ox} = 3.0$ m_0 and an oxide thickness $d_{ox} \approx 4.5$ nm. Similarly, from the slope of -11.3 for the same sample in the linear region of the "TAT-plot", i.e. j/V^2 plotted over $1/V$ in Fig. 6.11d, the defect levels can be estimated to lie at 1.5 eV using the phenomenological TAT-equation, found e.g. in [15]. Most remarkably, for amorphous TiO_2 $E_D = 1.6$ eV has just recently been reported for oxygen vacancies.[263] The kMC-simulations tell that the defects must lie lower than 1.0 eV. Thus, this part of the jV-curve could originate from deep oxygen vacancies around 1.5 - 1.6 eV, which would be in accordance not only with literature and kMC, but also with an amorphous TiO_x expected from the plasma-growth process and the rather oxygen-deficient conditions during its growth.
Eventually, the discussed values calculated exemplarily from this phenomenological analysis agree well enough with the results from the kMC-simulations in section 6.2.5 and can be considered a further indicator for the validity of the kMC-model. Most importantly, however, from this combined experimental, plotting and kMC-analysis the samples A2-A7 and B1-B7 are confirmed to be MOS-contacts, while A1 and the measured nTP-pillar resembled a Schottky-contact. In agreement with our estimate from the reference samples, we confirm especially the oxide thickness for the strongest treatment, 1200s at 600 W, as derived by kMC to be $d_{ox} \approx 12$ nm.

This information on the oxide thickness can be employed for a final characterization of the plasma-grown oxides by complementary CV-measurements. Being a highly established measurement technique, extensive theoretical backgrounds on CV-measurements can be found in [186, 213, 214] and a description of this is out of focus at this point. For this purpose the most insulating sample B7, i.e. the one with 600 W, 1200 s plasma treatment and the 10 nm Ti-layer, was characterized with the probe station operated as capacitance meter applying a DC bias to the Au/Ti top contact by the needle and driving a high-frequency AC signal of 20 kHz through the structure. Thus, essentially, CV-curves like the one presented in Fig. 6.12 were measured. The saturating accumulation capacitance for negative bias is a further proof of the tunneling dielectric formed by the plasma process attributed to an amorphous TiO_x-layer. The accumulation capacitance at the plateaeu at negative bias has a value of $C_{acc} = 374pF$ or $C_{acc}/A = 934$ nF/cm^2.

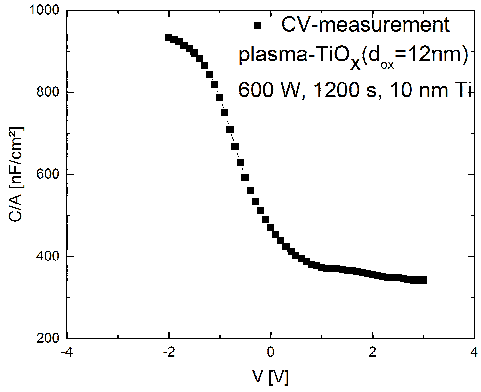

Figure 6.12: *CV-curves from high-frequency measurements on transfer-printed Au/Ti/TiO_x/p^+-Si-pillars, 200μm x 200μm-pads, plasma 600 W, 1200 s, 10 nm Ti evaporated.*

Assuming the validity of the kMC-derived thickness with $d_{ox} = 12$ nm and the formula for a plate capacitor $C = \epsilon_r \epsilon_0 \frac{A}{d_{ox}}$ one can estimate the relative permittivity of the plasma-grown oxide, arriving at a value of $\epsilon_r \approx 12.7 \approx 13$. This is in accordance with typical values for amorphous TiO_x or even nm-thin TiO_2[15, 26, 29], so it indicates the validity of our assumptions on the plasma-oxide formation, at least for a sufficiently strong plasma, and the reliability of our measurements. In contrast to this, for sample A1 such CV-curves could not be obtained, which supports once more the results of the analysis above identifying A1 as a Schottky-contact.

6.2.8 Summary of the Application of nTP and Plasma Oxidation for Oxide Fabrication

In total the findings from this kMC-model validate the assumptions on the formation of the oxide by the plasma treatments even more, such as the qualitative increase in oxide thickness with stronger treatment. The typical and stable jV-curves are statistically robust (see given error bars) and thus prove the reliable transfer and uniform electrical functionality of the MOS-diodes. By an appropriate, large-scale plasma treatment of the Ti surface on the stamps one can produce desired oxide thicknesses like $d_{ox} \approx 12$ nm for 600 W for 1200 s on 10 nm e-beam evaporated Ti. Combined with the fast and efficiently fabricated nTP-protocol, this process is a well-controllable enabling technique to produce further miniaturized MOS-devices for electronic or electrochemical applications. This holds, in particular, if such devices desire current densities in the range already measured successfully here, i.e. $\sim 10^{-6}\frac{A}{cm^2} - 10^{-3}\frac{A}{cm^2}$ for voltages between 0 and 3 V.[§] The kMC-simulations on the μm-samples with plasma-grown TiO_x support

[§]This is far enough below dielectric breakdown starting around 3.5 V for the structures fabricated by this nTP/plasma-process.

the experimental findings and allow for a determination of the dominant current mechanisms and experimentally hardly accessible material parameters. The step-up in the slope for higher voltages cannot clearly be attributed to FN-tunneling or TAT, but TAT is favorized due to the agreement of the defect energy derived from the j/V^2 over V^{-1} plot with literature values for oxygen vacancies in amorphous TiO_2 at 1.6 eV. However, it can not be excluded that this is a hole tunneling branch which is not included in the kMC-model. In the end we suppose that the produced oxide is amorphous and nonstoichiometric, but in particular defective. Hence, we propose to investigate the properties of such plasma-grown oxide layers in future studies, e.g. combined with suitable spectroscopic techniques (XPS, XAS) and a more differentiated kMC-model. For further research opportunities, refer to the outlook in chapter 7.

6.3 kMC-Simulation of Defects in Anatase TiO_2

As motivated in chapter 1 this part of the thesis studies defects in TiO_2 by kinetic Monte Carlo (kMC). KMC is supposed to be a useful tool to bridge the gap between the explanatory power of measurements and practical limitations of analytic calculations. The employed model was introduced in the previous chapters. The particular assumptions applied in the physical models must be valid for the specific material, as done for TiO_2 by qualitative arguments in section 5.5. Then, a very reliable parameterization with an exact and consistent choice of all input parameters is needed, especially with respect to the trap levels. Therefore this kMC-study begins with a theoretical evaluation of the trap parameters in titanium dioxide in section 6.3.1. An overview on the categorization of defect types and energies in TiO_2 in recent literature, focusing on anatase, and their dependence on the chemical treatment of the sample is given. This forms the basis for a short description of the assumptions in section 6.3.2 as introduced for the kMC-model in section 5, but in terms of the present situation and the further parameterization. This includes a short validation of the kMC-related assumptions specific to TiO_2, in section 6.3.3. The information from section 6.3.1 is also very important for the discussion of the results in section 6.3.5. From our simulation results of several experimental IV-curves from literature we derive a correlation between the nature of dominant defects in TiO_2 and typical chemical processing and fabrication methods. By the analysis of the fits in section 6.3.5 consistent values and evidence for shallow or deep trap states in accordance to their chemical treatment is found.

6.3.1 Defects in TiO_2

Just as in other transition metal oxides, bulk defects as well as interface defects can contribute notably to the current density in TiO_2, either indirectly by influencing the charge carrier generation and recombination at the interface or in the bulk as well as by impurity scattering of electrons or directly via the trap-specific charge transport

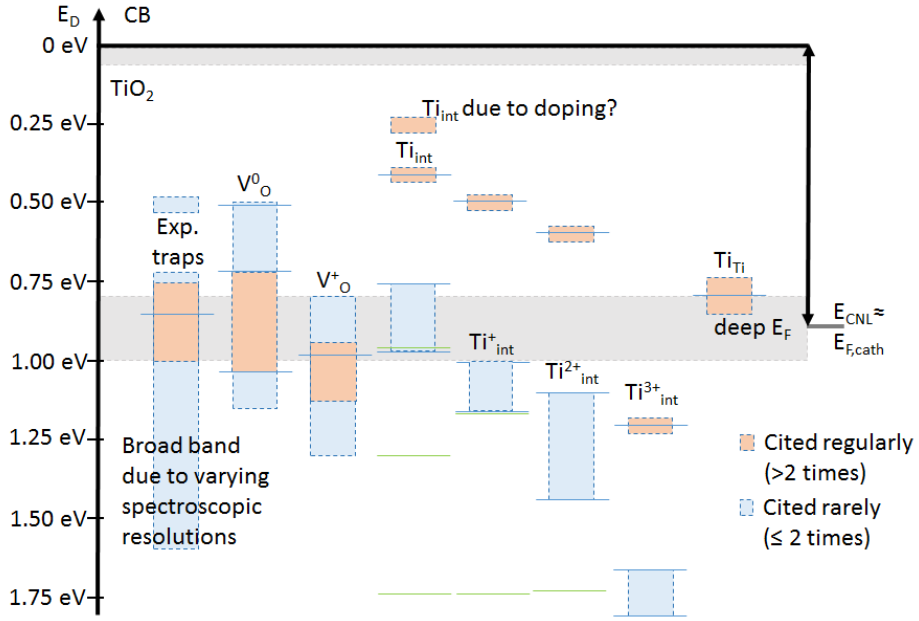

Figure 6.13: *Overview over typical energies of the most important defect states in TiO2 anatase. Blue bars(≠lines) indicate rarer cited ranges for defect levels, values in the range of the red bars are cited more often and were considered more reliable for this reason. The blue lines indicate values cited explicitly for these defects. In terms of Ti_{int} green lines indicate higher ionization energies of its different charge states. For the exact corresponding values, applied methods (experimental or theoretical), further explanations and references see the summary in Tab. 6.3 and the text. The grey region gives the mostly cited values for E_F in intrinsic anatase assuming the existence of primarily deep traps, as focused on in this paper, or shallow traps (accurate definition of the two terms in [264]).*

processes TAT and PF emission, cf. section 6.3.2. This influences also the charge carrier mobility, the number of free charge carriers in the CB and thus the drift-diffusion-transport in the CB. Thus defects in TiO_2 influence the bulk fermi level E_F and further significant physical quantities related to it, such as the interface charge neutrality level E_{CNL} (or just "CNL"), the interface DOS and interface band bending and finally also the CBO between the electrode materials and TiO_2. We do not treat the impact of defects on the free carrier mobility in this study. Rather we focus on the defect density n_D and the energetic positions of defect levels E_D themselves - measured with respect to the CBM in the bandgap of anatase TiO_2 in the first place, as these determine the mentioned electronic properties to a high extent. The defect level E_D is in fact the most detrimental parameter of the kMC-model, cf. section 6.3.2. To parameterize it correctly, we provide an overview of the values in anatase either taken from theoretical studies explicitly referring to this phase of TiO_2 or experiments being done on pure anatase or an anatase-rutile polymorph. In the first place, one sees from Fig. 6.13 that, generally, calculated and measured values are rather widely spread in a range between ∼0.4 eV and ∼1.8 eV. Referring to Tab. 6.3, both experiments (PL, PES, XPS, UPS, RPS, XAS) and

Exp. traps	V_O^0 (e-trap)	V_O^+ (e-trap)	Ti_{int}	Ti_{int}^+	Ti_{int}^{2+}	Ti_{int}^{3+}	Ti_{Ti}
0.8 {XPS, XAS, PES} [37, 39, 40, 265, 266]	0.5 {HSE} [143, 171]	0.94-0.99 {GGA+U, B3LYP} [262]	0.0 {GGA+U} [88, 173, 260]	0.5 {GGA+U} [88, 173, 260]	0.6 {GGA+U} [88, 173, 260]	1.2 {GGA+U} [88, 173, 260]	0.73, 0.82 {DFT+U} [261]
0.9 {XPS, UPS,RPS} [267, 268]	0.65-0.7 {B3LYP} [269]	1.0 {STS+ DFT+U} [270]	0.39 {GGA+U} [172]	-	-	-	-
1.0 {XAS, RPS} [265, 271, 272, 273]	0.7{GGA+U} [173] 0.72 {GGA+U} [274]	1.0 {GGA+U} [173]	0.74,0.98, 1.3, 1.74 {GGA+U} [170]	1.0,1.17, 1.74 {GGA+U} [170]	1.09,1.73 {GGA+U} [170]	1.71 {GGA+U} [170]	0.82 {GGA+U} [170]
0.5-1.7{PL, others}[91, 141] [265, 267, 270, 271, 272, 273]	1.08 {GGA+U} [172]	1.17 {GGA+U} [171, 172]	0.98 {GGA+U} [275]	1.16 {GGA+U} [275]	1.46 {GGA+U} [275]	1.84 {GGA+U} [275]	-
	1.16, 1.28 {B3LYP} [276]	1.35 {GGA+U} [170]					
	1.15, 1.48 {B3LYP} [170]						
	1.5 {GGA+U} [275]						

Table 6.3: *Overview on defect types, energies and method to derive them for most important electron traps in anatase.*

calculations (DFT, e.g. LDA, GGA+U, B3LYP, sX, HSE06) agree at least that defects in TiO_2 are Ti^{3+}-type located around 1 eV below the CB [37, 91, 265, 268, 277], showing d-d transitions/3d-character and an EPR signal of paramagnetic Ti^{3+}. [278, 279] The measured peaks suffered from ~ 0.5 eV FWHM, with the maximum mostly between 0.5 to 1.7 eV,[91, 141, 143, 265, 267, 270, 271, 272, 273] so that the defects in TiO_2 can be caused either by oxygen vacancies, V_O, or Ti interstitials, Ti_{int}, and titania layers could

correspondingly be a reduced form of TiO_2, i.e. O-poor TiO_{2-x}, or a Ti-poor $Ti_{1-x}O_2$. The consecutive experimental difficulty to distinguish between those two defect types promoted the still ongoing debate on the nature of defects in TiO_2, found in the references of this paragraph. This issue has also high significance for the structural properties, as the oxygen vacancies would be accompanied by a Schottky disorder resulting only into deep defects, while Ti_{int} are associated with Frenkel disorder and would induce deep or shallow traps with the latter ones most probably dominating the electrical conductivity of TiO_2. [280, 281] The deep V_O are mostly reported to be dominant in density, but also Ti_{int} are considered to contribute to the conductivity of TiO_2. [282, 283] Experimentally, the localization of defects in the bandgap and their categorization (in terms of type) suffers from a too low energy resolution, as indicated in Fig. 6.13. In UPS, XPS, XAS or PL measurements mostly peaks with the maximum around 0.8-0.9 eV are reported, as seen in Tab. 6.3. However, the major drawback of these techniques, especially of EELS, for example, is their limitation to surface states. [143] Exemplarily, Tang, et al. attributed the 0.8 eV state measured by XPS to Ti^{3+} defects from V_O[36, 37], Wendt et al. exposed rutile surfaces to oxygen flows of 0 L, 4 L, 40 L and 420 L, monitored the defects by PES and the surface by STM in parallel and still observed a Ti^{3+} peak at 0.85 eV despite of optimal oxygen bridging rows. Finally, they concluded that defects should be due to near-surface Ti_{int} rather than bridging oxygen vacancies on the surface.[40] In a similar study Wang et al. determined chemically reactive Ti^{3+}-type defects on anatase surfaces by XPS/UPS and, assisted by STM images, they suggested a model of sub-surface Ti interstitials ("intercalated Ti-pairs").[39] Like most of the surface-restricted experiments, also Henderson claimed Ti_{int} to be dominant on ion-sputtered TiO_2 surfaces [143], while other studies, such as the ones by Krüger et al. or Hengerer et al. with Grätzel favored oxygen vacancies in anatase at ∼0.9 eV. [265, 268, 271] Former theoretical models also favored oxygen vacancies as dominant defect.[40, 284] To resolve contradictions to some of the experiments, new DFT calculations on TiO_2 were performed, but one has to note that in DFT, as in any theoretical model, the exact location of the calculated defect levels depends strongly on the method used and on the choice of parameters for the model, e.g. the U value in GGA+U, used to account for an underestimation of the exchange-correlation in DFT resulting into a too small bandgap.[275] Thus defect values are widely spread in TiO_2, as indicated in Fig. 6.13. For example, Robertson et al. computed the defect levels in rutile by sceened exchange (sX) hybrid density functional methods resulting into a localized state at 0.7 eV for V_O and Ti_{int} distributed between 0.7 eV and 1.3 eV in the bandgap for its four different positive charge states.[174] Di Valentin et al. - as one of the few - determined values for self-trapped electrons Ti_{Ti} on hydroxylated rutile surfaces with energy levels of ∼0.73 eV and 0.82 eV, similar to V_O values, as they stated that additional hydrogen atoms could have a similar effect like the removal of oxygen atoms.[284] On amorphous TiO_2, Pham and Wang report states at 1.6 eV and 1.9 eV for oxygen vacancies much deeper than for rutile or anatase.[263] Concerning our material of focus, anatase, di Valentin, Pacchioni and Selloni derived $V_O^{0/+}$ and $V_O^{2+/+}$ charge states at ∼1.2 eV and 1.3 eV as

well as ∼0.7 eV by the B3LYP-method [269], whereas by GGA+U, with U=3 eV, they report both a shallow energy level, 0.15 eV below CBM, delocalized, and a deep one, 0.94 eV below CBM, localized, for the same defects.[262] Janotti et al. also reported a state at 0.9 eV below CBM attributed to oxygen vacancies (charge state unspecified) with the electrons localized at the nearest neighbours of the vacancy, derived using HSE06 functionals. By the same method Deák and Frauenheim found one electron trap due to $V_O^{+/0}$ at 0.5 eV and one due to $V_O^{2+/+}$ at 1.3 eV. [171] Morgan and Watson published two studies on anatase providing vertical transition values (which differ by about ∼0.15-0.25 eV for the two studies, see Tab. 6.3) of 1.15 eV and ∼1.35 eV for $V_O^{+/0}$ and $V_O^{2+/+}$ which should be dominant for O-rich conditions meaning low T or high oxygen partial pressure during growth or annealing. [170, 275] In an extended study on both rutile and anatase Mattioli et al. attributed deep defects in anatase at 0.7 eV and 1.0 eV to V_O, stating like most of the authors mentioned above that electrons hop through those localized states as small polarons. [173] The defect levels of $V_O^{+/0}$ and $V_O^{2+/+}$ in anatase from a GGA+U study by Yamamoto et al. are comparably, located at 1.08 eV and 1.17 eV.[172] In most of the mentioned studies also Ti interstitials were calculated and are mostly categorized to be shallow, just as in the latter one, with only one value at 0.39 eV.[172] Especially for Ti_{int} we will refer to this comprehensive and extensive study in the subsequent sections. Bonapasta et al. and Mattioli et al. reported from LSD+U calculations also one delocalized, shallow state at 0.1 eV and one localized, deep state at 0.9 eV in bulk anatase in good agreement with experimental observations and close to former values for Ti_{int} derived by them and placed as single states at 0 eV, 0.5 eV and 0.6 eV. [88, 260] Only their Ti^{3+} defect value was energetically deeper with 1.2 eV below CBM. [173] Morgan and Watson reported four occupied states associated to a mixing of four different occupied Kohn-Sham orbitals contributing to the neutral Ti_{int} state resulting into the values for the peaks of 0.74 eV, 1.00 eV, 1.09 eV and 1.71 eV, indicated by blue bars in Fig. 6.13 stretching over the range of vertical transition energies needed to bring the specific charge state into a state of higher valence.[170, 275] They expected the Ti_{int} states to become comparable in concentration to V_O under O-poor conditions and state that they are particularly favored only in rutile. Furthermore they consent with Deskins and Dupuis that electrons in TiO_2 form localized small polarons and are transported via hopping [285] which we hence implemented into our model, see section 6.3.2.

The reviewed results on defects in TiO_2 can be summarized as follows: From spectroscopy (PES, UPS, XPS) one can, also in anatase, find basically only a broad peak with a maximum at 0.8 0.9 eV, partly also 0.5 eV, below CBM in the bandgap, attributable to "Ti^{3+} nature" of the defects, but not to the specific chemical origin of the defect. Ab initio methods can differentiate between defect types, esp. V_O and Ti_{int}, by choosing suitable models, methods and parameterizations. Though limited by their practical viability, we could categorize basically three groups of defect energies as results of DFT which will be the point of reference for our trap levels in the simulations: A) deep, positively charged oxygen vacancies V_O^+ that can act as donors or can also accept an

electron themselves, with 0.7 eV $< E_D <$ 1.2 eV, B) "shallow"[¶] 0/1+ Ti_{int}, with $E_D <$ 0.6 eV, which stem either from excess Ti or are induced by oxygen vacancies, and C) deep, 0/1+, 1+/2+, 2+/3+ Ti_{int} with 1.0 eV $< E_D <$ 1.75 eV. The latter ones are harder to distinguish from the oxygen vacancies, but in the end they should also depend strongly on the chemical processing (the "history") of the sample and be much lower in concentration the deeper they are located. Since this chemical processing is also important for the dominant type of defect in other oxide metals, Robertson et al.[286] summarized the qualitative effects of the most common metal oxide growth techniques which we reproduce here for the reader's convenience in Tab. 6.4. The quality measures of the four given physical properties must be understood relative to each other. The scale is "graded" like very good, good, average, bad, n/a (no information). "Coverage" means homogeneity and conformality of a film, e.g. no pin-holes as for MOCVD or ALD is "good", while homogeneity and number of pinholes of films from PVD or sputtering is just "average". "Crystal Phase purity" means purity of the crystalline oxide, definition of the phase and crystalline order. So "good" as for PVD or sputtering means well-defined phase and crystallinity and the better it is the more certain is the phase and at the same time the fewer the number interstitials due to Frenkel disorder. This implies less Ti interstitials, for example. ALD and MOCVD can show mixture of phases making it "average" and proposing more disorder and more Ti interstitials. For the "defect" density "good" means few defects $\sim 10^{18}\text{cm}^{-3}$) like for MOCVD or ALD, "average" is $\sim 10^{19}\text{cm}^{-3}$ like for PVD, sputtering is "bad" causing up to $\sim 10^{20}\text{cm}^{-3}$ and requiring careful annealing to reduce them. Fourth, "Thickness" means control of thickness, e.g. atomic monolayer-$\sim$nm range, like in ALD, is "very good", $\sim \pm$1-3 nm as possible with PVD or MOCVD is still "good".

Thus, Tab. 6.4 serves as a basic reference for the discussion in section 6.3.5, to analyze

Fabrication technique	Coverage	Crystal Phase Purity	Defects	Thickness	Used in Ref.
MOCVD	very good	average	good (few)	good	[16]
PVD+therm.Oxid.	average	good	average	good	[14, 15]
Sputtering	average	good	bad (many)	n/a	n/a
ALD	very good	average	good	very good	[12, 13]

Table 6.4: *Overview on impact of common fabrication methods for nm-thin TiO_2 films on fundamental physical properties.*

the consistency of the results of our simulations with respect to the chemical or physical treatment used for the computationally fitted experiments. It shows that MOCVD

[¶]The author is aware that the term "shallow" is used differently for example in EPR-studies where it refers to defects that are located at an energy below CBM in the thermal range, i.e. 0.025 eV. However, also this definition is not unambiguous. For the most accurate definition of "shallow" and "deep" defects found in literature, refer to [264].

and ALD are the methods of choice to get homogeneous, pin-hole-free, nm-thin films of controlled thickness and few defects, where the crystallic phase is not the highest criterion, whereas for pure, well-defined crystalline films, that do not require an nm-exact control over the thickness or coverage PVD or sputtering is preferable, especially if they can be annealed to reduce defects.

6.3.2 The adapted kMC-Model for TiO_2

The kMC-model, as introduced in chapter 5 shall be briefly reviewed here. The simulation of the current density used the five, partly correlated, charge carrier transport processes, SE, DT, FN, PF and TAT. These processes compete and are selected statistically in each step of the kMC-simulation as explained in chapter 4.[189] Three of the five processes, i.e. SE, DT and FN, are computed by the Tsu-Esaki-Formula [222] corrected by us for asymmetric electrode contacts with different effective masses. As explained beforehand, $E_{F,ca}$ (dashed line left in Fig. 6.14a) is taken as 0-eV-reference in kMC. We assumed, that the cathode Fermi level $E_{F,ca}$ is pinned due to interface traps indicated by the grey distributions in Fig. 6.14a so that charge neutrality is given at the interface, cf. also the metal-induced-gap-states ('MIGS'-model') in section 6.3.4. The CBO to TiO_2, E_B, together with a linear voltage drop $V_{ox}/d \cdot x$ of $E_{F,TiO2}$ in the oxide starting at $E_{F,ca}$, determines $E_{F,an}$. Though a possible CB bending is skteched in Fig. 6.14a, it is neglected just as a bending of $E_{F,TiO2}$ is neglected, so both the CB and $E_{F,TiO2}$ drop approximately linearly. If a non-linear drop was present, then only in a negligibly small spatial region at the electrodes. This has been confirmed by the supplementary DD-simulations from section 5.5 given again in Fig. 6.14b for the case of a Pt-TiO_2-p^+-Si contact under accumulation relevant here. In the image CB, VB and E_F for $V_g = -2.0$ V (red), $V_g = -1.27$ V (green) and $V_g = -0.55$ V (blue) are shown with Pt as metallic cathode and p^+-Si as anode. With $\phi_{Pt} = 5.3$ eV, pinning factor $S_{TiO2} = 0.3$, $E_{CNL,TiO2} = 1.0$ eV and $E_{CNL,Si} = 0.8$ eV the barriers are $E_{B,ca} \approx 1.1$ eV and $E_{B,an} \approx 0.4$ eV according to the MIGS-model, see section 6.3.4. The inset shows the derived calibration of the oxide voltage V_{ox} in dependence of the gate voltage for such a MOS-contact. Thus further complications from a potential band bending could be neglected, for examples such ones from a dynamic interplay of electrode work functions ϕ and oxide electron affinity χ, charge states and densities of defects in the oxide, especially at the metal-oxide interface, which finally influences also the CBOs in the MIGS-model. The cathode is always assumed to be metallic with the CBM 3.0 eV - 9.0 eV below the cathode Fermi level $E_{F,cath}$. The temperature T was fixed at 298 K and the electric fields were higher than 0.1 MV/cm in all simulations, so thermionic emission is improbable and we expected to see only DT and FN. The energy-dependent transmission coefficient $T(E_x)$ is calculated in WKB-approximation and for the effective mass in TiO_2 a parabolic dispersion was assumed, cf. section 5.1.1. The image potential of the electrodes is said to be omitted for tunneling electrons, as justified in section 5.1.2 according to Weinberg, Hartstein and Schenk.[225, 227, 228, 230] So the linear voltage drop is not amended by image terms. Hence, the tunneling integral could be evalu-

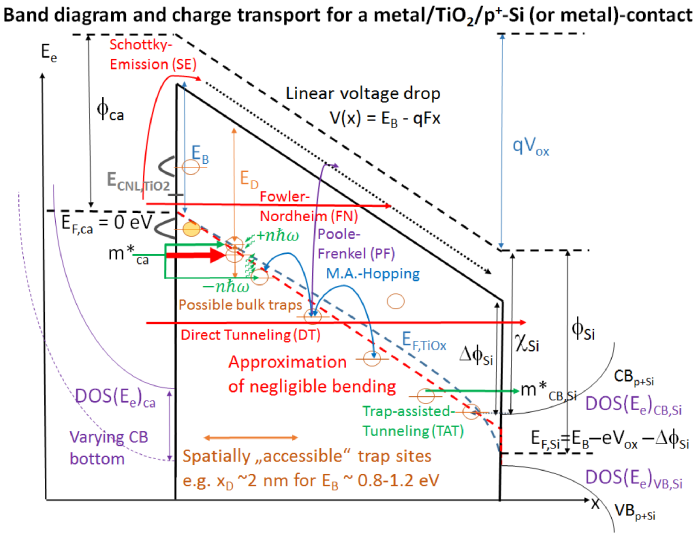

(a) *Exemplary MOS-(accumulation) or MOM-bandstructure and charge transport processes reproduced from section 5.*

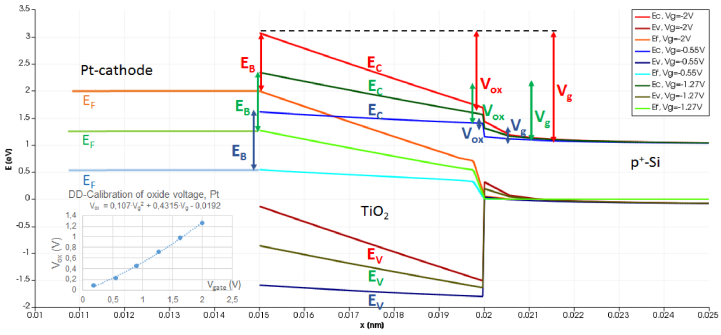

(b) *Pt-TiO_2-p^+-Si contact under accumulation with the calibration of V_{ox} in dependence of V_g shown in the inset.*

Figure 6.14: *(a) MOS- or MOM-bandstructure: For the convenience of the reader, the five transport channels through the oxide are given again, i.e. SE, DT, FN, PF, TAT plus hopping through oxide traps, for details see text and chapter 5. According to the MIGS-model, see section 6.3.4, $E_{F,ca}$ is pinned towards $E_{CNL,TiO2}$ by (un-filled) orange trap levels at the interface, donors or acceptors, indicated by the grey distributions. (b) Supplementary DD simulations of a Pt-TiO_2-p^+-Si contact under accumulation, band bending in TiO_2 is negligible and allows for a calibration of V_{ox} in dependence of V_g as shown in the inset.*

ated analytically according to Eq. (5.8). The parametrization of the barrier height is determined by the MIGS-model, see section 6.3.4. The complementary numerical evaluations of the integral by our previously demonstrated kMC-simulator [189] in section 5.1.2 showed that the classical image terms caused a barrier reduction increasing lineraly from ∼0.1 eV ($V_{ox} < 1.0$ V) to 0.2 eV (constant for $V_{ox} > 3.0$ V) to a high accuracy, while computations get much more intense if the image potential is included by calculating

$T(E)$ numerically. Hence barrier heights in our fits in section 6.3.5 are assumed to be on average ∼0.15 eV higher, if the image potential was included.[225, 227, 228] Each kMC-sampling step starts with an electron of energy E_x injected from the cathode into the anode, i.e. by SE, DT, FN, or into trap levels at E_D (with respect to the CBM of TiO_2). This occurs either elastically or inelastically, i.e. phonon-assisted (energy $\hbar\omega$, indicated by green arrows, in Fig. 6.14a). These injection rates depend on E_B, the $DOS(E)$ (i.e. m^*_{ca}) and the oxide trap parameters E_D, x_D, m^*_{ox} and n_D. Injection is favored for "resonance" of $E_{F,ca}$ and E_D , so there is a trade-off between pre-defined trap levels E_D and (random) trap locations x_D, as discussed in detail in section 5.1.3. Similar rates as the ones here for the elastic process have already been derived [229, 233, 234] and implemented for metals [6, 149, 168, 189, 191, 232, 287, 288, 289, 290], but we confectioned the formula for elastic injection from semiconductor electrodes derived by Svensson and Lundstroem, as given in section 5.2. [237] In fact, we model a highly-doped p-type Silicon substrate in accumulation by setting the kinetic energy E_x of the electrons in the electrode to a fixed value of ∼200 meV, assuming an effective mass in the Si electrode of ∼0.3 m_0 ($N_C \sim 10^{22}cm^{-3}$) and an electron density of $5{\times}10^{19}cm^{-3}$ at the accumulated interface. Inelastic, i.e. multiple-phonon-assisted, injection and emission rates were employed in the same way as outlined in section 5.2.[229, 234, 291] and tested in [6, 149, 168, 189], for example. Electrons injected into an initially positively charged trap can be emitted by PF. Therefore the optical dielectric constant was varied around a reference value of TiO_2 of ϵ_{opt} ∼5.8. [30, 244] The investigated deep defects of TiO_2 are localized, see section 6.3.1, so transport occurs via small polarons. Accordingly, we refer to the Miller-Abrahams-hopping rates for TAT processes.[292] Hereby the Coulomb-potential of initially positively charged traps is neglected. This is reasonable to save computational costs, but stay accurate, because hopping is only dependent on the mere difference between the initial and the final state and for PF emission the Coulomb contributions are inherently included. The kMC-simulations could be performed without respecting the band bending or CB processes as well as retrapping which occur on much shorter time scales, as discussed in section 5.5. Once an electron is emitted to the conduction band by SE or PF, it can be assumed to have readily reached the anode. Eventually, also hole tunneling transport between the electrodes is neglected due to the generally high valence band offsets of TiO_2 of at least 1.6 eV in the most conservative estimate on p^+-Si.

6.3.3 Parametrization of TiO_2

Due to its high sensitivity to correct input parameters the correct parameterization of the model is essential. The two for TiO_2 most controversial parameters of focus, the trap energies and densities, have already been discussed in section 6.3.1. Defect levels in amorphous TiO_2 or rutile are structurally and energetically comparable to the ones in anatase which is an advantageous property for the parameterization.[263] Hence, in agreement with our review in 6.3.1, we tested parameter values for E_D of 0.2 to 1.5 eV, i.e. from shallow to deep states, with step sizes as fine as 0.02 eV. The defect densities (on

which the corresponding current components depended linearly) were varied between $1\times10^{18}\text{cm}^{-3}$ and $1\times10^{20}\text{cm}^{-3}$, i.e. for example minimum 1 up to ∼100 defects in a simulation volume with d_{ox} = 10 nm, times squared lateral dimensions of 10 nm x 10 nm. Regarding the further parameters, as introduced in section 6.3.2, most of them can be treated quickly, since appropriate literature values are available, such as for the electron masses in the electrodes, which are 1 m_0 for metals and ∼0.28 m_0 for Si. We varied the effective mass in TiO_2 from 0.5 m_0 up to 5 m_0 (step size ∼0.2-0.5 m_0), which is the most frequently reported range,[36, 293] although literature values range from 0.35 m_0[181] up to 15 m_0.[36, 143] The optical dielectric constant ϵ_{opt} of TiO_2 is generally well-reported in a tight range of ∼6.8-8.4 for rutile and ∼5.6-5.8 [244, 294, 295] for anatase. Staying consistent this way, these independent literature values were used for all samples. The bandgap E_g of anatase is commonly known to be 3.2 eV [244] (rutile: 3.0 eV) and was a fixed constant in all simulations. Same holds for the static dielectric constant which was fixed to a value of 30.[34, 35, 36, 37] The band offset to the anode $\phi_{B,an}$ is mainly determined by the charge neutrality level (CNL) of TiO_2 in the MIGS-Model, outlined in section 6.3.2, and could therefore usually be kept at ∼0.4-0.6 eV. One has to note that our kMC-model is less sensitive to the last four, better reported quantities (ϵ_{opt}, E_g, ϵ, $\phi_{B,r}$) in contrast to the more controversial ones mentioned before. This high sensitivity to the less certain physical quantities is a welcome property of the simulator, because as soon as a specific fit is achieved it supports the validity of the parameterization.

6.3.4 Barrier Heights by MIGS-Model and Fermi-level Pinning

The CBO to the cathode $\phi_{B,ca}$, is a very sensitive and crucial parameter of the simulation and must be accurately parameterized. With respect to experimental references, metal-oxide and semiconductor-oxide interfaces are very sensitive to the specific chemical and physical treatments which induce different interface defect densities, defect levels, electron affinities, Fermi-levels and work functions of the contacts at their interfaces and thus also band bending. Apparently, such processes can hardly be controlled exactly, so should always be determined experimentally. Reported CBOs of MOM or MOS-structures with TiO_2 as oxide layer and electrical contacts, such as Al, Ti, Au, Pt or Si vary broadly and are much lower than expected from Mott-Schottky-theory which gives the barrier:

$$E_B = \phi_B = \phi_m - \chi_{TiO_2} \tag{6.2}$$

By kMC-simulations this problem of the Mott-Schottky-approximation can be circumvented by performing an extensive parameterization-analysis resulting into a best fit that gives the CBO. This strategy was pursued here. To obtain the best approximation of the band offsets in advance, they were calculated by the well-known MIGS-model for the Fermi-level-pinning caused by interface defects on metal oxide surfaces, studied into

detail by J. Robertson et al.[244, 247, 296, 297], Mönch et al. [298] and Cowley and Sze[299]. It modifies the conduction band offsets via a pinning factor S, e.g. assuming a Silicon electrode:

$$\phi_B = (\chi_{Si} - \phi_{CNL,Si}) - (\chi_{TiO_2} - \phi_{CNL,TiO_2}) + S \cdot (\phi_{CNL,Si} - \phi_{CNL,TiO_2}) \tag{6.3}$$

The charge neutrality level (CNL) is the level below which all interface defect states must be filled to obtain charge neutrality at the interface. [248, 300] If the Fermi-level of a material lies below CNL the interface is positively charged, whereas it is negatively charged, if E_F is above CNL. The CNL of TiO_2 has been reported by Robertson to lie at 1.0 eV below CBM.[247] To determine the pinning factor S we employ the empirical model by Mönch using the optical dielectric constant of 5.8, cf. above:[244, 298]

$$S = \frac{1}{[1 + 0.1(\epsilon_{opt,TiO_2} - 1)^2]} \approx 0.3 \tag{6.4}$$

The relevant contact materials here were Al, Ti, Au, Pt and Si. The work functions of Al and Ti are similar and range between 4.1 and 4.3 eV as found in literature[9, 301], the one of Au between 4.8 and 5.4 eV [301, 302] and the one of Pt between 4.9 and 5.7 eV. [157, 301] The electron affinity of Si is well-known to be ∼4.05 eV, while the work function depends on doping via $E_{F,Si}$, which we assumed to be ∼1.0 eV below CBM for highly p-type Si, resulting into ϕ_{Si} = 5.05 eV and the CNL of Si lies at 0.3 eV.[247] A more controversial parameter, however, remains χ_{TiO_2}, since values found in literature are broadly distributed from 3.2 eV to 5.0 eV and accordingly spread are the work functions of TiO_2 between 4.0 eV to 5.8 eV, while, additionally, DFT calculations do not agree at all with experimental values.[303, 304, 305] But mostly values around 3.6 and 3.9 eV (or 4.0) are cited for χ_{TiO_2} [286, 296, 297, 306, 307] making these values the most reliable benchmark for the electron affinity. Using typical S-factors for TiO_2 of at least 0.1 (strong pinning) and 0.3 (strong-moderate pinning), as presented above, one can thus narrow the variation ranges for the CBO to TiO_2 depending on the contact material to ∼0.4-0.7 eV for Ti or Al, ∼0.6-0.9 eV for Au, ∼0.7-1.0 eV for Pt and ∼0.35 to 0.7 eV for p^+-Si. So, to summarize, the issue of the quite uncertain parameter space for the CBO between the cathode and TiO_2 is tackled in kMC by simply varying the CBO $\phi_{B,l}$ in a range from 0.3 eV to 1.2 eV with fine step sizes down to 0.01-0.05 eV for all investigated samples, as documented in Tab. 6.4. This variation of $\phi_{B,l}$, indicated by the blue dashed lines in the bandstructures sketched in Fig. 6.14a, is also in qualitative agreement with experimental values for barrier heights on TiO_2, which are maximally 1.2 eV for all electrode materials considered in this study. By the pinning of the cathode Fermi level in the bandgap at the CNL of TiO_2 according to Eq. (6.3) also the Fermi level in TiO_2 is fundamentally defined over the whole oxide structure. This is indicated by the slight non-linear drop of the Fermi levels in the very vicinity of the TiO_2-metal-interface

in Fig. 6.14a and 6.14b. The first image is a sketch overemphasizing this drop (under accumulation conditions in p^+-Si) to illustrate it better, but the latter one is the result of complementary drift-diffusions (DD) simulation of the band bending in TiO_2 performed with TiberCAD[245]. As mentioned before, by these DD simulations it got clear that charge compensation effects can be neglected and the whole oxide can be assumed to be neutral in the kMC-model neglecting drift-diffusion of charge carriers in its CB at the same time. Thus the Fermi-level in TiO_2 can be assumed to drop constantly with voltage throughout the oxide. However, to determine this voltage drop, the V_{ox} in our model, accurately in case of MOS samples, like sample #3 and sample #4 in section 6.3.5[‖], we accounted for the band bending in Si by the results of the DD-simulations for the $Pt/TiO_2/p^+$-Si structure shown in Fig. 6.14b. Therefore, the bias in the experimental curves samples #3 and #4 were rescaled to the simulation parameter V_{ox} according to $V_{ox} = 0.107V_g^2 + 0,4315V_g - 0,0192$ to account for the voltage drop in Si. Thus the merely linear voltage drop in TiO_2 is considered an accurate assumption and the Fermi-levels in the materials are determined basically by the CBOs according to the MIGS-model. Besides, defects are assumed to be positively charged traps at the beginning of each simulations. This is also in accordance with defect formation energies in dependence of the Fermi level in TiO_2 given in the most important atomistic calculations cited here, i.e. by Yamamoto et. al, Morgan et al. and Déak et al. which usually favor Ti_{int} and V_O, partly also Ti_{Ti} as dominant defects for a Fermi level between 0.3-1.2 eV (=CBO) below CBM[171].[**]

6.3.5 kMC-Fits and Fabrication of Five TiO_2 Samples

By the described compact model and accurate parametrization we were able to accomplish fits to six curves taken from literature, shown in Fig. 6.15a-6.15e. We took samples of nm-thin TiO_2 films deposited by different methods to check, if the parameters for the best fits are consistent with the defect levels in TiO_2, compiled in section 6.3.1, Tab. 6.4, and with the qualitative expectations for the specific way of fabrication, particularly in terms of purity of the crystalline phase and the defects, cf. Tab. 6.4. The five samples were deposited and oxidized at temperatures below 700 °C. This favors the formation of anatase crystals, which the parameterization was focused on. Sample #1, Fig. 6.15a and 6.15b, is a polymorph evaporated by plasma-enhanced atomic layer deposition (PEALD) at 180 °C between two Al contacts.[12] Sample #2, Fig. 6.15c, is reported to be polycrystalline anatase evaporated by PEALD at 250 °C with two Pt contacts.[13]

[‖] Sample #5 had already been corrected for the band bending in Si by the authors in the respective study.

[**] While some groups reported the Fermi level in TiO_2 to be rather shallow ∼0.25-0.4 eV below CBM (which might be the case for illuminated TiO_2 in DSSCs, since $E_F - E_{Fo}$=qV_{oc}), there is – in agreement with our assumptions – a consent by a number of different active groups who calculated or measured the bulk Fermi-level of TiO_2 (static, i.e. without photogenerated or other injected charge carriers) by different methods at about 0.8-1.2 eV below CBM.[10, 182, 307] Such a deep value is also consistent with the "average" difference between the reported widely spread electron affinities (3.2-5.0 eV) and work functions (4.0-5.8 eV) in TiO_2, the typically reported dominant defect levels in the bulk influencing E_F which are located also around 0.8-1.2 eV below CBM, cf. section 6.3.1, as well as the interface CNL of 1.0 eV, a kind of "interface Fermi-level".

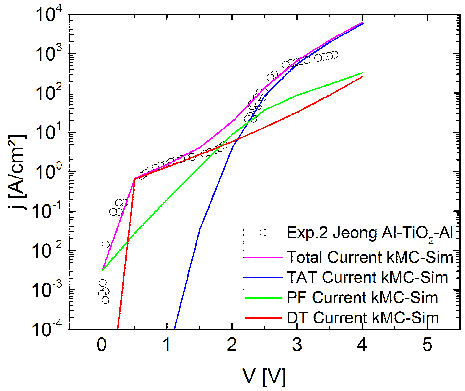

(a) *Curve 1, sample #1, symmetric Al-contacts to ALD-grown TiO_2.*

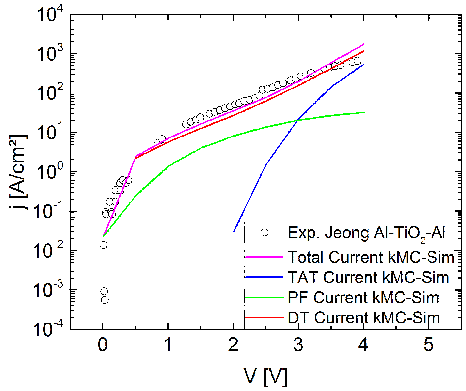

(b) *Curve 2, sample #1, symmetric Al-contacts to ALD-grown TiO_2.*

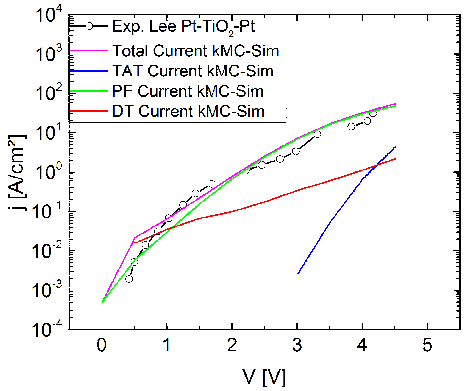

(c) *Sample #2, symmetric Pt-contacts to ALD-grown TiO_2.*

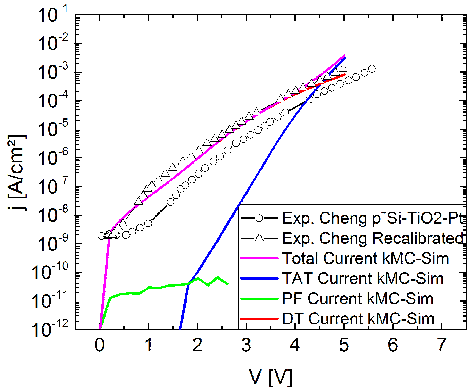

(d) *Curve 1, sample #3, with its DD-recalibration, asymmetric p^+-Si and Al-contacts to PVD-grown TiO_2.*

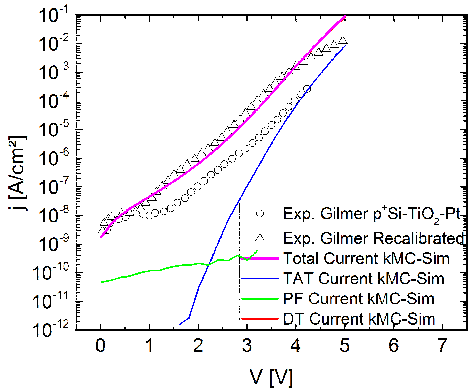

(e) *Curve 1, sample #4, with its DD-recalibration, asymmetric p^+-Si and Al-contacts to MOCVD-grown and annealed TiO_2.*

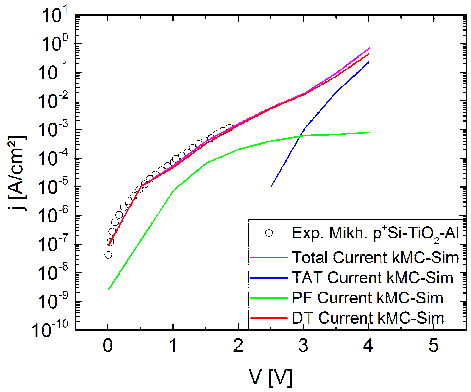

(f) *Sample #5, asymmetric p^+-Si and Al-contacts to PVD-grown and low-T-annealed TiO_2.*

Figure 6.15: *Six jV-characteristics of five differently processed samples. For details on the fabrication process refer to text.*

Sample #3, Fig. 6.15d, was e-beam evaporated from Ti followed by thermal oxidation at 500 °C favoring the formation of anatase.[14] Sample #4, Fig. 6.15e was deposited by molecular organic chemical vapor deposition (MOCVD), subsequently annealed in O_2 atmosphere and showed also predominantly anatase.[16] Sample #5, Fig. 6.15f, was also e-beam evaporated, just as sample #3, however, followed by annealing in O_2 environment at a temperature of 700 °C, which induced typical characteristics of pure anatase, as reported by the authors, and low density of defects, as expected from Tab. 6.4.[15] Note that also sample #5 has Al as injecting electrode, just as sample #1, while samples #2, #3 and #4 have Pt as injecting cathode for the given biasing conditions. The resulting fittings parameters for the jV-profiles of all these samples, given in Fig. 6.15 and 6.18, are summarized in Tab. 6.5. Firstly, one can see that most fitting parameters show an excellent agreement with literature values provided in sections 6.3.1 and 6.3.3. Particularly, the thickness, a very sensitive model parameter, was rigorously fixed to the experimental values in the specific studies. For the CBOs fitting values were obtained that are considerably lower than the simple Mott-Schottky-barriers for all stacks. But they agree well with the ones expected from the MIGS-model, as documented in section 6.3.3 and Tab. 6.5. The effective oxide mass, as only slight outlier, had to be set to 3 m_0 for sample #2, but this is still well inside the range of literature values. All further, material specific parameters, i.e. the bandgap, the CBO to the anode, the electrode mass and the optical dielectric constant could be fixed to the reference values. This proves the validity and consistency of kMC-model and parametrization in the first place. Secondly, it is consistent that the defect densities are comparably small in all samples, because all the deposition methods (PEALD, PVD, i.e. e-beam and/or thermal oxidation, and MOCVD) are considered to keep defect densities rather low in general. From the two curves of the ALD-grown sample #1 we could extract a defect density of $5{\times}10^{18} cm^{-3}$, in agreement with the statement that ALD keeps defects low, cf. Tab. 6.4. Sample #2 has a higher defect density of $2 \times 10^{19} cm^{-3}$ in our simulations which might be because it was not annealed. Besides, for such a high thickness higher defect densities are still not influence current transport via TAT. Sample #3 is e-beam-deposited, a PVD-technique, which is supposed to induce more defects and correspondingly ends up into $1 \times 10^{19} cm^{-3}$. For sample #4 we report only $5 \times 10^{18} cm^{-3}$ again, which agrees well with MOCVD to give less defects. Also for sample #5 best fits needed a defect density as low as $5{\times}10^{18} cm^{-3}$, although it was e-beam-deposited. But this sample was annealed in O_2 atmosphere which decreases defects, or oxygen vacancies, in particular. In total, we could justify in the first place the relation between defect densities and fabrication methods for the specific samples.

6.3.6 Fabrication-Dependent Current Transport Channels through Defects in TiO_2

Most importantly, kMC is uniquely able to itemize the total current into its components. This allowed to analyze the five implemented current channels for all five simulated TiO_2 samples in terms of defect levels and how these are correlated to the processing

Parameter	Reference (cf. text)	Variation range	kMC-Fit #1 Al/TiO_2/Al ALD	kMC-Fit #2 Pt/TiO_2/Pt ALD	kMC-Fit #3 p-Si/TiO_2/Pt e-beam/Ox.	kMC-Fit #4 p-Si/TiO_2/Pt MOCVD	kMC-Fit #5 p-Si/TiO_2/Al E-Beam
$\phi_{B,l}$ [eV]	0.3-1.2	0.3-1.5	(a) 0.48 // (b) 0.52	0.6	1.0	1.01	0.88
n_D [cm^{-3}]	10^{18}-10^{20}	10^{18}-10^{20}	5×10^{18}	2×10^{19}	1×10^{19}	5×10^{18}	5×10^{18}
E_D [eV]	0.3-1.3	0.2-1.5	(a) 0.24 // (b) 0.38	0.4	>1.1	>1.06	>0.65
m^*_{ox} [m_0]	0.5-15	0.5-5.0	1.5	3	0.48	0.5	1.0
m_{cat} [m_0]	0.28	0.3	1	1	0.3	0.3	0.3
ϵ_{opt,TiO_2}	5.8	5.8±1	5.8	5.8	5.8	5.8	5.8
$\phi_{B,r}$ [eV]	0.5-0.7	0.3-1.5	0.4	0.5	0.4	0.4	0.4
E_g [eV]	3.2	3.2	3.2	3.2	3.2	3.2	3.2
d [nm]	From spec. study	Ref.±20%	15	60	18	19	15

Table 6.5: *Overview on fixed or varied parameter values of the kMC-model for the 6 fitted curves of the 5 samples.*

of the TiO_2 films. Starting with the ALD-grown samples #1 and #2 the formation of energetically shallow Ti_{int} is approved corresponding to the expectations from the less pure fabrication method ALD. It fundamentally relies on the chemical reactions of the educts on the target surface. This allows for a good control of the growth of single layers, i.e. the thickness, and few extrinsic defects, but cannot guarantee the best crystallinity as compared to PVD-methods, cf. Tab. 6.4. From the subsequent discussion of the simulation results one can see that the expectations agree well with the kMC-fits which are achieved by shallow traps at $E_D = 0.24$ eV in particular from the TAT branch in curve (a) of sample #1. Same holds for sample #2 where the dominating PF branch is caused by traps located at $E_D = 0.4$ eV.
To validate the simulated curves physically, one can start from Fig. 6.15a, curve (a) of sample #1, where DT prevails below 2 V without TAT and with only slight PF contributions for the lowest bias, while it is surpassed by TAT above 2 V. Using a moderate defect density of only $5\times10^{18}cm^{-3}$, the kMC-simulations show that only TAT via shallow traps at $E_D = 0.24-0.26$ eV, can explain the pronounced upswing in current density by more than two orders of magnitude above 2 V. The cited study refers to the Al/TiO_2/Al-junction as a memristor-stack, hence it refers to this upswing as switching from "OFF" to "ON" state when applying forward bias. So curve (a), Fig. 6.15a, starts with the OFF or high resistance state for this memristor sample and switches to ON

state by this upswing. For the ON state in resistive switching studies the existence of conductive filaments is assumed. These are essentially pictured as understoichiometric spatial regions of in TiO_{2-x} of small lateral extensions stretching from anode to cathode inside TiO_2. Whether such regions with strong accumulation, i.e. high density, of active, unfilled V_O^+ oxygen vacancies in them extends completely to the cathode for the respective basing, or whether there is still a nm-thin layer of insulating TiO_2 inside, determines the ON or OFF state respectively. Thus, simulating defects distributed equally over the whole oxide range at high density in our model applies to this picture of the ON state. However, even for high defect densities up to 10^{20}cm^{-3}, corresponding physically almost to a transition into the Magnéli phase already, the correct current densities could not be achieved in our simulations for typical defect levels of oxygen vacancies deeper than ∼0.5 eV in the bandgap. But the latter value is below the border of deep defects in our categorization according to the literature values from section 6.3.1. Thus, we argue TAT through shallow traps with 0.2 eV$\lesssim E_D \lesssim$ 0.6 eV is accountable for the high currents observed e.g. in the ON state of TiO_2 memristor structures, if physically viable defect densities (resembling still TiO_{2-x} and not Ti_4O_7 already) between 10^{18} cm^{-3} and 10^{20} cm^{-3} are allowed. This energy range corresponds exactly to Ti_{int} according to our literature review. Curve (b), Fig. 6.15b, is the high resistive state of the same sample (after the switching to OFF state), but for reversed polarity. Switching cycles are repeatable, so the defect density should be the same as for curve (a). But to fit curve (b) of sample #1 by kMC, DT must be the dominant current channel over the whole measurement range up to 4 V. DT dominated the fit, while keeping the same defect density as for curve (a), i.e. 5×10^{18}cm^{-3}, and reducing the injection barrier only slightly to $\phi_{B,l} = 0.48$ eV. But the fit required trap levels to be no shallower, i.e. to be deeper, than $E_D = 0.38$ eV for curve (b) of sample #1 under the given restrictions for the other parameters. Otherwise the blue TAT branch in Fig. 6.15b is too high and would dominate for only slightly lower defect energies or higher defect densities. Thus we further argue that TAT in shallow defects is the transport channel which is responsible for the high-conductive ON-state in memristors and which is deactivated when switched to OFF state, potentially by ion migration, but possibly also due to a trap-controlled SCLC. But this is still discussed heavily in literature and needs a closer investigation by our kMC-model. For the moment we can only state that for the OFF-state of a TiO_2 memristor stack as in sample #2, assuming the insulating, low-defective region stretches over the whole oxide, trap shallower than $E_D = 0.38$ eV cannot be present at physically viable densities of 5×10^{18} cm^{-3} $\lesssim n_D \lesssim$ 1×10^{20} cm^{-3}, in the insulating layer, or alternatively, shallower traps could still be present at high density, but are somehow "deactivated". Only this way the blue TAT branch in Fig. 6.15b does not alter the fit. Traps shallower than $E_D \approx 0.2$ eV would require an unphysically low density of defects, i.e. virtually 0. To conclude, we argue that the shallower traps are responsible for the ON-state and must be deactivated or tremendously reduced in density. Furthermore, the fact that TAT based on Miller-Abrahams-hopping in our model fits the higher voltage range of curve (a) shows well that small polaron hopping prevails in TiO_2 and that it

can explain the trap-related transport through the TiO_2 films in accordance with Setvin et al. and Henderson.[143, 270]
Sample #2, Fig. 6.15c, showed also shallow traps at $E_D \approx 0.4$ eV, most probably from Ti_{int}. With 60 nm thickness Sample #2 was the thickest of all simulated TiO_2 structures. The defect density of $2{\times}10^{19}\text{cm}^{-3}$ corresponded to 120 defects in the total simulation volume which is close to the computational limit of the method.[††] Comparing the total jV-characteristics and single current components of the MOM-structure to the two MOM-curves of sample #1, one clearly observes a reduced SE/DT/FN-channel. Taking into account the CBO of 0.6 eV, which is comparable to the one ∼0.5 eV of sample #1, this observation is consistent with the four times larger thickness, since for a 60 nm thick oxide DT is expected to be exponentially less relevant. Most remarkably, the FN channel is supposed to start at voltages above the voltage equivalent of $\phi_{B,l} \approx 0.6$ eV and rises quickly for higher voltages and becomes higher than the SE/DT-part at about 2 V here, marked by the step-up in slope for the red curve in Fig. 6.15c. This step-up is noteably smaller in sample #2 than for sample #1, whereas the current density for sample #2 is dominated and clearly explained by PF emission from shallow traps located ∼0.4 eV below CBM. This is consistent with the expectations, because it has a 0.1 eV higher CBO due to the high work function electrode material Pt in contrast to the Al as cathode for sample #1 and it is four times thicker. Thus DT must decrease, TAT is also less probable and only PF from shallow traps can be responsible.
From these validations one can see that the kMC-results on sample #1 and #2 are plausible with respect to expectations. The derived shallow traps levels located at $E_D = 0.24$ eV and $E_D \gtrsim 0.38$ by the TAT branch in curve (a) and (b), respectively, of sample #1 and at $E_D = 0.4$ eV for sample #2 located by the dominating PF branch, agree both with the energetic region "A" of 0.2-0.6 eV under which the Ti_{int} values were subsumed from our review in section 6.3.1. Furthermore, besides the agreement with literature values and the valid parametrization by our kMC-simulated jV-fits, we attribute these defect energies to Ti_{int} defects, because the existence of interstitials instead of vacancies agrees better with the worse crystallinity expected from the less pure chemical-growth-method, ALD, which is known to cause intrinsic, i.e. not impurity-induced, Ti interstitials [‡‡],as detailed also in section 6.3.7. For the jV-profiles of the anatase films on p^+-Si in sample #3 and sample #4 the experimentally applied gate voltages had to be recalibrated to the oxide voltage drop by the formula from the drift-diffusion-simulations given in section 6.3.2 to account for the band bending in the accumulated Si substrate. They were fabricated by the purest methods and show jV-characteristics similar to each other corresponding to their nearly identical thicknesses, 18 nm and 19 nm. The jV-fits require also very similar further fitting parameters, especially trap levels deeper than 1.1 eV and 1.06 eV, respectively, which we will attribute to oxygen vacancies by subsequent arguments. Only the effective mass was varied slightly between the two and for the lowest

[††]But still the highest number related defect sites found in state-of-the-art literature on kMC-simulations of jV-curves.
[‡‡]These stand also few 0.1 eV deeper in energy than the extrinsic Ti interstitials, cf. section 6.3.1

voltages the model still deviates slightly from the measurements, but in an acceptable range. Above ∼0.3 V and ∼0.5 V, respectively, DT and FN dominate the current densities over the remaining bias range. Though their thickness was comparable or even lower than for the other three samples, only DT/FN over a higher barrier and, in particular, PF from traps deeper than 1.05 eV could explain the low current densities for samples #3 and #4 which stands in contrast to the findings on the other samples. Traps deeper than 1.1 eV and 1.06 eV, respectively, are necessary to reduce PF and TAT sufficiently so that they do not superimpose on the fitting DT-branch at lowest or highest bias, respectively. Defect densities above $\sim 10^{19}\text{cm}^{-3}$ are possible, too, to find a fit, because they increase PF and TAT only linearly according to the model, but the sensitive parameter defect energy E_D must not be lowered by more than ~ 0.05 eV, as otherwise the fit is not possible anymore. This strongly indicates such deep oxygen vacancies which can be present at moderate to high defect densities and excludes the existence of Ti_{int}. This is also in agreement with the purer and less-defective fabrication methods of these samples. Thus for sample#3 e-beam-evaporation, a PVD-method, i.e. least interstitials, and moderate defect densities. So the e-beam-evaporation of sample #3, indicates high crystal phase purity and hence no shallow defects due to interstitial Ti atoms, so that for the e-beam-grown anatase film of sample #3 such deep traps at low density are favored. Sample #4 was produced by MOCVD, a chemical growth method which is considered moderately pure, cf. Tab. 6.4.[73] However, it was combined with a high-T annealing step, reducing extrinsic and intrinsic defects and favoring the crystal formation. Thus the crystallinite is improved, Ti_{int} reduced and deeper V_Os are pronounced. So the potential energetic location of traps below 1.06 eV in this sample makes sense. Eventually, for sample #3 and #4 defects shallower than $E_D \lesssim 1.05$ eV are not present, since they would influence transport otherwise. Values for E_D around 0.9-1.0 eV lie perfectly in the range of the peak commonly observed by spectroscopic measurements (mostly PES,XPS,UPS) and in the range of the huge compilation of DFT calculations for oxygen vacancies in the V_O^+ state which is supposed to enable electron capture and release from states at ∼0.7-1.2 eV, or to be more precise, at ∼0.9-1.1 eV. Hence we suppose from the agreement of model and literature, that if defects are present at physically viable densities of $5 \times 10^{18}\ \text{cm}^{-3} \lesssim n_D \lesssim 1 \times 10^{20}\ \text{cm}^{-3}$, these defects are deep oxygen vacancies at ∼0.9-1.1 eV.

Besides, one can compare the absolute magnitude of the PF branches in samples #3 and #4 to the two of sample #1 which has a comparable thickness, but a several 100 meV higher defect level. Obviously, PF is strongly reduced and even clearer dominated by DT in samples #3 and #4 than in sample #1 where PF emission from the shallower traps still contributes slightly to the total current. In contrast to that the two minor relevant PF branches of sample #1 are both still comparable in magnitude to the PF channel of sample #2, although the oxide thicknesses deviate strongly from each other. Thus one can furtherly observe that PF emission from traps is thickness independent, but scales strongly with the depth of the defects. Consequentially, PF, even from deep traps, will always dominate the transport, if the oxide is thick enough to reduce the DT/FN

branch sufficiently, or the other way round as for sample #2. Conclusively, as one would expect it physically, our kMC-model consistently demonstrates that it is the balanced interplay of CBOs, defect levels and the oxide thickness that determines the current characteristics. Finally, comparing the MOS-contact of sample #5, by the kMC-results in Fig. 6.15f shallow traps can be determined as insignificant in agreement with the higher purity expected from PVD growth. So the simulations approve again that PVD-grown TiO_2 should have less shallow Ti_{int} induced by intrinsic or extrinsic defects. To derive this statement, one first has to note that this curve, which exhibits a remarkably low current density, is well explained by a dominating DT transport mechanism despite of the relatively high oxide thickness of 15 nm and the high barrier of 0.88 eV for this fit which reduces DT in the first place. Hence, DT can only be visible, if rather shallow traps have either vanished or are sufficiently low in density for this sample, so that PF or TAT are insignificant. Few shallow traps can be understood also in terms of sample processing which was e-beam-evaporation, i.e. a PVD-method, of TiO_2 and subsequent O_2-annealing.[15] The first method implies higher crystal purity, cf. Tab. 6.4. This means less structural defects and less extrinsic dopants, so less intrinsic or extrinsic Ti_{int} in the end, while annealing must reduce the V_Os. Thus in agreement with expectations from Tab. 6.4, the kMC-fits were only possible for a defect density of only $5{\times}10^{18}\mathrm{cm}^{-3}$ with defects located shallower than 0.65 eV. For only 0.1 eV shallower defects the number of defects would have to be decreased to virtually 0, so resembling lower limits of physically viable defect density for dominant defect species. Otherwise the slightly contributing PF branch in Fig. 6.15f would get too strong, i.e. comparable in strength to DT, and thus alter the simulated trend from the experimental one. If one assumes a higher defect density, e.g. $1{\times}10^{19}\mathrm{cm}^{-3}$ the traps must in turn be even deeper than 0.65 eV to avoid an experimentally not visible PF- or TAT-like-trend. Hence defects cannot be closer to the CBM than 0.65 eV in this sample. Referring to section 6.3.1, this excludes the measureable presence of Ti_{int} energy levels, which were localized from the given references in the energetic region "A", i.e. around 0.2-0.6 eV. This agreement provides strong evidence that the higher purity expected from PVD growth implies less shallow Ti_{int} caused by intrinsic defects or extrinsic impurities. In contrast to that, deeper defect energies would not alter the fits and are possible, too. So the value of $E_D > 0.65$ eV of sample #5 agrees, if not supports our findings that for PVD-grown samples oxygen vacancies are dominant and they are located around 0.9-1.1 eV. In terms of the fabrication method, also referring sample #3, deeper defect are even likely and can be explained by a higher crystal purity exhibiting only deep V_O remaining in the oxide potentially at a higher density than $\sim 5 \times 10^{18}\mathrm{cm}^{-3}$, but definitely excluding Ti_{int}. This in agreement with the fabrication method, as compared to e.g. the fits for ALD-grown samples #1 and #2 which both required shallow traps and whose fabrication method is supposed to favor the formation of interstitials. In total, if e-beam evaporation is combined with an annealing step, as for sample #5 the best sample quality of all methods enlisted in Tab. 6.4 in terms of crystallinity and defects is produced.

6.3.7 Discussion of Defect Levels in ALD- and PVD-grown TiO_2 films

In total, one can derive from the presented kMC-simulations that TiO_2 films formed by a well-controlled e-beam evaporation-process followed by an optional low temperature annealing, but also MOCVD-grown-TiO_2 accompanied by an obligatory annealing step, favor the formation of anatase films with (i) deep defects at (ii) sufficiently low density. PVD methods in general, as confirmed by the model, keep defects deep and low in density, if combined with annealing, and thus prevent TAT or PF current channels from increasing the current density. Combined with a high CBO, achieved by providing clean surfaces and low pinning of the Fermi-levels of the (quasi-)metallic substrates in the CNL of TiO_2, located 1.0 eV below CBM, we suppose PVD-methods to be preferential to guarantee low current densities and (electronic) dominance of deep oxygen vacancies, esp. when combined with annealing. In contrast to this for TiO_2 grown by ALD, expected to be less pure in terms of crystallinity, the electronically dominant traps are clearly categorized as shallow and they do not vanish by annealing, like seen for sample #1. The existence of Ti_{int} as such in the ALD-grown samples #1 and #2 confirmed by the simulations, has been repeatedly presumed and measured in experiments and DFT calculations. Most prominently, in a recent thorough PES-study by Reckers et al. shallow gap states were once more located at ∼0.2 eV below CBM in annealed, low-temperature-ALD-grown anatase films.[167] Apparently, similar experimental conditions apply for the fabrication of samples #1 and #2 which were both ALD-grown at low temperature. Assisted by the defect overview in section 6.3.1, our kMC-approach provides evidence that the shallow traps in TiO_2 are Ti_{int} and, most particularly, ALD-growth favors their formation. Since shallow traps dominate the transport even for ∼60 nm thick films, as in sample #2, or thicker ones, ALD-growth is not the method of choice, if leakage currents should be kept low for the specific desired application, such as in gate dielectrics for MOSFETs or capacitors. Deep traps might be present there, too, but their contributions to the defect related current channels are orders of magnitude lower. Finally, by comparing the trap levels from the kMC-fits to the structured overview on the literature values of different defect types in section 6.3.1, the shallower ones in TiO_2, i.e. those in the range of 0.2-0.4 eV, are also attributed to Ti interstitials, while deep defects, i.e. those around ∼0.9-1.1 eV, as oxygen vacancies. Further defect types which were not dominant in these samples can, of course, still coexist in the titanium oxide layers and are not accessible for investigations by our method as only the hypothetically dominant defect type is reflected by the model. In total, by the measured jV-profiles from literature we found a consistency of (i) the broad literature of DFT calculations and spectroscopic experiments on defects in TiO_2, (ii) expectations from fabrication methods and (iii) our kMC-simulations.

6.4 kMC-fits and Parametrization of Transfer-Printed AlO_x-MOM-layers

6.4.1 Motivation for kMC-Simulations of Transfer-Printed AlO_x-layers

Research on thin alumina films started already decades ago, mainly due to their potential as ultrathin tunneling barriers promoted by their outstanding property to form compact, but still insulating dielectric films of only 2-3 nm thickness. [308, 309, 310] In fact, aluminum oxide, AlO_x, turned out to be useful for many more electronic applications such as silicon-on-sapphire for CMOS technology [311, 312] high-temperature ceramics, organic devices [313, 314], THz-nano-rectennas [72], nTP tunnel diodes [57], but also as a gate metal on III/V-semiconductors [315, 316, 317] and for resistive switches [318, 319]. In these applications AlO_x films are mostly produced by ALD [286, 315, 320], RIE-plasma-oxidation [251] or thermal oxidation [308].
Al-Al_2O_3-Al tunneling contacts were also addressed analytically already in 1963[321] while more refined models for ultrathin AlO_x have been derived later on, taking defects into account.[322] Recently, the types of defects in AlO_x, especially oxygen vacancies, have been investigated due to their influence on conduction pathways, like TAT and field-assisted PF emission. They are even supposed to form a conducting band depending on their state of occupation which is decisive in resistive switches.[319] The charge state of defects is another critical issue in alumina. In this context more and more density functional theory (DFT) studies, see section 6.4.3, provide significant information on defects in aluminum oxide. However, ab initio methods are limited in their practical viability, e.g. for deriving current densities, if multiple transport channels are relevant.
Therefore, we employed kinetic Monte Carlo (kMC) simulations to study charge transport through ultrathin AlO_x-films for MOM-applications. KMC has established as a computational tool, next to drift-diffusion-simulations, to bridge the gap between the applicability of ab initio calculations and the explanatory power of experiments. [42, 219] Firstly, our extensive kMC-model[189] for the current density through conductive oxides is briefly summarized. Secondly, we compare our simulation to experimental jV-data from Al/AlO_x/Au-junctions, where a thin AlO_x-film was prepared by a combination of oxygen plasma and thermal treatment of the Al electrodes prior to Au deposition. From this (validation) we obtain a parameterization of our model which was justified by recent DFT-studies on defects in alumina. Afterwards, most importantly, we extensively employ the validated model for the theoretical investigation of experimentally less accessible regions, i.e. we vary oxide thicknesses, barrier heights, effective masses, defect distributions and defect levels in the AlO_x layers, which were normally less than 8 nm thin in the experiments. Finally, we draw conclusions from the parametrization and discuss practical implications of the parameter-dependent characteristics of the oxide-layer.

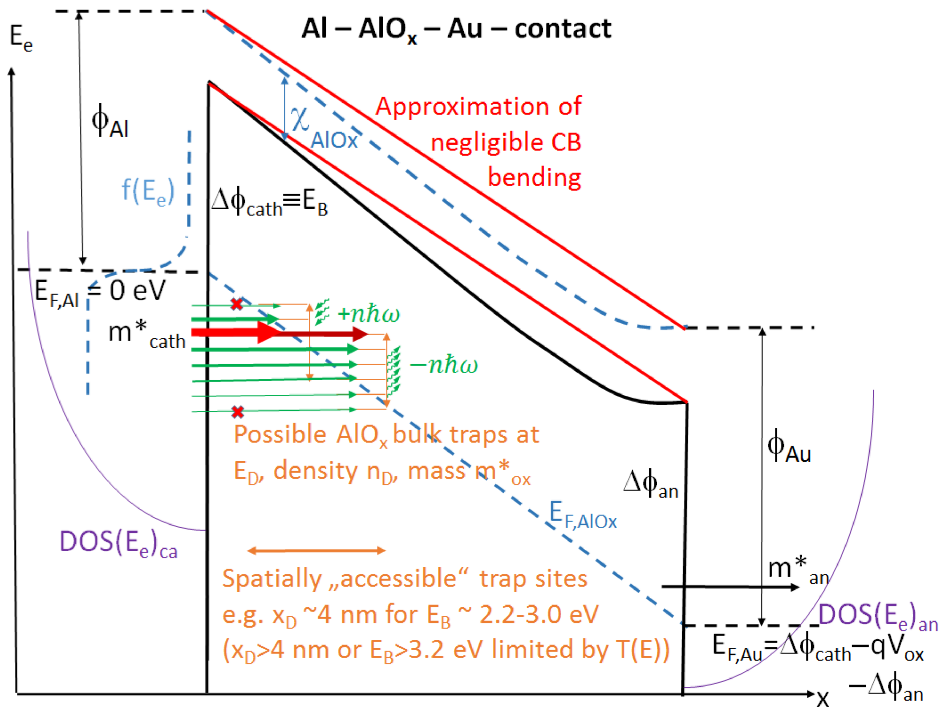

Figure 6.16: *Electronic band structure of Al-AlO_x-Au under bias subject to our kMC-model - Fermi level $E_{F,Al}$ (dashed line) is taken as reference point (0 eV). CBOs $\Delta\phi_{ca}$ and $\Delta\phi_{an}$ obey Mott-Schottky-rule and, with a linear voltage drop $V_{ox}/d \cdot x$, they determine $E_{F,Au}$. Bands are assumed to bend only in negligibly small regions at the anode, so are approximately linear in voltage,(red instead of black line) just as $E_{F,AlOx}$. Electrons are injected from Al into trap levels at E_D below CBM in AlO_x, either elastically (red arrows) or inelastically (green), i.e. phonon-assisted (energy $\hbar\omega$). Injection is favored for "resonance" of $E_{F,Al}$ and E_D, i.e. there is a trade-off between pre-defined trap levels E_D and (random) trap locations x_D determining the injection rates. For further details see text.*

6.4.2 Methods - kMC-model for Al/AlO_x/Au-layers

The kMC-model shall be briefly sketched here. For a detailed description of our kMC-simulator, we refer to [6, 189, 190]: According to the band diagram in Fig. 6.16 and the summary of the simulation parameters in Tab. 6.6, we included five, partly correlated, electron transport processes (holes are omitted due to the high VB offset) chosen in each simulation step after the Gillespie algorithm [41] to simulate current densities through the MOM-structures. Firstly, SE, DT and FN are subsumed into the Tsu-Esaki-Formula, given in section 5.1.[222]. Assuming metallic contacts the effective electron mass in the electrodes is the free electron one. At room temperature and very high electric fields >0.1 MV/cm only FN-branches and neither SE nor DT were visible in our simulations. An important correction to [6, 190] was the energy-dependent transmission coefficient

$T(E)$ for electrons tunneling between x_0 and x_1 calculated in WKB-approximation as

$$T(E) \approx e^{-\frac{4d}{3eV_{ox}}\sqrt{\frac{2m^*_{ox}}{\hbar^2}}\left[(\phi_B - e\frac{V_{ox}}{d}x_1 - E)^{3/2} - (\phi_B - e\frac{V_{ox}}{d}x_0 - E)^{3/2}\right]} \tag{6.5}$$

where $V(x) = \phi_B - e\frac{V_{ox}}{d}x$ is the x-dependent potential, $\phi_B = \phi_{B,Al/AlOx}$ is the barrier height between Al and AlO_x and m_e^* is the effective mass in AlO_x, cf. section 5.1. Although the model is sensitive to E_B, omitting the image potential for tunneling electrons is a valid approximation referring to conclusions by Weinberg [227, 228] and Schenk [230], presented in 5.1.2. According to them the image potential reduces E_D by a constant value. Evaluating T(E) numerically results in ~ 0.15 eV higher barriers on average which must be simply added on the fitting value in section 6.4.3. As we have asymmetric electrodes, i.e. barriers, for the special case of tunneling to $x_1 = d$, the second barrier height ϕ_B in Equ. (6.5) was set to $\phi_B = \phi_{B,AlOx/Au} = 4.0$ eV. Considering TAT, first the elastic and inelastic injection rates between defect levels at E_D with respect to CBM and the electrodes were employed according to [6, 189, 229, 236, 291] including multiple-phonon-assisted-processes. Carrier transport processes between traps in AlO_x were modelled by Miller-Abrahams-rates [292] according to the assumption of hopping of small polarons in AlO_x [323], as discussed in section 6.4.3, and excluding recently employed phonon-assisted ionization rates after Ridley [234]. Finally, electrons captured in a trap can be emitted by field-assisted PF-emission according to the 3D-PF-emission formulas in [188, 243].

6.4.3 kMC-Model Validation by Transfer-Printed Al/AlO_x/Au-layers

With the kMC-simulator being validated in several studies [251, 286, 313, 314], we shall concentrate here on the accurate parameterization of the model with respect to defect levels. In these terms, Matsunaga et al. identified neutral oxygen vacancies V_O^0 in bulk α-Al_2O_3 as donors about 2.9 eV below CBM,[324] confirmed by Carrasco et al. who positioned them as the dominant defect about 3.2 eV below CBM (and slightly below E_F).[323] To overcome the problems of LDA or GGA in DFT, which underestimate the bandgap, Weber, Janotti and Van de Walle used GGA methods with hybrid functionals for κ-Al_2O_3. They derived the dominant native defect levels to be oxygen vacancies in different charge states, acting as donors at $\sim 2.8-3.0$ eV below CBM (Further defects: 3+ Aluminum interstitials (Al_i^{+3}), and Al vacancies (V_{Al}^{-3})).[325] Similarly, for α-Al_2O_3, they reported most interestingly in our terms, that V_O and Al_i are the dominant defect types located at ~ 4.1 eV and ~ 1.9 eV below CBM, respectively, and also transition levels due to Al dangling bonds at ~ 2.8 eV below CBM.[326] Most recently, Liu, Lin and Robertson provided defect levels for both θ-Al_2O_3 and amorphous (am-)Al_2O_3, i.e. V_O^0 levels near midgap at 3.1 eV, V_O^+ at 2.8 eV below CBM for θ-Al_2O_3 and V_O^0 levels in amorphous-Al_2O_3 at 2.0 eV.[169] However, the latter value also suffered from an underestimation of the bandgap being only 6.2 eV. As we expect to get primarily amorphous alumina from our plasma oxidation process, this latter value is the most important reference here. To

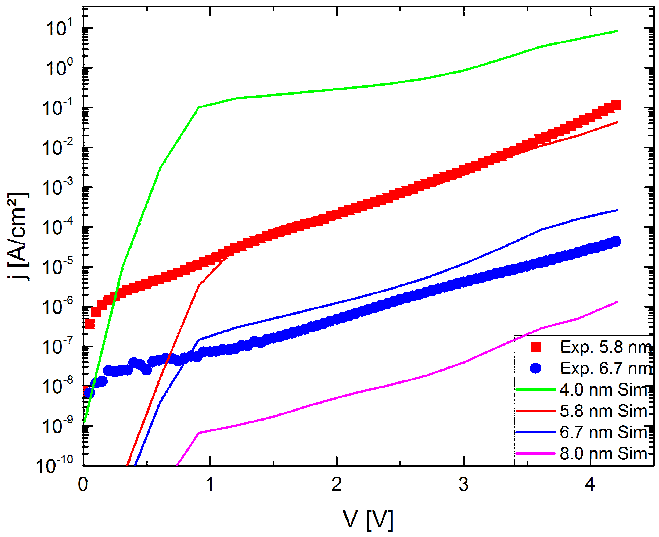

Figure 6.17: *Two fits to experimental curves for two different measured thicknesses (5.8 nm, red and 6.7 nm, green) and two further simulated thicknesses (4 nm, green and 8 nm, pink). All model parameters were kept constant, except defect levels deviating by only 0.2 eV.*

correct it for the underestimated bandgap, we assume to have the usually cited bandgap of 6.5 eV and linearly transform the defect level accordingly to 2.1 eV. The reported values categorized by defect types and phases differ just slightly and due to their approved methodology we considered the values by Robertson and van de Walle as the most reliable ones. The cited authors agree that electrons are localized in the V_O or Al_i defects. Thus hopping conduction via small polarons must be the correct trap-trap-transport mechanism, as outlined in the model section. Because the defect levels are the most critical parameter for the transport processes then, we performed a full parameterization of the defect values between 2.0 eV up to 3.2 eV with 0.2 eV step size in our simulations. For the next critical parameter, the trap mass, we stick to a smaller range of 0.2-0.4 m_0 at 0.05 m_0 step size, according to common literature values for Al_2O_3, like 0.25 m_0 or 0.35 m_0.[322] The same is true for the electron affinity of aluminum oxide which we assume to be $\sim 1.0-1.3$ eV [248] resulting into a CBO of $\sim 2.8-3.1$ eV to the Al cathode (work function 4.1-4.2 eV [72]) and $\sim 3.6-4.3$ eV to the Au anode (work function 4.9-5.0 eV [327, 328]). The bandgap was set to 6.5 eV resembling am-Al_2O_3 [322] We determined the dielectric constant ϵ_r of a plasma-oxidized AlO_x layer with 3.6 nm thickness [251] and a capacitance of 1.68 $\mu F/cm^2$ to be 6.8. While typically a value of $\sim$ 9.0 is cited for stoichiometric Al_2O_3 [286], our value is in good agreement with other plasma-grown AlO_x dielectrics.[314] With $\epsilon_r = 6.8$, the thicknesses of different plasma-grown oxide layers could be estimtated from CV-measurements, yielding capacitances of 0.9 $\mu F/cm^2$ and 1.04 $\mu F/cm^2$ and corresponding AlO_x thicknesses of 5.8 nm and 6.7 nm, respectively.

Reference values and variation ranges of these parameters are summarized in Tab. **??**. Using this parameterization, the model could provide well matching fits to experimental jV-curves, shown in Fig. 6.17. It must be noted that the parameter set could be defined well without any further experimental anchor points. Nonetheless, the parameter set is in excellent agreement with cited literature values, especially the extracted barrier height of 2.8 eV and the effective mass of 0.35 m_0. We can therefore infer that the parabolic approximation (EMA) must be valid for the effective mass. The slight deviation of 2.8 eV barrier height from the theoretical and experimentally-validated values of ~3.0 eV, would most probably vanish when using a numerical evaluation of the transmission coefficient including image forces, but the analytical computation of $T(E)$ employed by us neglects the image potential in favor of being several times faster. This offers the advantage of covering a broader parameter range without a severe systematic change of the physical processes. Moreover, our barrier height must only be increased by ~0.15 eV to obtain the "effective" value from experiments, as stated already by Weinberg earlier. [225] The defect density of $4 \times 10^{18}\mathrm{cm}^{-3}$ is in accordance with typical values for oxide trapped charges $2 \times 10^{12}\mathrm{cm}^{-2} = (8 \times 10^{18}\mathrm{cm}^{-3})^{2/3}$ for ALD-grown AlO_x. [308] Considering the broadly spread values of different defect levels in Al_2O_3, we tend to attribute the defect values of 2.3-2.5 eV, extracted by us, to oxygen vacancies in am-Al_2O_3, because they stand close in energy at ~ 2.1 eV, are supposed to be dominant [169] and the plasma process is likely to form an amorphous oxide. Another possible explanation would be the forming of alumina polymorphs, including several phases of Al_2O_3, which exhibit also several energies for the dominant V_O or Al_i, as cited above. Then the kMC-value could resemble merely a "statistical average", but the implementation of several defect types would be necessary to parametrize the AlO_x correctly. This would increase the parameter space to an impracticable extent. As discussed in the next section we are already able to see the relevant transport channels from the presented, sensible approximations (no image force, EMA, hopping conduction instead of multiple-phonon-ionization, just one type of defects).

Parameter	Reference (ab initio) value	Variation range	kMC-Fit-value # 1, d= 5.8 nm	kMC-Fit-value # 2, d = 6.7 nm
$E_{B,Al-AlOx}$ [eV]	2.8-3.0	1.6-3.2	2.8	2.8
n_D [cm^{-3}]	5×10^{18}	2×10^{18}-8×10^{18}	4×10^{18}	4×10^{18}
E_D [eV]	2.0 (α-Al_2O_3), 2.8-3.0 (κ-Al_2O_3)	2.0-3.0	2.3	2.5
m^*_{ox} [m_0]	0.25-0.3	0.2-0.4	0.35	0.35

Table 6.6: *Physical parameters varied in the simulations for the validating fits. Abbreviations: Al: Aluminum, AlO_x: aluminum oxide, B: barrier height, D: defect, ox: oxide.*

6.4.4 kMC-Parameterization of Transfer-Printed Al/AlO_x/Au-contacts

In order to extract further conclusions on the simulated AlO_x gate oxides, we proceeded with its full parameterization on the basis of the validated model. This was done with respect to its sensitivity on the most critical physical parameters, namely (in order of increasing priority) n_D, m^*_{ox}, E_B and E_D, and analyze their effects on the device performance and characteristics of the MOM-structure. Fig. 6.18 depicts the $j_{TAT}/j_{TOT} = j_{TAT}/(j_{TAT} + j_{DT})$, as only TAT and DT are relevant and PF-transport is irrelevant due to generally deep defect levels in AlO_x. If not stated otherwise, in all the plots our best fit values $n_D = 4 \times 10^{18}$ cm^{-3}, $m^*_{ox} = 0.35$ m$_0$, $E_B = 2.8$ eV, $E_D = 2.4$ eV for $d = 6.7$ nm and a typical operating voltage of 4.2 V are kept constant, apart from the parameters varied explicitly. A voltage of 4.2 V has been chosen since it is a typical value for devices and corresponds to a regime where TAT and DT rates become comparable in magnitude and competitive in kMC. In contrast, in Fig. 6.18b 1.2 V is used, as for such low voltages there is only TAT, while for voltages higher than 4.2 V there is only DT/FN visible. These two exemplary voltages mark borders of operating regions of the dielectric, i.e. sufficiently high voltages, at the onset of dielectric breakdown.
In both Fig. 6.18a and Fig. 6.18b one can notice a clear positive correlation between E_D and E_B separating such combinations (E_D,E_B) for which TAT dominates (red) and such for which DT dominates (blue). Both show that the deeper the defects lie in the gap the higher must the barrier be to have mostly TAT as transport channel. However, for 4.2 V, Fig. 6.18a, the barrier value E_B must be higher than for 1.2 V to obtain a dominance of DT over TAT. This is consistent with the expectations that DT increases stronger than TAT for higher voltages. So, SE and DT are strongly suppressed by the high barrier between Al and AlO_x. This is remarkable comparing literature values, or our fittings from section 6.4.3, with the barrier height $E_B \approx 3.0$ eV, TAT should be dominant for the whole simulated range of operating voltages ≤ 4.2V independent of the defect level E_D, but especially for $E_D < 3.0$ eV.
In Fig. 6.18c and 6.18d , showing j_{TAT}/j_{TOT} in dependence of (n_D, E_D) and (m^*_{ox}, E_D) for an operating voltage of 4.2 V and d = 6.7 nm, other values fixed, one can see a transition from TAT to DT as soon as the dominant defect level is deeper than 3.0 eV, independent of the variable effective mass m^*_{ox} or defect density n_D, respectively. Hence, with m^*_{ox} being a material constant, as long as the defect density cannot be driven below the relatively low values of 2×10^{18}cm^{-3}, the TAT-dominated total current in the oxide layer can only be suppressed by having only defects deeper than E_D= 3.0 eV present. Thus, a fabrication method providing a good crystallinity of the particuar phase of Al_2O_3, is preferential.
Figure 6.18e and 6.18f depict j_{TAT}/j_{TOT} over the whole simulated voltage range in dependence of E_D and E_B, respectively. Fig. 6.18e confirms the evident expectation that the deeper the traps, the lower the voltage at which j_{DT} surpasses j_{TAT}, but also shows that for traps shallower than ∼2.8 eV TAT is that high that DT/FN will become visible only for voltages above 4.2 eV. Similarly, in Fig. 6.18f, for barriers higher than 2.7 eV TAT is dominant for all voltages, while for lower barriers DT surpasses TAT for continu-

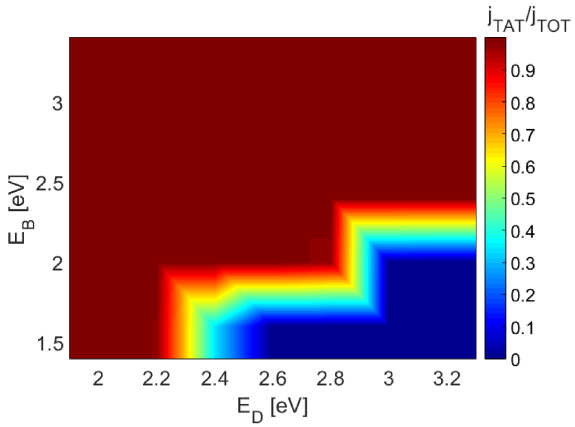

(a) j_{TAT}/j_{TOT} *with* E_D *and* E_B *varied.*

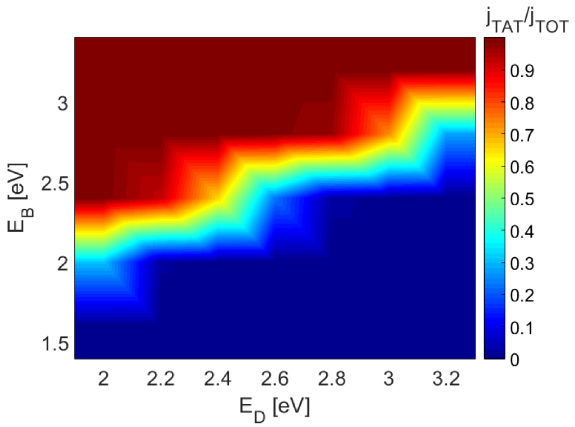

(b) j_{TAT}/j_{TOT} *with* E_D *and* E_B *varied.*

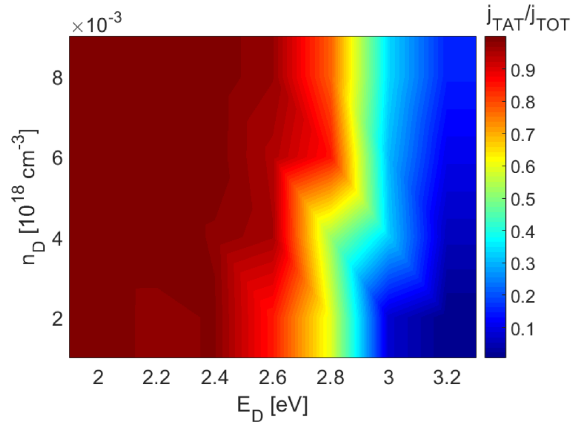

(c) j_{TAT}/j_{TOT} *with* E_D *and* n_D *varied.*

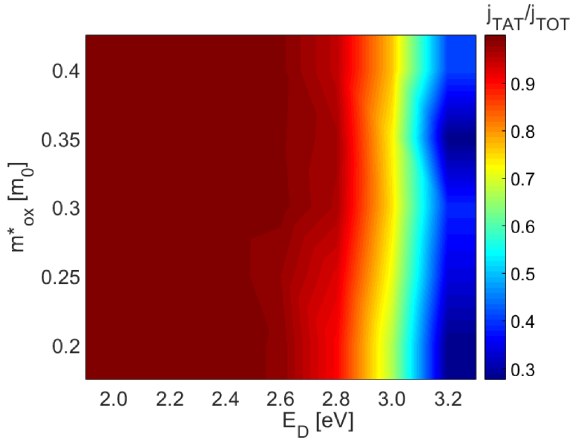

(d) j_{TAT}/j_{TOT} *with* m^*_{ox} *and* E_D *varied.*

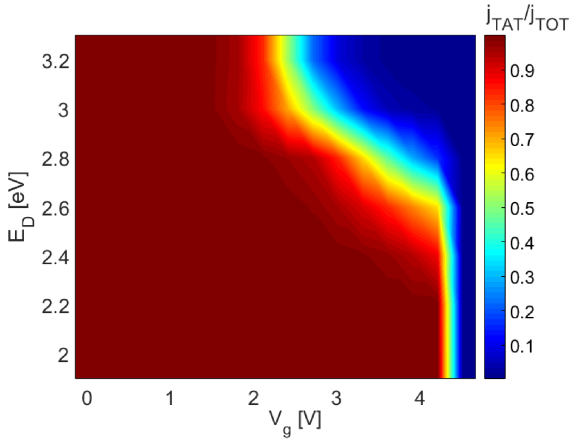

(e) j_{TAT}/j_{TOT} *with* E_D *and* V *varied.*

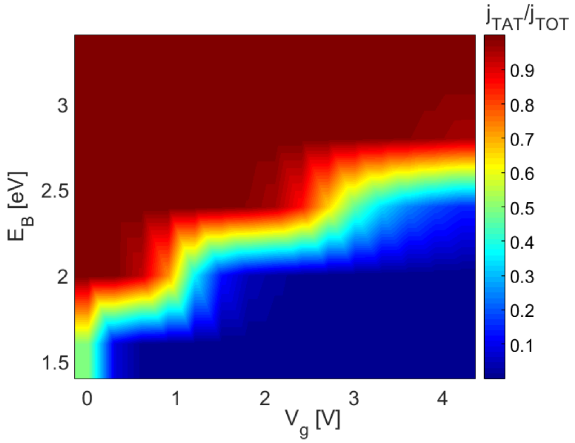

(f) j_{TAT}/j_{TOT} *with* E_B *and* V *varied.*

Figure 6.18: *Results from spanning the parameter space of the Al-AlO$_x$-Au-system by kMC: Scatterplots with* j_{TAT}/j_{TOT} *on z-axis, resembling the fraction of* j_{TAT} *(maximum: 1.0, i.e. only TAT and no DT, red color; minimum: 0.0, i.e. only DT and no TAT, blue color) in total total current density as well as potential correlative effects from simulationously varying the parameters* n_D, m^*_{ox}, E_B *and* E_D *as given. Parameters not explicitly varied in a plot, were set to the best fit values* $n_D = 4 \times 10^{18}$ *cm*$^{-3}$, $m^*_{ox} = 0.35$ m$_0$, $E_B = 2.8$ *eV*, $E_D = 2.4$ *eV*, $d = 6.7$ *nm*, $V = 4.2$ *V, see the text for further explanations.*

ously decreasing gate voltages. Thus both images also show a correlation separating the TAT (red) and DT (blue) dominated regimes. This implies that defects should be kept deeper than 2.8 eV, while the band offset of AlO_x to the cathode should be kept higher than 2.7 eV for an optimal operation as gate dielectric. Additionally, from Fig. 6.18e and 6.18f one can see that independent of E_D and E_B, FN will always be dominant for voltages higher than 4.5 V.
Apart from the graphs depicted in this last section, randomly distributed defects could also be spatially shifted through the oxide in our model allowing for introducing kind of "interface" or "bulk" defects. Confining the defects computationally to a region less than $\sim 1-2$ nm away from the Al cathode, which included the same amount of defects, made it impossible to find a fit with a physically viable parameter set. Hence we furtherly conclude that TAT occurs via "bulk" defects distributed over the entire oxide film which is in accordance with experimental observations.[308]

6.4.5 Summary with respect to Applications

Especially from the last part, we can conclude for applications that require low leakage currents ($\sim 1\mu A/cm^2$), like gate dielectrics, that defect densities must be minimized, because with an increase in defect density of only $\sim 10^{18}cm^{-3}$ TAT and thus leakage increases by a factor of 10. Secondly, defect levels must be kept below 2.8 eV. So especially the V_Os around this value are harmful in AlO_x. Hence, growth techniques providing good crystallinity and stoichiometry of AlO_x are required to guarantee its applicability as gate dielectrics. O-rich conditions, for example, induce a Fermi-level within Al-AlO_x-Au-contacts that causes less rather shallow V_Os and Al_{int}s, but more deep V_{Al}s.[326]. Thirdly, the barrier height must not be reduced, e.g. due to fermi level pinning, to guarantee a low DT current. In this context interface traps must be avoided (by clean processing conditions), because they reduce the CBOs which is detrimental both for DT and TAT. Fourth, to keep the TAT-caused leakage current for 4-8 nm-thin gate oxides below $1\mu A/cm^2$, m^*_{ox} must be > 0.2 m_0), if defect energies E_D is < 2.6 eV and densities $n_D \sim 10^{18}cm^{-3}$. Since such defect levels are likely in plasma-oxidized AlO_x, a spectroscopic determination of the effective mass in AlO_x is required to evaluate its usage as a gate dielectric. Therefore the barrier height must not be reduced, e.g. due to Fermi level pinning, to guarantee a low DT current. In this context interface traps that might reduce the band offset are particularly detrimental both for DT and TAT and hence must be avoided, e.g. by proper sample cleaning and ambient conditions.

Chapter 7

Conclusion and Outlook

7.1 Conclusions

The first, experimental part of this work demonstrated the efficent fabrication of Au-Ti-TiO_x-p^+Si structures for MOS-applications by a temperature-enhanced nTP-protocol combined with a confectioned plasma oxidation process. By structures of good fidelity and sizes ranging from sub-70nm up to 200 μm, we infer the good scalability of our transfer protocol applicable over large substrate areas. C-AFM and probe station measurements proved the electrical functionality of Au/Ti-p^+Si and Au/Ti/TiO_x/p^+Si-diodes with different contacting modes and tips. The current density through single pillars measured over larger areas could be simulated accurately by a kMC-model. It showed that for nm-thin TiO_x layers the energy and density of defects in the oxide is crucial for device characteristics. Moreover, the combined nTP-plasma process allows for the MOS-fabrication by a sufficiently strong plasma, where the thickness can also be increased systematically or even kept negligibly thin, e.g. by evaporating only 5 nm Ti and a plasma activation time of 30 s at 200 W power. Our central result is the growth of the oxide with the plasma strength determined by electrical characteristics and calibrated from decreasing current densities with increasing plasma time/power-combinations, i.e. plasma work. It turned out to be sytematically decisive for the thickness of the plasma-grown-TiO_x, that the e-beam-deposited Ti formed a closed film on the stamps. The jV-characteristics of all such TiO_x-samples and their according plasma strength could be attributed to different oxide thicknesses which were determined in a range of ± 2 nm by kMC-fits up to a voltage of at least 3 V. The main conduction mechanism through the oxide obtained from these fits as well as a plotting analysis was DT/FN-tunneling, with probably TAT in defects with $E_D \approx 1.5$ eV being responsible for the onset of dielectric breakdown above ~ 3.5 V. All kMC-parameters were consistent with literature values of TiO_x and the simulations allowed for a determination of the oxide thicknesses created by the plasma. Thus, regressing the oxide thicknesses in dependence of the applied plasma work confirmed the validity of a typical Deal-Grove-like power law for the oxide formation with $R^2 = 0.95$. Finally, CV-measurements allowed for a determina-

tion of the relative permittivity of the thickest titanium oxide layer from the strongest plasma treatment of 600 W for 1200 s on 10 nm Ti resulting into a value of 13 which is comparable to typical values of TiO_2. Our results are also in good agreement with other studies on partly insulating, functional TiO_x generated by plasma oxidation of Ti. In total these findings confirm the realibility, validity and versatile applicability of our combined nTP-plasma-oxidation process to fabricate MOS-diodes over large scales.

In the second part, we focused on the theoretical investigations on TiO_2 as a conductive oxide. The existing kMC-model for jV-simulations of MOM contacts was applied for amorphous and anatase titanium dioxid. The validation of the model from the excellent fits to fabricated samples with at least major anatase components showed that electronic transport through this material can be modelled properly by kMC-simulations. Most importantly, we have seen by the kMC-analysis that the energy of the dominant defects in TiO_2 depends on the specific fabrication method: We obtain deep traps at 0.9 eV to 1.1 eV for such fabrication methods producing more crystalline materials, i.e. PVD-methods like e-beam-evaporation, especially if combined with high-T annealing, or also MOCVD with a mandatory annealing step. In contrast to that, such methods producing less crystalline films, like ALD, produce shallow at 0.2 eV to 0.4 eV dominating the jV-characteristics. Considering the fabrication techniques the shallower levels at $\sim$0.2-0.4 eV from less crystalline ALD were attributed to Ti interstitials, while the deep ones $\sim$0.9-1.1 eV from purer crystalline PVD are oxygen vacancies as determined by our model in accordance with most literature values. Thus the consistency of these three approaches (kMC-model, literature on defects, fabrication methods) supports our findings. This demonstrates the capability of kMC to discriminate between electrically dominant defect types of differently processed samples and makes it a useful tool, also for experimentalists, to quickly control the specific fabrication and sample processing methods for its impact on defect configurations and evaluate it with respect to the desired application.

Thirdly, the kMC-analysis was extended to another oxide, aluminum oxide. By this second dielectric material the kMC-model was once more approved as an accurate tool to analyze defects in oxides. We could reproduce experimental characteristics using ab initio values as input. The results support the viability of the parameter set determined by the fits. Thus dominant defects at 2.3-2.5 eV below CBM in AlO_x, $m^*_{ox} = 0.35$ m_0 and a barrier $E_{B,Al/AlOx} \approx 2.8$ eV were extracted*. Moreover, EMA holds also in thin AlO_x layers. Furthermore, our model was used to predict expected electrical characteristics of ultra-thin AlO_x and analyze its usefullness for gate dielectrics. We saw that, for $m^*_{ox} = 0.35$ m_0, TAT is dominant at low bias, while FN tunneling dominates at gate voltages above 4.5 V. This causes dielectric breakdown, independent of defect energies $E_D \gtrsim 2.0eV$ and barriers $E_B \lesssim 3.2$ eV for $n_D \in [2 \times 10^{18}\ \mathrm{cm}^{-3}, 8 \times 10^{18}\ \mathrm{cm}^{-3}]$. Particularly, for $n_D \gtrsim 4 \times 10^{18}\mathrm{cm}^{-3}$ defects and effective masses $m^*_{ox} \in [0.2\ m_0, 0.4\ m_0]$ and $E_B \in [2.0\ \mathrm{eV}, 3.2\ \mathrm{eV}]$ there will be more TAT than DT at low volts. So electrons tend to be

*That is without image forces, $E_{B,Al,AlOx} \approx 2.95$ eV with image forces.

injected from Al into AlO_x defect levels and are transported via small-poloran hopping confirming ab initio predictions on AlO_x.[326]) Hence, we suggest an optimization of the work function by minimizing interface defects to guarantee $E_{B,Al/AlOx} > 2.7$ eV and good control of bulk defects so that $E_D > 2.8$ eV and $n_D \lesssim 4 \times 10^{18}$ cm^{-3}, especially for $d_{ox} \sim$ 4 nm or high operating voltages $V_{ox} \gtrsim 4$ V. Finally, it was shown that for the use of aluminum oxide as a gate dielectric, the effective mass must be $m^*_{ox} > 0.2$ m$_0$ to keep the TAT-caused leakage current below $1\mu A/cm^2$), if defect levels are below 2.6 eV at defect densities $\sim 10^{18}$ cm^{-3} and typical ultra-thin gate oxide thicknesses, like our simulated ones of 4 nm to 8 nm.
Thus, in total, an accurate determination and control of defects in terms of energy and density is decisive for device performance. Since defect levels around 2.6 eV have to be expected in plasma-oxidized AlO_x, as probably also in stoichiometric Al_2O_3, an exact spectroscopic determination of the effective mass in Al_2O_3 and AlO_x would be very helpful to better evaluate this kind of oxide for MOSFET devices. It has been supposed by several theoretical studies that the effective tunneling mass decreases with increasing oxide thickness [309, 324, 325, 329] we propose that there should be an optimized oxide thickness thick enough to suppress DT (thicker barrier), but still thin enough (causing the effective mass to increase) to suppress also TAT as good as possbile.

7.2 Outlook

Regarding the experimental efforts of this work, the characteristics of the produced MS and MOS-structures showed the functionality of the transfer-printed structures, so that their usage as actual devices fabricated over large-scales by nTP is proposed. Thus, demonstrating the large-scale fabrication of such MOS-devices also with industrial-scale, at best polymer-replicated Si stamps is definitely an auspicious next task. In parallel, their usage for concrete devices has to be addressed further on the fundamental level by going for a characterizatiion of ensembles of nanostructures. Microscale test measurements showed already characteristics as normally reported for TiO_x memristors for transfer-printed, plasma-oxidized Au/Ti/TiO_x-structures after annealing them on a hotplate for 1 h at 350 °C under ambient conditions. A confirmation of such measurements could be a first step towards nTP-registers of memristors. In these terms also further c-AFM measurements are definitely useful to characterize the electrical properties of the pillars on a mesoscopic scale. Besides, valid kMC-simulations are a complementary tool to explain such measurements. Due to the favorable properties of TiO_2 as an electrode material for photocatalysis, especially if combined with catalytically active metals like Au or Pt, transfer-printed structures long for an investigation with respect to these applications. Their design and geometries have to be optimized further, i.e. basically minimized or hierarchically structured, at first and then their electrochemical characteristics as well as potential effects under illumination have to be investigated. Also their usage as oxide tunneling layers or hole blocking layers turned out to be a promising

field of investigation that has to be addressed by both electrical CV-measurements on single-pillars and electrochemical CV-measurements on larger structured areas and also under illumnination.
However, very first practical steps into this direction based on the present stage is the analysis of the oxide thicknesses, as quantified by kMC in here, by actual TEM-measurements on such samples. Thus calibration of the oxide thickness in terms of the plasma can be checked reliably to derive improvements of both model and process. Being able to determine the thickness properly and having it under control, is also necessary to determine the relative permittivity in dependence of the plasma-oxidation process by electrical CV-measurements. We suppose that the produced oxide is amorphous and nonstoichiometric, but in particular defective. This has recently been highlighted for ALD-grown oxides, opening interesting applications of such - formerly undesired - "leaky" oxides as hole-blocking layers for photocatalysis.[26] The specific crystalline or amorphous phase of the formed TiOx should be studied by appropriate methods like XPS or XAS to investigate the properties of such plasma-grown oxide layers in future studies, e.g. combined with more differentiated kMC-model accounting also for hole transport and different defect species. Besides, electrical and electrochemical characterizations, structural measurements are important to draw conclusions on the dielectric properties of the plasma-grown TiO_x and further judge its usability for the mentioned applications. The j-V-characteristics also show high similarity to the ones interesting for MOS-applications with amorphous TiO_x, like oxide layers for resistive switches or for photocatalysis.[27, 28] By a further minimization of defect densities an application as insulating, high-k oxides for storage capacitors is also expected.
Regarding kMC-simulations there are basically three opportunities for future work. The first one is to go for more accurate simulations of MOM and MOS structures for storage or logic devices to complement the research of other leading groups in this field, as in [168, 191]. Based on today's status of the simulator, it would be a straightforward task to implement and simulate potential conduction pathways due to holes in an analogous way as done for the electrons. Although neglected here, hole conduction might be relevant under certain conditions, just as it is also persumed in some experimental literature on leaky oxides for water oxidation.[26] Also theoreticians regularly report defects in TiO_2 which can act as hole traps.[171, 172, 174] The first question to answer here into more detail would be, if holes are significant for transport in conductive oxides or not by reproducing measured curves with hole currents, e.g. for TiO_2 and its different phases. Another task to refine the MOS-model is to introduce an additional, naturally grown oxide layer, as of SiO_2, which is supposed to be mostly present in material stacks fabricated on Si-substrates. Such a layer has already crudely been implemented in the code by defining parameters with spatial restrictrictions. By demonstrating the functionality of this important feature the kMC-model would completely resemble today's state-of-the-art in kMC transport simulations of MOM and MOS-layers. Going further towards a compact integration of the competing hole transport and multiple layer stacks of dielectric materials would already exceed it. Moreover, the recalibration of the band

bending in the semiconductor contacts by coupling the kMC-code appropriately and automatically to drift-diffusion-simulations, e.g. by TiberCAD, is an interesting next task and useful feature and such an accurate recalibration has not been done by other groups yet up to our knowledge.
Thus coming to the second opportunity, which are memristor studies, the simulator actually has some features for spatially restricted parameter defintions, such as to place a group of defects at a certain density close to the interface and another group distantly at another density and at spatially defined regions. Having that at hand, effects of interface-close and bulk defects at extremely high or low density can be simulated already. This would allow for a direct test of common memristor models, as discussed in literature [158, 254, 330, 331], and complement the rare computational and even rarer kMC studies on this application which are to a big part covered by [193, 195, 254, 332, 333]. This way a further refinement of the charge transport picture in memristors is to be expected, e.g. scrutinizing the defects responsible for transport further, as started here. Related to that, currently defects are reflected in positions, densities and energies. Implementing groups of defects of different kind, by further physical or chemical characteristics, so that one can better distinguish between them, would be very interesting for the case of TiO_2, but also other further (conductive) oxide materials. For example, the effects of trap relaxations, i.e. different energy levels whether defects are occupied or not, could be analyzed also for TiO_2 at first. However, a much more sophisticated way to improve the model, especially the part for multiple-phonon TAT, the "Ridley rates", would be by implementing the approximate spatial form of defect orbitals. Thus, defects could be modelled and located more accurately based on DFT calculations and one could specify the defects much better according to their chemical properties.
The third opportunity is photocatalysis. Although the hopping transport model presented here was also validated with regard to these applications, a proper model for the morphologies, as well as photoillumination and charge carrier injection from electrodes, e.g. by Marcus injection from Dyes in DSSCs or injection of hot electrons from metallic electrodes in plasmonic photocatalysis, has to be accounted for. Continuous-time random walk models as by Nelson [177], Walker [180] or Bisquert [161, 185] are supposed to be complemented very well or even replaced with the more extensive kMC-models presented here by adding only few features, such as "illumination" by placing electrons spatially defined on the simulation grid and let them hop in defects or diffuse also in the CB with rates reported in literature while allowing for trapping, too. The processes after trapping are readily fully included in the present model, so the way to driving the code to that application is quite evident. Going further than the mentioned authors, the simulation of holes is relevant in photovoltaic devices and has to be included, since electron-hole pairs will be created or gain relevance at some point and their transport has to be simulated.
A challenging task is the extension of the simulation grid to the contacts and implement the band bending at the interfaces within the kMC-simulations by solving the Poisson equation during every (or every 10th, 100th, ...) kMC-simulation step, while charge car-

rier transport is still computed according to the kMC-scheme. This would increase the universality and flexibility of the simulator tremendously. However, in all such activities the researcher always has to minimize the number of model parameters, too, in order not to dilute its explanatory power and ensure a certain degree of and user-friendliness.

Appendix

A. Process Conditions: Hydrophilicity, Temperature, Pressure, Imprinting Time

In previous works at the Institute for Nanoelectronics the nTP protocol with the Obducat 2.5 Nanoimprinter had already been optimized in terms of the four main determining process variables: hydrophilicity, pressure, temperature, imprint duration.
The hydrophilicity determines the electrostatic forces between substrate and stamp. From phenmonelogical investigations [8, 73] these forces which are active on the most basic molecular level are supposed to have the biggest influence on transfers, but are also hardest to control externally. Our nTP process yielded best results by a dry chemical treatment of the stamp and substrate by plasma ashing.
Pressure as external mechanical force has to be high enough to bring the entire stamp area in closest contact to the substrates. Thus, for hard, inflexible Si stamps, pressures below 5-10 bars are useless for successful transfers. Normally pressures around 30-50 bars are used.
Similarly, the temperature has to be high enough in order to evaporate as much H_2O forming in the surface reaction. Thus at least 100 $°C$ are needed. Accounting also for an overshoot and uncontrollable drop, as seen in Fig. 7.1, at the end of the heating step.
The actual imprint duration has to be high enough to guarantee a transfer of the entire structured stamp area, i.e. at least 60-120 s long, but must be short enough, i.e. less than ca. 500 s, in order not to alter or degrade the structures risking e.g. to break the stamp.
A typical protocol of the control variables as taken by the Obducat 2.5 Nanoimprinter is shown in Fig. 7.1.

B. Drift-Diffusion-Simulation Framework

In the following the theoretical framework of equations governing the Drift-Diffusion simulations as conducted by TiberCAD in section 5.5 shall be provided. The semiclassical Drift-Diffusion model describes the steady-state charge transport of semiconductor

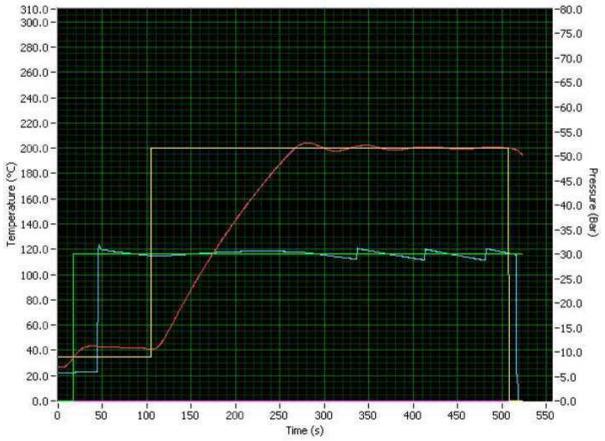

Figure 7.1: *Screenshot of a typical, preferential course of the process for high-yield transfers as displayed on the Obducat Nanoimprinter.*

structures. The current density **J** is comparted of a drift component which is driven by an electric field and a diffusion component which is driven by a charge carrier density gradient, according to

$$\mathbf{J}_\mathrm{n} = en\mu_\mathrm{n}\mathbf{E} + eD_\mathrm{n}\nabla n \quad , \quad \mathbf{J}_\mathrm{p} = ep\mu_\mathrm{p}\mathbf{E} - eD_\mathrm{p}\nabla p \quad , \tag{7.1}$$

where n (p) is the electron (hole) density, μ_n (μ_p) is the electron (hole) mobility and D_n (D_p) is the diffusiion coefficient of electrons (holes).
The Einstein-Smoluchowski equation relates the diffusion coefficent and the mobility

$$D = \frac{\mu k_\mathrm{B} T}{e} \quad . \tag{7.2}$$

Inserting this into Eq. 7.1 one obtains

$$\mathbf{J}_\mathrm{n} = en\mu_\mathrm{n}\left[\nabla\left(\frac{E_\mathrm{C}}{e} - \phi\right) + \frac{k_\mathrm{B}T}{e}\frac{N_\mathrm{C,0}}{n}\,\nabla\left(\frac{n}{N_\mathrm{C,0}}\right)\right] \quad , \tag{7.3}$$

$$\mathbf{J}_\mathrm{p} = ep\mu_\mathrm{p}\left[\nabla\left(\frac{E_\mathrm{V}}{e} - \phi\right) - \frac{k_\mathrm{B}T}{e}\frac{N_\mathrm{V,0}}{p}\,\nabla\left(\frac{p}{N_\mathrm{V,0}}\right)\right] \quad , \tag{7.4}$$

including a a spatially dependent conduction (valence) band edges E_C (E_V), effective masses given by the effective DOS $N_\mathrm{C,0}$ ($N_\mathrm{V,0}$). The electrical charge is conserved and obeys the continuity equation

$$\nabla\mathbf{J}_\mathrm{n} = eR_\mathrm{net} + e\frac{\partial n}{\partial t} \quad , \tag{7.5}$$

$$-\nabla\mathbf{J}_\mathrm{p} = eR_\mathrm{net} + e\frac{\partial p}{\partial t} \quad , \tag{7.6}$$

where R_{net} is the net recombination rate. Inserting equations (7.3) and (7.4) into equations (7.5) and (7.6), one obtains two second order parabolic differential equations to be solved together with the Poisson equation for the electrostatic potential

$$\nabla(\epsilon_0\epsilon_{\mathrm{r}}\nabla\phi) = e\left(n - p + N_{\mathrm{D}}^{+} - N_{\mathrm{A}}^{-}\right) \quad . \tag{7.7}$$

Here, N_{D}^{+} (N_{A}^{-}) is the concentration of ionized donors (acceptors) and ϵ_{r} is the dielectric constant of the specific material. This non-linear set of equations (7.3,7.4. 7.5, 7.6, 7.7) can be solved iteratively by numerical methods.

The numerical algorithm, as conducted also by TiberCAD, starts with an initial guess of the potential which is inserted into the Poisson equation to calculate the carrier concentrations. Those are inserted into the continuity equations calculating the potential again. If this value agrees with the initial value within a certain tolerance, the algorithm terminates with this self-consistent solution, otherwise the algorithm is looped through again.
Prior to the solution the mesh has to be set up according to a predefined geometry. Also all physical models, e.g. the mobility model, and material parameters need to be defined and the settings for the simulated voltage range, numerical methods and input/output files have to be adjusted. Details on this process can be found in the TiberCAD Manual as well as, e.g. the PhD thesis of M. Auf der Maur, who set up this framework for TiberCAD. [246] The best convergence of the algorithm was obtained for a LU-solver with no further numerical methods switched on and the maximum number of iteration set to 100000 per voltage step.
The parameter settings for the metal fermi level, the Si valence band and the TiO_2 valence band which determine the CB relative CV positions must satisfy also the MIGS-model, see section 6.3.4, in order to allow for a correct calibration of the oxide voltage drop in dependence of the gate voltage as used in the kMC-code afterwards. The following table summarizes the parameter sets for TiberCAD to model different, important metal electrodes (defined over the work function) and charge neutrality levels of TiO_2:

C. Analytical Versions of Transmission Coefficients with Franz-type Dispersion

As mentioned in section 5, also other dispersion relations than the parabolic one can be used to compute the transmission coefficient. Those were of minor importance and only tested against the parabolic one showing that they introduce only a linear shift, as expected from the correction factor on the order of 10%. First, there is, the Franz singe-mass model[223]: Starting from

$$k_F(E_x, x) = \sqrt{\frac{2m_F^*(V(x) - E_x)}{\hbar^2}}\sqrt{1 - \frac{V(x) - E_x}{E_g}} \tag{7.8}$$

CNL, TiO2			0,6	0,8	1
Pt with ϕ= 5,3	TiberCAD-Metal-Fermi-Level 2,0 eV	CBO Metal-TiO2	0,85	1	1,1
		VB, TiO2	-1,35	-1,2	-1,1
		CB, Si	1,8	1,8	1,8
		VB, Si	0,7	0,7	0,7
Au with ϕ= 4,8	TiberCAD-Metal-Fermi-Level 1,5 eV	CBO Metal-TiO2	0,7	0,9	1
		VB, TiO2	-1	-0,8	-0,7
		CB, Si	2,2	2,2	2,2
		VB, Si	1,1	1,1	1,1
Ti with ϕ= 4,3	TiberCAD-Metal-Fermi-Level 1,0 eV	CBO Metal-TiO2	0,5	0,7	0,8
		VB, TiO2	-0,65	-0,5	-0,4
		CB, Si	2,5	2,5	2,5
		VB, Si	1,4	1,4	1,4

Figure 7.2: *Determining system variables for DD-simulations that obey the MIGS-model with pinning factor $S_{TiO_2} \approx 0.3$, see section 6.3.4. Input parameters for TiberCAD are underlaid in red.*

the exponent in the transmission coefficient can be done analytically, as done by Weinberg et.al. [225], which introduces a correting factor compared to the parabolic dispersion in Eq. 5.7:

$$-2\int_{x_0}^{x_1} dx k_F(E_x,x) = -\frac{4}{3}\sqrt{\frac{2m_F^* d^2}{\hbar^2 e V_{ox}}}\phi_B^{3/2}\left(1-\frac{3}{10}\frac{\phi_B}{E_g}\right) \tag{7.9}$$

Second, there is the Franz 2-mass model: Similarly, by the introduction of two different masses for CB and VB, m^*_{CB} and m^*_{VB}, the Franz-type dispersion was refined further to[224]

$$k_D(E_x,x) = \sqrt{\frac{2m^*_{CB}(V(x)-E_x)}{\hbar^2}}\sqrt{\frac{1-\frac{V(x)-E_x}{E_g}}{1-(1-\frac{m^*_{CB}}{m^*_{VB}})\times\frac{V(x)-E_x}{E_g}}} \tag{7.10}$$

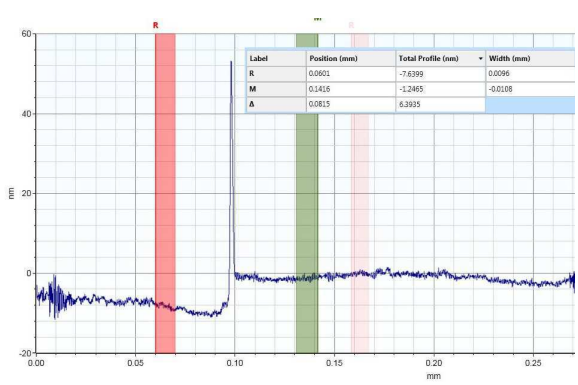

(a) *Dektak measurement* 7 ± 2 *nm e-beam-sample.*

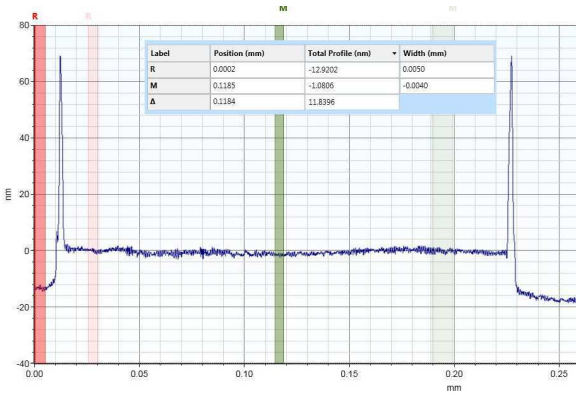

(b) *Dektak measurement* 10 ± 2 *nm e-beam-sample.*

Figure 7.3: *Raw data measurements of the oxide thickness with the Dektak.*

One can analytically derive the exponent in the transmission coefficient [224, 225]

$$-2\int_{x_0}^{x_1} dx k_F(E_x, x) = -\frac{4}{3}\sqrt{\frac{2m^*_{CB}d^2}{\hbar^2 eV_{ox}}}\phi_B^{3/2}\left(1 - \frac{3}{10}\frac{m_{CB}}{m_{VB}}\frac{\phi_B}{E_g}\right) \tag{7.11}$$

D. Profilometer Measurements

The oxide thickness for the e-beam reference samples in section 6.2 were determined by a profilometer from Bruker Dektak. For that purpose on flat Si-wafers only the TiO_x-layers, but no Au, was evaporated and the pads were also defined by optical lithography, as for the parallelly processed actual e-beam-samples with Au on top. The Dektak measurements were performed in a Bruker Dektak-XT Stylus Surface Profiling System scanning with a tip across the edge of a mere TiO_x pad. After levelling-out thus oxide thicknesses were determined as 3 ± 2 nm , $7nm \pm 2$ nm, $10nm \pm 2$ nm. Exemplary results of these measurements are shown in 7.3.

Bibliography

[1] G. E. Moore. Cramming more components onto integrated circuits. *Electronics*, 38(8):114 117, 1965.

[2] Peter Lambert. The international technology roadmap for semiconductors. Technical report, ITRS, 2013. www.itrs.net.

[3] Hiroshi Iwai. High-κ, metal gate, channel materials new material integration in cmos technologies. Technical report, Frontier Research Center, Tokyo Institute of Technology, 2012. ULIS 2012, Tutorial, Minatec, Grenoble - France.

[4] M. Blamire B. O. Satishchandra, T. Venky Venkatesan. *Functional Metal Oxides, New Science and Novel Applications*, volume 1. Wiley-VCH, 1 edition, 2013.

[5] Nobuo Tsuda, Keiichiro Nasu, Akira Yanase, and Kiiti Siratori. *Electronic Conduction in Oxides*, volume 94. Springer Series in Solid-State Sciences, Berlin, Heidelberg, Springer Berlin Heidelberg, 10 edition, 1991.

[6] Gunther Jegert, Alfred Kersch, Wenke Weinreich, Uwe Schroeder, and Paolo Lugli. Modeling of leakage currents in high-κ dielectrics three-dimensional approach via kinetic monte carlo. *Applied Physics Letters*, 96(6):27 30, 2010.

[7] Intel Corporation. Platform brief, 6th generation intel core desktop processor family with intel q170 and intel h110 chipsets. Technical report, Intel Corporation, 2015. http://www.intel.com/content/www/us/en/embedded/products/skylake/s-desktop/6th-generation-core-processor-deskop-platform-brief.html?wapkw=skylake+14+nm.

[8] Andrew Carlson, Audrey M. Bowen, Yonggang Huang, Ralph G. Nuzzo, and John A. Rogers. Transfer printing techniques for materials assembly and micro/-nanodevice fabrication. *Advanced Materials*, 24(39):5284 5318, 2012.

[9] Q Fan, B McQuillin, a K Ray, M L Turner, and a B Seddon. High density, non-porous anatase titania thin films for device applications. *Journal of Physics D Applied Physics*, 33(21):2683 2686, Nov 2000.

[10] Chittaranjan Das, Karsten Henkel, Massimo Tallarida, Dieter Schmeißer, Hassan Gargouri, Irina Kärkkänen, Jessica Schneidewind, Bernd Gruska, and Michael Arens. Thermal and plasma enhanced atomic layer deposition of TiO_2 - comparison of spectroscopic and electric properties. *Journal of Vacuum Science & Technology A*, 33(1), 2015.

[11] Chao Zhao, M.N. Hedhili, Jingqi Li, Qingxiao Wang, Yang Yang, Long Chen, and Liang Li. Growth and characterization of titanium oxide by plasma enhanced atomic layer deposition. *Thin Solid Films*, 542:38 44, 2013.

[12] Hu Young Jeong, Jeong Yong Lee, Min Ki Ryu, and Sung Yool Choi. Bipolar resistive switching in amorphous titanium oxide thin film. *Physica Status Solidi - Rapid Research Letters*, 4(1-2):28 30, 2010.

[13] Min Hwan Lee, Kyung Min Kim, Gun Hwan Kim, Jun Yeong Seok, Seul Ji Song, Jung Ho Yoon, and Cheol Seong Hwang. Study on the electrical conduction mechanism of bipolar resistive switching TiO_2 thin films using impedance spectroscopy. *Applied Physics Letters*, 96(15):1 3, 2010.

[14] Lit Ho Chong, Kanad Mallik, C H De Groot, and Reinhard Kersting. The structural and electrical properties of thermally grown TiO_2 thin films. *Journal of Physics Condensed Matter*, 18(2):645 657, Jan 2006.

[15] V. Mikhelashvili and G. Eisenstein. Effects of annealing conditions on optical and electrical characteristics of titanium dioxide films deposited by electron beam evaporation. *Journal of Applied Physics*, 89(6):3256 3269, 2001.

[16] S. A. Campbell, H.-S. Kim, D. C. Gilmer, B. He, T. Ma, and W. L. Gladfelter. Titanium dioxide TiO_2-based gate insulators. *IBM Journal of Research and Development*, 43(3):383 392, May 1999.

[17] T. Asanuma, T. Matsutani, C. Liu, T. Mihara, and M. Kiuchi. Structural and optical properties of titanium dioxide films deposited by reactive magnetron sputtering in pure oxygen plasma. *Journal of Applied Physics*, 95(11 I):6011 6016, 2004.

[18] Yueh-lin Loo, Robert L Willett, Kirk W Baldwin, John A Rogers, Bell Laboratories, Lucent Technologies, and Murray Hill. Interfacial chemistries for nanoscale transfer printing. *Journal of the American Chemical Society*, 124(26):7654 7655, jun 2002.

[19] J.C. Tinoco, M. Estrada, and G. Romero. Room temperature plasma oxidation mechanism to obtain ultrathin silicon oxide and titanium oxide layers. *Microelectronics Reliability*, 43(6):895 903, 2003.

[20] J.C. Tinoco, M. Estrada, B. Iñiguez, and A. Cerdeira. Conduction mechanisms of silicon oxide/titanium oxide {MOS} stack structures. *Microelectronics Reliability*, 48(3):370 381, 2008.

[21] M. Bareiß, D. Kaaelblein, C. Jirauschek, a. Exner, I. Pavlichenko, B. Lotsch, U. Zschieschang, H. Klauk, G. Scarpa, B. Fabel, and et al. Ultra-thin titanium oxide. *Applied Physics Letters*, 101(8):083113, 2012.

[22] Yueh-Lin Loo, David V Lang, John A Rogers, and Julia W P Hsu. Electrical Contacts to Molecular Layers by Nanotransfer Printing. *Nano Letters*, 3(7):913 917, Jul 2003.

[23] Hyunsoo Lee, Young Keun Lee, Trong Nghia Van, and Jeong Young Park. Nanoscale schottky behavior of Au islands on TiO_2 probed with conductive atomic force microscopy. *Applied Physics Letters*, 103(17):173103, 2013.

[24] Tae-il Kim, Ju-hyung Kim, Sang Jun Son, and Soon-min Seo. Gold nanocones fabricated by nanotransfer printing and their application for field emission. *Nanotechnology*, 19(29):295302, Jul 2008.

[25] Yi Wei Chen, Jonathan D Prange, Simon Duehnen, Yohan Park, Marika Gunji, Christopher E D Chidsey, and Paul C McIntyre. Atomic layer-deposited tunnel oxide stabilizes silicon photoanodes for water oxidation. *Nature materials*, 10(7):539 544, 2011.

[26] Shu Hu, Matthew R Shaner, Joseph a Beardslee, Michael Lichterman, Bruce S Brunschwig, and Nathan S Lewis. Amorphous TiO_2 coatings stabilize Si, GaAs, and GaP photoanodes for efficient water oxidation. *Science (New York, N.Y.)*, 344(6187):1005 9, 2014.

[27] Ladislav Kavan, Nicolas Tétreault, Thomas Moehl, and Michael Grätzel. Electrochemical characterization of TiO_2 blocking layers for dye-sensitized solar cells. *The Journal of Physical Chemistry C*, 118(30):16408 16418, 2014.

[28] Petra J. Cameron, , and Laurence M. Peter. Characterization of titanium dioxide blocking layers in dye-sensitized nanocrystalline solar cells. *The Journal of Physical Chemistry B*, 107(51):14394 14400, 2003.

[29] Maofeng Dou and Clas Persson. Comparative study of rutile and anatase SnO_2 and TiO_2 Band-edge structures, dielectric functions, and polaron effects. *Journal of Applied Physics*, 113(8):083703, 2013.

[30] A Thilagam, D J Simpson, and A R Gerson. A first-principles study of the dielectric properties of TiO_2 polymorphs. *Journal of Physics Condensed matter*, 23(2):025901, Jan 2011.

[31] Ming-Kwei Lee, Jung-Jie Huang, and Tsung-Shun Wu. Electrical characteristics improvement of oxygen-annealed MOCVD-TiO_2 films. *Semiconductor Science and Technology*, 20(6):519, 2005.

[32] Seong Keun Kim, Wan Don Kim, Kyung Min Kim, Cheol Seong Hwang, and Jaehack Jeong. High dielectric constant TiO_2 thin films on a Ru electrode grown at 250 ∘c by atomic-layer deposition. *Applied Physics Letters*, 85(18):4112 4114, 2004.

[33] Wenli Yang, Joseph Marino, Alexander Monson, and Colin a Wolden. An investigation of annealing on the dielectric performance of TiO_2 thin films. *Semiconductor Science and Technology*, 21(12):1573 1579, Dec 2006.

[34] B.-S. Jeong, D.P. Norton, and J.D. Budai. Conductivity in transparent anatase TiO_2 films epitaxially grown by reactive sputtering deposition. *Solid-State Electronics*, 47(12):2275 2278, Dec 2003.

[35] Stephen a. Campbell, David C. Gilmer, Xiao Chuan Wang, Ming Ta Hsieh, Hyeon Seag Kim, Wayne L. Gladfelter, and Jinhua Yan. Mosfet transistors fabricated with high permitivity TiO_2 dielectrics. *IEEE Transactions on Electron Devices*, 44(1):104 109, 1997.

[36] H. Tang, K. Prasad, R. Sanjines, P. E. Schmid, and F. Levy. Electrical and optical properties of TiO_2 anatase thin films. *Journal of Applied Physics*, 75(4):2042, 1994.

[37] R. Sanjines, H. Tang, H. Berger, F. Gozzo, G. Margaritondo, and F. Levy. Electronic structure of anatase TiO_2 oxide. *Journal of Applied Physics*, 75(6):2945 2951, 1994.

[38] John Robertson. High dielectric constant gate oxides for metal oxide Si transistors. *Reports on Progress in Physics*, 69(2):327 396, 2005.

[39] Yang Wang, Huijuan Sun, Shijing Tan, Hao Feng, Zhengwang Cheng, Jin Zhao, Aidi Zhao, Bing Wang, Yi Luo, Jinlong Yang, and et al. Role of point defects on the reactivity of reconstructed anatase titanium dioxide (001) surface. *Nature communications*, 4:2214, Jan 2013.

[40] Stefan Wendt, Phillip T Sprunger, Estephania Lira, Georg K H Madsen, Zheshen Li, Jonas Ø Hansen, Jesper Matthiesen, Asger Blekinge-rasmussen, L Erik, Bjørk Hammer, and et al. The role of interstitial sites in the ti 3d defect state in the band gap of titania. 1(110):1 5.

[41] Daniel T Gillespie. A general method for numerically simulating the stochastic time evolution of coupled chemical reactions. *Journal of Computational Physics*, 22(4):403 434, 1976.

[42] C. Jacoboni and P. Lugli. *The Monte Carlo Method for Semiconductor Device Simulation*. Springer-Verlag, Vienna, Austria, 3rd edition, 1989.

[43] Gunther Jegert. *Modeling of Leakage Currents in high-κ Dielectrics*, volume 137. Selected Topics of Semiconductor Physics and Technology, Schriftenreihe des Walter-Schottky-Instituts, 1 edition, 2012.

[44] J. Christopher Love, Lara A. Estroff, Jennah K. Kriebel, and Ralph G. Nuzzo, and George M. Whitesides. Self-assembled monolayers of thiolates on metals as a form of nanotechnology. *Chemical Reviews*, 105(4):1103 1170, 2005. PMID: 15826011.

[45] Yueh-Lin Loo, Julia WP Hsu, Robert L Willett, Kirk W Baldwin, Ken W West, and John A Rogers. High-resolution transfer printing on GaAs surfaces using alkane dithiol monolayers. *Journal of Vacuum Science & Technology B*, 20(6):2853 2856, 2002.

[46] Nahla A. Abu Hatab, Jenny M. Oran, and Michael J. Sepaniak. Surface-enhanced raman spectroscopy substrates created via electron beam lithography and nanotransfer printing. *ACS Nano*, 2(2):377 385, 2008.

[47] Tae-Wook Kim, Kyeongmi Lee, Seung-Hwan Oh, Gunuk Wang, Dong-Yu Kim, Gun-Young Jung, and Takhee Lee. A direct metal transfer method for cross-bar type polymer non-volatile memory applications. *Nanotechnology*, 19(40):405201, 2008.

[48] Fangfang Wang, Mianqi Xue, and Tingbing Cao. Thermochemical patterning of polymer thin films with tunable size-reduction effects using metal-coated poly(dimethylsiloxane) stamps. *Advanced Materials*, 21(21):2211 2215, 2009.

[49] Jana Zaumseil, and Julia W. P. Hsu Matthew A. Meitl, Bharat R. Acharya, Kirk W. Baldwin, Yueh-Lin Loo, , and John A. Rogers. Three-dimensional and multilayer nanostructures formed by nanotransfer printing. *Nano Letters*, 3(9):1223 1227, 2003.

[50] Kimberly Felmet, Yueh-Lin Loo, and Yangming Sun. Patterning conductive copper by nanotransfer printing. *Applied Physics Letters*, 85(15):3316 3318, 2004.

[51] John A. Rogers and Ralph G. Nuzzo. Recent progress in soft lithography. *Materials Today*, 8(2):50 56, 2005.

[52] Etienne Menard, Matthew A Meitl, Yugang Sun, Jang-Ung Park, Daniel Jay-Lee Shir, Yun-Suk Nam, Seokwoo Jeon, and John A Rogers. Micro-and nanopatterning techniques for organic electronic and optoelectronic systems. *Chemical reviews*, 107(4):1117 1160, 2007.

[53] Etienne Menard, Lise Bilhaut, Jana Zaumseil, and John A Rogers. Improved surface chemistries, thin film deposition techniques, and stamp designs for nanotransfer printing. *Langmuir*, 20(16):6871 6878, 2004.

[54] Stefan Harrer, Sebastian Strobel, Guillermo Penso Blanco, Giuseppe Scarpa, Gerhard Abstreiter, Marc Tornow, and Paolo Lugli. Technology assessment of a novel high-yield lithographic technique for sub-15-nm direct nanotransfer printing of nanogap electrodes. *Nanotechnology, IEEE Transactions on*, 8(6):662 670, 2009.

[55] Sebastian Strobel, Stefan Harrer, Guillermo Penso Blanco, Giuseppe Scarpa, Gerhard Abstreiter, Paolo Lugli, and Marc Tornow. Planar nanogap electrodes by direct nanotransfer printing. *Small*, 5(5):579 582, 2009.

[56] Mario Bareiß, Andreas Hochmeister, Gunther Jegert, Ute Zschieschang, Hagen Klauk, Rupert Huber, Dirk Grundler, Wolfgang Porod, Bernhard Fabel, Giuseppe Scarpa, and et al. Printed array of thin-dielectric metal-oxide-metal (mom) tunneling diodes. *Journal of Applied Physics*, 110(4):044316, 2011.

[57] Mario Bareiß, Frederik Ante, Daniel Ka, Gunther Jegert, Christian Jirauschek, Giuseppe Scarpa, Bernhard Fabel, Edward M Nelson, Gregory Timp, Ute Zschieschang, and et al. High-yield transfer printing of metal a insulator a metal nanodiodes. *ACS Nano*, 6(3):2853 2859, 2012.

[58] Xuesong Li, Yanwu Zhu, Weiwei Cai, Mark Borysiak, Boyang Han, David Chen, Richard D. Piner, Luigi Colomba, and Rodney S. Ruoff. Transfer of large-area graphene films for high-performance transparent conductive electrodes. *Nano Letters*, 9(12):4359 4363, 2009.

[59] Omar Fakhr, Philipp Altpeter, Khaled Karrai, and Paolo Lugli. Easy Fabrication of Electrically Insulating Nanogaps by Transfer Printing. *Small*, 7(17):2533 2538, Jul 2011.

[60] G Scarpa, a Abdellah, a Exner, and S Harrer. Patterning poly (3-hexylthiophene)(P3HT) in the sub-50-nm Region by Nanoimprint Lithography. *Nanotechnology, IEEE Transactions on*, PP(99):1, 2010.

[61] Robin Nagel. *Personal communication on fabrication and nanotransfer-printing with Hybridpolymer Ormostamps*, 2015.

[62] Jae Won Jeong, Se Ryeun Yang, Yoon Hyung Hur, Seong Wan Kim, Kwang Min Baek, Soonmin Yim, Hyun-Ik Jang, Jae Hong Park, Seung Yong Lee, Chong-Ook Park, and Yeon Sik Jung. High-resolution nanotransfer printing applicable to diverse surfaces via interface-targeted adhesion switching. *Nature Communications*, 5(5387), 2014.

[63] S.L. Lehoczky, R.J. Lederich, and J.J. Bellina Jr. Oxidation of thin titamium films in ambient conditions. *Thin Solid Films*, 55(1):125 135, 1978.

[64] Jong-Woo Kim, Ki-Yeon Yang, Sung-Hoon Hong, and Heon Lee. Formation of Au nano-patterns on various substrates using simplified nano-transfer printing method. *Applied Surface Science*, 254(17):5607 5611, 2008.

[65] Adrien Plecis and Yong Chen. Fabrication of microfluidic devices based on glass pdms glass technology. *Microelectronic Engineering*, 84(5 8):1265 1269, 2007. Proceedings of the 32nd International Conference on Micro- and Nano-Engineering.

[66] Kiwon Oh, Byoung H. Lee, Jae K. Hwang, Haiwon Lee, Seongil Im, and Myung M. Sung. Water-mediated al metal transfer printing with contact inking for fabrication of thin-film transistors. *Small*, 5(5):558 561, 2009.

[67] Byoung H Lee, Yeon H Cho, Haiwon Lee, K-D Lee, Sang H Kim, and Myung M Sung. High-resolution patterning of aluminum thin films with a water-mediated transfer process. *Advanced Materials*, 19(13):1714 1718, 2007.

[68] Chun-Hung Chen and Yung-Chun Lee. Contact printing for direct metallic pattern transfer based on pulsed infrared laser heating. *Journal of Micromechanics and Microengineering*, 17(7):1252, 2007.

[69] Jiwen Wang, Raymond C. Y. Auyeung, Heungsoo Kim, Nicholas A. Charipar, and Alberto Piqué. Three-dimensional printing of interconnects by laser direct-write of silver nanopastes. *Advanced Materials*, 22(40):4462 4466, 2010.

[70] Changsoon Kim, Max Shtein, and Stephen R Forrest. Nanolithography based on patterned metal transfer and its application to organic electronic devices. *Applied Physics Letters*, 80(21):4051 4053, 2002.

[71] C. Kim and S.R. Forrest. Fabrication of organic light-emitting devices by low-pressure cold welding. *Advanced Materials*, 15(6):541 545, 2003.

[72] M. Bareiss, B.N. Tiwari, A. Hochmeister, G. Jegert, U. Zschieschang, H. Klauk, B. Fabel, G. Scarpa, Gregor Koblmuller, G.H. Bernstein, W. Porod, and P. Lugli. Nano antenna array for terahertz detection. *Microwave Theory and Techniques, IEEE Transactions on*, 59(10):2751 2757, Oct 2011.

[73] M. Bareiss. *Nanodiodes and Nanoantennas Fabricated by Transfer Technology*. PhD thesis, Technical University Munich, TUM, Arcisstrasse 21, 80033 Muenchen, Nov 2012.

[74] Debashis Chanda, Kazuki Shigeta, Sidhartha Gupta, Tyler Cain, Andrew Carlson, Agustin Mihi, Alfred J. Baca, Gregory R. Bogart, Paul Braun, and John A. Rogers.

Large-area flexible 3d optical negative index metamaterial formed by nanotransfer printing. *Nature Nanotechnology*, 6(7):1748 3387, Jul 2011.

[75] Elizabeth J. Smythe, Michael D. Dickey, George M. Whitesides, and Federico Capasso. A technique to transfer metallic nanoscale patterns to small and non-planar surfaces. *ACS Nano*, 3(1):59 65, 2009.

[76] Audrey M. Bowen and Ralph G. Nuzzo. Fabrication of flexible binary amplitude masks for patterning on highly curved surfaces. *Advanced Functional Materials*, 19(20):3243 3253, 2009.

[77] Nicholas A. Melosh, Akram Boukai, Frederic Diana, Brian Gerardot, Antonio Badolato, Pierre M. Petroff, and James R. Heath. Ultrahigh-density nanowire lattices and circuits. *Science*, 300(5616):112 115, 2003.

[78] James R. Heath. Superlattice nanowire pattern transfer (snap). *Accounts of Chemical Research*, 41(12):1609 1617, 2008. PMID: 18598059.

[79] S. Harrer. *Next-Generation Nanoimprint Lithography Innovative Approaches towards Improving Flexibility and Resolution of Nanofabrication in the sub-15-nm Region*. PhD thesis, Technical University Munich, TUM, Arcisstrasse 21, 80333 Muenchen, Feb 2008.

[80] Jun ho Choi, Kyung-Ho Kim, Se-Jin Choi, and Hong H Lee. Whole device printing for full colour displays with organic light emitting diodes. *Nanotechnology*, 17(9):2246, 2006.

[81] D. Suh, S.-J. Choi, and Lee. Rigiflex lithography for nanostructure transfer. *Advanced Materials*, 17(12):1554 1560, 2005.

[82] Moon Kyu Kwak, Tae-il Kim, Pilnam Kim, Hong H. Lee, and Kahp Y. Suh. Large-area dual-scale metal transfer by adhesive force. *Small*, 5(8):928 932, 2009.

[83] J. W. P. Hsu, Y. L. Loo, D. V. Lang, and J. A. Rogers. Nature of electrical contacts in a metal molecule semiconductor system. *Journal of Vacuum Science & Technology B*, 21(4), 2003.

[84] Dong-Wook Oh, Seok Kim, John A. Rogers, David G. Cahill, and Sanjiv Sinha. Interfacial thermal conductance of transfer-printed metal films. *Advanced Materials*, 23(43):5028 5033, 2011.

[85] Mario Bareiss, Muhammad Atyab Imtaar, Bernhard Fabel, Giuseppe Scarpa, and Paolo Lugli. Temperature Enhanced Large Area Nano Transfer Printing on Si/SiO_2 Substrates Using Si Wafer Stamps. *The Journal of Adhesion*, 87(9):893 901, Sep 2011.

[86] Xuming Zhang, Yu Lim Chen, Ru-Shi Liu, and Din Ping Tsai. Plasmonic photocatalysis. *Reports on progress in physics. Physical Society (Great Britain)*, 76(4):046401, Apr 2013.

[87] D. J. Mowbray, J. I. Martinez, J. M. García Lastra, K. S. Thygesen, and K. W. Jacobsen. Stability and electronic properties of tio2 nanostructures with and without b and n doping. *The Journal of Physical Chemistry C*, 113(28):12301 12308, 2009.

[88] Aldo Amore Bonapasta, Francesco Filippone, Giuseppe Mattioli, and Paola Alippi. Oxygen vacancies and OH species in rutile and anatase TiO_2 polymorphs. *Catalysis Today*, 144(1-2):177 182, Jun 2009.

[89] A. Janotti, J. B. Varley, P. Rinke, N. Umezawa, G. Kresse, and C. G. Van de Walle. Hybrid functional studies of the oxygen vacancy in TiO_2. *Physical Review B*, 81(8), 2010.

[90] M Batzill and U Diebold. The surface and materials science of tin oxide. *Progress in Surface Science*, 79(2-4):47 154, 2005.

[91] Ulrike Diebold. The surface science of titanium dioxide. *Surface Science Reports*, 48(5-8):53 229, 2003.

[92] Amy L Linsebigler, Amy L Linsebigler, John T Yates Jr, Guangquan Lu, Guangquan Lu, and John T Yates. Photocatalysis on TiO_2 surfaces principles, mechanisms, and selected results. *Chemical Reviews*, 95(3):735 758, 1995.

[93] Alexandra C Ford, Johnny C Ho, Zhiyong Fan, Onur Ergen, Virginia Altoe, Shaul Aloni, Haleh Razavi, and Ali Javey. Synthesis, contact printing, and device characterization of ni-catalyzed, crystalline inas nanowires. *Nano Research*, 1(1):32 39, 2008.

[94] Zhiyong Fan, Johnny C Ho, Toshitake Takahashi, Roie Yerushalmi, Kuniharu Takei, Alexandra C Ford, Yu-Lun Chueh, and Ali Javey. Toward the development of printable nanowire electronics and sensors. *Advanced Materials*, 21(37):3730 3743, 2009.

[95] Ali Javey, SungWoo Nam, and and Charles M Lieber Robin S. Friedman, and Hao Yan. Layer-by-layer assembly of nanowires for three-dimensional, multifunctional electronics. *Nano Letters*, 7(3):773 777, 2007. PMID: 17266383.

[96] Yu Huang, Xiangfeng Duan, and Charles M. Lieber. Nanowires for integrated multicolor nanophotonics. *Small*, 1(1):142 147, 2005.

[97] Otto L. Muskens, Silke L. Diedenhofen, Bernard C. Kaas, Rienk E. Algra, Erik P. A. M. Bakkers, Jaime Gómez Rivas, and Ad Lagendijk. Large photonic strength of highly tunable resonant nanowire materials. *Nano Letters*, 9(3):930 934, 2009.

[98] Zhiyong Fan and Jia G. Lu. Gate-refreshable nanowire chemical sensors. *Applied Physics Letters*, 86(12): , 2005.

[99] Daihua Zhang, Zuqin Liu, Chao Li, Tao Tang, Xiaolei Liu, Song Han, Bo Lei, , and Chongwu Zhou. Detection of nO_2 down to ppb levels using individual and multiple In_2O_2 nanowire devices. *Nano Letters*, 4(10):1919 1924, 2004.

[100] Hong Jin Fan, Peter Werner, and Margit Zacharias. Semiconductor nanowires from self-organization to patterned growth. *Small*, 2(6):700 717, 2006.

[101] J. A. Liddle C. Soennichsen B. Boussert A. P. Alivisatos Yi Cui, M.T. Bjoerk. Integration of colloidal nanocrystals into lithographically patterned devices. *Nano Letters*, 4(6):1093 1098, 2004.

[102] Hao-Chih Yuan, Zhenqiang Ma, Michelle M. Roberts, Donald E. Savage, and Max G. Lagally. High-speed strained-single-crystal-silicon thin-film transistors on flexible polymers. *Journal of Applied Physics*, 100(1): , 2006.

[103] J. A. Rogers, M. G. Lagally, and R. G. Nuzzo. Synthesis, assembly and applications of semiconductor nanomembranes. *Nature*, 477:45 53, Sep 2011.

[104] Hongjun Yang, H Pang, Z Qiang, Zhenqiang Ma, and Weidong Zhou. Surface-normal fano filters based on transferred silicon nanomembranes on glass substrates. *Electronics Letters*, 44(14):858 859, 2008.

[105] Zexuan Qiang, Hongjun Yang, Li Chen, Huiqing Pang, Zhenqiang Ma, and Weidong Zhou. Fano filters based on transferred silicon nanomembranes on plastic substrates. *Applied Physics Letters*, 93(6): , 2008.

[106] Yugang Sun, Seiyon Kim, Ilesanmi Adesida, and John A. Rogers. Bendable GaAs metal-semiconductor field-effect transistors formed with printed GaAs wire arrays on plastic substrates. *Applied Physics Letters*, 87(8): , 2005.

[107] Yugang Sun, Etienne Menard, John A. Rogers, Hoon-Sik Kim, Seiyon Kim, Guang Chen, Ilesanmi Adesida, Ross Dettmer, Rebecca Cortez, and Alan Tewksbury. Gigahertz operation in flexible transistors on plastic substrates. *Applied Physics Letters*, 88(18): , 2006.

[108] Keon Jae Lee, Jaeseob Lee, Heedon Hwang, Zachary J Reitmeier, Robert F Davis, John A Rogers, and Ralph G Nuzzo. A printable form of single-crystalline gallium nitride for flexible optoelectronic systems. *Small*, 1(12):1164 1168, 2005.

[109] Yugang Sun, Hoon-Sik Kim, Etienne Menard, Seiyon Kim, Ilesanmi Adesida, and John A. Rogers. Printed arrays of aligned GaAs wires for flexible transistors, diodes, and circuits on plastic substrates. *Small*, 2(11):1330 1334, 2006.

[110] Yugang Sun and John A. Rogers. Fabricating semiconductor nano/microwires and transfer printing ordered arrays of them onto plastic substrates. *Nano Letters*, 4(10):1953 1959, 2004.

[111] Yugang Sun, Rachel A. Graff, Michael S. Strano, and John A. Rogers. Top-down fabrication of semiconductor nanowires with alternating structures along their longitudinal and transverse axes. *Small*, 1(11):1052 1057, 2005.

[112] D. R. Hines, S. Mezhenny, M. Breban, E. D. Williams, V. W. Ballarotto, G. Esen, A. Southard, and M. S. Fuhrer. Nanotransfer printing of organic and carbon nanotube thin-film transistors on plastic substrates. *Applied Physics Letters*, 86(16): , 2005.

[113] D. R. Hines, A. Southard, and M. S. Fuhrer. Poly(3-hexylthiophene) thin-film transistors with variable polymer dielectrics for transfer-printed flexible electronics. *Journal of Applied Physics*, 104(2): , 2008.

[114] Sang-Il Park, Yujie Xiong, Rak-Hwan Kim, Paulius Elvikis, Matthew Meitl, Dae-Hyeong Kim, Jian Wu, Jongseung Yoon, Chang-Jae Yu, Zhuangjian Liu, Yonggang Huang, Keh-chih Hwang, Placid Ferreira, Xiuling Li, Kent Choquette, and John A. Rogers. Printed assemblies of inorganic light-emitting diodes for deformable and semitransparent displays. *Science*, 325(5943):977 981, 2009.

[115] Jong-Hyun Ahn, Hoon-Sik Kim, Keon Jae Lee, Seokwoo Jeon, Seong Jun Kang, Yugang Sun, Ralph G. Nuzzo, and John A. Rogers. Heterogeneous three-dimensional electronics by use of printed semiconductor nanomaterials. *Science*, 314(5806):1754 1757, 2006.

[116] Jongseung Yoon, Sungjin Jo, Ik Su Chun, Inhwa Jung, Hoon-Sik Kim, Matthew Meitl, Etienne Menard, Xiuling Li, James J Coleman, Ungyu Paik, et al. GaAs photovoltaics and optoelectronics using releasable multilayer epitaxial assemblies. *Nature*, 465(7296):329 333, 2010.

[117] Dawen Li and L Jay Guo. Organic thin film transistors and polymer light-emitting diodes patterned by polymer inking and stamping. *Journal of Physics D Applied Physics*, 41(10):105115, 2008.

[118] Dawen Li and L Jay Guo. Micron-scale organic thin film transistors with conducting polymer electrodes patterned by polymer inking and stamping. *Applied Physics Letters*, 88(6): , 2006.

[119] Kyung-Ho Kim, Ki-Wan Bong, and Hong H. Lee. Alternative to pentacene patterning for organic thin film transistor. *Applied Physics Letters*, 90(9): , 2007.

[120] Joonhyung Park, Sang-Oak Shim, and Hong H. Lee. Polymer thin-film transistors fabricated by dry transfer of polymer semiconductor. *Applied Physics Letters*, 86(7): , 2005.

[121] T. Borzenko, M. Tormen, G. Schmidt, L. W. Molenkamp, and H. Janssen. Polymer bonding process for nanolithography. *Applied Physics Letters*, 79(14), 2001.

[122] Lu Zhang, Zhijie Chen, J. Joshua Yang, Bryant Wysocki, Nathan McDonald, and Yiran Chen. A compact modeling of TiO_2-TiO_{2-x} memristor. *Applied Physics Letters*, 102(15): , 2013.

[123] Brian O'Regan and Michael Graetzel. A low-cost, high-efficiency solar cell based on dye-sensitized colloidal TiO_2 films. *Nature*, 353(6346):737 740, 1991.

[124] S Y Huang, G Schlichthorl, A J Nozik, M Grätzel, and A J Frank. Charge recombination in dye-sensitized nanocrystalline TiO_2 solar cells. *Journal of Physical Chemistry B*, 101(14):2576 2582, 1997.

[125] U Bach, D Lupo, P Comte, J E Moser, F Weissoertel, J Salbeck, H Spreitzer, and M Grätzel. Solid-state dye-sensitized mesoporous TiO_2 solar cells with high photon-to-electron conversion efficiencies. *Nature*, 395(6702):583 585, 1998.

[126] A. Vittadini, A. Selloni, F. P. Rotzinger, and M. Grätzel. Structure and energetics of water adsorbed at TiO_2 anatase 101 and 001 surfaces. *Physical Review Letters*, 81(14):2954 2957, 1998.

[127] Arthur J. Frank, Nikos Kopidakis, and Jao Van De Lagemaat. Electrons in nanostructured TiO_2 solar cells transport, recombination and photovoltaic properties. *Coordination Chemistry Reviews*, 248(13-14):1165 1179, Jul 2004.

[128] Seigo Ito, Paul Liska, Pascal Comte, Raphaël Charvet, Peter Pechy, Udo Bach, Lukas Schmidt-Mende, Shaik Mohammed Zakeeruddin, Andreas Kay, Mohammad K Nazeeruddin, and et al. Control of dark current in photoelectrochemical (TiO_2/i i3-)) and dye-sensitized solar cells. *Chemical communications (Cambridge, England)*, (34):4351 3, Sep 2005.

[129] Qing Wang, Seigo Ito, Michael Grätzel, Francisco Fabregat-Santiago, Iván Mora-Seró, Juan Bisquert, Takeru Bessho, and Hachiro Imai. Characteristics of high efficiency dye-sensitized solar cells. *The Journal of Physical Chemistry B*, 110(50):25210 21, Dec 2006.

[130] Suresh Gubbala, Vidhya Chakrapani, Vivekanand Kumar, and Mahendra K. Sunkara. Band-edge engineered hybrid structures for dye-sensitized solar cells based on SnO_2 nanowires. *Advanced Functional Materials*, 18(16):2411 2418, Aug 2008.

[131] Henry J Snaith, Adam J Moule, Klaus Klein, Cederic Meerholz, Richard H Friend, and Michael Grätzel. Efficiency enhancements in solid-state hybrid solar cells via reduced charge recombination and increased light capture. *Nano Letters*, 7(11):3372 3376, 2007. PMID: 17918905.

[132] Lukas Schmidt-Mende and Michael Grätzel. TiO_2 pore-filling and its effect on the efficiency of solid-state dye-sensitized solar cells. *Thin Solid Films*, 500(1 2):296 301, 2006.

[133] Jihuai Wu, Gentian Yue, Yaoming Xiao, Jianming Lin, Miaoliang Huang, Zhang Lan, Qunwei Tang, Yunfang Huang, Leqing Fan, Shu Yin, and et al. An ultraviolet responsive hybrid solar cell based on titania/poly (3-hexylthiophene). *Scientific Reports*, 3, 2013.

[134] Jessica Krueger, Udo Bach, and Michael Grätzel. Modification of TiO_2 heterojunctions with benzoic acid derivatives in hybrid molecular solid-state devices. *Advanced Materials*, 12(6):447 451, 2000.

[135] Jan C Brauer, Joël Teuscher, Angela Punzi, and Jacques-e Moser. Transient photoconductivity of dye-sensitized TiO_2 nanocrystalline films probed by optical pump-thz probe spectroscopy. *Ultrafast Phenomena XVII, New York Oxford University Press, 2011*, page 358 360.

[136] Weijun Ke, Guojia Fang, Jing Wang, Pingli Qin, Hong Tao, Hongwei Lei, Qin Liu, Xin Dai, and Xingzhong Zhao. Perovskite solar cell with an efficient TiO_2 compact film. *ACS Applied Materials & Interfaces*, 6(18):15959 15965, 2014. PMID: 25166513.

[137] Julian Burschka, Norman Pellet, Soo-Jin Moon, Robin Humphry-Baker, Peng Gao, Mohammad K Nazeeruddin, and Michael Grätzel. Sequential deposition as a route to high-performance perovskite-sensitized solar cells. *Nature*, 499(7458):316 9, 2013.

[138] Pablo Docampo, Stefan Guldin, Ullrich Steiner, and Henry J. Snaith. Charge transport limitations in self-assembled TiO_2 photoanodes for dye-sensitized solar cells. *The Journal of Physical Chemistry Letters*, 4(5):698 703, 2013. PMID: 26281921.

[139] Priti Tiwana, Patrick Parkinson, Michael B. Johnston, Henry J. Snaith, and Laura M. Herz. Ultrafast terahertz conductivity dynamics in mesoporous TiO_2 influence of dye sensitization and surface treatment in solid-state dye-sensitized solar cells. *Journal of Physical Chemistry C*, 114(2):1365 1371, 2010.

[140] Ştefan Neaţu, Juan Antonio Maciá-Agulló, and Hermenegildo Garcia. Solar light photocatalytic CO_2 reduction general considerations and selected bench-mark

photocatalysts. *International Journal of Molecular Sciences*, 15(4):5246 5262, 2014.

[141] Michael a. Henderson, J. Michael White, Hiroshi Uetsuka, and Hiroshi Onishi. Photochemical charge transfer and trapping at the interface between an organic adlayer and an oxide semiconductor. *Journal of the American Chemical Society*, 125(49):14974 14975, 2003.

[142] Kimfung Li, Xiaoqiang An, Kyeong Hyeon Park, Majeda Khraisheh, and Junwang Tang. A critical review of CO_2 photoconversion catalysts and reactors. *Catalysis Today*, 224:3 12, 2014.

[143] Michael a. Henderson. A surface science perspective on TiO_2 photocatalysis. *Surface Science Reports*, 66(6-7):185 297, Jun 2011.

[144] Anton Visikovskiy, Kei Mitsuhara, and Yoshiaki Kido. Role of gold nanoclusters supported on TiO_2(110) model catalyst in co oxidation reaction. *Journal of Vacuum Science & Technology A Vacuum, Surfaces, and Films*, 31(6):061404, 2013.

[145] Enzhou Liu, Limin Kang, Yuhao Yang, Tao Sun, Xiaoyun Hu, Changjun Zhu, Hanchen Liu, Qiuping Wang, Xinghua Li, and Jun Fan. Plasmonic ag deposited TiO_2 nano-sheet film for enhanced photocatalytic hydrogen production by water splitting. *Nanotechnology*, 25(16):165401, 2014.

[146] Michael a Henderson. Structural sensitivity in the dissociation of water on TiO_2 single-crystal surfaces. *Langmuir*, 12(21):5093 5098, 1996.

[147] H. Kohlstedt, N. a. Pertsev, J. Rodríguez Contreras, and R. Waser. Theoretical current-voltage characteristics of ferroelectric tunnel junctions. *Physical Review B - Condensed Matter and Materials Physics*, 72(12):1 10, 2005.

[148] Sang Woon Lee, Oh Seong Kwon, Jeong Hwan Han, and Cheol Seong Hwang. Enhanced electrical properties of $SrTiO_3$ thin films grown by atomic layer deposition at high temperature for dynamic random access memory applications. *Applied Physics Letters*, 92(22):1 3, 2008.

[149] Dan Popescu, Bogan Popescu, Gunther Jegert, Sebastian Schmelzer, Ulrich Boettger, and Paolo Lugli. Feasibility study of $SrRuO_3$ / $SrTiO_3$ / $SrRuO_3$ thin film capacitors in DRAM applications. 61(6):2130 2135, 2014.

[150] Jose Antonio Gomez-Pedrero, James Ginn, Javier Alda, and Glenn Boreman. Modulation transfer function for infrared reflectarrays. *Appl. Opt.*, 50(27):5344 5350, Sep 2011.

[151] Hongzhong Liu, Bangdao Chen, Xin Li, Weihua Liu, Yucheng Ding, and Bingheng Lu. A metal/insulator/metal field-emission cannon. *Nanotechnology*, 22(45):455302, 2011.

[152] F. Argall. Switching phenomena in titanium oxide thin films. *Solid-State Electronics*, 11(5):535 541, 1968.

[153] Rainer Waser and Masakazu Aono. Nanoionics-based resistive switching memories. *Nat Mater*, 6(11):833 840, Nov 2007.

[154] Kyung Min Kim, Byung Joon Choi, Min Hwan Lee, Gun Hwan Kim, Seul Ji Song, Jun Yeong Seok, Jeong Ho Yoon, Seungwu Han, and Cheol Seong Hwang. A detailed understanding of the electronic bipolar resistance switching behavior in pt/TiO_2/Pt structure. *Nanotechnology*, 22(25):254010, Jun 2011.

[155] Kyung Min Kim, Seungwu Han, and Cheol Seong Hwang. Electronic bipolar resistance switching in an anti-serially connected pt/TiO_2/Pt structure for improved reliability. *Nanotechnology*, 23(3):035201, Jan 2012.

[156] Deok-Hwang Kwon, Kyung Min Kim, Jae Hyuck Jang, Jong Myeong Jeon, Min Hwan Lee, Gun Hwan Kim, Xiang-Shu Li, Gyeong-Su Park, Bora Lee, Seungwu Han, and et al. Atomic structure of conducting nanofilaments in TiO_2 resistive switching memory. *Nature nanotechnology*, 5(2):148 153, 2010.

[157] Sanghee Won, Seunghee Go, Kwanwoo Lee, and Jaegab Lee. Resistive switching properties of Pt / TiO_2 / n -Si ReRAM for nonvolatile memory application. *Electronic Materials Letters*, 5(1):29 33, 2008.

[158] K Szot, M Rogala, W Speier, Z Klusek, a Besmehn, and R Waser. TiO_2 a prototypical memristive material. *Nanotechnology*, 22(25):254001, Jun 2011.

[159] Doo Seok Jeong, Herbert Schroeder, and Rainer Waser. Mechanism for bipolar switching in a Pt / TiO_2 / Pt resistive switching cell. *Physical Review B*, 79(19):195317, May 2009.

[160] Eike Linn, Roland Rosezin, Carsten Kuegeler, and Rainer Waser. Complementary resistive switches for passive nanocrossbar memories. *Nature materials*, 9(5):403 406, 2010.

[161] Juan Bisquert. Theory of the impedance of electron diffusion and recombination in a thin layer. *The Journal of Physical Chemistry B*, 106(2):325 333, Jan 2002.

[162] Ivan Mora-Seró and Juan Bisquert. Fermi level of surface states in TiO_2 nanoparticles. *Nano Letters*, 3(7):945 949, 2003.

[163] Laurence M Peter, Alison B Walker, Gerrit Boschloo, and Anders Hagfeldt. Interpretation of apparent activation energies for electron transport in dye-sensitized nanocrystalline solar cells. *The journal of physical chemistry. B*, 110(28):13694 9, Jul 2006.

[164] Annamaria Petrozza, Chris Groves, and Henry J Snaith. Electron transport and recombination in dye-sensitized mesoporous TiO_2 probed by photoinduced charge-conductivity modulation spectroscopy with monte carlo modeling. *Journal of the American Chemical Society*, 130(39):12912 20, Oct 2008.

[165] Alessio Gagliardi, Matthias Auf der Maur, Desiree Gentilini, and Aldo Di Carlo. Simulation of dye solar cells through and beyond one dimension. *Journal of computational electronics*, 10(4):424 436, 2011.

[166] Desirée Gentilini, Alessio Gagliardi, Matthias Auf der Maur, Luigi Vesce, Daniele D'Ercole, Thomas M Brown, Andrea Reale, and Aldo Di Carlo. Correlation between cell performance and physical transport parameters in dye solar cells. *The Journal of Physical Chemistry C*, 116(1):1151 1157, 2011.

[167] Philip Reckers, Mariel Dimamy, Joachim Klett, Sara Trost, Kirill Zilberberg, Thomas Riedl, Bruce a Parkinson, Joachim Broetz, Wolfram Jaegermann, and Thomas Mayer. Deep and shallow TiO_2 gap states on cleaved anatase single crystal (101) surfaces, nanocrystalline anatase films, and ALD titania ante and post annealing. *The Journal of Physical Chemistry C*, (101):150413112938002, 2015.

[168] L. Vandelli, a. Padovani, L. Larcher, R. G. Southwick, W. B. Knowlton, and G. Bersuker. A physical model of the temperature dependence of the current through SiO_2/HfO_2 stacks. *IEEE Transactions on Electron Devices*, 58(9):2878 2887, 2011.

[169] D. Liu, Y. Guo, L. Lin, and J. Robertson. First-principles calculations of the electronic structure and defects of Al_2O_3. *Journal of Applied Physics*, 114(8):083704, 2013.

[170] Benjamin J. Morgan and Graeme W. Watson. Polaronic trapping of electrons and holes by native defects in anatase TiO_2. *Physical Review B*, 80:233102, Dec 2009.

[171] Peter Deák, Bálint Aradi, and Thomas Frauenheim. Quantitative theory of the oxygen vacancy and carrier self-trapping in bulk TiO_2. *Physical Review B*, 86(19):195206, Nov 2012.

[172] Takenori Yamamoto and Takahisa Ohno. A hybrid density functional study on the electron and hole trap states in anatase titanium dioxide. *Physical chemistry chemical physics*, 14(2):589 598, Jan 2012.

[173] Giuseppe Mattioli, Paola Alippi, Francesco Filippone, Ruggero Caminiti, and Aldo Amore Bonapasta. Deep versus shallow behavior of intrinsic defects in rutile and anatase TiO_2 polymorphs. *Journal of Physical Chemistry C*, 114(49):21694 21704, 2010.

[174] Hsin-Yi Lee, Stewart J. Clark, and John Robertson. Calculation of point defects in rutile TiO_2 by the screened-exchange hybrid functional. *Physical Review B*, 86(7):075209, Aug 2012.

[175] H. Baessler. Charge transport in disordered organic photoconductors a monte carlo simulation study. *physica status solidi (b)*, 175(1):15 56, 1993.

[176] Jenny Nelson. Continuous-time random-walk model of electron transport in nanocrystalline tio$_2$ electrodes. *Phys. Rev. B*, 59:15374 15380, Jun 1999.

[177] Juan A. Anta, Jenny Nelson, and N. Quirke. Charge transport model for disordered materials Application to sensitized TiO_2. *Physical Review B*, 65(12):125324, Mar 2002.

[178] Jenny Nelson and Rosemary E. Chandler. Random walk models of charge transfer and transport in dye sensitized systems. *Coordination Chemistry Reviews*, 248(13-14):1181 1194, Jul 2004.

[179] M. J. Cass, F. L. Qiu, Alison B. Walker, a. C. Fisher, and L. M. Peter. Influence of Grain Morphology on Electron Transport in Dye Sensitized Nanocrystalline Solar Cells. *The Journal of Physical Chemistry B*, 107(1):113 119, Jan 2003.

[180] Peter K Watkins, Alison B Walker, and Geraldine L B Verschoor. Dynamical Monte Carlo modelling of organic solar cells The dependence of internal quantum efficiency on morphology. *Nano letters*, 5(9):1814 8, Sep 2005.

[181] Juan Bisquert. Hopping transport of electrons in dye-sensitized solar cells. *The Journal of Physical Chemistry C*, 111(46):17163 17168, 2007.

[182] Juan Bisquert. Hopping transport of electrons in dye-sensitized solar cells. *The Journal of Physical Chemistry C*, 111(46):17163 17168, Nov 2007.

[183] J P Gonzalez-Vazquez, Juan a Anta, and Juan Bisquert. Random walk numerical simulation for hopping transport at finite carrier concentrations diffusion coefficient and transport energy concept. *Physical chemistry chemical physics PCCP*, 11(44):10359 67, Nov 2009.

[184] J. P. Gonzalez-Vazquez, Juan a. Anta, and Juan Bisquert. Determination of the Electron Diffusion Length in Dye-Sensitized Solar Cells by Random Walk Simulation Compensation Effects and Voltage Dependence. *The Journal of Physical Chemistry C*, 114(18):8552 8558, May 2010.

[185] Juan Bisquert, Iván Mora-Sero, and Francisco Fabregat-Santiago. Diffusion-Recombination Impedance Model for Solar Cells with Disorder and Nonlinear Recombination. *ChemElectroChem*, pages n/a n/a, Sep 2013.

[186] S.M. Sze and K.K. Ng. *Physics of Semiconductor Devices*. Wiley, 2006.

[187] David K. Ferry, Stephen M. Goodnick, and Jonathan Bird. *Transport in Nanostructures*. Cambridge University Press, 2nd edition, Sep 2009.

[188] Gunther Jegert, Alfred Kersch, Wenke Weinreich, and Paolo Lugli. Ultimate scaling of TiN/ZrO_2/TiN capacitors leakage currents and limitations due to electrode roughness. *Journal of Applied Physics*, 109(1), 2011.

[189] Gunther Jegert, Alfred Kersch, Wenke Weinreich, Paolo Lugli, Senior Member, and Abstract Leakage. Monte carlo simulation of leakage currents in TiN / ZrO_2 / TiN capacitors. *IEEE Transactions on Electron Devices*, 58(2):327 334, 2011.

[190] Gunther Jegert, Dan Popescu, Paolo Lugli, Martin Johannes Häufel, Wenke Weinreich, and Alfred Kersch. Role of defect relaxation for trap-assisted tunneling in high-κ thin films a first-principles kinetic monte carlo study. *Physical Review B*, 85(4):045303, Jan 2012.

[191] Andrea Padovani, Luca Larcher, Gennadi Bersuker, and Paolo Pavan. Charge transport and degradation in HfO_2 and HfO_x dielectrics. *IEEE Electron Device Letters*, 34(5):680 682, 2013.

[192] Herbert Schroeder, Sam Schmitz, and Paul Meuffels. Leakage currents in high-permittivity thin films. *Applied Physics Letters*, 82(5), 2003.

[193] G. Bersuker, D. C. Gilmer, D. Veksler, P. Kirsch, L. Vandelli, A. Padovani, L. Larcher, K. McKenna, A. Shluger, V. Iglesias, M. Porti, and M. Nafría. Metal oxide resistive memory switching mechanism based on conductive filament properties. *Journal of Applied Physics*, 110(12), 2011.

[194] D. Manger, B. Kaczer, N. Menou, S. Clima, D.J. Wouters, V.V. Afanas'ev, and J.A. Kittl. Comprehensive investigation of trap-assisted conduction in ultra-thin $SrTiO_3$ layers. *Microelectronic Engineering*, 86(7 9):1815 1817, 2009.

[195] Herbert Schroeder, Alexander Zurhelle, Stefanie Stemmer, Astrid Marchewka, and Rainer Waser. Resistive switching near electrode interfaces estimations by a current model. *Journal of Applied Physics*, 113(5), 2013.

[196] Marc J. Madou. *Fundamentals of microfabrication The science of miniaturization*. CRC Press, 2nd edition, Mar 2002.

[197] M. Ritala and M. Leskelae. *Handbook of Thin Film Materials Volume 1 Deposition and Processing of Thin Films, Chapter 2*. Nalwa, H.S., Academic Press, San Diego, CA, 2nd edition.

[198] Electron Microscopy Sciences. Barrel asher data sheets. Technical report, Electron Microscopy Sciences, 1560 Industry Road, Hatfield, PA 19440.

[199] J.C. Tinoco, M. Estrada, H. Baez, and A. Cerdeira. Room temperature plasma oxidation - a new process for preparation of ultrathin layers of silicon oxide, and high dielectric constant materials. *Thin Solid Films*, 496(2):546 554, 2006.

[200] Kyu Won Lee, SM Yoon, SC Lee, W Lee, IM Kim, Cheol Eui Lee, and DH Kim. Secondary electron generation in electron-beam-irradiated solids resolution limits to nanolithography. *J. Kor. Phys. Soc*, 55:1720 1723, 2009.

[201] Stephen Y Chou, Peter R Krauss, and Preston J Renstrom. Imprint of sub-25 nm vias and trenches in polymers. *Applied physics letters*, 67(21):3114 3116, 1995.

[202] L J Guo. Nanoimprint Lithography Methods and Material Requirements. *Advanced Materials*, 19(4):495 513, Feb 2007.

[203] R. Morasch. Nanopatterning using nil and ntp an investigation on the reusability of the stamps, Sep 2012.

[204] www.obducat.com Obducat AB. *Operation and maintenance manual for NIL-2.5 inch Nanoimprinter*, 2004. 41 pages.

[205] M. Bareiß, B. Weiler, D. Kölblein, U. Zschieschang, H. Klauk, G. Scarpa, B. Fabel, P. Lugli, and W. Porod. Nano-transfer printing of functioning mim tunnel diodes. *2012 IEEE Silicon Nanoelectronics Workshop (SNW), 1-2 (2012)*, pages 1 2, Jun 2012.

[206] B. Weiler, D. Kalblein, U. Zschieschang, H. Klauk, G. Scarpa, B. Fabel, W. Porod, P. Lugli, and M. Bareiß. Conductive afm of transfer printed nano devices. *12th IEEE Conference on Nanotechnology (IEEE-NANO)*, pages 1 5, Aug 2012.

[207] Qiong Cheng, W. Ahmad, Guohua Liu, and Kaiying Wang. Structural evolution of amorphous thin films of titanium dioxide. In *Nanotechnology (IEEE-NANO), 2011 11th IEEE Conference on*, pages 1598 1601, Aug 2011.

[208] Carl Zeiss AG. *Product Information 1.3, Zeiss GeminiSEM Family*, version 2.0 edition, 31.03.2015. 19 pages.

[209] Asylum Research. *Imaging and Spectroscopy Applications Guide*, version alpha edition, September 21, 2012. 170 pages.

[210] USA Bruker Corporation, Santa Barbara. *SPM Training Guide, AFM, AFM Modes*. http://www.nanophys.kth.se/nanophys/facilities/nfl/afm/icon/bruker-help/Content/SPM

[211] Asylum Research. *MFP-3D Manual*, version 04.08. edition, April 2008. 270 pages.

[212] Korea Park Atomic Force Microscope. *Conductive AFM, Probing the Local Electronic Structure of a Sample's Surface*, September 2011. http://www.parkafm.com/images/spmmodes/electrical/Conductive-AFM.pdf.

[213] Cleveland Ohio Keithley Instruments, Inc. *Series 2400 SourceMeter User's Manual*, 2400s-900-01 rev. k edition, September 2011. 496 pages.

[214] Cleveland Ohio Keithley Instruments, Inc. *Keithley Application Note Series, No. 2896*, 2227 edition, December 2007. 10 pages.

[215] P. Kratzer. *Monte Carlo and kinetic Monte Carlo Methods - a tutorial, published in Multiscale Simulation Methods in Molecular Sciences*. J. Grotendorst, N. Attig, S. Bluegel, D. Marx (Eds.), Institute for Advanced Simulation, Forschungszentrum Juelich, NIC Series, 2nd edition.

[216] R. Car and M. Parrinello. Unified approach for molecular dynamics and density-functional theory. *Phys. Rev. Lett.*, 55:2471 2474, Nov 1985.

[217] Nicholas Metropolis, Arianna W. Rosenbluth, Marshall N. Rosenbluth, Augusta H. Teller, and Edward Teller. Equation of state calculations by fast computing machines. *The Journal of Chemical Physics*, 21(6), 1953.

[218] W. K. Hastings. Monte carlo sampling methods using markov chains and their applications. *Biometrika*, 57(1):97 109, 1970.

[219] S. M. Goodnick and P. Lugli. Effect of electron-electron scattering on nonequilibrium transport in quantum-well systems. *Phys. Rev. B*, 37:2578 2588, Feb 1988.

[220] James R Norris. *Markov Chains*. Number 2008. Cambridge University Press, 1998.

[221] Peter Kratzer. Monte Carlo and kinetic Monte Carlo methods. page 30, Apr 2009.

[222] R. Tsu and L. Esaki. Tunneling in a finite superlattice. *Applied Physics Letters*, 22(11):562 564, 1973.

[223] W. Franz. *Handbuch der Physik*, volume 17. Fluegge G.S., Springer-Verlag, Berlin, 1956.

[224] J. Maserjian. Tunneling in thin mos structures. *Journal of Vacuum Science & Technology*, 11(6), 1974.

[225] Z. a. Weinberg. On tunneling in metal-oxide-silicon structures. *Journal of Applied Physics*, 53(7):5052 5056, 1982.

[226] G. Dresselhaus, A. F. Kip, and C. Kittel. Spin-orbit interaction and the effective masses of holes in germanium. *Phys. Rev.*, 95:568 569, Jul 1954.

[227] A. Hartstein and Z. A. Weinberg. Unified theory of internal photoemission and photon-assisted tunneling. *Phys. Rev. B*, 20:1335 1338, Aug 1979.

[228] Z.A. Weinberg. Tunneling of electrons from Si into thermally grown SiO_2. *Solid-State Electronics*, 20(1):11 18, 1977.

[229] M. Herrmann and A. Schenk. Field and high-temperature dependence of the long term charge loss in erasable programmable read only memories measurements and modeling. *Journal of Applied Physics*, 77(9):4522 4540, 1995.

[230] Andreas Schenk and Gernot Heiser. Modeling and simulation of tunneling through ultra-thin gate dielectrics. *Journal of Applied Physics*, 81(12):7900, 1997.

[231] Andreas Schenk. *Advanced Physical Models for Silicon Device Simulation*. Springer-Verlag Wien, 1st edition.

[232] R Entner, A Gehring, H Kosina, T Grasser, and S Selberherr. Impact of multi-trap assisted tunneling on gate leakage of cmos memory devices. 3(4):45 48, 2005.

[233] D. V. Lang and C. H. Henry. Nonradiative recombination at deep levels in GaAs and GaP by lattice-relaxation multiphonon emission. *Physical Review Letters*, 35(22):1525 1528, 1975.

[234] D. Pons and S. Makram-Ebeid. Phonon assisted tunnel emission of electrons from deep levels in GaAs. *Journal de Physique*, 40(12):1161 1172, 1979.

[235] Brian K Ridley. On the multiphonon capture rate in semiconductors. 21:1319 1323, 1978.

[236] Ingemar Lundström and Christer Svensson. Tunneling to traps in insulators. *Journal of Applied Physics*, 43(12):5045 5047, 1972.

[237] Christer Svensson and Ingemar Lundstroem. Trap-assisted charge injection in mnos structures. *Journal of Applied Physics*, 44(10):4657 4663, 1973.

[238] J. Bardeen. Tunnelling from a many-particle point of view. *Phys. Rev. Lett.*, 6:57 59, Jan 1961.

[239] A. Kiveris, Š Kudžmauskas, and P. Pipinys. Release of electrons from traps by an electric field with phonon participation. *physica status solidi (a)*, 37(1):321 327, 1976.

[240] F I Dalidchik. Multiphonon tunnel process in a homogeneous electric field. *Zh. Eksp. Teor. Fiz.*, 74(2):472 482, Feb 1978.

[241] C. Kittel. *Einführung in die Festkörperphysik*. Oldenbourg, 2006.

[242] Allen Miller and Elihu Abrahams. Impurity conduction at low concentrations. *Phys. Rev.*, 120:745 755, Nov 1960.

[243] J. L. Hartke. The three dimensional poole frenkel effect. *Journal of Applied Physics*, 39(10), 1968.

[244] John Robertson. Band offsets, schottky barrier heights, and their effects on electronic devices. *Journal of Vacuum Science & Technology A Vacuum, Surfaces, and Films*, 31(5):050821, 2013.

[245] F. Sacconi, M. Auf der Maur, and et.al. *TiberCAD User Manual*, 1.2.2-1446 edition, May 12, 2009. 104 pages.

[246] M. Auf der Maur. *A Multiscale Simulation Environment for Electronic and Optoelectronic Devices, PhD Thesis*. PhD thesis, Universita di Roma Tor Vergata, 2008.

[247] J. Robertson and S. J. Clark. Limits to doping in oxides. *Physical Review B*, 83(7):075205, Feb 2011.

[248] John Robertson. Band offsets of wide-band-gap oxides and implications for future electronic devices. *Journal of Vacuum Science & Technology B*, (3):1785 1791, may 2000.

[249] S. Makram-Ebeid and M. Lannoo. Quantum model for phonon-assisted tunnel ionization of deep levels in a semiconductor. *Phys. Rev. B*, 25:6406 6424, May 1982.

[250] Christian Wehrenfennig, Claudia Maria Palumbiny, Henry J. Snaith, Michael B Johnston, Lukas Schmidt-Mende, and Laura M. Herz. Fast charge-carrier trapping in TiO_2 nanotubes. *The Journal of Physical Chemistry C*, 2015.

[251] Ute Zschieschang, Frederik Ante, Matthias Schloerholz, Maike Schmidt, Klaus Kern, and Hagen Klauk. Mixed self-assembled monolayer gate dielectrics for continuous threshold voltage control in organic transistors and circuits. *Advanced Materials*, 22(40):4489 4493, 2010.

[252] Tao Yang, Simon Hertenberger, Stefanie Morkoetter, Gerhard Abstreiter, and Gregor Koblmueller. Size, composition, and doping effects on in(ga)as nanowire/Si tunnel diodes probed by conductive atomic force microscopy. *Applied Physics Letters*, 101(23), 2012.

[253] Ashish Agrawal, Joyce Lin, Michael Barth, Ryan White, Bo Zheng, Saurabh Chopra, Shashank Gupta, Ke Wang, Jerry Gelatos, Suzanne E. Mohney, and et al. Fermi level depinning and contact resistivity reduction using a reduced titania interlayer in n-silicon metal-insulator-semiconductor ohmic contacts. *Applied Physics Letters*, 104(11):112101, Mar 2014.

[254] Doo Seok Jeong, Herbert Schroeder, and Rainer Waser. Mechanism for bipolar switching in a Pt / TiO_2 / Pt resistive switching cell. *Physical Review B*, 79(19):195317, May 2009.

[255] Woo Young Park, Gun Hwan Kim, Jun Yeong Seok, Kyung Min Kim, Seul Ji Song, Min Hwan Lee, and Cheol Seong Hwang. A Pt/TiO_2/Ti schottky-type selection diode for alleviating the sneak current in resistance switching memory arrays. *Nanotechnology*, 21(19):195201, May 2010.

[256] P. Bousoulas, J. Giannopoulos, K. Giannakopoulos, P. Dimitrakis, and D. Tsoukalas. Memory programming of TiO_{2-x} films by conductive atomic force microscopy evidencing filamentary resistive switching. *Applied Surface Science*, 332:55 61, Mar 2015.

[257] B Kinaci, T Asar, Y özen, and S özçelİk. The analysis of Au / TiO_2 / n-Si schottky barrier diode at high temperatures using i-v characteristics. 5(4):434 437, 2011.

[258] Sarves Verma. Tunnel barrier engineering for flash memory technology. *Ph.D Dissertation of Stanford University*, (May), 2010.

[259] Qiong Cheng, Waqas Ahmad, Guohua Liu, and Kaiying Wang. Structural evolution of amorphous thin films of titanium dioxide. *2011 11th IEEE International Conference on Nanotechnology*, pages 1598 1601, 2011.

[260] G. Mattioli, F. Filippone, P. Alippi, and a. Amore Bonapasta. Ab initio study of the electronic states induced by oxygen vacancies in rutile and anatase TiO_2. *Physical Review B*, 78(24):3 6, 2008.

[261] Cristiana Di Valentin, Annabella Selloni, and Via R Cozzi. Bulk and surface polarons in photoexcited anatase TiO_2. page 2223 2228, 2011.

[262] Emanuele Finazzi, Cristiana Di Valentin, Gianfranco Pacchioni, and Annabella Selloni. Excess electron states in reduced bulk anatase TiO_2 comparison of standard gga, gga+u, and hybrid dft calculations. *Journal of Chemical Physics*, 129(15), 2008.

[263] Hieu H. Pham and Lin-Wang Wang. Oxygen vacancy and hole conduction in amorphous TiO_2. *Phys. Chem. Chem. Phys.*, 17(1):541 550, 2015.

[264] Peter Vogl. Chemical trends of deep impurity levels in covalent semiconductors. *Festkörperprobleme 21*, 21:191 219, 1981.

[265] a. Thomas, W. Flavell, a. Mallick, a. Kumarasinghe, D. Tsoutsou, N. Khan, C. Chatwin, S. Rayner, G. Smith, R. Stockbauer, and et al. Comparison of the electronic structure of anatase and rutile TiO_2 single-crystal surfaces using resonant photoemission and x-ray absorption spectroscopy. *Physical Review B*, 75(3):1 12, 2007.

[266] Estephania Lira, Stefan Wendt, Peipei Huo, Jonas Hansen, Regine Streber, Søren Porsgaard, Yinying Wei, Ralf Bechstein, Erik Lægsgaard, and Flemming Besenbacher. The importance of bulk Ti^{3+} defects in the oxygen chemistry on titania surfaces. *Journal of the American Chemical Society*, 133(17):6529 6532, 2011.

[267] Richard L. Kurtz, Roger Stockbauer, Theodore E. Madey, Elisa Román, and JoseL. de Segovia. Synchrotron radiation studies of H_2O adsorption on TiO_2(110). *Surface Science Letters*, 218(1):A400, 1989.

[268] P. Krueger, S. Bourgeois, B. Domenichini, H. Magnan, D. Chandesris, P. Le Fevre, a. M. Flank, J. Jupille, L. Floreano, a. Cossaro, and et al. Defect states at the TiO_2(110) surface probed by resonant photoelectron diffraction. *Physical Review Letters*, 100(5):2 5, 2008.

[269] Emanuele Finazzi, Cristiana Di Valentin, and Gianfranco Pacchioni. Nature of ti interstitials in reduced bulk anatase and rutile TiO_2. *Journal of Physical Chemistry C*, 113(9):3382 3385, 2009.

[270] Martin Setvin, Cesare Franchini, Xianfeng Hao, Michael Schmid, Anderson Janotti, Merzuk Kaltak, Chris G Van De Walle, Georg Kresse, and Ulrike Diebold. Direct view at excess electrons in TiO_2 rutile and anatase. *Physical Review Letters*, 086402(August):086402, 2014.

[271] a. Thomas, W. Flavell, a. Kumarasinghe, a. Mallick, D. Tsoutsou, G. Smith, R. Stockbauer, S. Patel, M. Grätzel, and R. Hengerer. Resonant photoemission of anatase TiO_2 (101) and (001) single crystals. *Physical Review B*, 67(3):1 7, 2003.

[272] W. Göpel, U. Kirner, H.D. Wiemhöfer, and G. Rocker. Surface and bulk properties of TiO_2 in relation to sensor applications. *Solid State Ionics*, 28:1423 1430, 1988.

[273] Matthias Batzill, Khabibulakh Katsiev, Daniel J. Gaspar, and Ulrike Diebold. Variations of the local electronic surface properties of TiO_2 (110) induced by intrinsic and extrinsic defects. *Physical Review B*, 66(23):235401, Dec 2002.

[274] Zhaohui Zhou, Mingtao Li, and Liejin Guo. A first-principles theoretical simulation on the electronic structures and optical absorption properties for o vacancy and ni impurity in TiO_2 photocatalysts. *Journal of Physics and Chemistry of Solids*, 71(12):1707 1712, Dec 2010.

[275] Benjamin J Morgan and Graeme W Watson. Intrinsic n-type defect formation in TiO_2 a comparison of rutile and anatase from gga + u calculations. page 2321 2328, 2010.

[276] Cristiana Di Valentin, Gianfranco Pacchioni, and Annabella Selloni. Reduced and n-type doped TiO_2 nature of ti 3+ species. *The Journal of Physical Chemistry C*, 113(48):20543 20552, 2009.

[277] Junguang Tao and Matthias Batzill. Role of surface structure on the charge trapping in TiO_2 photocatalysts. *The Journal of Physical Chemistry Letters*, 1(21):3200 3206, Nov 2010.

[278] Shan Yang, L. E. Halliburton, a. Manivannan, P. H. Bunton, D. B. Baker, M. Klemm, S. Horn, and a. Fujishima. Photoinduced electron paramagnetic resonance study of electron traps in TiO_2 crystals oxygen vacancies and Ti^{3+} ions. *Applied Physics Letters*, 94(16):2 5, 2009.

[279] Min Li, Wilhelm Hebenstreit, Ulrike Diebold, Alexei M. Tyryshkin, Michael K. Bowman, Glen G. Dunham, and Michael a. Henderson. The influence of the bulk reduction state on the surface structure and morphology of rutile TiO_2 (110) single crystals. *The Journal of Physical Chemistry B*, 104(20):4944 4950, 2000.

[280] A. Weibel, R. Bouchet, and P. Knauth. Electrical properties and defect chemistry of anatase TiO_2. *Solid State Ionics*, 177(3-4):229 236, Jan 2006.

[281] N. D M Hine, K. Frensch, W. M C Foulkes, and M. W. Finnis. Supercell size scaling of density functional theory formation energies of charged defects. *Physical Review B - Condensed Matter and Materials Physics*, 79(2):1 13, 2009.

[282] Anderson Janotti and Chris G. Van de Walle. Lda + u and hybrid functional calculations for defects in zno, SnO_2, and TiO_2. *Advanced Calculations for Defects in Materials Electronic Structure Methods*, 804(4):155 164, 2011.

[283] K. Mitsuhara, H. Okumura, A. Visikovskiy, M. Takizawa, and Y. Kido. The source of the ti 3d defect state in the band gap of rutile titania (110) surfaces. *The Journal of Chemical Physics*, 136(12):124707, 2012.

[284] Cristiana Di Valentin, Gianfranco Pacchioni, and Annabella Selloni. Electronic structure of defect states in hydroxylated and reduced rutile TiO_2(110) surfaces. *Physical Review Letters*, 97(16), 2006.

[285] N. Aaron Deskins and Michel Dupuis. Electron transport via polaron hopping in bulk ti O_2 a density functional theory characterization. *Physical Review B - Condensed Matter and Materials Physics*, 75(19):1 10, 2007.

[286] J Robertson. High dielectric constant oxides. *Eurpoean Physical Journal Applied Physics*, 28:265 291, 2004.

[287] A. Gehring and S. Selberherr. Modeling of tunneling current and gate dielectric reliability for nonvolatile memory devices. *IEEE Transactions on Device and Materials Reliability*, 4(3):306 319, Sep 2004.

[288] Ai Chou, Kafai Lai, and Kiran Kumar. Modeling of stress-induced leakage current in ultrathin oxides with the trap-assisted tunneling mechanism. *Applied Physics Letters*, 70(1997):3407 3409, 1997.

[289] Kristina G. Young-Fisher, Gennadi Bersuker, Brian Butcher, Andrea Padovani, Luca Larcher, D. Veksler, and David C. Gilmer. Leakage current-forming voltage relation and oxygen gettering in HfO_x RRAM devices. *IEEE Electron Device Letters*, 34(6):750 752, 2013.

[290] Andrea Padovani, Luca Larcher, Sarves Verma, Paolo Pavan, Prashant Majhi, Pawan Kapur, Krishna Parat, Gennadi Bersuker, and Krishna Saraswat. Statistical modeling of leakage currents through SiO_2/high-κ dielectrics stacks for non-volatile memory applications. *2008 IEEE International Reliability Physics Symposium*, page 616 620, 2008.

[291] C. H. Henry and D. V. Lang. Nonradiative capture and recombination by multiphonon emission in GaAs and GaP. *Physical Review B*, 15(2):989 1016, 1977.

[292] H Krause. Tunnel hopping current and trap filling in insulating layers. *Physica Status Solidi (a)*, 52:565 575, 1979.

[293] Takahira Miyagi, Masayuki Kamei, Takefumi Mitsuhashi, and Atsushi Yamazaki. Discovery of the deep level related to hydrogen in anatase TiO_2. *Applied Physics Letters*, 88(13):132101, 2006.

[294] R Asahi, Y Taga, W Mannstadt, and A J Freeman. Electronic and optical properties of anatase TiO_2. 61(11):7459 7465, 2000.

[295] Letizia Chiodo, Juan García-Lastra, Amilcare Iacomino, Stefano Ossicini, Jin Zhao, Hrvoje Petek, and Angel Rubio. Self-energy and excitonic effects in the electronic and optical properties of TiO_2 crystalline phases. *Physical Review B*, 82(4):1 12, 2010.

[296] J. Robertson. Interfaces and defects of high-κ oxides on silicon. *Solid-State Electronics*, 49(3):283 293, Mar 2005.

[297] J. Robertson, K. Xiong, and S.J. Clark. Band gaps and defect levels in functional oxides. *Thin Solid Films*, 496(1):1 7, Feb 2006.

[298] Winfried Moench. Metal-semiconductor contacts electronic properties. *Surface Science*, 299-300(1):928 944, 1994.

[299] A.M. Cowley and S.M. Sze. Surface states and barrier height of metal-semiconductor systems. *J. Appl. Phys.*, 36:3212 3220, 1965.

[300] Francesco Santoni, Alessio Gagliardi, Matthias Auf Der Maur, and Aldo Di Carlo. The relevance of correct injection model to simulate electrical properties of organic semiconductors. *Organic Electronics physics, materials, applications*, 15(7):1557 1570, 2014.

[301] Paul A. Tipler and Ralph A. Llewellyn. *Modern Physics*. W.H. Freeman, 3 edition, 1999.

[302] Hyunsoo Lee, Young Keun Lee, Trong Nghia Van, and Jeong Young Park. Nanoscale schottky behavior of Au islands on TiO_2 probed with conductive atomic force microscopy. *Applied Physics Letters*, 103(17):173103, 2013.

[303] Andreas Klein, Christoph Koerber, Andre Wachau, Frank Saeuberlich, Yvonne Gassenbauer, Steven P. Harvey, Diana E. Proffit, and Thomas O. Mason. Transparent conducting oxides for photovoltaics manipulation of fermi level, work function and energy band alignment. *Materials*, 3(11):4892 4914, Nov 2010.

[304] David et al. Scanlon. Band alignment of rutile and anatase TiO_2. *Nature materials*, 12(9):798 801, 2013.

[305] Jenny Schneider, Masaya Matsuoka, Masato Takeuchi, Jinlong Zhang, Yu Horiuchi, Masakazu Anpo, and Detlef W. Bahnemann. Understanding TiO_2 photocatalysis: Mechanisms and materials. *Chemical Reviews*, 114(19):9919 9986, 2014.

[306] Amilcare Iacomino, Giovanni Cantele, Domenico Ninno, Ivan Marri, and Stefano Ossicini. Structural, electronic, and surface properties of anatase TiO_2 nanocrystals from first principles. *Physical Review B - Condensed Matter and Materials Physics*, 78(7):1 11, 2008.

[307] Andrew J. Haring, Spencer R. Ahrenholtz, and Amanda J. Morris. Rethinking band bending at the p3ht-TiO_2 interface. *ACS Applied Materials and Interfaces*, 6(6):4394 4401, 2014.

[308] James Kolodzey, Ahmed Chowdhury, Thomas N. Adam, Guohua Qui, I. Rau, Johnson Olufemi Olowolafe, John S. Suehle, and Yuan Chen. Electrical conduction and dielectric breakdown in aluminum oxide insulators on silicon. *IEEE Transactions on Electron Devices*, 47(1):121 128, 2000.

[309] K Gloos, P J Koppinen, and J P Pekola. Properties of native ultrathin aluminium oxide tunnel barriers. *Journal of Physics Condensed Matter*, 15(10):1733 1746, 2003.

[310] D M Schaefer, P F P Fichtner, M Carara, L F Schelp, and L S Dorneles. Tunnelling barriers. *Journal of Physics D Applied Physics*, 44(13):135403, 2011.

[311] G.a. Garcia, R.E. Reedy, and M.L. Burgener. High-quality cmos in thin (100 nm) silicon on sapphire. *IEEE Electron Device Letters*, 9(1):32 34, 1988.

[312] Robb a. Johnson, Paul R. De La Houssaye, Charles E. Chang, Pin Fan Chen, Michael E. Wood, Graham a. Garcia, Isaac Lagnado, and Peter M. Asbeck. Advanced thin-film silicon-on-sapphire technology microwave circuit applications. *IEEE Transactions on Electron Devices*, 45(5):1047 1054, 1998.

[313] Daniel Kaelblein, Hyeyeon Ryu, Frederik Ante, Bernhard Fenk, Kersten Hahn, Klaus Kern, and Hagen Klauk. High-performance zno nanowire transistors with aluminum top-gate electrodes and naturally formed hybrid self-assembled monolayer/AlO_x gate dielectric. *ACS Nano*, 8(7):6840 6848, 2014.

[314] Kang Dae Kim and Chung Kun Song. Low voltage pentacene thin film transistors employing a self-grown metal-oxide as a gate dielectric. *Applied Physics Letters*, 88(23):2004 2007, 2006.

[315] Byungha Shin, Justin R. Weber, Rathnait D. Long, Paul K. Hurley, Chris G. Van De Walle, and Paul C. McIntyre. Origin and passivation of fixed charge in atomic layer deposited aluminum oxide gate insulators on chemically treated inGaAs substrates. *Applied Physics Letters*, 96(15):2013 2016, 2010.

[316] Eun Ji Kim, Lingquan Wang, Peter M. Asbeck, Krishna C. Saraswat, and Paul C. McIntyre. Border traps in Al_2O_3/ In0.53Ga0.47As (100) gate stacks and their passivation by hydrogen anneals. *Applied Physics Letters*, 96(1):2008 2011, 2010.

[317] Jenny Hu and H.-S. Philip Wong. Effect of annealing ambient and temperature on the electrical characteristics of atomic layer deposition Al_2O_3/In0.53Ga0.47As metal-oxide-semiconductor capacitors and mosfets. *Journal of Applied Physics*, 111(4):0 8, 2012.

[318] Young Ho Do, June Sik Kwak, Jin Pyo Hong, Kyooho Jung, and Hyunsik Im. Al electrode dependent transition to bipolar resistive switching characteristics in pure TiO_2 films. *Journal of Applied Physics*, 104(11):114512, 2008.

[319] Seisuke Nigo, Masato Kubota, Yoshitomo Harada, Taisei Hirayama, Seiichi Kato, Hideaki Kitazawa, and Giyuu Kido. Conduction band caused by oxygen vacancies in aluminum oxide for resistance random access memory. *Journal of Applied Physics*, 112(3), 2012.

[320] G. W. Paterson, S. J. Bentley, M. C. Holland, I. G. Thayne, J. Ahn, R. D. Long, P. C. McIntyre, and a. R. Long. Admittance and subthreshold characteristics of atomic-layer-deposition Al_2O_3 on in 0.53ga 0.47as in surface and buried channel flatband metal-oxide-semiconductor field effect transistors. *Journal of Applied Physics*, 111(10):0 7, 2012.

[321] Thomas Hartman and Jay Chivian. Electron tunneling through thin aluminum oxide films. *Physical Review*, 134(4A):A1094 A1101, 1964.

[322] M. Zemanova Dieskova, a. Ferretti, and P. Bokes. Tunneling through al/AlO_x/al junction - analytical models and first-principles simulations. *Physical Review B - Condensed Matter and Materials Physics*, 87(19):1 8, 2013.

[323] Javier Carrasco, José Gomes, and Francesc Illas. Theoretical study of bulk and surface oxygen and aluminum vacancies in α-Al_2O_3. *Physical Review B*, 69(6):1 13, 2004.

[324] Katsuyuki Matsunaga, Tomohito Tanaka, Takahisa Yamamoto, and Yuichi Ikuhara. First-principles calculations of intrinsic defects in Al_2O_3. *Physical Review B*, 68(8):1 9, 2003.

[325] J. R. Weber, A. Janotti, and C. G. Van de Walle. Native defects in Al_2O_3 and their impact on iii-v/Al_2O_3 metal-oxide-semiconductor-based devices. *Journal of Applied Physics*, 109(3):033715, 2011.

[326] Minseok Choi, Anderson Janotti, and Chris G. Van de Walle. Native point defects and dangling bonds in α-Al_2O_3. *Journal of Applied Physics*, 113(4):044501, 2013.

[327] Christoph Erlen, Paolo Lugli, and Senior Member. Analytical model of trapping effects in organic thin-film transistors. *IEEE Transactions on Electron Devices*, 56(4):546 552, 2009.

[328] C Erlen, F Brunetti, and P Lugli. Trapping effects in organic thin film transistors. *IEEE Proceedings on Electron Devices*, 78(c):3 6, 2006.

[329] M. Städele, F. Sacconi, a. Di Carlo, and P. Lugli. Enhancement of the effective tunnel mass in ultrathin silicon dioxide layers. *Journal of Applied Physics*, 93(5):2681, 2003.

[330] Herbert Schroeder, Ramanathaswamy Pandian, and Jun Miao. Resistive switching and changes in microstructure. *physica status solidi (a)*, 208(2):300 316, 2011.

[331] Kyung Jean Yoon, Seul Ji Song, Jun Yeong Seok, Jung Ho Yoon, Tae Hyung Park, Dae Eun Kwon, and Cheol Seong Hwang. Evolution of the shape of the conducting channel in complementary resistive switching transition metal oxides. *Nanoscale*, 6(4):2161 9, 2014.

[332] Duo Li, Maozhi Li, Ferdows Zahid, Jian Wang, and Hong Guo. Oxygen vacancy filament formation in TiO_2 a kinetic monte carlo study. *Journal of Applied Physics*, 112(7), 2012.

[333] Miao Hu, Yu Wang, Qinru Qiu, Yiran Chen, and Hai Li. The stochastic modeling of TiO_2 memristor and its usage in neuromorphic system design. In *Design Automation Conference (ASP-DAC), 2014 19th Asia and South Pacific*, pages 831 836, Jan 2014.

List of Own Publications and Conference Contributions

B. Weiler, A. Gagliardi, P. Lugli.
KMC-simulation of Defects in Anatase Titanium Dioxide.
J. Phys. Chem. C, 2016, 120 (18), pp 10062 10077 2016-03, 2016

B. Weiler, T. Haeberle, A. Gagliardi, P. Lugli.
KMC-simulation of plasma-grown Al-AlO_x-Au-structures - Impact of Defect Levels.
Kinetic Monte Carlo of transport processes in Al/AlOx/Au-layers: Impact of defects. AIP Advances 6, 095112 (2016) 2016-09, 2016

B. Weiler, R. Nagel, T. Albes, T. Haeberle, S. Mendisch, A. Gagliardi, P. Lugli.
Electrical and morphological characterization of transfer-printed Au/Ti/TiO_x/p^+Si-nano- and microstructures with plasma-grown oxide layers.
J. Appl. Phys. 119, 145106 (2016) 2016-04, 2016

M.A. Niedermeier, G. Tainter, B. Weiler, P. Lugli, and P. Müller-Buschbaum.
Fabrication of hierarchically structured titania thin films via combining nano-imprint lithography with block copolymer assisted sol-gel templating.
J. Mater. Chem. A, 2013,1, 7870-7873, pages 7870 7873, May 2013.

B. Weiler, D. Kalblein, U. Zschieschang, H. Klauk, G. Scarpa, B. Fabel, W. Porod, P. Lugli, and M. Bareiß.
Conductive AFM of transfer printed nano devices.
12th IEEE Conference on Nanotechnology (IEEE-NANO), pages 1 5. IEEE Xplore Digital Library, Aug 2012.

B. Weiler, C. Ostermayr, U. Stimming, and G. Scarpa.

Nanoimprinting and nanotransfer for electrochemical systems.
The Energy and Materials Research Conference (EMR2012), Jun 2012.

K. Schönleber, B. Weiler, G. Scarpa, P. Lugli, and K. Krischer.
Size dependence of the photoelectrochemical properties of gold structures on p-type silicon.
The 63rd Annual Meeting of the International Society of Electrochemistry, Electrochemistry for Advanced Materials, Technologies and Instrumentation, Prague, Czech Republic, August 19-24, 2012., Aug 2012.

K. Schönleber, B. Weiler, G. Scarpa, P. Lugli, and K. Krischer.
Photoelectrochemical properties of gold structures on p-type silicon.
The 63rd Annual Meeting of the Int. Society of Electrochemistry, Electrochemistry for Advanced Materilas, Technologies and Instrumentation, 2012.

K. Schönleber, B. Weiler, G. Scarpa, P. Lugli, and K. Krischer.
Photoelectrochemical activity of metal arrays on p-type Si.
Fundamental and Engineering Needs for Sustainable Development, Electrochemistry 2012, Munich, Germany, 2012.

List of Acronyms

μCP	micro-Contact-Printing
2D	Two-Dimensional
3D	Three-Dimensional
AFM	Atomic Force Microscopy
ALD	Atomic Layer Deposition
an, anode	anode
ASL	Anti-Sticking-Layer
B3LYP	Becke 3-Parameter Lee-Yang-Parr
BTO	$BaTiO_3$
ca, cath	cathode
c-AFM	conductive Atomic Force Microscopy
CB	Conduction Band
CBM	Conduction Band Minimum
CBO	Conduction Band Offset
CNL	Charge Neutrality Level
CNT	Carbon Nanotube
CV	Capacitance-Voltage
CVD	Chemical Vapor Deposition
DD	drift-diffusion
DFT	Density Functional Theory
DRAM	Dynamic Random Access Memory
DSSC	Dye Sensitized Solar Cell
DT	Direct Tunneling
EBL	Electron Beam Lithography
EDX	Energy Diffraction X-Ray Spectroscopy
EELS	Electron Energy Loss Spectroscopy
el	electrode
EMA	Effective Mass Approximation
EOT	Equivalent Oxide Thickness
FN	Fowler Nordheim
FTO	Fluorine doped Tin Oxide
GGA	Generalized Gradient Approximation

HF	Hydrofluoric Acid
HSE	Heyd-Scuseria-Ernzerhof
ITO	Indium Tin Oxide
ITRS	International Technology Roadmap for Semiconductors
IV	Current-Voltage
jV	Current-density-Voltage
kMC	kinetic-Monte-Carlo
LDA	Local Density Approximation
LDT	Laser Decal Transfer
LED	Light Emitting Diode
MA	Miller-Abrahams
MBE	Molecular Beam Expitaxy
MC	Monte-Carlo
MD	Molecular Dynamics
MIGS	Metal-Induced Gap States
MIM	Metal-Insulator-Metal
MOCVD	Molecular Organic Chemical Vapor Expitaxy
MOS	Metal-Oxide-Semiconductor
MPTAT	Multiple-Phonon Trap Assisted Tunneling
MS	Metal-Semiconductor
NIL	Nanoimprint Lithography
nTP	Nanotransfer Printing
OLED	Organic Light Emitting Diode
ox	oxide
pb	parabolic
PDF	Probability Density Function
PDMS	Polydimethylsiloxane
PE-ALD	Plasma-Enhanced Atomic Layer Deposition
PEDOT:PSS	Poly(3,4-ethylenedioxythiophene) Polystyrene Sulfonate
PES	Photoelectron Spectroscopy
PET	Polyethylene Terephthalate
PF	Poole-Frenkel
PFPE	Perfluoropolyethers
PL	Photoluminescence
PUA	Polyurethane Acrylate
PVD	Physical Vapor Deposition
ReRAM	Resistive Random Access Memory
RIE	Reactive Ion Etching
RPS	Photoelectron Spectroscopy
RT	room temperature
SAM	Self-Assembled Monolayer
SE	Schottky Emission

SEM	Scanning Electron Microscopy
SFIL	Step-and-Flash Imprint Lithography
SNAP	Superlattice Nanowire Patterns
STM	Scanning Tunneling Microscopy
STO	$SrTiO_3$
STS	Scanning Tunneling Spectroscopy
TAT	Trap-Assisted-Tunneling
TCO	Transparent Conductive Oxide
UPS	Ultraviolet Photon Spectroscopy
UV	Ultra-Violet
VB	Valence Band
WKB	Wentzel Kramer Brillouin
XAS	X-ray Absorption Spectroscopy
XPS	X-ray Photoelectron Spectroscopy
ZNN	Zentrum für Nanotechnologie und Nanomaterialien

[redacted]

[redacted]

Assurance

Surname:	**Weiler**
Forename:	**Benedikt**

I assure the single handed composition of this PhD thesis, only supported by the declared resources.

(Place, date) (Signature)